Numerical studies of the interstellar medium on galactic scales

Numerical studies of the interstellar medium on galactic scales

Proefschrift

ter verkrijging van
de graad van Doctor aan de Universiteit Leiden,
op gezag van de Rector Magnificus Dr. D. D. Breimer,
hoogleraar in de faculteit der Wiskunde en
Natuurwetenschappen en die der Geneeskunde,
volgens besluit van het College voor Promoties
te verdedigen op woensdag 16 maart 2005
te klokke 16.15 uur

door

Federico Inti Pelupessy

geboren te Callao, Peru
in 1977

Promotiecommissie

Promotor: Prof. dr. V. Icke
Co-promotor: Dr. P. P. van der Werf

Referent: Prof. dr. L. Hernquist (Harvard University)

Overige leden: Dr. S. Portegies Zwart (Universiteit van Amsterdam)
Dr. E. Tolstoy (Rijksuniversiteit Groningen)
Prof. dr. M. A. M. van de Weygaert (Rijksuniversiteit Groningen)
Prof. dr. H. J. Habing
Prof. dr. P. T. de Zeeuw

Contents

1 **Introduction** 1
- 1.1 Star forming galaxies 2
- 1.2 The challenge of modelling galaxies 3
- 1.3 Outline of the thesis 5
- 1.4 Future Prospects 6

2 **Global models for the interstellar medium** 9
- 2.1 Introduction 9
- 2.2 The N-body/SPH method 10
- 2.3 Physical processes of the ISM 13
- 2.4 Equilibrium models 20
- 2.5 Star formation and its effects 24
- 2.6 Putting it all together 29
- 2.7 Discussion 34
- 2.8 Conclusions 38

3 **Feedback in SPH simulations of galaxies** 41
- 3.1 Introduction 41
- 3.2 Smoothed particle hydrodynamics 43
- 3.3 Supernova feedback methods 44
- 3.4 Sedov blast wave test 47
- 3.5 Feedback in dwarf galaxies 49
- 3.6 Conclusions 60

4 **Periodic bursts of star formation in irregular galaxies** 63
- 4.1 Introduction 63
- 4.2 Method 65
- 4.3 Simulation results 70
- 4.4 Star formation: comparison with observations 74
- 4.5 Discussion & conclusions 75

5 **Small star forming galaxies: the role of gas and halo parameters** 81
- 5.1 Introduction 81
- 5.2 Method 83
- 5.3 Initial conditions 85
- 5.4 Results 88

5.5 Observational properties of simulated galaxies 90
5.6 Discussion and conclusions 92

6 Molecular gas and star formation 95
6.1 Introduction 95
6.2 H_2 formation and destruction 97
6.3 Implementation 105
6.4 Application to a dwarf galaxy model 109
6.5 Results for the dwarf galaxy model 111
6.6 Conclusions 120

7 Density Estimators in Particle Hydrodynamics 125
7.1 Introduction 126
7.2 DTFE and SPH density estimates 128
7.3 Case study: two-phase interstellar medium 131
7.4 The DTFE particle method 135
7.5 Delaunay tessellations and ‘moving grid’ hydrocodes 137
7.6 Summary & discussion 138

Appendix 142

Samenvatting 145

Curriculum vitae 149

Nawoord 150

Chapter 1

Introduction

How do galaxies work? The question may sound a bit odd, but it is the question that, in essence, galactic astronomers are trying to answer. For good reasons. The Galaxies are the most visible components of the universe. Their stars and black holes are the main sources of energy and metals after the Big Bang. Galaxies are the places where solar systems like our own form, and the dynamic and chemical evolution of our own galaxy has determined the environment from which our solar system emerged. The question how galaxies are formed and how they evolve is one of the most difficult and most interesting in astrophysics today.

Some aspects of galaxy evolution are relatively well understood. Progress on the collisionless gravitational dynamics of stars has been made in strides, and for stellar systems the distribution functions describing the population of the different possible orbits in the galaxy potential can be determined in great detail from integral field spectroscopy units (de Zeeuw et al. 2002, Cappellari et al. 2004). Also, the initial conditions of galaxy formation are becoming clear. The Λ-cold dark matter (ΛCDM) model shows very good agreement with observations of the variations in the microwave background, the large scale matter distribution and the isotopic abundances of elements formed in the Big Bang (Spergel et al. 2003). This has made the ΛCDM model the standard model of cosmology. It makes precise predictions about the evolution of primordial density fluctuations which form the very beginnings of the galaxy formation process.

However, two unsolved problems remain in the theory of galaxy formation and evolution. The first is the nature of about 90% of the mass of galaxies as deduced from the study of rotation curves (Rubin et al. 1980) that cannot be accounted for. According to ΛCDM this unseen mass cannot be ordinary baryonic matter. Particle physicists believe that there are some good candidates among the weakly interacting sub-atomic particles that are not yet detected but expected to exist. This problem will possibly be solved in the coming years as experiments to detect these dark matter candidates are being conducted.

The second problem, which is the subject of this thesis, concerns the processes of star formation and the drastic effects that result from the input of energy by stellar winds and supernova explosions (and similar problems involving the formation of massive black holes in the centre of galaxies). The problem is that there is no theory for the star formation process in galaxies (Elmegreen 2002). For spiral galaxies, empirical relations based on an instability criterion for self-gravitating disks go some way in explaining star formation (Kennicut 1989), but tests for other objects, such as dwarf galaxies, show a poor relation of this and other simple instability criteria (Hunter & Elmegreen 1998). In addition, current semi-analytic work on galaxy formation and simulations that follow the non-linear collapse of structures in the early universe fail to reproduce the observed properties of galaxies. Given the successes of the ΛCDM model reproducing the large scale matter distribution and microwave background, this is thought to be due to the simplified prescriptions for the star formation and feedback processes used in these simulations. This makes sense: star formation and the associated feedback effects are complex processes that can in principle heavily modify the dynamics of the gas that is ultimately converted into stars.

The aim of this thesis is to use computer simulations to explore the star formation and feedback processes that are at work inside galaxies. All the processes related to star formation can be studied as they are taking place, because it is an ongoing process that can be studied in our own Milky Way and in nearby galaxies under a range of conditions. Therefore it is worthwhile to model current star forming systems. Our goal is then to model the structure of the interstellar medium, star formation patterns and the dynamics of the stars. Where will stars be formed in a given galaxy and how many? What is the effect of star formation on the interstellar medium and further evolution of the galaxy? To what extent does star formation trigger or inhibit further star formation? Doing this we try to match results with observed systems, which gives both insight into the evolution of these systems and constraints on theoretical model parameters.

1.1 Star forming galaxies

Star forming galaxies come in a number of forms. Our own galaxy is a large star forming spiral galaxy. It has a mass of 10^{11} $\mathrm{M}_\odot$ in stars, 10^{10} $\mathrm{M}_\odot$ in gas and a star formation rate of approximately 1 $\mathrm{M}_\odot$/yr. Spiral galaxies come in a variety of sizes with stellar masses of $10^9 - 10^{11}$ $\mathrm{M}_\odot$ and typical gas contents of about 10%. They form stars scattered over the disk in a characteristic spiral pattern, which can take the form of a classical ‘grand design’ spiral.

The most active star forming systems are mergers of gas rich spiral galaxies. They can show very high (> 100 $\mathrm{M}_\odot$/yr) rates of star formation, often obscured by dust, rendering them extremely bright in the infrared. It is thought that all Ultra Luminous Infrared Galaxies (ULIRGs) are merger events (Sanders & Mirabel 1996). These objects are, with their luminosities exceeding 10^{12} $\mathrm{L}_\odot$ among the brightest objects in the universe. At least part of current elliptical galaxies may very well be remnants from such mergers, although it remains to be seen if this formation scenario holds up against direct observation of the evolution of Ellipticals (e.g. van der Wel et al. 2004).

More modest is the group of dwarf irregular (dIrr) galaxies, with masses of $10^7 - 10^9$ $\mathrm{M}_\odot$. They are generally gas rich systems with gas fractions that can exceed 50%. These small star forming galaxies are similar to spiral galaxies in the sense that their stars and gas are distributed in a disk, but they show a very different pattern of star formation. The star formation is scattered in an irregular patchy structure. Moreover, dIrr form stars at widely different efficiencies, varying four orders of magnitude in star formation rate per unit area (Hunter 1997). They range from blue compact dwarfs, which are characterized by a strong central star bursts to low surface brightness dwarfs which are almost too faint to be detected.

These dIrr galaxies form interesting model systems: the facts that they do not show spiral structure and exhibit solid body rotation means that the star formation processes in these systems take place in its most simple form, without the effects of spiral density waves or shear. In this sense these systems are ideal star formation "laboratories." In addition their small sizes mean that we can simulate them easier at a given spatial resolution. For these reasons we will use dwarf galaxies extensively as tests and applications of our model.

In all star forming systems the same basic physical processes are at work. Star forming systems may differ in their physical properties -size, distribution of matter or chemical composition- but the basic interplay between the interstellar medium collapsing into stars and young stars injecting energy back into the surrounding gas, is the same. Thus the insights that we gain through the modelling of dIrr systems are generally applicable.

1.2 The challenge of modelling galaxies

To follow in sufficient detail the star formation processes we must be able to follow the collapse of gas due to gravitational and thermal instabilities, have a prescription for star formation, account for heating and stirring of the interstellar medium due to intense radiation, stellar winds and supernova explosions emanating from young star clusters, and to be able to follow the gas-dynamical reaction to these violent processes. We will discuss briefly the concepts behind the modelling of gravitational dynamics, the physics of ISM and the method we will use to model star formation.

The method we use for simulating galaxies is the N-body/smoothed particle hydrodynamics (SPH) method (Hernquist & Katz 1989). Here stars and gas are represented by particles. Hence, to include self-gravity, we must solve the gravitational N-body problem. In principle this is a matter of calculating all the pairwise gravitational forces. This is costly in terms of computing power, needing $\mathrm{O}(\mathrm{N}^2)$ operations per force evaluation (although see Makino et al. 2003 for hardware solutions to this problem). A number of approximate methods, sacrificing accuracy for speed, have been devised. We use the Barnes-Hut (BH) method (Barnes & Hut 1986).

1.2.1 The interstellar medium

The interstellar medium consists of a number of phases with differing physical properties. It ranges from dense molecular clouds to the neutral phases, cold and warm, to hot ionized gas. An overview of the ISM in the solar vicinity is given in Table 1.1. The different phases are intermixed in a complex, frothy, fractal-like pattern, with shells of hot gas, filaments of neutral gas and knots of dense clouds. The mass fractions and volume filling factors of the various phases of the ISM that are given in Table 1.1 are expected to vary according to local conditions. However, the different phases should be present everywhere where stars form, as these phases arise naturally from

Table 1.1: Overview of the phases of the ISM in the solar vicinity. Given are the densities n, temperatures T, volume filling factors $\mathrm{f_{vol}}$, mass fractions $\mathrm{f_{mass}}$ and fractions $\mathrm{f_E}$ of total ISM thermal energy in the respective phases (Cox 1999).

component	$\langle \mathrm{n} \rangle$	T	$\mathrm{f_{vol}}$	$\mathrm{f_{mass}}$	$\mathrm{f_E}$
H_2	> 100	10	0.001	0.5	1.5×10^{-3}
cold HI	$10 - 100$	100	0.02	0.3	0.01
warm HI	$0.1 - 10$	8000	0.44	0.15	0.4
HII regions	$10 - 10^4$	8000	0.04	0.01	0.03
Hot H^+	< 0.01	10^6	0.5	0.002	0.5

the star formation process, with molecular clouds being the sites of star formation, and heating by the stars producing ionized gas.

The gas physics in our simulations is a representation mainly of the neutral gas. An important feature of the neutral interstellar medium is its two phase nature. Field (1965) considered the stability of dilute gasses and found that a two phase medium of cold and warm gas arises naturally under quiet general conditions on the cooling properties of the gas. This basic picture can be applied to the neutral phases of the ISM. It turns out that the properties of the cold and warm neutral medium could be explained in a model where they were heated by cosmic rays (Field et al. 1969). Recent modelling of the thermal equilibrium properties of the neutral phases by Wolfire et al. (1995, 2003) incorporating a wider range of processes, still retains this thermal instability. A major criticism of this picture may be that it does not account for time dependent processes. In fact, observations show large gas fractions with temperatures in the unstable regime (Heiles & Troland 2003, Kanekar 2003). Modern high resolution simulations of the thermal instability (Kritsuk & Norman 2002), show that a time varying UV field may induce ISM turbulence. The models we develop to calculate the non-equilibrium thermal evolution of the gas has similar equilibrium properties as the models of Wolfire et al. (1995, 2003).

1.2.2 Star formation and feedback

The processes of star formation and the stellar wind and supernova feedback from young stars are the most critical ingredients of the model. We cannot follow the collapse, fragmentation and accretion processes that give rise to individual stars in a simulation that follows galaxy scale evolution. All giant molecular clouds (GMCs), which are the sites of most star formation, seem to produce similar populations of stars. Observations are consistent with a distribution of the number of stars formed of different masses that is the same everywhere, regardless of environment (except maybe for the most extreme metal poor or UV irradiated regions, e.g. Lamers et al. 2002). This distribution of initial masses is well approximated by a Salpeter initial mass function (IMF). What remains is to identify the regions of the ISM where GMCs start collapsing and determine the efficiency of star formation. To do this, we will use the method developed by Gerritsen & Icke (1997), which is based on the most simple criterion possible, namely one based on the Jeans instability.

Apart from maintaining the hot ionized medium, supernova and stellar wind feedback can have a profound effect on the surrounding ISM. On the one hand it stops the star formation locally, but it can enhance the star formation further out by compressing clouds. The collective effect of the young massive stars in an OB-association will form a hot bubble in the ISM that can sweep up material that can become unstable to star formation. The question to what extent this can give rise to propagating star formation is difficult and probably this depends on local conditions. A problem for any simulation that includes supernova feedback is that a naive implementation of the energy injection as a heating term may give rise to serious errors in a cooling medium such as the ISM (Katz 1992, Fragile et al. 2003). Part of this thesis is devoted to development of a good method to account for supernova feedback.

1.3 Outline of the thesis

Chapter 2 presents the basic model of the interstellar medium that we will use to simulate galaxy sized objects. This is an extension of the model used by Gerritsen & Icke (1997) and Bottema (2003). We include for the first time realistic photoelectric heating efficiencies and we solve for the ionization, invoking cosmic rays as ionizing agent. Star formation and feedback are included, using simple but realistic prescriptions, resulting in self-regulated star formation. Different assumptions regarding cooling, heating and ionization are tested using a simple model of a star forming galaxy. The model is compared with previous models used in galactic simulations. We find that proper inclusion of stellar feedback is essential for modelling the interstellar medium.

Chapter 3 examines two new methods of implementing supernova and stellar wind feedback in N-body/SPH simulations of galaxies. The first is based upon the return of energy as random motions in the gas. The second method is based on the equations of motion of an ordinary SPH particle in the zero mass limit: we construct a separate type of particle, which we will call a *pressure particle*, that acts on the gas through these equations. Such a particle will be associated to each newly born stellar particle. It is checked by comparing to simple particle heating that both these methods give acceptable solutions to the Sedov blast wave test. The new methods are then tested in a dwarf galaxy model, where it is shown that they do not suffer from the problems of conventional feedback implementations. We also examine the relation between HI properties and star formation, showing that our model reproduces observed correlations.

The above ISM and feedback models are then applied to the evolution of an isolated dwarf galaxy in **Chapter 4**. Depending on the strength of the feedback, the modelled dwarf galaxy shows periodic or quasi-periodic bursts of star formation of moderate strength. The period of the variation is related to the dynamical timescale, of the order of 1.5×10^8 yr. We show that the results of these simulations are in good agreement with observations of dwarf irregulars (dIrr) and that the peculiar kinematic and morphological properties of these objects, as revealed by high resolution HI studies, are reproduced. These results are discussed in the context of recent surveys of dwarf galaxies and it is pointed out that, if the star formation pattern of our model galaxy is typical of dwarf irregulars, this could explain the scatter of observed properties of dwarf galaxies. Specifically, the time-sampled distribution of the ratio between the instantaneous star formation rate and its mean is shown to match the distribution in an observed sample of dwarf galaxies.

Star forming dwarf galaxies are further examined in **Chapter 5**, where we focus on the role of the observed structural differences between blue compact dwarfs (BCDs) and dwarf Irregular (dIrr) galaxies. Models with different gas and halo distributions are run. The resulting galaxies show a variety of star formation patterns. Galaxies with a high central gas surface density show high star formation rates, while the presence of a high central halo density will produce a central star burst. By comparing the simulations with observations it is concluded that both high central gas surface and a high central halo density are necessary for a system to exhibit BCD features.

Chapter 6 presents a method to incorporate the formation of molecular gas as part of the model. This is done by formulating a sub-grid model for molecular clouds, assumed to obey well-known scaling relations, and solving for the HI$\leftrightarrow$$H_2$ balance set by the H_2 formation on dust grains and its FUV-induced photodissociation. This allows tracking of the evolution of the molecular gas seamlessly along with that of its precursor cold neutral medium HI gas. The method is applied to identify molecular regions of the interstellar medium during the evolution of a typical dwarf galaxy. We find a significant dependence of the HI $\rightarrow$ H_2 transition and the resulting H_2 gas mass on the ambient metallicity and the H_2 formation rate.

In **Chapter 7** we show that a particle hydrodynamics method based on the Delaunay triangulation field estimate (DTFE, Schaap & van de Weygaert 2000) holds special promise as an alternative to conventional SPH. The reason for this is that the DTFE density estimate is fully adaptive: the particle distribution itself generates the density field - there is no arbitrary choice kernel function or local lengthscale involved. We will show that especially in cases where the density field shows large contrasts and/or has large anisotropic features, like sheets or filaments, the DTFE estimate is markedly superior to the kernel density estimate of the local density. For a hydrodynamic method based on the DTFE this will mean increased resolving power for a given number of particles. We also show that the DTFE estimate has convenient properties that will make the implementation of viscous forces better defined.

1.4 Future Prospects

The methods we have developed are suited to a wide range of problems. Two immediate applications are to explore the evolution of dwarf galaxies further and to model molecular gas in mergers.

In view of the recent realization that there is a deficit in the number of observed small galaxies as compared to predictions of cold dark matter models of galaxy formation (Klypin et al. 1999), it is interesting to consider what happens to galaxies of progressively smaller masses. From the results obtained for dIrr we may expect a similar behavior of varying star formation, but with variations on longer time scales (because of the scaling of the dynamical timescales as $\rho^{-0.5}$) and greater in amplitude (because the feedback becomes relatively stronger as the escape velocity decreases). Ultimately, halos will be too small to retain their ISM, leaving them bare (Ferrara & Tolstoy 2000). The mass ranges for which this happens, the influence of other galactic parameters, and the timescales on which these processes take place will be of interest to validate cosmological and galaxy formation models.

Recent simulations (Mayer et al. 2001, Pasetto et al. 2003) have shown that a transition from dIrr to dE or dwarf Spheroidal (dSph) is plausible as a result of the repeated action of tidal fields if the dIrr orbits a large galaxy. It has not been conclusively determined whether a transition from dIrr to dE is to be expected in general. Various groups have put forward arguments in favour (Davies & Phillipps 1988) and against (Bothun et al. 1986, Marlowe et al. 1999) such a descendancy for the dE. Simulations testing a wider range of galactic properties and following the evolution on longer time scales may answer whether this is a viable scenario and whether we can put the various classes of small galaxies into an unified evolutionary framework.

An interesting application of the H_2 formation model developed in Chapter 6 would be the case of colliding galaxies. Systems like the Antennae (NGC 4038/4039), Arp 220 and NGC 6240, which are all merging systems in different stadia of their evolution, show large concentrations of molecular gas residing in between the nuclei of the original galaxies (e.g. Stanford et al. 1990, van der Werf et al. 1993), preceding or concurrent with the starbursts associated to these events. Hithero little work has been done in the context of numerical simulations to model the global distribution of H_2 gas and its relation to star formation, although a lot of work has been done on these systems using conventional N-body and N-body/SPH simulations (e.g. Toomre & Toomre 1972, Barnes 1992, Mihos & Hernquist 1994). The H_2 formation model is ideally suited to be applied to these kind of systems because it is fast and integrates seamlessly with these N-body simulations.

A number of improvements could be made to the code. The model should be extended to include enrichment of the interstellar medium and follow the chemodynamical evolution using metallicity dependent yields. Also, the star formation recipe may be refined further, possibly based on the identification of star forming clouds rather than on local criteria, to make it more realistic in extreme environments. Ultimately such developments will allow us to follow the evolution of galaxies all the way from early universe to the present.

Acknowledgments. I would like to thank Natan de Vries for working with me on Chapter 5, Padelis Papadopoulos for co-authoring Chapter 6, and Willem Schaap for our pleasant collaboration on Chapter 7. I would also like to thank Jeroen Gerritsen and Roelof Bottema for providing software and analysis tools.

This work was sponsored by the stichting Nationale Computerfaciliteiten (National Computing Facilities Foundation) for the use of supercomputer facilities, with financial support from the Nederlandse Organisatie voor Wetenschappelijk Onderzoek (Netherlands Organisation for Scientific Research, NWO)

References

Barnes, J. & Hut, P., 1986, *Nature* **324**, 446

Barnes, J. E., 1992, *ApJ* **393**, 484

Bothun, G. D., Mould, J. R., Caldwell, N., & MacGillivray, H. T., 1986, *AJ* **92**, 1007

Bottema, R., 2003, *MNRAS* **344**, 358

Cappellari, M. et al., 2004, in *Coevolution of Black Holes and Galaxies*

Cox, A. N., 1999, *Allen's Astrophysical Quantities*, Springer-Verlag, fourth edition

Davies, J. I. & Phillipps, S., 1988, *MNRAS* **233**, 553

de Zeeuw, P. T. et al., 2002, *MNRAS* **329**, 513

Elmegreen, B. G., 2002, *ApJ* **577**, 206

Ferrara, A. & Tolstoy, E., 2000, *MNRAS* **313**, 291

Field, G. B., 1965, *ApJ* **142**, 531

Field, G. B., Goldsmith, D. W., & Habing, H. J., 1969, *ApJ* **155**, L149+

Fragile, P. C., Murray, S. D., Anninos, P., & Lin, D. N. C., 2003, *ApJ* **590**, 778

Gerritsen, J. P. E. & Icke, V., 1997, *A&A* **325**, 972

Heiles, C. & Troland, T. H., 2003, *ApJ* **586**, 1067

Hernquist, L. & Katz, N., 1989, *ApJS* **70**, 419

Hunter, D., 1997, *PASP* **109**, 937

Hunter, D. A., Elmegreen, B. G., & Baker, A. L., 1998, *ApJ* **493**, 595

Kanekar, N., Subrahmanyan, R., Chengalur, J. N., & Safouris, V., 2003, *MNRAS* **346**, L57

Katz, N., 1992, *ApJ* **391**, 502

Kennicutt, R. C., 1989, *ApJ* **344**, 685

Klypin, A., Kravtsov, A. V., Valenzuela, O., & Prada, F., 1999, *ApJ* **522**, 82

Kritsuk, A. G. & Norman, M. L., 2002, *ApJ* **569**, L127

Lamers, H. J. G. L. M., Panagia, N., Scuderi, S., Romaniello, M., Spaans, M., de Wit, W. J., & Kirshner, R., 2002, *ApJ* **566**, 818

Makino, J., Fukushige, T., Koga, M., & Namura, K., 2003, *PASJ* **55**, 1163

Marlowe, A. T., Meurer, G. R., & Heckman, T. M., 1999, *ApJ* **522**, 183

Mayer, L., Governato, F., Colpi, M., Moore, B., Quinn, T., Wadsley, J., Stadel, J., & Lake, G., 2001, *ApJ* **559**, 754

Mihos, J. C. & Hernquist, L., 1994, *ApJ* **431**, L9

Pasetto, S., Chiosi, C., & Carraro, G., 2003, *A&A* **405**, 931

Rubin, V. C., Thonnard, N., & Ford, W. K., 1980, *ApJ* **238**, 471

Sanders, D. B. & Mirabel, I. F., 1996, *ARA&A* **34**, 749

Schaap, W. E. & van de Weygaert, R., 2000, *A&A* **363**, L29

Spergel, D. N. et al. , 2003, *ApJS* **148**, 175

Toomre, A. & Toomre, J., 1972, *ApJ* **178**, 623

van der Wel, A., Franx, M., van Dokkum, P. G., & Rix, H.-W., 2004, *ApJ* **601**, L5

Wolfire, M. G., Hollenbach, D., McKee, C. F., Tielens, A. G. G. M., & Bakes, E. L. O., 1995, *ApJ* **443**, 152

Wolfire, M. G., McKee, C. F., Hollenbach, D., & Tielens, A. G. G. M., 2003, *ApJ* **587**, 278

Chapter 2

Global models for the interstellar medium

Abstract

Here we present a model of the interstellar medium (ISM) for use in simulations of galaxies. The model includes the main processes important for the neutral ISM. We include for the first time realistic photo-electric heating efficiencies and we solve for the ionization, invoking cosmic rays as ionizing agent. Using an N-body/SPH model of a star forming galaxy, we test models with different assumptions regarding cooling, heating and ionization. Star formation and feedback are included using simple but realistic prescriptions, resulting in self-regulated star formation. We test the influence of metallicity and cosmic ray flux. Varying the chemical abundances, we find that C depletion gives lower star formation, while Fe depletion decreases the amount of cold gas, leaving the star formation rate relatively unaffected. We also compare with previous models and show that if realistic photo-electric heating is used, stellar feedback is essential.

2.1 Introduction

Our understanding of the formation and evolution of galaxies is limited by our knowledge of the behaviour of the interstellar medium. Stellar dynamics and evolution are comparably well understood, and while practical problems remain there is a good understanding of phenomena. Of course, the nature of the dark matter in galaxies is a mystery , but to some extent this is a trivial problem as it only participates, almost by definition, in gravitational dynamics, and the distribution of dark matter on large scales can be reproduced in high detail through N-body simulations. It is not surprising then that a failure to match the observed number of dwarf galaxies and the mismatch in the properties of spirals and ellipticals of the current paradigm of structure formation in the universe, the Λ-cold dark matter (ΛCDM) model, is often attributed to a failure to account properly for physics of the ISM, especially the effects of feedback on the interstellar medium, rather than to defects of the basic properties of dark matter or the nature of gravitational forces in the model.

The state of the ISM determines where and when stars form. On the other hand, stars will seed the ISM with heavy elements and stir up the interstellar gas by putting in mechanical energy through the action of stellar winds, supernova (SN) explosions and UV radiation of young stars. From stellar evolution models the amount of metals, and energy produced are, except maybe for extremely low metallicity stars, well known input parameters.

The complexity of the dynamics and thermodynamics of the ISM have led to a prominence of computer modelling in galactic astrophysics. However the present models for the ISM used for galactic sized objects have been rather limited in the amount of physics that is included in these models. Most models represent the ISM as a smooth fluid, where the temperature of the gas, when not taken to be isothermal, is limited to be above 10^4 K.

In this chapter we will explore global models for the ISM in galaxies, and discuss their implementation in a smoothed particle hydrodynamics (SPH) code. The models we develop can be used to simulate a wide variety of objects and would be useful whenever star formation is important on galactic scales, such as in studies of collisions of galaxies, galaxy formation scenarios or studies of star formation in spiral galaxies or dwarf galaxies.

2.2 The N-body/SPH method

The ISM models we present below will be implemented in a derivative of the N-body/SPH code TREESPH (Hernquist & Katz 1989, Gerritsen 1997, Bottema 2003). The gravitational forces are calculated using the Barnes-Hut algorithm (Barnes & Hut 1986) and gas dynamics using SPH (Monaghan 1992). The models we present here are not limited in their applicability to N-Body/SPH codes: they can be implemented in other types of hydrodynamic codes, like Eulerian grid codes. We have opted for a first implementation into an existing N-body/SPH code, as this method is well suited for problems with open boundary conditions and arbitrary geometries, like galaxy evolution and collision problems. N-body/SPH codes are well established tools for the theoretical astrophysicists, so we will only describe both methods concisely with an emphasis on the most relevant features of the implementation used.

2.2.1 Barnes-Hut treecode

The first ingredient of any self consistent model for galaxies is self gravity, as large scale gravitational instabilities are thought to drive star formation in galaxies. In the context of particle codes a number of different approaches are possible. The most precise solution is simply the brute force method of direct summation (DS) of the pairwise gravitational forces. This is costly, needing $O(N^2)$ operations per force evaluation (although see Makino et al. 2003 for hardware solutions to this problem). Hence a number of approximate methods, sacrificing accuracy for speed, have been devised. We use the Barnes-Hut (BH) method (Barnes & Hut 1986). It is based on the following two concepts: 1) an approximation for the gravitational force of a group of particles by cutting off the multipole expansion after the quadrupole term, and 2) the hierarchical organization of particles in an oct-tree. A force evaluation for a particle is then done by recursive opening of the nodes in the tree, conditional upon a comparison of the size l of the node and the distance d to the centre of mass of the node:

$$\mathrm{l}/\mathrm{d} > \theta \tag{1}$$

where the parameter θ of the *cell opening criterion* controls the accuracy of the calculated gravitational forces. The BH method has been widely used in numerical N-body simulations, due to its $\mathrm{O}(\mathrm{N}\ \log \mathrm{N})$ scaling and its ability to be applied efficiently to general mass distributions. In astrophysics the method has found wide application in, for example, cosmological simulations, galaxy collision and star formation simulations. It has been shown that it is generally acceptable to use BH for collisionless N-body dynamics (Barnes & Hut 1989). However the classical BH opening criterion (1) can fail in exceptional circumstances (Salmon & Warren 1994). Also it was shown by Springel et al. (2001) that it will give large fractional force errors if particles are subjected to large cancelling forces such as those experienced in the smooth matter distributions found in the early universe. A similar problem may also occur for galaxy simulations, especially in the central regions of galaxies where particles experience large cancelling forces from the rest of the galaxy. Springel et al. (2001) propose an alternative opening criterion,

$$\mathrm{M}\mathrm{l}^4 > \alpha\, |\mathbf{a}|\, \mathrm{d}^6 \tag{2}$$

where M is the total mass contained in the node, $\mathbf{a}$ is an estimate of the acceleration, in practice this is the acceleration of the previous time step, and α the parameter controlling the accuracy of the force calculation. We have compared the accuracy of the BH criterion and the Springel criterion and found that the latter indeed gives smaller fractional force errors in the central regions of the galaxy.

2.2.2 Smoothed Particle Hydrodynamics

Smoothed Particle Hydrodynamics (Gingold & Monaghan 1977, Lucy 1977) is a particle based method for gas dynamics. It is based on an estimate of the local density of a continuous fluid respresented by a finite set of particles using a kernel function $\mathrm{W}(\mathrm{r}, \mathrm{h})$. Thus, for a set of particles with masses $\mathrm{m_i}$ and smoothing lengths $\mathrm{h_i}$ we have

$$\rho_\mathrm{i} = \sum_\mathrm{j} \mathrm{m_j} \mathrm{W}(|\mathrm{r_i} - \mathrm{r_j}|, \mathrm{h_i}) \tag{3}$$

for the density ρ_i at particle positions $\mathrm{r_i}$. The kernel function W is usually (and also here) taken to be the spline kernel of Monaghan & Lattanzio 1985:

$$\mathrm{W}(\mathrm{r}, \mathrm{h}) = \frac{1}{\pi \mathrm{h}^3} \begin{cases} 1 - \frac{3}{2}\left(\frac{\mathrm{r}}{\mathrm{h}}\right)^2 + \frac{3}{4}\left(\frac{\mathrm{r}}{\mathrm{h}}\right) & 0 \le \mathrm{r} \le \mathrm{h} \\ \frac{1}{4}(2 - \frac{\mathrm{r}}{\mathrm{h}})^3 & \mathrm{h} \le \mathrm{r} \le 2\mathrm{h} \\ 0 & \text{otherwise} \end{cases}$$

The idea of SPH is then to derive equations of motion for the particles starting from Eq. (3). This was originally done by substituting Eq. (3) into the equations of gas dynamics, but this is done more elegantly starting from the discretized Lagrangian for a compressible non dissipative flow, with adiabatic index γ (Rasio 1999),

$$\mathrm{L} = \sum_{\mathrm{i}=1}^{\mathrm{N}} \mathrm{m_i} \left(\frac{1}{2}\mathrm{v_i^2} + \frac{1}{\gamma - 1}\mathrm{A_i}\rho_\mathrm{i}^{\gamma-1} \right) , \tag{4}$$

where $\mathrm{m_i}$ is the mass of particle i ($1 \leq \mathrm{i} \leq \mathrm{N}$), $\mathrm{v_i}$ its velocity, $\mathrm{A_i}$ is the entropic function, defined by ($\mathrm{P_i}$ being the pressure): $\mathrm{P_i} = \mathrm{A_i}\rho_\mathrm{i}^\gamma$. We will formulate the dynamic evolution of the internal energy in terms of this entropic function. The internal energy $\mathrm{u_i}$ itself is obtained through

$$\mathrm{u_i} = \frac{\mathrm{A_i}}{\gamma - 1}\rho_\mathrm{i}^{\gamma-1} \tag{5}$$

Treating the flow adiabatic for the moment and assuming constant smoothing lengths $\mathrm{h_i}$, it is easy to recover the SPH formalism from the Lagrangian equations of motion for $(\mathbf{q}, \mathbf{p}) = (\mathrm{r_1}, ..\mathrm{r_N}, \mathrm{v1}, .., \mathrm{v_N})$. Notice that the procedure we have outlined here is not specific for the kernel based density estimate of Eq. (3), indeed in Chapter 7 we will present an alternative method for gas dynamics by using the Delaunay Triangulation Field Estimator for the density, which is a much better density estimate in regions of high density contrasts or anisotropy. The dynamic range of conventional SPH is improved by the use of adaptive smoothing lengths. Normally this is done by choosing the $\mathrm{h_i}$ such that the number of neighbours within a smoothing length $\mathrm{h_i}$ is (more or less) constant for every particle. This introduces errors in energy and/or entropy conservation (Hernquist 1993, Nelson & Papaloizou 1993). This is because the variability of $\mathrm{h_i}$ introduces extra $\nabla \mathrm{h}$ correction terms into the dynamical equations, inclusion of which is, although possible (see Nelson & Papaloizou 1994), cumbersome. An alternative approach is to consider $\mathrm{h_i}$ as dynamic variables in the Lagrangian (4) and introduce constraints which will determine these extra variables (Springel & Hernquist 2002). Taking as the set of constraints

$$\phi = \frac{4\pi}{3}\mathrm{h_i^3}(\rho_\mathrm{i} + \tilde{\rho}) - \mathrm{M_r} = 0 \tag{6}$$

which (for constant density) is simply the requirement that the mass enclosed within a smoothing length is fixed. In this equation $\mathrm{M_r} = \bar{\mathrm{m}}\mathrm{N_{nb}}$ with mean particle mass $\bar{\mathrm{m}}$ and a target number of neighbours $\mathrm{N_{nb}}$. Comparing with Springel and Hernquist (2002) we add a term $\tilde{\rho}$ to limit the smoothing length $\mathrm{h_i}$. Without this term the smoothing length grows as $\mathrm{h_i} \to \infty$ when $\rho_i \to 0$, leading to a very high number of neighbours for particles on the edge of the simulation. A maximum $\mathrm{h^3_{i,max}} = 3\mathrm{M_r}/4\pi\tilde{\rho}$ leads to a minimum $\rho_\mathrm{i,min} = \mathrm{m_i}/\pi\mathrm{h^3_{i,max}} = 4\tilde{\rho}/3\mathrm{N_{nb}}$, which, to ensure errors due to poor sampling for particles with $\rho_\mathrm{i} \lesssim \tilde{\rho}$, are limited, is set to be lower than the intergalactic medium density by a suitable choice of $\tilde{\rho}$.

From the Lagrangian (4) and the constraints (6) the equations of motion follow in the usual way using Lagrange multipliers (for step by step derivation see Springel & Hernquist 2002). Because the potential of the Lagrangian in Eq. (4) is symmetric in the coordinate differences, total energy, entropy momentum and angular momentum will be conserved. The $\nabla \mathrm{h}$ terms are implicitly included to all orders. In our case this yields the following system of dynamic equations we solve in the code, including artificial viscosity terms ($W_{ij}(h_i) = W(|r_i - r_j|, h_i)$):

$$\frac{dv_i}{dt} = -\sum_{j=1}^{N} m_j \left\{ f_i \frac{P_i}{\rho_i^2} \nabla_i W_{ij}(h_i) + f_j \frac{P_j}{\rho_j^2} \nabla_i W_{ij}(h_j) + \Pi_{ij} \nabla \bar{W}_{ij} \right\} \tag{7}$$

with the f_i defined by:

$$f_i = \left(1 + \frac{h_i}{3(\rho_i + \tilde{\rho})} \frac{\partial \rho_i}{\partial h_i} \right)^{-1} \tag{8}$$

The artificial viscosity Π_{ij} is necessary to smooth out discontinuities to resolvable scales, and we can take any one of the standard forms (Monaghan 1992, Hernquist & Katz 1989). Here, $\bar{W}_{ij} = W_{ij}(h_i) + W_{ij}(h_j)$ is a symmetrized form of the kernel. The thermodynamic state of the gas is determined by integrating the entropic function according to

$$\frac{dA_i}{dt} = -\frac{\gamma - 1}{\rho_i^{\gamma}} (\Gamma - \Lambda) + \frac{1}{2} \frac{\gamma - 1}{\rho_i^{\gamma - 1}} \sum_{j=1}^{N} m_j \Pi_{ij} v_{ij} \cdot \nabla_i \bar{W}_{ij} \tag{9}$$

Here Γ and Λ represent the external heating and cooling terms, which will be derived from a consideration of the physical processes that we want to include to model the ISM.

2.2.3 Some notes on implementation

The code we use is written in FORTRAN 90, and parallelised for use on shared memory architectures using OpenMP compiler directives.

We must solve Eq. (6) for the smoothing lengths h_i. This can be done efficiently using Newton-Raphson iteration, seconded by recursive bisection.

2.3 Physical processes of the ISM

Our model for the ISM will be mainly geared towards the representation of the neutral atomic phases of the ISM. Roughly speaking we will follow the ISM of our model galaxies as long as the temperature is higher than 100 K and densities are greater than $100\ \mathrm{cm}^{-3}$. We will consider the formation and subsequent evolution of molecular clouds to be part of the process of star formation. The process of star formation in these clouds is not explicitly present in our model, but implicitly in the recipe for star formation (section 2.5.1).

A comprehensive model for the warm and cold neutral medium (WNM, CNM) that is similar to our model, albeit more extensive, was formulated by Wolfire et al. (1995, 2003). They explored the thermal equilibrium of the neutral ISM, in the context of a static model of the Milky Way. They concluded that their model was consistent with a number of observations, amongst which dust emission and [CII] line observations.

The main ingredients of our model are: cosmic ray regulated ionization, photoelectric heating from polycyclic aromatic hydrocarbons (PAHs) and small grains and

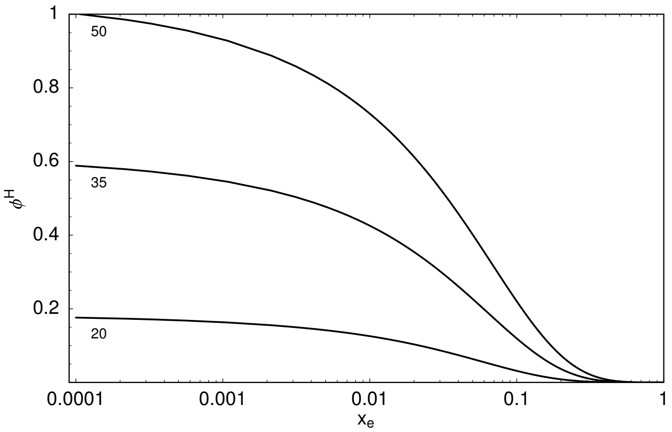

Figure 2.1: Secondary ionization function ϕ^{H} for different electron energies. Curves are labelled with the corresponding energy of the secondary electron (in eV).

realistic cooling by a variety of atomic species. This improves on the treatment of previous models used in galactic simulations by not assuming a priori the ionization and by taking into account the efficiency decrease of photoelectric heating by grain charging. Also our cooling curves are more accurate and composed for arbitrary abundances, which allows us to explore the effect of variations of composition on the ISM.

2.3.1 Ionization

Even neutral interstellar gas retains some ionization. Gerritsen & Icke (1997) found that the results of their model depended on the ionization fraction $\mathrm{x_e} \equiv \mathrm{n_e}/\mathrm{n_H}$ assumed for temperatures below $\mathrm{T} \approx 14000$. For example for $\mathrm{x_e} = 0.1$ they found a star formation rate 4 times higher than for $\mathrm{x_e} = 0.01$ while the amount of cold gas was roughly ten times lower for the low $\mathrm{x_e}$ case. The reason for this is that the cooling power is proportional to $\mathrm{x_e}$. At low temperatures cooling is mainly due, if molecular gas is absent, to excitation of fine structure levels of neutral and ionized species. The excitation efficiency for collisions by electrons is much higher than that of neutral hydrogen, so for quite low ionization levels ($\mathrm{x_e} > 0.001$) the electron fraction will determine the amount of cooling. Gerritsen & Icke (1997) did not solve for the ionization, so they had to assume a value and for their standard model they settled for $\mathrm{x_e} = 0.1$. This seems to be reasonable for the solar neighbourhood (Cox 1990), however one would expect it to vary with local temperature and density, hence it is necessary to solve for ionization.

The CNM and WNM (with temperatures below $\mathrm{T} < 14000$) are too cold for the residual ionization to be explained by collisional ionization equilibrium (CIE). Additional sources of this ionization can be photo-,X-ray and Cosmic ray ionization. As the ISM is opaque to UV photons with energies higher than ionization potential of hydrogen, photo-ionization of hydrogen is generally constrained to HII regions, the immediate surroundings of bright UV sources, active galactic nuclei or star formation regions. We will lump the effect of HII regions together with the effects of stellar winds and supernovae as the mechanical luminosity of young stellar clusters. Photons with energies below 13.6 eV will propagate freely through the ISM, and any elements with ionization potentials less than 13.6 eV will be assumed to be at least singly ionized. Of the elements we include in our model these are C, Fe and Si. In practice the minimum ionization fraction in the simulation will be determined by the abundance of carbon, as it is the most abundant. Ionization of these species is also important for the cooling, in the next section we will see that C^+, Si^+ and Fe^+ are important coolants.

The main source of ionization in the neutral medium is probably collisions with cosmic rays. To calculate the resulting electron fraction $\mathrm{x_e}$, we solve for the ionization equilibrium of H and He only,

$$\alpha^{\mathrm{i}}_{\mathrm{coll}}\mathrm{n_e n_i} + \xi_{\mathrm{CR}}\mathrm{n_i} = \alpha^{\mathrm{i+1}}_{\mathrm{re}}\mathrm{n_e n_{i+}} \tag{10}$$

with the $\mathrm{n_i}$ as the densities of i =H, He, He^+ and He^{++}, $\alpha^{\mathrm{i}}_{\mathrm{coll}} = \alpha^{\mathrm{i}}_{\mathrm{coll}}(\mathrm{T})$ and $\alpha^{\mathrm{i}}_{\mathrm{re}} = \alpha^{\mathrm{i}}_{\mathrm{re}}(\mathrm{T})$ the appropriate collisional ionization and recombination rates. For these we take the fits of Voronov (1997)[1]. Here, ξ_{CR} is the total cosmic ray ionization rate, which is determined by the primary ionization rate ζ_{CR} multiplied by a factor accounting for the secondary ionizations by the energetic electrons produced in primary ionization events (Wolfire et al. 1995),

$$\xi_{\mathrm{CR}} = \zeta_{\mathrm{CR}}\left(1 + \phi^{\mathrm{H}}(\mathrm{E},\mathrm{x_e}) + \phi^{\mathrm{He}}(\mathrm{E},\mathrm{x_e})\right). \tag{11}$$

The functions $\phi^{\mathrm{H}}(\mathrm{E},\mathrm{x_e})$ and $\phi^{\mathrm{He}}(\mathrm{E},\mathrm{x_e})$ give the number of secondary ionizations of hydrogen and helium per primary ionization. These depend on the energy E of the secondary electron (we take a typical value of 35 eV) and the electron fraction $\mathrm{x_e}$. We use the analytic fits for ϕ^{H} and ϕ^{He} provided in the appendix of Wolfire et al. (1995). Qualitatively, the number of secondary electrons increases with E, as expected, while for increasing $\mathrm{x_e}$, it decreases (the secondary electron will loose its energy more easily through Coulomb interactions for high ionization fractions). For the primary ionization rate we take a standard value of

$$\zeta_{\mathrm{CR}} = 1.8 \times 10^{-17}\mathrm{s}^{-1}. \tag{12}$$

Note that the primary cosmic ray ionization rate ζ_{CR} is mainly due to particles with energies below 100 MeV, which are shielded from direct observation by the heliosphere (extrapolation from Pioneer and Voyager data yields a rate of $\zeta_{\mathrm{CR}} = 3 \times 10^{-17}$, Webber 1998) and also expected to vary substantially due to their low travelling lengths. Presumably their production sites are regions of star formation, and calculation of the propagation of these cosmic rays is complicated. The canonical value (12) comes from chemical modelling of molecular clouds (Van Dishoeck & Black 1986) and may not be appropriate for the diffuse ISM (McCall et al. 2003). So the actual value of the cosmic ray flux that is appropriate is uncertain (however this does not mean that details as (11) are superfluous, because it introduces a feedback of $\mathrm{x_e}$ on the ionization rate that is present regardless of the actual value for ζ_{CR}).

The system of Equations (10) is easily solved by iterating over $\mathrm{x_e}$, in practice we also tabulate its solutions for quick referencing by interpolation in temperature T

---

[1] http://www.pa.uky.edu/˜verner/atom.html

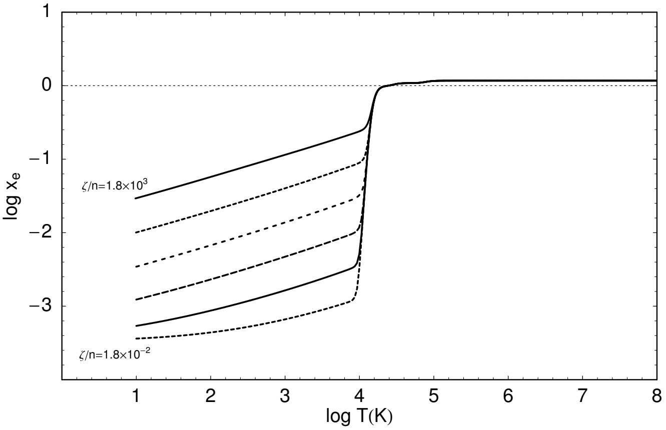

Figure 2.2: Ionization fraction $x_e = n_e/n$ for different values of ζ_{CR}/n, increasing from $\zeta_{CR}/n = 1.8 \times 10^{-2}$ to $\zeta_{CR}/n = 1.8 \times 10^{3}$ in factors of 10.

and ζ_{CR}/n. In Fig. 2.2 we have plotted the resulting ionization fraction for solar metallicities.

We solve for the ionization to get an estimate of x_e. Metals will not contribute significantly and hence we do not solve for their ionization. The abundance of the different ionized species needed for the cooling rates (see below) will be assumed to be in CIE. For calculation of CIE a more complete set of processes including charge exchange is considered (included in the *Doric* package, Raga et al. 1997, Mellema & Lundqvist 2002).

Apart from cosmic ray ionization a seizable contribution is expected from X-ray ionizations. We will not consider these separately, because of the above mentioned uncertainties in the cosmic ray ionization rate, and because the physical process of X-ray ionization is similar to cosmic ray ionization.

2.3.2 Cooling processes

A heated, partially ionized gas cools through the conversion of kinetic energy into luminosity by collision processes, and the efficiency of cooling is a sensitive function of the composition of the gas. The cooling in the low density limit can be approximated by

$$\Lambda = n^2 \Lambda^\star(T) \tag{13}$$

For the cooling curve $\Lambda^\star(T)$ a number of pre-compiled cooling curves for specific metallicities exist (e.g. Dalgarno & McCray 1972, Sutherland & Dopita 1993). We calculate the cooling curve for general abundances using recent atomic data. In Fig. 2.3 we have plotted the cooling curve

$$\Lambda^\star(T) = \sum_{i,j} X_{ij} \left(x_e L^{e}_{X_{ij}}(T) + L^{H}_{X_{ij}}(T) \right) \tag{14}$$

for solar and $0.2\times$ solar metallicity. The functions $L^{e}_{X_{ij}}$ and $L^{H}_{X_{ij}}$ give the cooling power for collisions with electrons and neutral hydrogen of ionization stage j of element i

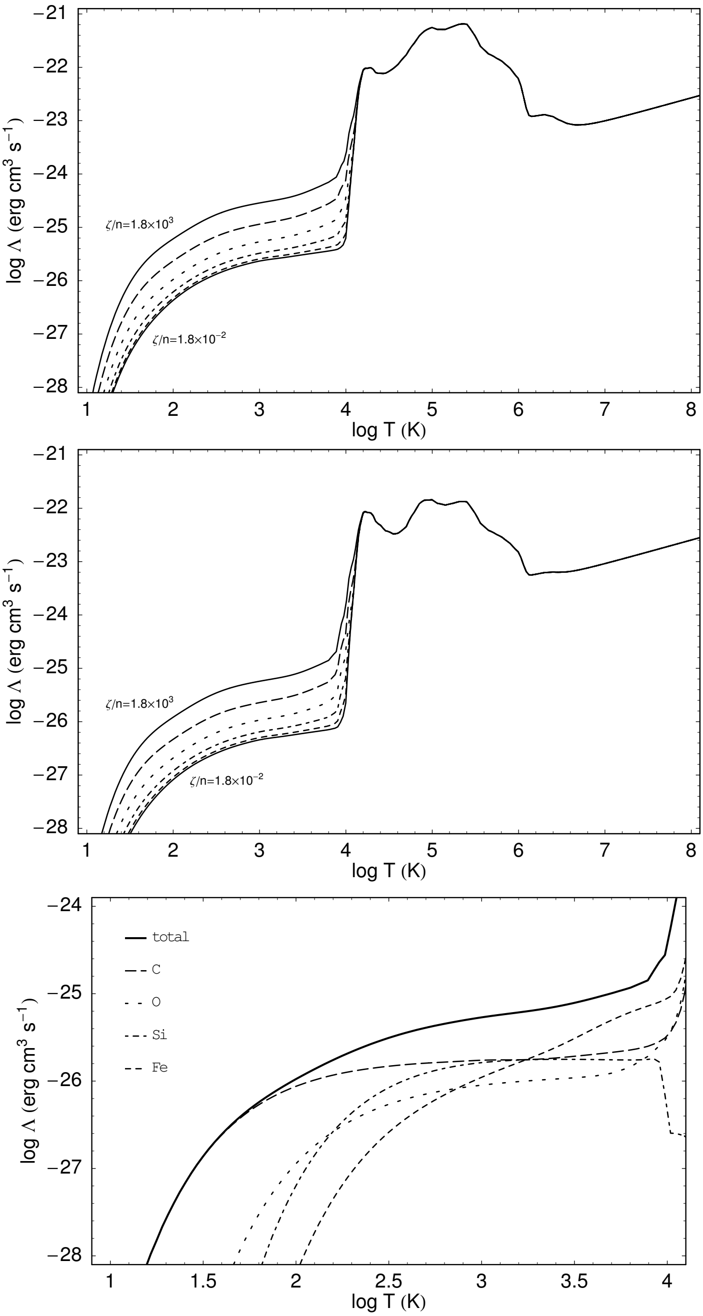

Figure 2.3: Cooling curves. **Top panel:** Cooling curves for $Z = Z_{\odot}$, labelled with values of ζ/n as in Fig. 2.2. **Centre panel:** Cooling curves for $Z = 0.2 \times Z_{\odot}$, idem. **Bottom panel:** contributions to cooling curves for the most important elements, for $\zeta_{\mathrm{CR}}/\mathrm{n} = 18$ and $Z = Z_{\odot}$.

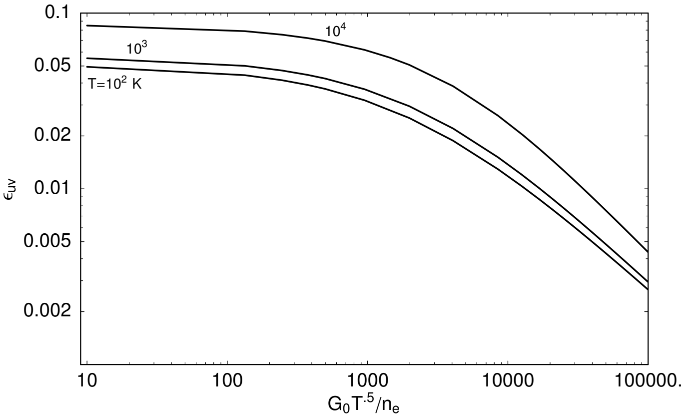

Figure 2.4: Full UV heating efficiency $\epsilon_{\rm UV}$.

with a relative abundance X_{ij}. We take $L^e_{X_{ij}}$ from a recent compilation of atomic data from the *Doric* package (Raga et al. 1997, Mellema & Lundqvist 2002), while we calculate $L^H_{X_{ij}}$, using the *Popratio* program (Silva & Viegas 2001). Also in Fig 2.3 we have plotted the contributions of the various elements to the cooling for the most important coolants. For solar metallicity carbon (in the form of CII) is the main coolant at low temperatures ($T < 1000$ K). Iron is dominant at temperatures between 3000 and 10000 K. Si can also be a substantial coolant at intermediate temperatures (around 1000 K).

Note that apart from the dependency on the composition of the gas, cooling is strongly dependent on the ionization fraction, because $L^e_{X_{ij}}$ is typically a factor 1000 bigger than $L^H_{X_{ij}}$.

2.3.3 Heating processes

The most important heating mechanism in the neutral ISM is photoelectric heating from small grains and PAHs (Watson 1972): UV radiation will heat gas in the presence of dust through the ejection of electrons from these particles. We will use the results of modelling by Bakes & Tielens (1994) to calculate this heating. The heating for a radiation field G_0, normalised to Habing's (1.6×10^{-3} erg cm^{-2} s^{-1}, 1968), is given by

$$\Gamma = 10^{-24}\, \epsilon_{\rm UV} n \,(Z/Z_\odot)\, G_0 \;\; {\rm erg\, cm^{-3}\, s^{-1}}, \tag{15}$$

where the heating efficiency $\epsilon_{\rm UV}$ is fitted by

$$\epsilon_{\rm UV} = \frac{4.9 \times 10^{-2}}{1 + [\xi_{\rm gr}/1925]^{0.73}} + \frac{3.7 \times 10^{-2}\left(T/10^4\right)^{0.7}}{1 + [\xi_{\rm gr}/5000]} \tag{16}$$

with $\xi_{\rm gr} = G_0 T^{0.5}/n_e$ the grain charge parameter. This parameter is proportional to the rate of ionization of the dust grains divided by the recombination rate. As discussed in Wolfire (1995), for small values of $\xi_{\rm gr}$ the dust grains are mainly neutral, whereas for large values of this parameter the grains become positively charged, and

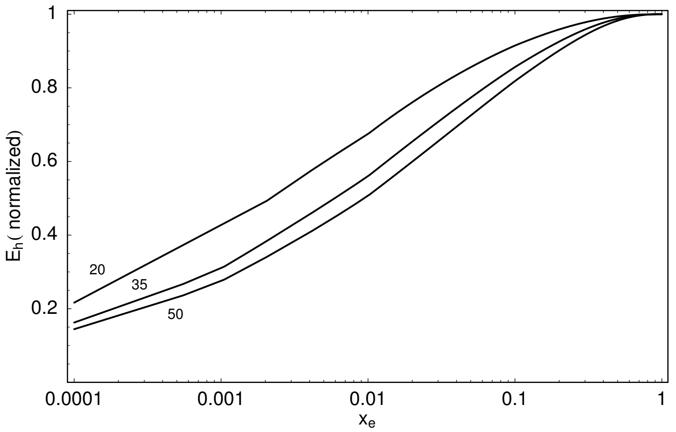

Figure 2.5: Cosmic ray heating function $\mathrm{E_h}$. Plot of the fraction of the secondary electron energy used for heating. Curves are labelled with secondary electron energy.

electrons need to overcome an extra potential barrier to get expelled from the grains. This lowers the energy available for heating the gas, which decreases the efficiency for increasing ξ_{gr} (Fig. 2.4). This has important implications for the heating rates in our model, effectively reducing the strength of the radiative feedback for high radiation fields to $\propto \mathrm{G}_0^{0.27}$. So compared to Gerritsen & Icke (1997) and Bottema (2003), who took a constant efficiency, the UV radiation feedback will be less important for establishing star formation equilibrium. Note also that in this case the heating becomes a strong function of ionization, as high ionization reduces grain charging.

The heating of Eq. (15) scales with metallicity (assuming the dust-to-gas ratio scales with Z), UV field, density and takes into account grain charging. We do not take into account the finer points of dust physics, notably the dependence of the heating on the shape of the spectral energy distribution of the impinging radiation field and the dependence of the heating on size and shape distribution of the dust grains. Both effects can change the heating rate by 25%, when varying the parameters under reasonable constraints (Wolfire 1995). In principle the distribution of the grain sizes, shapes etc could come out of a model for the formation, processing and destruction of dust grains and PAHs, but clearly this is a very complicated problem. We will just assume the same grain distribution to be present everywhere.

The UV field needed in Eq. (15) is calculated from the distribution of stars, analogous to the way the gravitational forces are calculated. Dust extinction is not taken into account explicitly, although we do roughly model the extinction of UV light from young stellar clusters by the remnants of the natal clouds by increasing the emission of UV light from 25% to 100% of the nominal luminosity over a period of 4 Myr.

Normally photoelectric heating dominates over X-ray and cosmic ray heating, but this is not the case in the outer parts of galaxies where both density and radiation field drop. In these regions we will provide for heating by including cosmic ray heating, which for a primary ionization rate ζ_{CR} is given by

$$\Gamma = \mathrm{n}\zeta_{\mathrm{CR}}\mathrm{E_h}(\mathrm{E}, \mathrm{x_e}) \qquad (17)$$

The function $\mathrm{E_h(E, x_e)}$ gives the heat deposited for every primary electron of energy E (of typically 35 eV), given in Wolfire (1995). We have plotted this function in Fig. 2.5.

In principle X-ray heating may also be important, but as its effect and magnitude is similar to that of cosmic ray heating (and this term is subject to some uncertainty, see discussion in section 2.3.1), we do not include it separately.

2.3.4 Molecular gas

We will not consider the formation of molecular gas in this chapter. However in view of the importance of molecular gas, both as fuel for the formation of stars, and as a diagnostic tool in extra-galactic studies of star formation, we will here give an overview of the relation of molecular gas and the gaseous phase of our simulation. In Chapter 6 we will investigate the formation of the most important molecule, H_2, in some detail.

A direct implementation of H_2 formation from first principles in current galaxy scaled computer simulations is, both from the viewpoint of the necessary resolution as from the viewpoint of necessary physics, impractical. In our simulation the physics of molecular cloud formation is considered to be part of the star formation process, captured in a basic but plausible model (see below). A result of this approach is that the star formation rates will not be set by molecular cloud physics, but at a larger scale: by the surface density of the gas, cooling properties of the neutral medium and large scale instabilities. This is consistent with the prevailing view of star formation (Elmegreen 2002). The mass that is contained in the molecular phase will be present in the cold phase in our simulation, and thus, while assessing the amount of cold gas resulting from our simulations, one must keep in mind that this includes a considerable amount of what would be molecular gas.

Note that diffuse H_2 gas is also absent in our model. This may be a more serious omission. Diffuse H_2 may be present at abundances of $10^{-3} - 10^{-4}$ in the neutral medium (Richter et al. 2001) and at this level it could affect the cooling of the neutral medium substantially, as the cooling efficiency of H_2 gas is about a factor 10^3 higher than for our neutral gas (Le Bourlot et al. 1999).

2.4 Equilibrium models

The different heating and cooling processes we have discussed in section 2.3 constitute a reasonably complex model for the ISM. It is certainly more realistic than most previous models that have been used in galaxy simulations, as it attempts to include the cold and warm phases of the neutral ISM. To get an idea of the properties of the resulting ISM it is instructive to explore the thermal equilibrium state of our model and compare it to the previous models of Gerritsen & Icke (1997), Bottema (2003) and also to the equilibrium models of Wolfire et al. (1995).

The models we present will be incorporated into a fully dynamical simulation, where we solve for the thermal evolution of the gas. To see to what extent the thermal equilibrium state is relevant as a description of the state of the ISM, we can compare the timescales of different processes. As we will demonstrate below, there are a range of processes in the ISM that are acting on timescales comparable to the timescales associated with the thermal evolution of the gas.

A region of cold gas subjected to an increase in UV radiation will quickly heat to a temperature of $\mathrm{T_{eq}} = 10^4$ K in a time

$$\mathrm{t_{heat}} = \frac{\rho \mathrm{u_{eq}}}{\Gamma} = \frac{3/2\mathrm{kT_{eq}}}{\Gamma} \approx \frac{10^6}{(\mathrm{Z}/\mathrm{Z}_\odot)\,\mathrm{G}_0}\ \mathrm{yr} \tag{18}$$

The time a region of density ρ and internal energy $\mathrm{u} = 3/2\mathrm{kT}$ needs to return to equilibrium after a significant perturbation is given by the cooling time,

$$\mathrm{t_{cool}} = \frac{\rho \mathrm{u}}{\Lambda} = \frac{3/2\mathrm{kT}}{\mathrm{f_H n}\Lambda^\star} \tag{19}$$

which gives roughly $\mathrm{t_{cool}} \approx 10^5$ yr ($\mathrm{n} = 10\ \mathrm{cm}^{-3}$, $\mathrm{T} = 100$ K) for the CNM and $\mathrm{t_{cool}} \approx 10^7$ yr ($\mathrm{n} = 0.1\ \mathrm{cm}^{-3}$, $\mathrm{T} = 10^4$ K) for the WNM.

Variations in the local UV field were studied by Parravano et al. 2003. They found variations on timescales of 10^{7-8} yr. This is comparable to timescales in the WNM but much slower than the timescales of the CNM. A similar conclusion holds for supernova perturbations. Wolfire et al. (2003) estimated for the characteristic time of these that $\mathrm{t_{shock}} = 5.3 \times 10^6$ yr.

So we see that under quiescent (solar neighbourhood) conditions thermal equilibrium is a reasonable assumption for the CNM and marginally good for the WNM, whereas for more active regions this assumption will become increasingly questionable, especially for the WNM but also for the CNM, since the frequency of most of the perturbing agents scales with star formation rate. A large fraction of out-of-equilibrium gas is consistent with recent HI absorption line studies, which find that a substantial fraction (around 50%) of the WNM is in an unstable temperature range, and thus presumably not in equilibrium (Heiles & Troland 2003, Kanekar 2003).

2.4.1 Heating and ionization assumptions

To explore the effect of the different heating and ionization processes that are new to our ISM model and to compare these to previous work, we explore a number of different models, designated A B C and D, of increasing complexity. For the moment we consider solar metallicity. The first of these models (model A) is the same, except for the cooling, as the model used in Gerritsen & Icke (1997): a constant heating efficiency ($\epsilon_{\mathrm{UV}} = 0.05$) and a constant ionization fraction ($\mathrm{x_e} = 0.1$). Model B has the heating efficiency of Eq. (16), while retaining constant ionization. Model C has constant heating efficiency while solving for ionization and finally model D is our complete model solving for the ionization and using the full heating efficiency. Fig. 2.6 shows for these four models the equilibria of pressure, temperature, electron fraction and heating (=cooling) rate.

The plots in this figure show that as density increases, the equilibrium state of the gas changes from a high temperature ($\mathrm{T} = 10^4$ K) at low densities, to a low temperature ($\mathrm{T} < 100$ K) at high densities. For all four models there is a density domain in between where the negative slope of the P-n relation indicates that the gas is unstable to isobaric pressure variations, the classic thermal instability (Field 1965). We

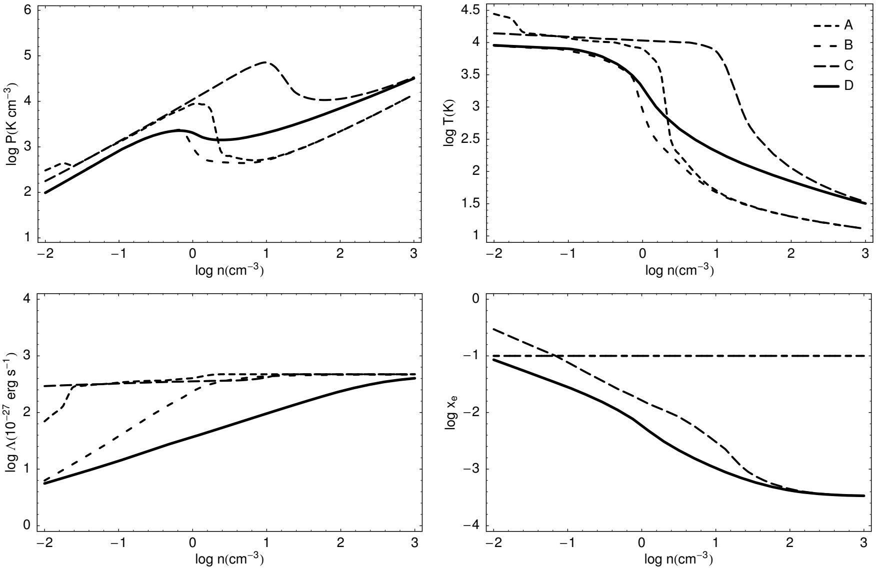

Figure 2.6: Thermal equilibrium properties of models A,B,C and D. Shown are (in order: top left, top right, bottom left and bottom right) the pressure, temperature, cooling rate and ionization fraction in thermal equilibrium as a function of density. In the plot results are shown for $Z = Z_{\odot}$ and $G_0 = 10$.

see that the models which do not solve for the ionization (A and B) seriously overestimate the ionization at high densities and thus overestimate the cooling resulting in lower temperatures. The models which do not use the full heating efficiency (A and C) overestimate the heating, especially at low densities, hence these have higher temperatures at low density. The total effect is that the range of pressures for which the ISM is unstable will be much greater in the simpler models.

If we compare Fig. 2.6 to Fig. 3 of Wolfire et al. (1995) we see that our model D is very similar, showing very similar trends for electron fraction and heating rate. Hence our model captures most of the essential physics of the Wolfire et al. model.

In a complete simulation the conditions of UV and supernova heating will vary from place to place. This will change the relations of Fig. 2.6. So next we will explore the effect of variation of UV and cosmic ray heating.

2.4.2 UV field and Cosmic rays

In Fig. 2.7 we have plotted an overview of model D for three different values of the UV field G_0. Note that as the UV field increases the density and pressure for which a cold phase is possible shift up. Also, if some region is collapsing, then, as long as no star formation is happening, the UV field may be expected to stay more or less constant and since density increases gas will stay at the lines of constant heating in for example the n-T relation. Then, as stars form, heating will suddenly increase, and

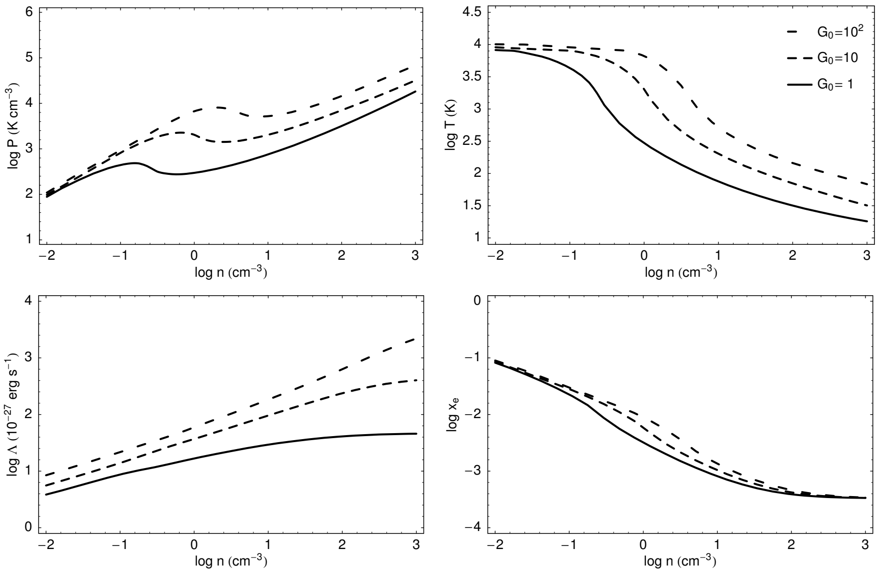

Figure 2.7: Thermal equilibrium properties of model D: varying UV heating. $\mathrm{Z} = \mathrm{Z}_{\odot}$.

gas will 'move up' quickly to a new G_0 curve , cf. (18).

An increase in cosmic ray flux shows a similar pattern: In Fig. 2.8 we have plotted the pressure-density relation for different cosmic ray fluxes. A high value for the cosmic ray ionization rate may very well be appropriate: for diffuse clouds in the solar neighbourhood McCall et al. (2003) found that a value of the cosmic ray ionization rate of up to $\zeta_{\mathrm{CR}} = 1.2 \times 10^{-15}$ was necessary to account for the observed abundance of H_3^+.

2.4.3 Varying chemical composition

In Fig. 2.9 we show the effect of varying the chemical composition. A lower metallicity shifts the unstable region to higher density and pressure, while also extending the range of unstable pressures. Note that the ISM model is still relatively insensitive to variations in metallicity. This is because we scale the dust-to-gas ratio, and thus the heating efficiency, with metallicity. Both cooling and heating are to first order proportional to metallicity. In Fig. 2.10 we show the $\mathrm{Z} = \mathrm{Z}_{\odot}/5$ model in more detail. Pressure, temperature and electron fraction are similar to the model for solar metallicity, although the cooling rate shifts down. The cooling and heating times (19) and (18) scale inversely with metallicity. So while varying the metallicity has relatively little effect on the equilibrium state, it will affect our full dynamical modelling.

In Fig. 2.9 we have also plotted the effect of separately depleting Fe+Si and C, as they affect cooling at completely different temperatures. Note that depletion of iron enlarges the pressure range of thermal instability, while depletion of carbon has the effect of heating the cool phase.

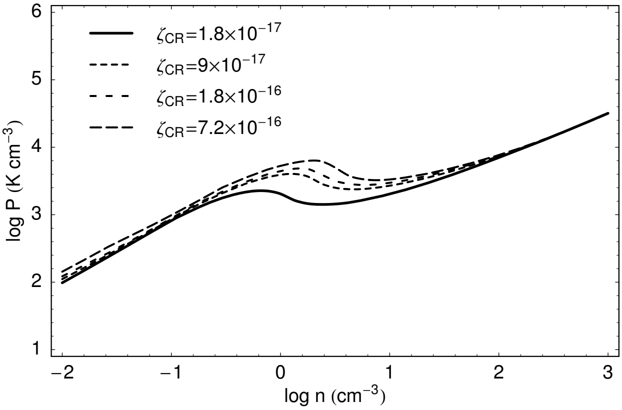

Figure 2.8: Equilibrium pressure-density relation for different cosmic ray fluxes, $G_0 = 10$.

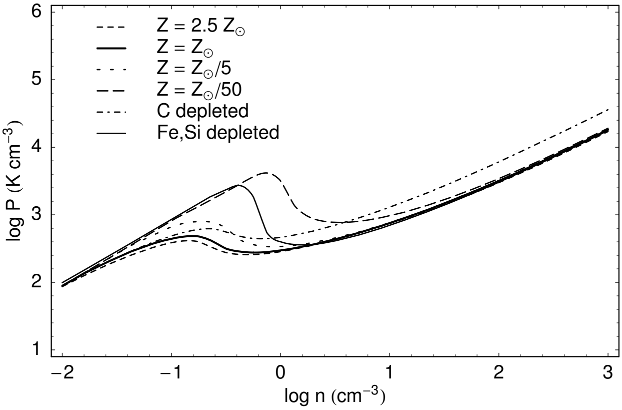

Figure 2.9: Equilibrium pressure-density relation for different chemical compositions, $G_0 = 1$.

2.5 Star formation and its effects

From the point of view of our simulation star formation is micro physics that is not resolved. The formation of stars in dense clouds of the interstellar medium is a complex process that is still very much an active field of research, and there is no general theory to predict the star formation rate of a given region of the ISM. However from observations and theory some key processes are identified. Probably the most influential observational relation is the *Schmidt law* (Schmidt 1959): the empirical finding that the star formation rate (SFR) of disk galaxies varies with gas surface density σ_g as $\mathrm{SFR} \propto \sigma_\mathrm{g}^{1.5}$. It can be explained by assuming that gravitational instabilities play the regulating role in star formation on large scales (Elmegreen 2002). Furthermore it seems that star formation is a self regulating process: young star clusters will disrupt the cloud in which they form by heating it with UV photons and by stirring the gas mechanically through the action of stellar winds and supernova feedback.

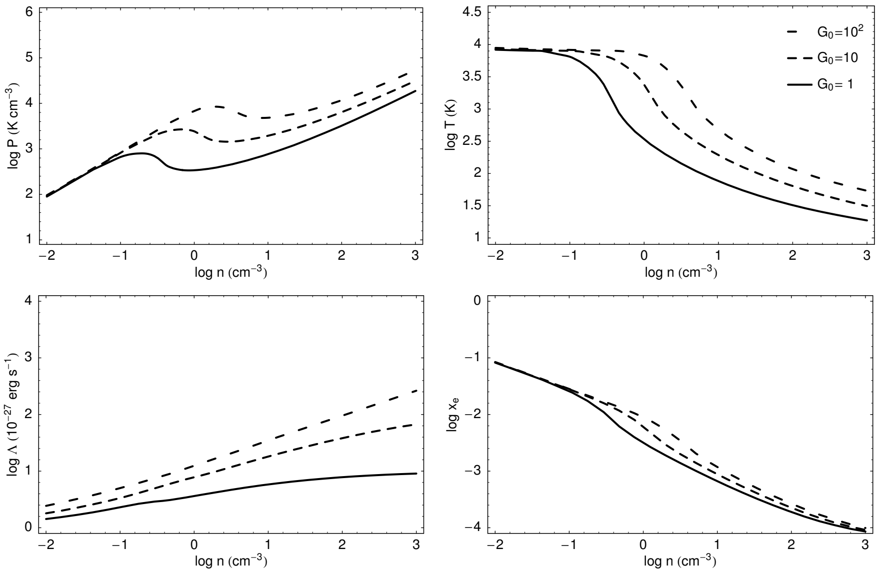

Figure 2.10: Thermal equilibrium properties of model D with $Z = Z_\odot/5$, varying G_0

2.5.1 Star Formation

We use the star formation recipe of Gerritsen & Icke (1997). A region is considered unstable to star formation if the local Jeans mass M_J,

$$M_J = \frac{\pi\rho}{6}\left(\frac{\pi s^2}{G\rho}\right)^{3/2} \tag{20}$$

with s the sound speed, is smaller than the mass of a typical molecular cloud M_{ref},

$$M_J < M_{ref}. \tag{21}$$

The rate of star formation is set to scale with the local free fall time,

$$\tau_{sf} = f_{sf} t_{ff} = \frac{f_{sf}}{\sqrt{4\pi G\rho}}. \tag{22}$$

The delay factor f_{sf} accounts for the fact that collapse of molecular clouds is inhibited by either turbulence or magnetic fields (Mac Low & Klessen 2004, Shu et al. 1987). Its value is uncertain, but from observations a value $f_{sf} \approx 10$ seems reasonable (Zuckerman & Palmer 1974).

There are many different ways to let stars form locally on the timescale given by Eq. (22). One way to achieve this, followed by Gerritsen & Icke (1997) is to wait for a time τ_{sf} and then proceed to form stars. Another is just to assign a probability $1 - \exp(-\Delta t/\tau_{sf})$ for star formation in a time step Δt. We have not found any compelling reason to prefer one method over the other. There are however also subtle numerical differences between the two methods: in the stochastic case star formation may also be delayed beyond $\tau_{\rm sf}$, and where this is the case the unstable region may collapse to higher densities than it would in the fixed delay case. The fixed delay case, on the other hand tends to synchronize star formation over regions that become unstable at the same time, which leads to a sudden onset of star formation, for example in the beginning of the simulation. We will note whenever a choice of either one has a substantial impact on the results.

Once a gas particle is determined to be forming stars, a fraction $\epsilon_{\rm sf}$ of the mass is converted to stars. This sets a minimum to the star formation efficiency (a neighbourhood of gas particles of about 64 particles that has become capable of star formation will thus form at least a fraction $\epsilon_{\rm sf}/64$ of stars). The actual efficiency of star formation is determined by the number of stars needed to quench star formation locally by the UV and SN heating and is determined by the cooling properties of the gas and the energy input from the stars.

Thus the local star formation rate will be given by

$$\frac{{\rm d}\rho_\star}{{\rm dt}} = -\frac{{\rm d}\rho_{\rm gas}}{{\rm dt}} = \frac{\epsilon_{\rm sf}}{\tau_{\rm sf}}\rho_{\rm JU} \tag{23}$$

where $\rho_{\rm JU}$ indicates the 'Jeans unstable' gas, satisfying (21). The effective timescale for star formation is $\tau_{\rm eff} = \tau_{\rm sf}/\epsilon_{\rm sf} = {\rm f_{sf}t_{ff}}/\epsilon_{\rm sf}$, so different combinations of $\rm f_{sf}$ and $\epsilon_{\rm sf}$ will give the same star formation rate. In case of a fixed delay time (Gerritsen & Icke method), it is appropriate to take a constant mass fraction $\epsilon_{\rm sf}$ for the newly formed star particles, while in the stochastic method we can form star particles of fixed mass, and thus bigger $\epsilon_{\rm sf}$ as gas particles become lighter, as long as we increase $\rm f_{sf}$ accordingly.

The recipe is certainly not unique, we have based our choice on the following considerations: it is simple and based on presence of substructure and the driving role of gas self gravity, and it reproduces the Schmidt law without actually imposing it (Gerritsen & Icke 1997). It does assume substructure to be present (actually its assumption is more restrictive still, namely that substructure is mainly at $\rm M_{ref}$ sized clouds, but this is not overly important). For this type of simulation one is always restricted by the limited ability to follow the star formation process, so we are forced to adopt a phenomenological description at some level.

Another concern that could be addressed is that the SF according to this recipe is independent of metallicity, other than that induced by the metallicity dependence of the cooling. If cloud collapse is regulated by magnetic fields (Shu et al. 1987), a more detailed dependence of the delay factor $\rm f_{sf}$ on for example ionization may be appropriate.

We assume the stellar initial mass function (IMF) to be universal. We take a Salpeter IMF with a lower mass cutoff of $0.1\ \rm M_\odot$ and an upper mass cutoff of $100\ \rm M_\odot$. The shape of the IMF determines the amount of heavy stars, and thus the amount of UV and supernova feedback. If the IMF would vary according to local conditions this will have its effect on star formation. Observations are consistent with a universal IMF over a wide range of ISM conditions, however there are some hints that for high radiation fields and/or low metallicities relatively more high mass stars are formed (e.g. Lamers et al. 2002).

The star formation recipe we employ has an additional advantage: namely, it prevents the simulation from violating the resolution requirements for self gravitating SPH of Bate & Burkert (1997) and Whitworth (1998). For SPH the local Jeans mass should be bigger than the local mass resolution,

$$\mathrm{M_J > Nm_{SPH}}, \tag{24}$$

otherwise artificial clumping or inhibition of clumping may occur. This condition is just Eq. (21), *if* $\mathrm{M_{ref}}$ is chosen equal to the local mass resolution, $\mathrm{M_{ref} = Nm_{SPH}}$ (N is the number of SPH neighbours, and $\mathrm{m_{SPH}}$ the mass of SPH particles). We will do so, and our simulation will thus follow collapse and fragmentation of the ISM from the WNM to the CNM, but at a certain point (Eq. 21) the simulation can no longer reliably follow this process. At this point further assumptions regarding the details of star formation enter through Eq. (22). In practice this limit lies at a very physically relevant region of parameter space, namely at temperatures and densities where molecular clouds should form in the CNM. So our simulation tracks the evolution of the WNM and CNM up to a point where a phase of the ISM forms that can be trusted to form stars, at efficiencies that are somewhat constrained by observations. As we increase resolution and decrease $\mathrm{m_{SPH}}$ we can decrease $\mathrm{M_{ref}}$ and follow the collapse further.

2.5.2 Stellar model

We calculate the FUV luminosities of the stellar particles from the age and metallicity of the stars and Bruzual & Charlot (1993, and updated) population synthesis models. For this the integrated flux between 912 and 2100 Å is calculated from single burst models with a salpeter IMF with a low mass cutoff of $0.1\ \mathrm{M_\odot}$ and high mass cutoff of $100\ \mathrm{M_\odot}$. It is not entirely clear if interpolation in metallicity from the coarse grid data available is the best strategy, so in case we run a model with a metallicity different from the Bruzual & Charlot models we just take the synthesis model with the closest matching metallicity. We roughly account for the extinction of UV light of young stars by their natal cloud by increasing the flux from 25% at birth to 100% at 4 Myr, in accordance with counts of UV sources in the neighbourhood of star forming clouds (Parravano et al. 2003, and references therein).

2.5.3 Feedback

In addition to heating by UV radiation, stars heat the surrounding gas through the injection of energy by stellar winds, supernovae and the expansion of HII regions. We will consider these three effects to constitute the *mechanical luminosity* of our stellar particles. Stars heavier than $8\ \mathrm{M_\odot}$ are generally assumed to explode as supernovae with energies of 10^{51} erg, so together with stellar lifetimes and the IMF, this fixes the contribution from supernovae. The contribution of stellar winds can be estimated from stellar evolution modelling and theoretical and observational mass loss rates and terminal velocities, (e.g. Leitherer et al. 1999). If we look at the mechanical energy output of a stellar cluster (Fig. 2.11) we see that stellar winds dominate early on, but the integrated luminosity indicates that they contribute less than about 6% to the the total mechanical energy. For metallicities lower than solar this value would be even lower.

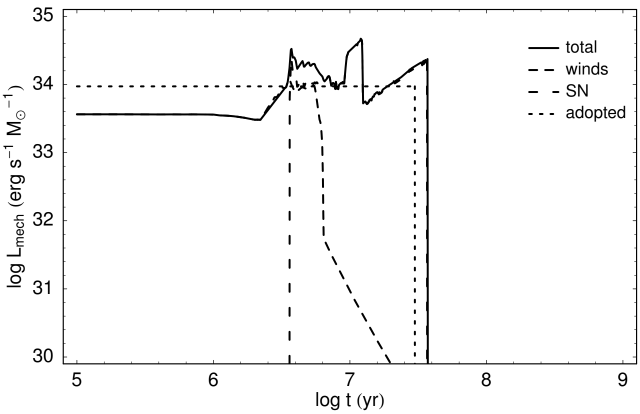

Figure 2.11: Mechanical energy output from stellar cluster. Plotted as a function of age of a single burst of star formation at $Z = Z_\odot$ are the separate contributions from stellar winds (short dashed) and supernovae (long dashed), as well as the total mechanical luminosity(drawn) from Leitherer et al. (1999). The dotted line indicates the mechanical luminosity of the stellar particles adopted in our simulation.

While the mechanical energy output of stars can thus be estimated with reasonable accuracy, it has proven to be difficult to include the effects of feedback completely self-consistently in galaxy sized simulations of the ISM. The reason for this is that the effective energy of feedback depends sensitively on the energy radiated away in thin shells around the bubbles created. This will mean that the effect of feedback is not reliable unless prohibitively high resolution is used. In SPH codes there have been conventionally two ways to account for mechanical feedback: by changing the thermal energy input and by acting on particle velocities. Both are unsatisfactory, as the thermal method suffers from over cooling (Katz 1992) and the kinetic method seems to be too efficient in disturbing the ISM (Navarro & White 1993). Here we use a new method based on the creation at the site of young stellar clusters of *pressure particles* that act as normal SPH particles in the limit that the mass of the particle $\mathrm{m} \rightarrow 0$, for constant energy (see Chapter 3 for more details). For the energy injection rate we take $\dot{\mathrm{E}} = \epsilon_{\mathrm{sn}} \mathrm{n}_{\mathrm{sn}} \mathrm{E}_{\mathrm{sn}} / \Delta \mathrm{t}$, with supernova energy $\mathrm{E}_{\mathrm{sn}} = 10^{51}$ erg, an efficiency parameter $\epsilon_{\mathrm{sn}} = 0.1$, number of supernova n_{sn} per solar mass of stars formed of $\mathrm{n}_{\mathrm{sn}} = 0.009$ and an active period $\Delta \mathrm{t} = 3 \times 10^7$ yr (approximately the lifetime of a $8\ \mathrm{M}_\odot$ star). The efficiency ϵ_{sn} thus assumes that 90% of the energy is radiated away, a value which comes from more detailed simulations of the effect of supernova and stellar winds on the ISM (Silich et al. 1996), and is also used in other simulations of galaxy evolution (e.g. Semelin & Combes 2002, Springel & Hernquist 2002, Buonomo et al. 2000). In Fig. 2.11 we have also plotted the mechanical luminosity of the stellar particles in our model. Note that the fact that we approximate the mechanical luminosity by a constant will not introduce big errors, as the energy of the pressure particles is a time integrated quantity.

2.6 Putting it all together

The combination of hydrodynamics, self-gravity and the ISM models of section 2.4 with our star formation and feedback recipes will set up a self regulated ISM. The distribution of temperature, density, etc. of the gas and amount and location of star formation will be the outcome of the interaction between the competing processes of heating and cooling, feedback and collapse. We will test this global model for the ISM of star forming galaxies by applying it in a simulation of a suitable galaxy.

2.6.1 Initial conditions

For our purposes we need a simple model galaxy. We construct a three component model of a typical star forming disk galaxy with a gaseous disk, a stellar disk and a dark halo.

The stellar disk has a mass of 10^{10} $\mathrm{M}_\odot$ and is constructed to be approximately exponential,

$$\rho_{\rm disk}(\mathrm{R},\mathrm{z}) = \frac{\Sigma_0}{2\mathrm{h_z}}\exp(-\mathrm{R}/\mathrm{R_d})\mathrm{sech}^2(\mathrm{z}/\mathrm{h_z}), \tag{25}$$

for a central surface density $\Sigma_0 = 5\times 10^8$ $\mathrm{M}_\odot/\mathrm{kpc}^2$, disk scale $\mathrm{R_d} = 1.8$ kpc and a vertical scale-height $\mathrm{h_z} = 0.4$ kpc. The disk is constructed using the approximate three-integral disk distribution function of Kuijken & Dubinski (1995). The initial ages of the stellar particles are distributed according to an exponentially decaying star formation rate with a burst time of 5.2 Gyr, resulting in a current star formation rate for this galaxy of $\mathrm{SFR} = 0.2$ $\mathrm{M}_\odot/\mathrm{yr}$.

For the gaseous disk we take a radial surface density

$$\Sigma = \Sigma_{\rm g}/(1+\mathrm{R}/\mathrm{R_g}), \tag{26}$$

with central density $\Sigma_{\rm g} = 0.008\times 10^9$ $\mathrm{M}_\odot/\mathrm{kpc}^2$ and radial scale $\mathrm{R_g} = 3$ kpc, truncated at 14 kpc. Thus it has a total mass of $\mathrm{M_{gas}} = 1.05\times 10^9 \mathrm{M}_\odot$. Initially the gas is given a temperature $\mathrm{T} = 10^4$ K.

Both the stellar and gas disk are represented by $\mathrm{N} = 10^5$ particles. The dark halo is represented by a static potential and has a Navarro, Frenk & White (1997, NFW) profile

$$\rho_{\rm halo}(\mathrm{r}) = \frac{\rho_{\rm s}}{(\mathrm{r}/\mathrm{r_s})(1+\mathrm{r}/\mathrm{r_s})^2}, \tag{27}$$

$\rho_{\rm s} = 4\times 10^7$ $\mathrm{M}_\odot/\mathrm{kpc}^3$ and $\mathrm{r_s} = 6$ kpc. The dark to baryonic mass ratio is thus $\mathrm{M_{dark}}/\mathrm{M_{baryon}} = 5$ at the edge of the gas disk.

2.6.2 Galaxy models without supernova feedback

First we will compare the models A, B, C and D of section 2.4.1 without the effect of mechanical feedback. We let the model galaxy evolve, using the different ISM models as well as our star formation and SN feedback processes. Quickly, after about 200 Myr, a steady state develops where the distribution of temperature and density of the gas changes only marginally due to the consumption of gas by star formation.

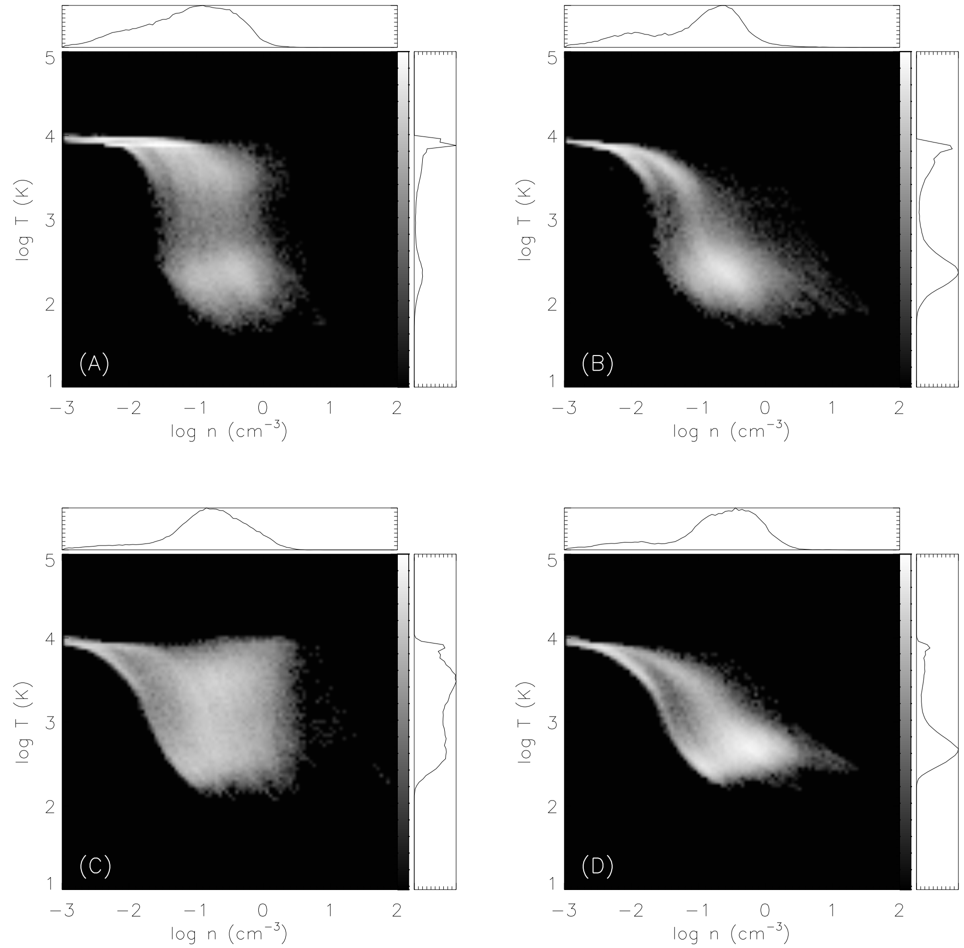

Figure 2.12: Temperature-density distribution of simulation runs of model A, B, C and D w/o feedback. Histograms of the corresponding quantity are plotted to the right and above the frames. These histograms are linear and scaled to the maximum bin.

In Fig. 2.12 we have plotted the density-temperature diagram for the different models. If we look at the panel of model A, which is equivalent to the model of Gerritsen & Icke 1997, we recognize the two phase structure as found by them. Most of the gas is at temperatures of around $\mathrm{T} = 10^4$ K. Note that gas cools to about $\mathrm{T} = 100$ K, but densities stay below $\mathrm{n} = 10$ cm^{-3}, due to the limited resolution. The star formation rate of $\mathrm{SFR} \approx 0.6\ \mathrm{M}_\odot$/yr is similar to that found by Gerritsen & Icke (Fig 2.13). We also find that the distribution of gas and stars has similar properties as in their simulations, more specifically: cold gas is confined to the midplane of the galaxy, showing a flocculent spiral structure caused by stretching of collapsing structures due to differential rotation.

However if we look at the temperature and density distribution of model D we

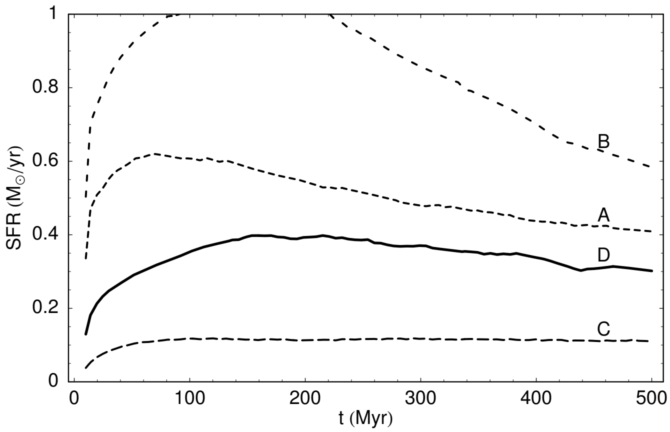

Figure 2.13: Star formation rate of simulation runs of model A, B, C and D without feedback.

see a qualitatively different picture: most of the gas at high densities is now concentrated at low temperature. Comparing with model B and C we see that this is due to the effect of using heating efficiency (16) rather than using a constant efficiency. Grain charging flattens the dependency (16) at high UV fields to $G_0^{0.27}$. In this case heating from stellar UV radiation is not sufficient to heat the gas back to 10^4 K. The effect of lower ionization keeps gas in models C and D at somewhat higher minimum temperatures compared to the constant ionization cases of model A and B.

If we look at the star formation rates of the model galaxies, we see that models A and D have similar star formation rates peaking at $\mathrm{SFR} = 0.6\ \mathrm{M}_\odot/\mathrm{yr}$ and $\mathrm{SFR} = 0.4\ \mathrm{M}_\odot/\mathrm{yr}$. Although a bit on the high side, these are reasonable SFR, considering the uncertainties present in the modelling. For model B, the peak star formation rate $\mathrm{SFR} = 1.2\ \mathrm{M}_\odot/\mathrm{yr}$ is clearly too high, and also results in a gas consumption time that is very short (≈ 1 Gyr). Model C has very low star formation rate, due to the combination of overestimated heating and realistic cooling. We see that the effect of ionization and grain charging are cancelling out for model D giving it a similar star formation rate as model A.

2.6.3 Galaxy models with SN-feedback

We ran the same models again, but this time including supernova feedback. Fig. 2.14 and 2.15 give the corresponding temperature-density plots and star formation rates. In this case additional heating from the SN masks the effect of grain charging. Although models with the complete heating efficiency still have a higher cool gas fraction, heating is sufficient to heat the gas back to 10^4 K, allowing for cycling between WNM and CNM: cold gas is heated and will expand back to low densities. If we look at the star formation rates we see that for model C the addition of SN heating makes very little difference, while lowering the star formation rate substantially for the other models.

For the remainder, we take model D with SN feedback as our standard model and compare to it the effects of varying abundances and cosmic ray fluxes.

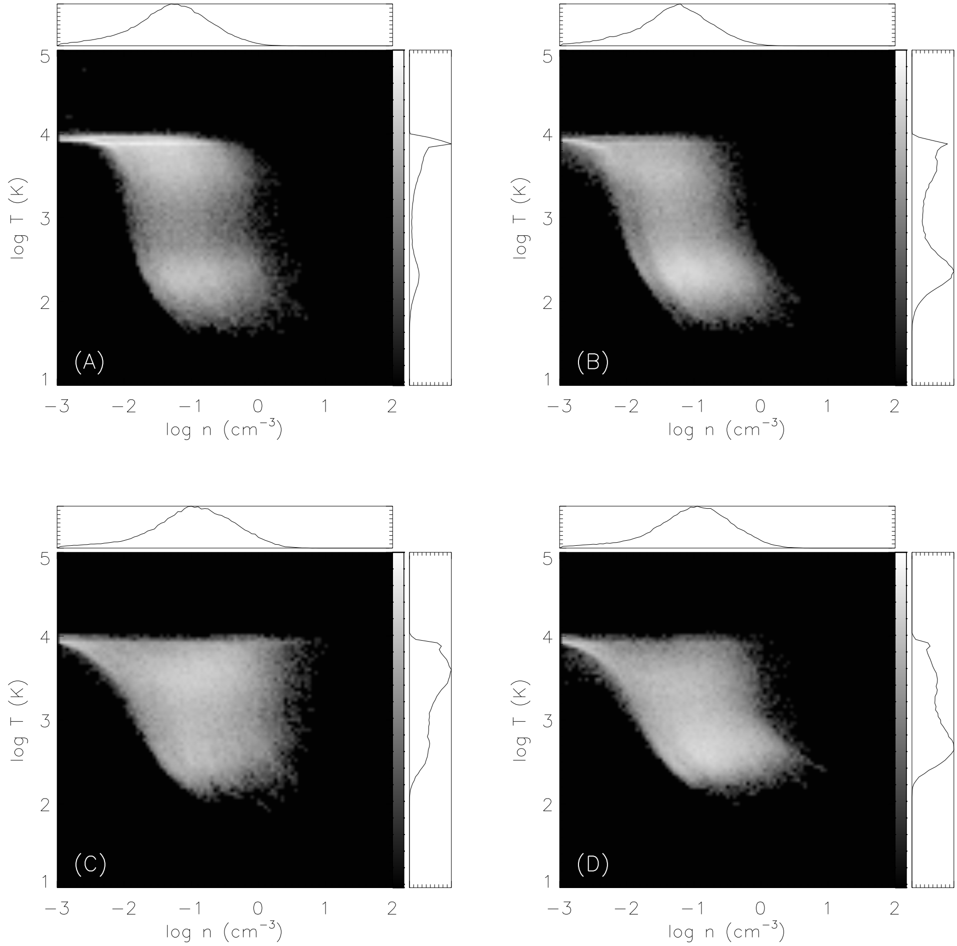

Figure 2.14: Temperature-density distribution of simulation runs of model A, B, C and D with feedback.

2.6.4 The effect of chemical composition

We ran a set of four simulations with varying chemical composition, but otherwise the same as the above model D. Two of these we ran with higher and lower metallicity scaled from solar: $Z = 2.5 \times Z_\odot$ and $Z = Z_\odot/5$, the remainder were the Fe+Si and C depleted models of section 2.4.3. Note that for the models where we use scaled metallicities we use a corresponding set of stellar models, while for the depleted models we use the standard solar metallicity population synthesis.

In Fig. 2.16 we have plotted the temperature-density distribution for these runs. The low metallicity run shows a markedly different temperature distribution, especially at low densities, being much warmer. This is due to cosmic ray heating, which becomes relatively important as metallicity goes down (we scale dust content, and thus grain heating with Z). The distribution of the high metallicity model is very sim-

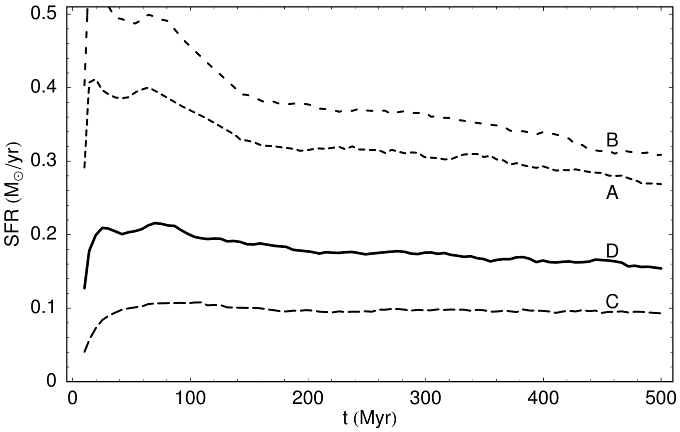

Figure 2.15: Star formation rate of simulation runs of model A, B, C and D with feedback.

ilar to solar metallicity. A plot of the star formation rates of these models, Fig. 2.17, shows that *both* have lower star formation rates. This suggests that the star formation efficiency attains a local maximum at solar metallicity. The decrease at higher metal contents is probably due to the fact that the UV flux is higher (by a factor 2-3) for Bruzual & Charlot (1993) stellar models with $Z = 2.5 \times Z_\odot$ compared to $Z = Z_\odot$ (as is the case for low metallicity).

Comparing the Fe and C depleted runs in Fig. 2.16, we see that for the Fe depleted run there is very little cold gas. The depletion of C has an effect mainly on the star formation rate, see Fig. 2.18, since C affects the cooling at low temperatures. Note that for the low iron simulation the star formation is also affected, but less so than one would expect from the temperature distribution: the abundance of C affects the star formation rate, while the Fe abundance affects the relative amounts of warm and cold neutral gas.

2.6.5 Cosmic rays and the star formation threshold

As discussed in section 2.3.1 the heating and ionization from cosmic rays and X-rays are not well constrained. Hence to see what the effect of this uncertainty is on our model we have run additional models with 5 and 40 times higher cosmic ray fluxes. The effect of increasing the cosmic ray flux is to heat the gas at low densities, while not affecting gas at high densities much (Fig. 2.19). An increase by a factor of 5 still has a minor effect on the total star formation, while a factor 40 increase only lowers the star formation rate with about 50%. If we look at the radial star formation density (Fig. 2.21) we see that star formation in the centre is decreased little for higher cosmic ray rates, but that the edge of star formation moves in as cosmic ray flux increases. This is consistent with models for the threshold of star formation that explain it as a thermal effect (Schaye 2004, Elmegreen & Parravano 1994). As was pointed out by Schaye (2004), the fact that the cold phase is absent beyond a certain radius means that the disk is gravitationally stable beyond this radius and thus star formation quenched. Note that in our model galaxy the radius of the edge of the star

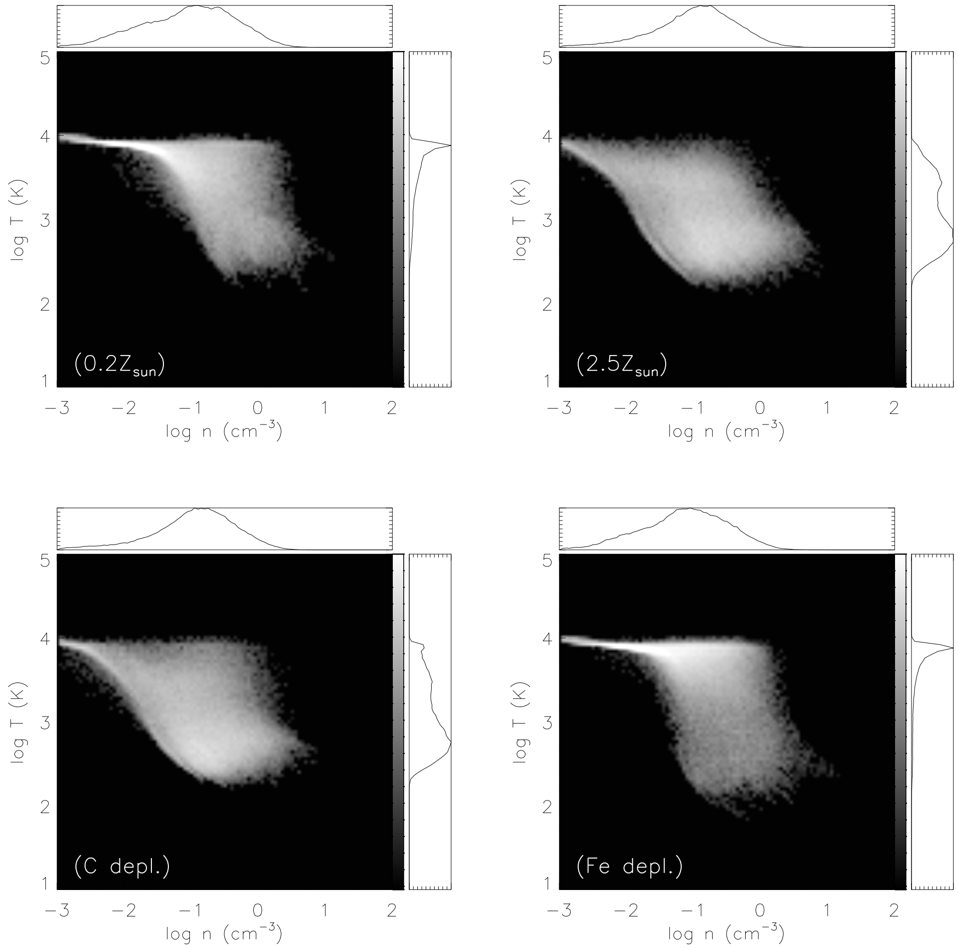

Figure 2.16: Temperature-density distribution of simulation runs of different chemical composition. **top left:** $Z = Z_{\odot}/5$, **top right:** $Z = 2.5 \times Z_{\odot}$, **bottom left:** C depleted ($\times 0.03$) model and **bottom right:** Fe and Si depleted ($\times 0.03$) model.

forming disk can vary, depending on $\zeta_{\rm CR}$, from 8 to 13 kpc , thus we could easily build a model consistent with the original stellar disk (which was cut off at 9 kpc).

2.7 Discussion

The main innovation of the simulations presented in this chapter is the application of a complex ISM model to a galaxy sized object. An obvious question is to what extent the new ingredients of grain charging and ionization are really needed for a realistic model. This can be seen in the role of feedback. For model A we found that SN feedback is not needed to regulate star formation. However, we find that

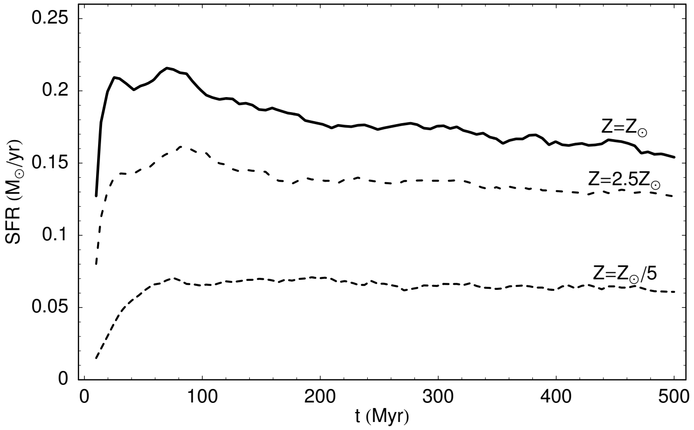

Figure 2.17: Star formation rate of low and high metallicity runs.

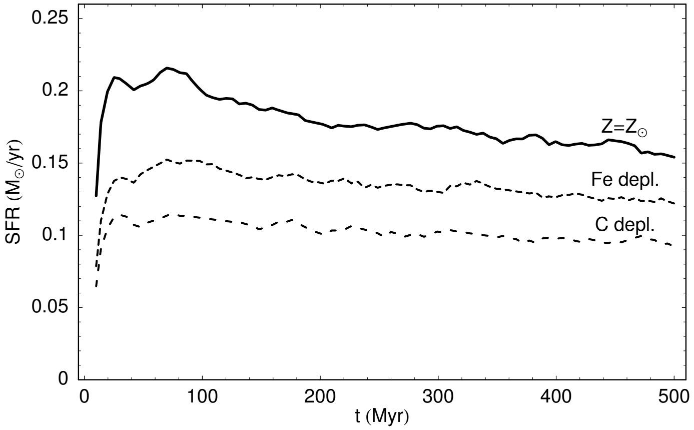

Figure 2.18: Star formation rate of depleted models

for realistic heating rates UV heating will not provide enough heating: in this case the temperature of heated regions will not rise above a few hundred Kelvin and SN heating becomes necessary.

It should be noted that our models are inherently limited by the numerical approach we have chosen. Obvious shortcomings of our model for the ISM are the absence of molecular gas, already discussed in section 2.3.4 and the poor representation of hot phases.

Hot tenuous phases of the ISM are a problem for SPH type codes because the mass in the hot phases is very low, so SPH, with its constant mass resolution, will by default represent low density regions poorly. Particle splitting methods may provide a way to alleviate this problem (Kitsionas & Whitworth 2002), however in our case we would also need to reassemble particles, as the gas cycles between phases.

But even the representation of the neutral phases of the ISM is hampered by resolution constraints. The cold phase can have structure roughly down to scales of the

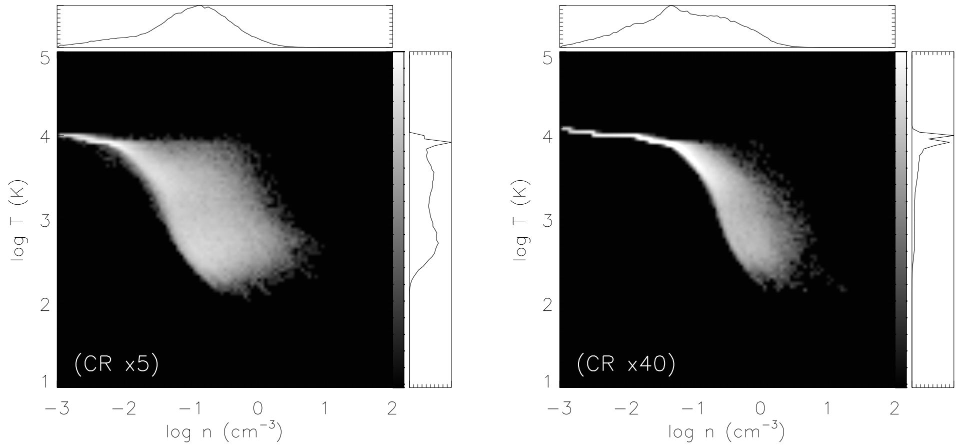

Figure 2.19: Temperature-density distribution of runs with higher cosmic ray fluxes (left: ×5 and right: ×40).

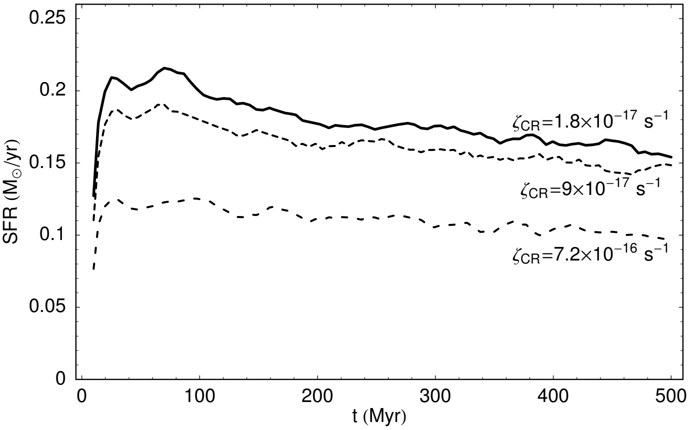

Figure 2.20: Star formation rate of runs with higher cosmic ray fluxes (×5 and ×40).

thermal diffusion length (Meerson 1996), which can be as small as 0.1 pc, which is below the scales we probe in our simulation. So a lot of substructure not resolved in our simulation would be present in the ISM. This can introduce errors in the cooling. Substructure will enhance the cooling by a factor ranging from anywhere from a few percent to very large values, depending on the nature of the substructure (a few percent would be for a typical random field, while for example a density field composed of polytropes of index > 1 would yield an unbounded factor). A more rigorous test of the effect of sub-resolution structure on the dynamics of multiphase gas would be very valuable.

Another shortcoming of the modelling is that we make the assumption of ionization equilibrium. A proper treatment of ionization could for example increase the ionization if the timescale of energy losses is shorter than the timescale for recombi-

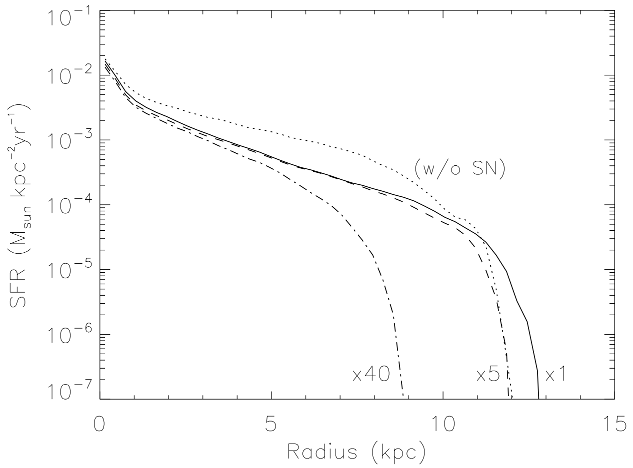

Figure 2.21: Star formation density as function of radius for standard runs and runs with higher cosmic ray fluxes (×5 and ×40).

nation. This would result in stronger cooling in regions that are experiencing cooling from an ionized phase.

2.7.1 Comparison with previous work

The methods we use are comparable to those of Gerritsen & Icke (1997) and Bottema (2003). As we have noted our model A is the same as the model explored by those authors, except for the cooling curve. The fact that the cooling is different has a minor effect on the temperature structure of the gas, but the picture remains qualitatively the same. Here we have followed up on the work of Gerritsen & Icke (1997) by extending the ISM model with two important ingredients, grain charging and ionization. We find that if these two effects are taken into account, UV heating can no longer be sufficient as the sole heating source of the ISM. However their conclusions regarding structure and distribution of the gas and the truncation of star formation seem not to be affected. Our models provide a good basis to explore these phenomena further.

Bottema (2003) has explored a model for NGC 628 in some detail. He found that unless supernova feedback was added, gas would aggregate in a few large clumps distributed over the disk. We have not found a similar effect for model A, which may be due to the fact that in his simulations the resolution requirement (24) was not fulfilled.

A number of other approaches have been followed to try to simulate a star forming ISM. Springel & Hernquist (2003) formulated a sub-grid model for the multiphase interstellar medium, producing a quiescent self-regulating ISM. Some authors have tried to represent the molecular phase by formulating a phenomenological ISM model in terms of 'sticky' particles (Andersen & Burkert 2000), sometimes in addition to a SPH component representing the WNM (Semelin & Combes 2002, Berczik et al. 2003). They successfully reproduce a self-regulated ISM, including some effects, like evaporation of molecular clouds, that are probably not well represented in our model. However, these models form stars from the cloud particles imposing a Schmidt law, not, as in our model, from the consideration of the instabilities in the ISM. Furthermore, our model has a consistent representation of the ISM linking phases by physical processes, rather than prescriptions.

2.8 Conclusions

We have presented global models for the ISM of galaxies that include a detailed model for the neutral ISM, star formation and radiative and SN feedback. We explored the effects of different heating and cooling assumptions, chemical composition and cosmic ray fluxes using a simple template of a star forming galaxy. We have found that:

- The effect of grain charging on the photo electric heating efficiency impairs heating of the ISM. In practice this means that the heating of (diffuse) gas around young stellar clusters by UV radiation alone can not heat the ISM beyond ≈ 500 K. As a result supernova feedback becomes more dominant.
- Solving for ionization is essential to have realistic cooling rates. A decrease in ionization rate at high densities/ low temperatures affects the cooling by atomic species.
- The effect of realistic heating and ionization act together to constrain the range of pressures of thermal instability. A decrease in metallicity, or depletion of Fe and Si extends the range.
- Star formation peaks at solar metallicities.
- Star formation is sensitive to the abundance of C, while the Fe abundance affects the relative amounts of warm and cold neutral gas.
- Our models produce a truncation radius for star formation. Cosmic ray (and X-ray) heating determines the location of this cutoff radius.

The models we have presented are of general validity, and suitable for a range of problems in galactic formation and evolution. They would be, for example, well suited to explore star formation and feedback effects for dwarf galaxies, galaxy interactions and collisions. Indeed we will study a few such applications.

References

Andersen, R.-P. & Burkert, A., 2000, *ApJ* **531**, 296

Bakes, E. L. O. & Tielens, A. G. G. M., 1994, *ApJ* **427**, 822

Barnes, J. & Hut, P., 1986, *Nature* **324**, 446

Barnes, J. E. & Hut, P., 1989, *ApJS* **70**, 389

Bate, M. R. & Burkert, A., 1997, *MNRAS* **288**, 1060

Berczik, P., Hensler, G., Theis, C., & Spurzem, R., 2003, *Ap&SS* **284**, 865

Bottema, R., 2003, *MNRAS* **344**, 358

Bruzual A., G. & Charlot, S., 1993, *ApJ* **405**, 538

Buonomo, F., Carraro, G., Chiosi, C., & Lia, C., 2000, *MNRAS* **312**, 371

Cox, D. P., 1990, in *ASSL Vol. 161: The Interstellar Medium in Galaxies*, pp 181–200

Dalgarno, A. & McCray, R. A., 1972, *ARA&A* **10**, 375

Elmegreen, B. G., 2002, *ApJ* **577**, 206

Elmegreen, B. G. & Parravano, A., 1994, *ApJ* **435**, L121+

Field, G. B., 1965, *ApJ* **142**, 531

Gerritsen, J. P. E., 1997, *Ph.D. thesis*, Groningen University

Gerritsen, J. P. E. & Icke, V., 1997, *A&A* **325**, 972

Gingold, R. A. & Monaghan, J. J., 1977, *MNRAS* **181**, 375

Habing, H. J., 1968, *Bull. Astron. Inst. Netherlands* **19**, 421

Heiles, C. & Troland, T. H., 2003, *ApJ* **586**, 1067

Hernquist, L., 1993, *ApJS* **86**, 389

Hernquist, L. & Katz, N., 1989, *ApJS* **70**, 419

Kanekar, N., Subrahmanyan, R., Chengalur, J. N., & Safouris, V., 2003, *MNRAS* **346**, L57

Katz, N., 1992, *ApJ* **391**, 502

Kitsionas, S. & Whitworth, A. P., 2002, *MNRAS* **330**, 129

Kuijken, K. & Dubinski, J., 1995, *MNRAS* **277**, 1341

Lamers, H. J. G. L. M., Panagia, N., Scuderi, S., Romaniello, M., Spaans, M., de Wit, W. J., & Kirshner, R., 2002, *ApJ* **566**, 818

Le Bourlot, J., Pineau des Forêts, G., & Flower, D. R., 1999, *MNRAS* **305**, 802

Leitherer, C., Schaerer, D., Goldader, J. D., Delgado, R. M. G., Robert, C., Kune, D. F., de Mello, D. F., Devost, D., & Heckman, T. M., 1999, *ApJS* **123**, 3

Lucy, L. B., 1977, *AJ* **82**, 1013

Mac Low, M. & Klessen, R. S., 2004, *Rev. of Mod. Phys.* **76**, 125

Makino, J., Fukushige, T., Koga, M., & Namura, K., 2003, *PASJ* **55**, 1163

McCall, B. J. et al., 2003, *Nature* **422**, 500

Meerson, B., 1996, *Rev. of Mod. Phys.* **68**, 215

Mellema, G. & Lundqvist, P., 2002, *A&A* **394**, 901

Monaghan, J. J., 1992, *ARA&A* **30**, 543

Monaghan, J. J. & Lattanzio, J. C., 1985, *A&A* **149**, 135

Navarro, J. F., Frenk, C. S., & White, S. D. M., 1997, *ApJ* **490**, 493

Navarro, J. F. & White, S. D. M., 1993, *MNRAS* **265**, 271

Nelson, R. P. & Papaloizou, J. C. B., 1993, *MNRAS* **265**, 905

Nelson, R. P. & Papaloizou, J. C. B., 1994, *MNRAS* **270**, 1

Parravano, A., Hollenbach, D. J., & McKee, C. F., 2003, *ApJ* **584**, 797

Raga, A. C., Mellema, G., & Lundqvist, P., 1997, *ApJS* **109**, 517

Rasio, F. A., 1999, *arXiv:astro-ph/9911360* p. 13

Richter, P., Sembach, K. R., Wakker, B. P., & Savage, B. D., 2001, *ApJ* **562**, L181

Salmon, J. K. & Warren, M. S., 1994, *Journal of Computational Physics* **111**, 136

Schaye, J., 2004, *ApJ* **609**, 667

Schmidt, M., 1959, *ApJ* **129**, 243

Semelin, B. & Combes, F., 2002, *A&A* **388**, 826

Shu, F. H., Adams, F. C., & Lizano, S., 1987, *ARA&A* **25**, 23

Silich, S. A., Franco, J., Palous, J., & Tenorio-Tagle, G., 1996, *ApJ* **468**, 722

Silva, A. I. & Viegas, S. M., 2001, *Computer Physics Communications* **136**, 319

Springel, V. & Hernquist, L., 2002, *MNRAS* **333**, 649

Springel, V. & Hernquist, L., 2003, *MNRAS* **339**, 289

Springel, V., Yoshida, N., & White, S. D. M., 2001, *New Astronomy* **6**, 79

Sutherland, R. S. & Dopita, M. A., 1993, *ApJS* **88**, 253

van Dishoeck, E. F. & Black, J. H., 1986, *ApJS* **62**, 109

Voronov, G. S., 1997, *Atomic Data and Nuclear Data Tables* **65**, 1

Watson, W. D., 1972, *ApJ* **176**, 103

Webber, W. R., 1998, *ApJ* **506**, 329

Whitworth, A. P., 1998, *MNRAS* **296**, 442

Wolfire, M. G., Hollenbach, D., McKee, C. F., Tielens, A. G. G. M., & Bakes, E. L. O., 1995, *ApJ* **443**, 152

Wolfire, M. G., McKee, C. F., Hollenbach, D., & Tielens, A. G. G. M., 2003, *ApJ* **587**, 278

Zuckerman, B. & Evans, N. J., 1974, *ApJ* **192**, L149

Chapter 3

Feedback in SPH simulations of galaxies

Abstract

We examine two new methods for including supernova and stellar wind feedback in smoothed particle hydrodynamics (SPH) simulations of galaxies. The first method is based upon the return of energy as random motions in the gas. The second is based on the equations of motion of an ordinary SPH particle in the zero mass limit: we construct a separate type of particle, which we will call a *pressure particle*, associated with young stellar clusters, that acts on the gas through these equations. We check that both these methods give equivalent solutions to the problem of energy injection in gaseous media, compared with direct heating of the gas. We furthermore show that these methods circumvent the problems of conventional feedback implementations in simulations including the cooling of the ISM and star formation. We also examine the relation between HI properties and star formation, showing that our model reproduces observed correlations.

3.1 Introduction

Probably the greatest source of uncertainty in the theory of galaxy formation and evolution is the injection of mechanical energy into the interstellar medium (ISM) by young stellar clusters. Hybrid hydrodynamics/ N-body codes have proved to be useful tools to get a grip on the complexity of gravitational dynamics and ISM physics. An important source of heating that needs to be included in simulations is the mechanical luminosity of stellar clusters, which is the collective result of stellar winds and successive supernovae (SNe) explosions of massive stars in approximately the first 30 Myr of the lifetime of a cluster. For a cluster of given age and initial mass function (IMF) this mechanical luminosity can be determined from current stellar evolution models (e.g.. Starburst99 models, Leitherer et al. 1999), which incorporate the most recent results of stellar evolution theory and dynamic atmosphere modelling. In principle it is then not difficult to account for this as an extra term in the thermal evolution equations of a hydrodynamic simulation of the ISM.

However as was first observed by Katz (1992) in smoothed particle hydrodynamics (SPH, Gingold & Monaghan 1977, Lucy 1977, Monaghan 1992) simulations of galaxy formation, this naive implementation of supernova feedback will have little effect on the dynamics of the ISM. The reason for this is that a realistic model for the ISM must take into account cooling of the gas. The heating from the mechanical luminosity is small compared with the potential for cooling if, as in practice is always the case, the resolution of the ISM simulation is limited. We can write the heating $\Gamma_{\rm sn}$ due to a young star cluster that returns its energy to a nearby gas particle or gas cell, as $\Gamma_{\rm sn} = \mathbb{L}_{\rm mech}\frac{\rm M_{star}}{\rm M_{gas}}$, with $\mathbb{L}_{\rm mech}$ the mechanical luminosity of the young stellar cluster per unit mass of stars formed, $\rm M_{star}$ the mass of the star particle and $\rm M_{gas}$ the mass of the gas particle that receives the SN energy. For values $\mathbb{L}_{\rm mech} = 5$ erg $\rm g^{-1}$ $\rm s^{-1}$ (assuming 0.01 supernova of 10^{51} erg $\rm M_\odot{}^{-1}$ of stars formed and an active period of 30 Myr, which is approximately the the mechanical energy luminosity for a Salpeter IMF with mass boundaries 0.1 $\rm M_\odot$ and 100 $\rm M_\odot$) and $\rm M_{star}/M_{gas}$ of order unity (appropriate for current star formation recipes) we then get a heating of $\Gamma_{\rm sn} = 5$ erg $\rm g^{-1}$ $\rm s^{-1}$, which is much smaller than the cooling Λ at the peak of the cooling curve at about 10^5 K of $\Lambda \approx 400$ $\rm n_H$ erg $\rm g^{-1}$ $\rm s^{-1}$, for H densities $\rm n_H \gtrsim 1$ $\rm cm^{-3}$. So returning the energy to the gas as heating will not result in temperatures higher than 10^5 K and usually much lower, and this is too small to alter the dynamics of the gas substantially. This is unrealistic: in practice hot gas will carve out a low density bubble where cooling is inefficient. Radiative losses are important, but occur in dense shells around this bubble. The problem of feedback implementation is not exclusive to SPH codes, it occurs also in other types of hydrodynamic codes, e.g. Eulerian grid codes (Fragile et al. 2003).

Note that increasing the resolution of the simulation alone will not solve the problem of radiative energy losses: increasing the resolution but keeping $\rm M_{star}/M_{gas}$ fixed, one will encounter the same problem. Only increasing the ratio $\rm M_{star}/M_{gas}$ to values $\gg 100$ would mitigate the problem, as this would allow the gas to attain a high temperature. This is normally the case in more detailed simulations of superbubbles (e.g. Mac Low & Ferrara 1999) due to starbursts. This is not practical in SPH simulations of galaxies that include star formation, because star formation in these simulations is sub-grid physics. Forming large star particles would impose graininess on the star formation rate. Furthermore, current methods of star formation use a local star formation method that changes a fraction of order unity of a gas particle's mass into stars conditional upon a criterion that depends on the thermodynamic state of that particle.

Many authors have tried to circumvent the loss of feedback energy by developing different methods of implementing feedback in SPH type codes. Navarro & White (1993) and Mihos & Hernquist (1994) examined returning part of the energy as a direct velocity "kick" to nearby particles. Gerritsen (1997) and Mori et al. (1997) returned all energy to a single particle which was then artificially inhibited from cooling. Similarly Thacker & Couchman (2000) modified the cooling properties of the particle receiving supernova energy, but they did so by defining a plausible cooling density for the unresolved hot bubble. A completely different approach was taken by Springel (2000), who introduced a separate variable to track the turbulent energy induced by feedback which was then returned slowly to internal energy of the particle. A different approach still is to forsake any pretention of resolving feedback and formulate a complete sub-grid model for the multiphase medium, where supernova feedback is taken into account deriving an effective equation of state for the gas (Springel & Hernquist 2003).

We will not give a complete overview of the different strengths and weaknesses of these methods. For a solid discussion of SPH feedback methods see Thacker & Couchman (2000) and Kay et al. (2002). A recurrent problem for the explicit feedback methods is that it is difficult to get unambiguous control over the strength of the feedback: either physically motivated values of the feedback efficiency give too strong feedback and a laborious and subjective search must be made for an acceptable value or the method gives too weak feedback and energy losses must be limited by an ad hoc intervention. On the other hand, the methods that try to account for feedback implicitly as either an extra reservoir of energy or in a sub-grid model suffer from the problem that it may be impossible to reproduce the effect of feedback on the distribution of gas, that is the occurrence of superbubbles and other phenomena related to the “frothy” ISM.

Here we will present and test two new methods for feedback in SPH codes that address some of the problems of previous feedback implementations.

3.2 Smoothed particle hydrodynamics

Different variants of SPH were tested recently for their ability to model feedback by Springel & Hernquist (2002). They formulated a new SPH scheme that conserves both energy and entropy, contrary to previous formulations and for this reason it turned out to be the most suitable for the implementation of feedback. We will also use this scheme. So we have the standard SPH estimate for the density ρ_i due to a distribution of particles with positions r_i using a kernel function W,

$$\rho_i = \sum_j m_j W(|r_i - r_j|, h_i), \tag{1}$$

where m_i is the mass of particle, h_i its smoothing length and for $W(r,h)$ we take the spline kernel of Monaghan & Lattanzio (1985). The Springel & Hernquist (2002) conservative SPH scheme gives the following equation of motion for the SPH particles,

$$\frac{dv_i}{dt} = -\sum_{j=1}^{N} m_j \left\{ f_i \frac{P_i}{\rho_i^2} \nabla_i W_{ij}(h_i) + f_j \frac{P_j}{\rho_j^2} \nabla_i W_{ij}(h_j) + \Pi_{ij} \nabla \bar{W}_{ij} \right\} \tag{2}$$

with particle velocities v_i, pressures P_i and the f_i defined by:

$$f_i = \left(1 + \frac{h_i}{3\rho_i} \frac{\partial \rho_i}{\partial h_i} \right)^{-1} \tag{3}$$

Here, $\bar{W}_{ij} = (W_{ij}(h_i) + W_{ij}(h_j))/2$ is a symmetrized form of the kernel. For the artificial viscosity tensor Π_{ij} we can take any one of the standard forms (Monaghan

1992, Hernquist & Katz 1989), we will use

$$\Pi_{\mathrm{ij}} = \frac{-\alpha\mu_{\mathrm{ij}}\bar{c}_{\mathrm{ij}} + \beta\mu_{\mathrm{ij}}^2}{\bar{\rho}_{\mathrm{ij}}}, \tag{4}$$

where

$$\mu_{\mathrm{ij}} = \begin{cases} \frac{\mathrm{v_{ij}} \cdot \mathrm{r_{ij}}}{\bar{\mathrm{h}}_{\mathrm{ij}}(\mathrm{r_{ij}^2}/\bar{\mathrm{h}}_{\mathrm{ij}}^2 + \eta^2)} & \text{for } \mathrm{v_{ij}} \cdot \mathrm{r_{ij}} < 0, \\ 0 & \text{for } \mathrm{v_{ij}} \cdot \mathrm{r_{ij}} \geq 0. \end{cases}$$

Here $\mathrm{v_{ij}} = \mathrm{v_i} - \mathrm{v_j}$ and $\mathrm{r_{ij}} = \mathrm{r_i} - \mathrm{r_j}$, α, and β are constants of order 1 ($\alpha = 0.5$, $\beta = 1$), η is a parameter to prevent numerical divergences and quantities overlaid with a bar are symmetrized, e.g. $\bar{\mathrm{c}}_{\mathrm{ij}} = (\mathrm{c_i} + \mathrm{c_j})/2$ for the average sound speed of particles i and j.

It is convenient to use the entropic function, defined by $\mathrm{P} = \mathrm{A}\rho^\gamma$, with γ (=5/3) the adiabatic index of the gas, to track the thermal evolution of the gas, integrating $\mathrm{A_i}$ according to

$$\frac{\mathrm{dA_i}}{\mathrm{dt}} = -\frac{\gamma - 1}{\rho_{\mathrm{i}}^{\gamma}}(\Gamma - \Lambda) + \frac{1}{2}\frac{\gamma - 1}{\rho_{\mathrm{i}}^{\gamma-1}} \sum_{\mathrm{j}=1}^{\mathrm{N}} \mathrm{m_j}\Pi_{\mathrm{ij}}\mathrm{v_{ij}} \cdot \nabla_{\mathrm{i}}\bar{\mathrm{W}}_{\mathrm{ij}} \tag{5}$$

Here, Γ and Λ represent the external heating and cooling terms. These are determined by consideration of the physical processes that we want to include to model the ISM (see Chapter 2).

3.3 Supernova feedback methods

Here we will examine two new methods to implement feedback in SPH simulations. The first is a variant of the kinetic energy feedback, but imparting random in stead of radial velocity kicks. The second is related to the idea of Gerritsen (1997) of giving one particle all the mechanical energy. We will compare both methods to “normal” particle heating.

3.3.1 Particle heating

As we have argued above simply considering the mechanical energy as a heating term is not a good method of modelling feedback in simulations of galaxies. On the other hand it has been shown by Springel & Hernquist (2002) to represent point explosions well. As such we will consider single particle (SP) heating here for comparison to the more elaborate methods.

We will add all energy $\mathrm{e_{sn}}$ that is to be injected into the gas, to the nearest gas particle, changing its entropy by:

$$\Delta\mathrm{A_i} = \frac{\mathrm{e_{sn}}}{\mathrm{m_i}}\frac{\gamma - 1}{\rho^{\gamma-1}} \tag{6}$$

There are different ways of applying particle heating (see also the discussion in Thacker & Couchman 2000). One could add a heating term proportional to the local mechanical luminosity to Γ in equation (5) or add the energy produced per time step directly to the thermal energy of neighbouring gas particles. Another method is simply letting every star formation event be accompanied by an injection of an instantaneous energy burst corresponding to all mechanical energy released over time by the mass of stars formed. These methods are very similar but they are expected to behave differently, for the following reasons: 1) the cooling curve has a strong peak so that in case of heating the feedback will be constrained by the peak value of the cooling, whereas an instantaneous thermal energy jump may bypass this peak; 2) in general the local time step is shorter by one or more orders of magnitude than the release time of the supernova energy (typically in the order of 3×10^7 yr). The various methods are described elsewhere (see e.g. Thacker & Couchman 2000) and we will not examine all of these methods. The general conclusion, that thermal energy feedback is not an efficient mechanism, is in all cases not altered.

3.3.2 Kinetic energy feedback

The alternative of adding the SN energy as kinetic energy by modifying the velocities of nearby particles was examined by Navarro & White (1993) and Gerritsen (1997). They found that imparting a radial velocity kick to particles in the neighbourhood of a SN particle results in strong feedback effects. Their conclusion was that, unless a very small fraction (≈ 0.0001) of the original SN energy was used for the velocity kick, the effects of feedback on the ISM would be too strong. This fraction differs substantially from the physically motivated value of ≈ 0.1 for the efficiency of the conversion of supernova energy to kinetic energy of the ISM.

However, we will examine an implementation of kinetic energy feedback (KF) that imparts velocity kicks to neighbouring SPH particles in random directions, as opposed to radial. This is based on the following basic observation about kinetic energy $\mathrm{E_k}$ in SPH, using the SPH identity $\sum_{\mathrm{j}} \frac{\mathrm{m_j}}{\rho_{\mathrm{j}}} \mathrm{W_{ij}} \approx 1$:

$$\begin{aligned}
\mathrm{E_k} &= \sum_{\mathrm{i}} \frac{1}{2} \mathrm{m_i v_i^2} \\
&\approx \sum_{\mathrm{i,j}} \frac{1}{2} \frac{\mathrm{m_i m_j}}{\rho_{\mathrm{j}}} \mathrm{v_i^2 W_{ij}} \\
&= \sum_{\mathrm{j}} \frac{1}{2} \mathrm{m_j} \sum_{\mathrm{i}} \frac{\mathrm{m_i}}{\rho_{\mathrm{j}}} \left\{ (\mathrm{v_i} - \bar{\mathrm{v}}_{\mathrm{i}}) + 2\mathrm{v_i} \bar{\mathrm{v}}_{\mathrm{i}} - \bar{\mathrm{v}}_{\mathrm{i}}^2 \right\} \mathrm{W_{ij}} \qquad (7) \\
&= \sum_{\mathrm{j}} \frac{1}{2} \mathrm{m_j} \sigma_{\mathrm{i}}^2 + \sum_{\mathrm{j}} \frac{1}{2} \mathrm{m_j} \bar{\mathrm{v}}_{\mathrm{i}}^2 \\
&= \mathrm{E_{random}} + \mathrm{E_{bulk}}
\end{aligned}$$

with $\bar{\mathrm{v}}_{\mathrm{i}}$ and σ_{i} the usual SPH estimates of the local velocity and velocity dispersion. The total kinetic energy of the particles in the simulation can be split (approximately) into a part $\mathrm{E_{bulk}}$, associated with bulk motions of the gas and a part $\mathrm{E_{random}}$ associated with random motions. The random kinetic energy will decrease, even in the absence of bulk motions, because of the coupling to the thermal energy through the effect of the artificial viscosity,

$$\dot{\mathrm{E}}_{\mathrm{random}} = \sum_{\mathrm{i,j}} \mathrm{m_i v_{ij}} \cdot \Pi_{\mathrm{ij}} \nabla \bar{\mathrm{W}}_{\mathrm{ij}} \tag{8}$$

and thus it will decay over time and be added to the internal energy of the particles. So by imparting particles with a random velocity we act in fact on a reservoir of energy in between thermal and bulk movements of the gas (one may want to interpret this as the smallest scale of turbulence in the simulation, however it is not entirely clear whether this is justified, numerical tests of relaxing random particle distributions suggest that the decay of kinetic energy (8) happens on timescales, scaled to physical units relevant to our simulation, of $\approx 10^6$ yr). As a result of feedback the velocity dispersion will be enhanced locally. The enhanced velocity dispersion acts as a pressure that can push out surrounding gas with lower dispersion and thus can still result in radial motions and superbubbles.

To be specific, the method consists of giving particles in the neighbourhood of SN particles a random velocity kick with mean magnitude:

$$\Delta \mathrm{v} = \sqrt{2\mathrm{e_{sn}} \Delta \mathrm{t W}} \tag{9}$$

Note that the $\sqrt{\Delta \mathrm{t}}$ dependence guarantees that the feedback does not depend on the size of the local time step. A possible shortcoming of this method is that momentum is not strictly conserved, locally we expect statistical variations due to the limited number of neighbours. It is not difficult to correct for these variations by imposing momentum conservation.

3.3.3 Pressure particle feedback

The mass of hot gas in SN remnants and hot bubbles is generally a small fraction of the total mass of the associated star formation event. The problem of feedback is thus in essence a resolution problem: we form stars at the minimum mass resolution, thus the hot gas mass is much too low to be resolved. Inspired by the fact that the mass of hot gas is very small and by previous feedback implementations that used single hot particles, we propose to model the feedback by considering the zero mass limit of an SPH particle, such that the product $\mathrm{m} \times \mathrm{P}$ of particle mass and pressure remains constant taking the limit $\mathrm{m} \to 0$. We will call such a particle a *pressure particle* (PP) (the connection between our pressure particles and those of Gerritsen will be explained shortly). Such pressure particles will be associated with every new star particle formed in the simulation. The contribution of a pressure particle to the acceleration of neighbouring (normal) SPH particles will be given by taking the limit $\mathrm{m_{PP}} \to 0$ of the ordinary expression for the SPH equations of motion, so for example in case of the conservative SPH formulation (from Eq.2):

$$\begin{aligned} \left.\frac{\mathrm{dv_i}}{\mathrm{dt}}\right|_{\mathrm{PP}} &= \mathrm{m_{PP}}(\mathrm{f_{PP}} \frac{\mathrm{P_{PP}}}{\rho^2_{\mathrm{PP}}} \nabla \mathrm{W}(\mathrm{h_{PP}}) + \mathrm{f_i} \frac{\mathrm{P_i}}{\rho^2_{\mathrm{i}}} \nabla \mathrm{W}(\mathrm{h_i}) + \Pi \nabla \bar{\mathrm{W}}) \\ &\to \mathrm{A_{PP}} \rho^{\gamma-2} \nabla \mathrm{W}(\mathrm{h_i}), \quad \mathrm{as}\ \mathrm{m_{PP}} \to 0. \end{aligned} \tag{10}$$

Here, $\mathrm{A_{PP}} = \mathrm{P_{PP}}/\rho^{\gamma}_{\mathrm{PP}} = (\gamma - 1)\mathrm{e_{PP}}/\rho^{\gamma-1}_{\mathrm{PP}}$ is the entropic function of the pressure particle. The artificial viscosity term of the SPH equations does not contribute to the

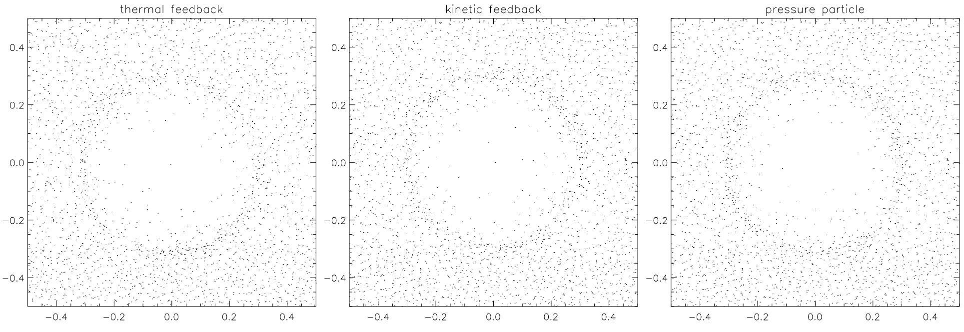

Figure 3.1: Cuts through the particle distribution for the point explosion test. Plotted are the particles closer than 0.05 to the equatorial plane. Each panel shows the results for different feedback method (from left to right: thermal, kinetic and pressure particle feedback).

acceleration as $m_{PP}\Pi_{iPP} \rightarrow 0$ for $m_{PP} \rightarrow 0$. The acceleration of the particle itself will formally diverge in the limit, but we fix the pressure particles to star particles. As a result we lose momentum, in reality this momentum would be carried by the hot gas "pushing" against the surrounding gas, and it would be returned to the ISM at some point. We correct for this by assigning all momentum to the particle in the neighbourhood of the pressure particle that is most "antipodal" to the direction of the lost momentum (This also ensures to first order angular momentum conservation). The entropy A_{PP} is the variable that determines the strength of feedback, and its evolution in time is an input to the model that depends on the amount of star formation but also on assumptions about energy loss and remnant evolution that are not resolved in the code. It is acceptable to fix this as an input model, as we had determined that we cannot in any way follow realistically the evolution of SN remnants. Here we will use relatively simple prescriptions for A_{PP} (which we will describe below); in principle one could invoke results of more detailed models/ simulations in its evolution. Note that the method is in some ways similar to the approaches of Gerritsen (1997) and of Tacker & Couchman (2000), in that the feedback is effected by one particle, but rather than just fixing and preventing an ordinary SPH particle from cooling (Gerritsen) or defining an effective density (Tacker & Couchman) we choose to explicitly treat SN particles as separate entities. The advantage of our approach is that we have a well defined model (namely the prescription for A_{PP}) which we can vary according to our assumptions for the unresolved physics. Furthermore, it is numerically well behaved and does not suffer from the numerical instabilities that can occur in Gerritsen's method (Bottema 2002, priv. comm.).

3.4 Sedov blast wave test

In order to assess the capabilities of the various feedback schemes to model explosive events we test the ability of the methods to model a point explosion in a background of constant density and zero thermal energy. In this test we do not use cooling. This test is described in Springel and Hernquist (2002) for single particle heating. They found that, for the conservative SPH formulation, SPH reproduces the speed of the

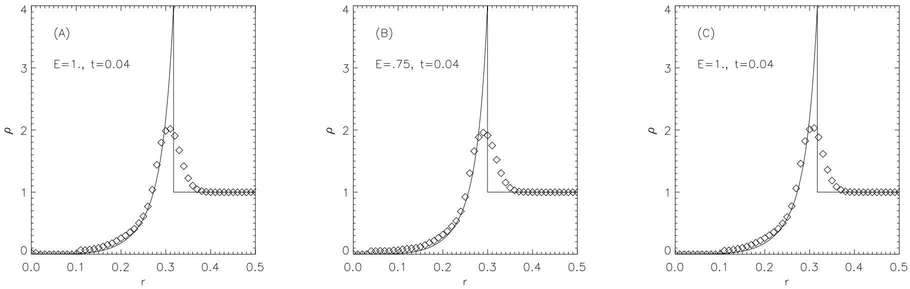

Figure 3.2: Radial density profiles for the point explosion test. A: thermal feedback, B: kinetic feedback C: pressure particle feedback. Diamonds indicate the spherically averaged density for a $\mathrm{N} = 64000$ run. The analytical solution follows the drawn line.

shock front and the shape of the inner density profile of the analytic solution (e.g. Landau & Lifschitz 1987). The density contrast at the shock location is generally too low at moderate resolution due to the smoothing properties of the SPH kernel estimate for the density. Also visible in the particle plots of Springel & Hernquist (their Figure 2) are some artifacts due to the use of a regular grid as the initial particle distribution. The solution for this problem is the use of initial conditions without preferred directions (Thacker & Couchman 2000). This is not really a restriction as this is also the case for the typical particle distributions that are present in the course of a simulation. For the test we therefore used as the initial particle distribution a glass state: a smooth gas box of consisting of an SPH particles relaxed from a Poisson distribution. Drawback of this approach is that the density exhibits variations of order $\delta\rho/\langle\rho\rangle \sim 0.01$ (which is much smaller than the scatter in density of the non-relaxed initial condition, ~ 0.1). We show results for $\mathrm{N} = 64000$, results for other resolutions are similar and consistent with the resolution study in Springel and Hernquist (2002). The mean density is set to $\langle\rho\rangle = 1$, the temperature of the gas is set at the minimum allowed. At the start of the simulation a point explosion with energy $\mathrm{E} = 1$ is set off at the origin, implemented in accordance with the respective feedback methods. For SP feedback this means that at $\mathrm{t} = 0$ all energy is put into one particle in the centre of the box. For the KF method an instantaneous random velocity kick is given in the centre of the gas distribution according to Eq. 9. For PP feedback a pressure particle with $\mathrm{A} = 2/3$ is placed at the origin. The pressure particle is evolved adiabatically so A (the entropy) stays constant.

In Fig. 3.1 we plot the particle distributions after $\mathrm{t} = 0.04$ for all three methods while in Fig. 3.2 we have plotted the radial density distributions. If we compare these to Fig. 2-4 in Springel & Hernquist (2002) we see that the particle distributions show slight deviations from spherical symmetry. This is due to the fact we have started from initial conditions with small perturbations. Otherwise the results are qualitatively the same. Note especially that for KF there is no remnant visible from the initial anisotropic velocity kicks. All three methods show very similar behaviour, and are certainly equivalent. We conclude that all three methods considered here can be used to model point explosions, and so are in principle good candidates for use as supernova feedback models in galaxies.

3.5 Feedback in dwarf galaxies

Next we will test our feedback prescriptions in a realistic model for a dwarf irregular (dIrr) galaxy. These dwarf galaxies are ideal feedback "labs." Free from the effects of differential rotation and spiral density waves the prime regulator of star formation activity is probably the energy input by young stars (Hunter 1997). Thus the outcome of the modelling will be sensitive to the quality of the feedback implementation. We will test our feedback methods implemented in a code that has a realistic model for ISM and star formation.

dIrrs are a well studied group of galaxies: HI observations show that their ISM is heavily perturbed: their HI distribution is dominated by holes, shells and filaments, giving a frothy structure (e.g. Walter 1999, Stil 2002b). The velocity dispersions of HI in dwarf galaxies are generally in the order 10 km/s and some stirring force is needed to maintain this velocity dispersion against dissipation (Stil 2002a), SN explosions being one of the candidates. The challenge then is to have a feedback scheme that manages to reproduce a dwarf galaxy with a dynamic ISM, whose star formation properties and ISM structure are constrained by these observations.

3.5.1 ISM and star formation model

For the ISM model we use the model D of Chapter 2 for a subsolar metallicity of $\mathrm{Z} = \mathrm{Z}_{\odot}/5$. This model is a comprehensive model for the neutral ISM and it includes realistic cooling as well as heating by UV light from stars, including the effects of grain charging, and it solves the ionization balance including cosmic ray ionizations. For the primary cosmic ray ionization rate we take $\zeta_{\mathrm{CR}} = 3.6 \times 10^{-17}\ \mathrm{s}^{-1}$.

The most important feature of the ISM model is that it allows to follow cooling and collapse of the warm neutral medium (WNM) to the cold neutral medium (CNM): warm, partially ionized gas (with temperatures $\mathrm{T} = 10^4$ K and ionization fraction $\mathrm{x_e} \approx 0.1$) that is stable with respect to gravitational collapse, will cool down as soon as heating of the gas decreases (due to for example a decrease in UV irradiation as nearby stellar populations age). As a region cools down and loses its pressure support collapses it will become eligible to form stars.

Our star formation recipe is similar to that used by Gerritsen & Icke (1997), and is amply discussed in Chapter 2. In short it considers a particle unstable to star formation if the local Jeans mass $\mathrm{M_J}$ is smaller than a reference mass $\mathrm{M_{ref}}$,

$$\mathrm{M_J} = \frac{\pi\rho_\mathrm{i}}{6}\left(\frac{\pi \mathrm{c_i^2}}{\mathrm{G}\rho_\mathrm{i}}\right)^{3/2} < \mathrm{M_{ref}}. \tag{11}$$

The reference mass $\mathrm{M_{ref}}$ is chosen such that it is approximately equal to the smallest resolvable mass. If a particle is unstable to star formation it will form stars on a timescale τ_{sf} that scales with the free-fall timescale τ_{ff},

$$\tau_{\mathrm{sf}} = \mathrm{f_{sf}} \mathrm{t_{ff}} = \frac{\mathrm{f_{sf}}}{\sqrt{4\pi \mathrm{G}\rho}}. \tag{12}$$

Here, $\mathrm{f_{sf}}$ is a delay factor that accounts for the fact collapse is delayed by either turbulence or magnetic fields (Mac Low & Klessen 2004, Shu et al. 1987).

The stellar particles that are formed carry an age. We use Bruzual & Charlot (1993) models for a Salpeter IMF to calculate UV luminosities (in the range $912 - 2100$ Å) needed for the calculation of the local radiation field.

3.5.2 Initial conditions

We construct initial conditions by constructing a model for a dwarf galaxy consisting of 3 components: gaseous disk, stellar disk and a dark halo. In the simulations presented here the dark halo is taken to be a fixed background potential with a density profile

$$\rho(r) = \rho_0 \frac{e^{-r^2/R_{ct}^2}}{r^2 + r_c^2}, \tag{13}$$

with central density of $\rho_0 = 0.02\ \mathrm{M_\odot\ pc^{-3}}$, cutoff radius $\mathrm{R_{ct}} = 20$ kpc and core radius $\mathrm{r_c} = 2$ kpc. This halo profile is chosen rather than the Navarro, Frenk & White profile we used in Chapter 2 because the halos of dwarf galaxies are seen to have flat density cores (Burkert 1995). For the stellar component we construct an exponential disk,

$$\rho_{\mathrm{disk}}(\mathrm{R, z}) = \frac{\Sigma_0}{2\mathrm{h_z}} \exp(-\mathrm{R/R_d}) \mathrm{sech}^2(\mathrm{z/h_z}) \tag{14}$$

with central surface density $\Sigma_0 = 300\ \mathrm{M_\odot/pc^2}$, radial scale length $\mathrm{R_d} = 0.5$ kpc and vertical scale height $\mathrm{h_z} = 200$ pc. So the total stellar mass is $1.5 \times 10^8\ \mathrm{M_\odot}$. It is constructed using the approximation of a three integral distribution function of Kuijken & Dubinski (1995). The stellar particles are initialised randomly with ages of up to 12 Gyr old. The gas disk is constructed with a radial surface density profile,

$$\Sigma = \frac{\Sigma_\mathrm{g}}{1 + \mathrm{R/R_g}}, \tag{15}$$

with central density $\Sigma_\mathrm{g} = 8\ \mathrm{M_\odot/pc^2}$ and radial scale $\mathrm{R_g} = 0.5$ kpc, truncated at 6 kpc, for a total mass of $10^8\ \mathrm{M_\odot}$. Initially the gas disk is given a temperature of 8000 K.

3.5.3 The mechanical luminosity

The stellar particles that are formed in the simulation do not represent single stars but have masses in the order of a few hundred to few thousand solar masses. They can be considered to be stellar clusters, and we will assume that stars in these clusters are formed with masses distributed according to a Salpeter IMF, $\Phi \propto \mathrm{M}^{-1.35}$ with lower cutoff mass $\mathrm{M_{low}} = 0.1\ \mathrm{M_\odot}$ and upper cutoff $\mathrm{M_{upper}} = 100\ \mathrm{M_\odot}$. Gerritsen & Icke (1997) discussed the effect of other choices for the IMF, they found that because the amount of mechanical energy produced by a cluster depends sensitively on the shape of the IMF, the results with respect to star formation are sensitive to this choice. Note that this uncertainty is often encountered in astrophysical studies related to star formation, and, in the context of a self regulated model for star formation translates to an uncertainty in the exact star formation rates. The masses of the "star clusters" that are formed, are small enough that formally the number of heavy stars, and hence the mechanical luminosity, should vary from particle to particle due to sampling effects.

In practice we will still assume a complete sampling of the IMF even for low mass particles. At least this yields a reasonable estimate for the mechanical luminosity. The possible impact of this assumption is further reduced by the fact that a star forming region will in general produce multiple star particles, which increases the effective cluster size.

Given the distribution of initial masses of stars the mechanical luminosity can be derived from stellar evolution models. The following provides an estimate of this luminosity that is good enough for our purposes:

$$\mathbb{L}_{\mathrm{mech}} = \frac{\mathrm{n_{sn} E_{sn}}}{\Delta \mathrm{t_{sn}}} \ \text{erg s}^{-1} \ \mathrm{M_\odot}^{-1}. \tag{16}$$

Here, $\mathrm{n_{sn}} = 0.009 \ \mathrm{M_\odot}^{-1}$ is the number of supernova per solar mass of stars formed. This number is derived for our IMF assuming all stars with masses above $\mathrm{M} = 8 \ \mathrm{M_\odot}$ explode as type II supernovae. These supernovae yield an energy $\mathrm{E_{sn}} \approx 10^{51}$ erg, and while stellar winds can contribute significantly in the first few Myr, type II SNe constitute the bulk of the energy input. An active period of $\Delta \mathrm{t_{sn}} = 30$ Myr (approximately the lifetime of an $8 \ \mathrm{M_\odot}$ star), during which the mechanical luminosity is assumed constant, is adopted. In Chapter 2 (Fig. 2.11) we have plotted this prescription compared to a more detailed model.

For the SP and KF feedback methods the mechanical luminosity can be used directly as the amount of heat or kinetic energy to be injected into the ISM. However for the PP method we need to specify additionally the thermal evolution of the supernova particle. Here we evolve the entropy $\mathrm{A_{PP}}$ according to

$$\frac{\mathrm{dA_{PP}}}{\mathrm{dt}} = \frac{\gamma - 1}{\rho^{\gamma-1}} \epsilon_{\mathrm{PP}} \mathrm{m}_\star \mathbb{L}_{\mathrm{mech}}, \tag{17}$$

where $\rho = \rho(\mathrm{r_{PP}})$ is the density at the PP location, ϵ_{PP} the efficiency of PP feedback and $\mathrm{m}_\star$ the mass of the new stellar particle. After $\Delta \mathrm{t_{sn}}$ we assume that the hot gas in the bubble will quickly cool, and thus we set $\mathrm{A_{PP}} = 0$ and remove the pressure particle from the calculation. For the efficiency parameter we will assume that 90% of the available energy is radiated away (in structures we cannot resolve), thus $\epsilon_{\mathrm{PP}} = 0.1$. This value comes from more detailed simulations of the effect of supernova and stellar winds on the ISM (Silich et al. 1996), and is also used in other simulations of galaxy evolution (e.g. Semelin & Combes 2002, Springel & Hernquist 2002, Buonomo et al. 2000). A similar thermal evolution of SN remnants was shown by Oey & Clarke (1997) to be consistent with the size distribution of superbubbles in the Small Magellanic Cloud and Holmberg II.

Note that the constancy of the efficiency ϵ may not be valid. It may depend on the environment of the star formation location. In that case it may be worthwhile, especially for application of the model to extreme conditions (like dense cores in mergers, or formation of central clusters in galaxies), to explore this parameter further.

3.5.4 Feedback test runs

In addition to the three different methods for feedback we will let our model galaxy run without any SN feedback, letting the gas only experience heating by UV light of young stars. Thus we run 4 different runs indicated by their feedback method: FUV for the UV feedback only run, in addition to SP, KF and PP feedback runs.

In all simulations we use the full ISM and star formation model, the only difference between them being the feedback method. We will run simulations at low (20k gas particles and 20k star particles) and high resolution (200k resp. 200k). We stop the runs at approximately 1 Gyr, at which point any transient features from the initial conditions are gone.

3.5.5 Results

In Fig. 3.3 we show cuts through the central plane of the resulting galaxies at the end of the simulation showing density and temperature for the low resolution runs, while in Fig. 3.4 we have shown corresponding plots for the high resolution runs. If we look at the FUV runs first, we see that the ISM in these stay in a rather cold state at 20k resolution. The inner 2 kpc of the galaxy has a temperature $T \lesssim 1000$ K. For high resolution the disks collapses in dense clumps or stretched filaments, due to these the density distribution looks highly structured with many spiral arms. For the SP run we see that supernova feedback manages to create very small warm bubbles of $T = 10^4$ K. However the density distribution is still very structured.

The density distribution of the KF and PP are qualitatively very similar and show a density distribution with large voids (< 1 kpc big) caused by feedback. Note that area of the disk where star formation can happen is actually larger in case of the KF and PP runs than in FUV and SP runs. If we look at the the temperatures in case of PP feedback we see that they reach much higher values in those bubbles, this is due to the fact that in case of KF the energy is put into random motions of the gas, while the maps for PP feedback show the hotspots where pressure particles contribute to temperature. The temperatures in case of PP feedback fall short of the temperature of the gas associated with superbubbles (10^{5-6} K vs 10^{6-7} K). This is caused by the fact that the temperatures are derived using a smoothing procedure: the mass in the hot bubbles is lower than the mass resolution, so cold material contributes to the temperature estimate. As we increase resolution we see that the derived temperatures increase for a bubble of given size as it becomes better resolved. However, the strength of the feedback is not affected, because the strength of the feedback is not determined by this temperature.

Comparing the low and high resolution runs, we see that the high resolution runs show more structure on the small scales, as of course expected, but still high resolution runs are very similar in that there is still a similar number of large shells.

HI: morphology & kinematics

To facilitate comparison with observations, we extract HI data cubes from snapshots of the simulations using the position, velocity, temperature and ionization information of the gas particles. The three dimensional data cube consists of a projection of the 6-dimensional particle distribution in position-velocity on the spatial x-y plane and the z velocity axes, with particles smoothed according to their smoothing lengths in the spatial dimension and according to the Doppler-width corresponding to their temperature in velocity space. It contains the information an observer would be able

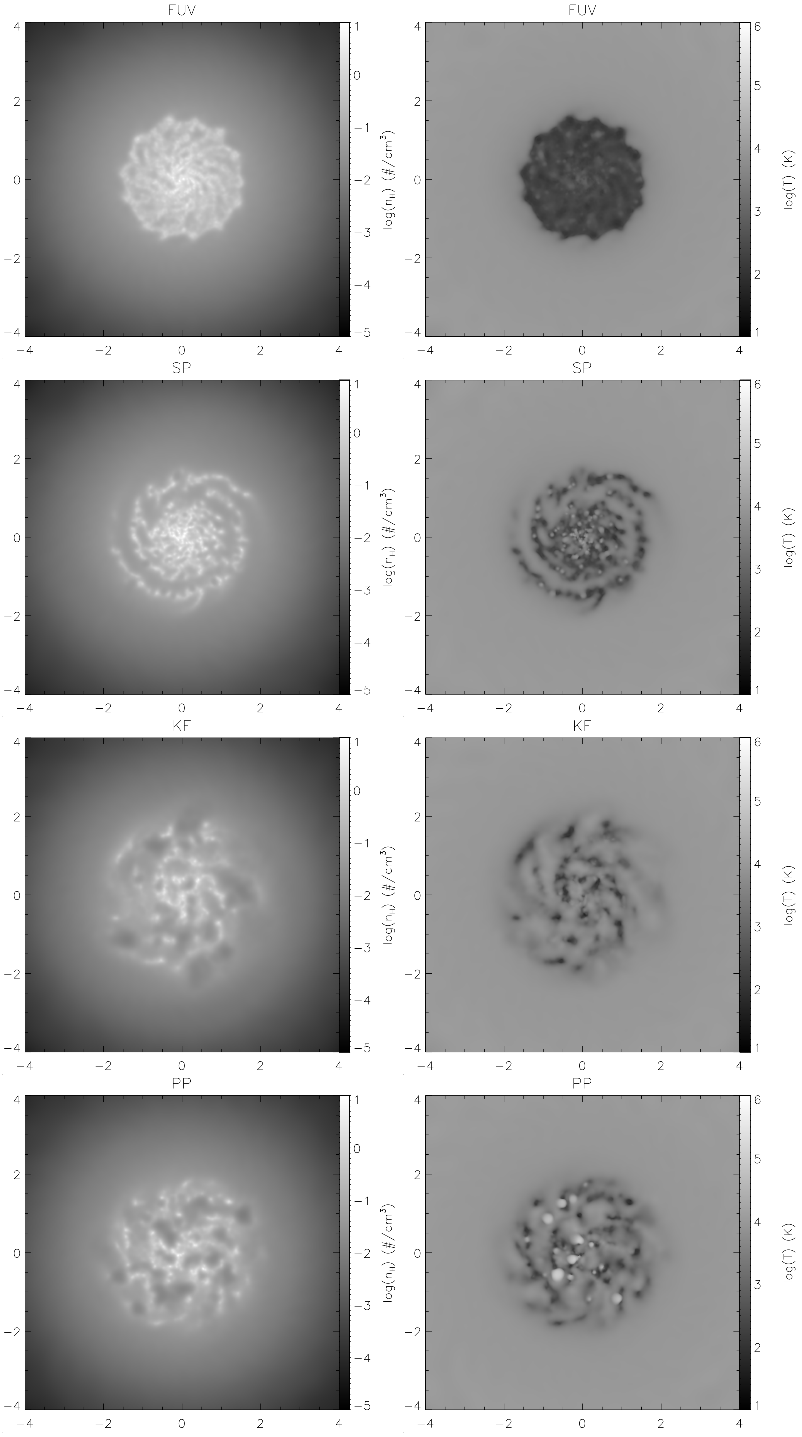

Figure 3.3: Density and temperature of the 20k runs. Shown are cuts through the midplane of H density (left panels) and temperature (right panels). Axes give image scale in kpc.

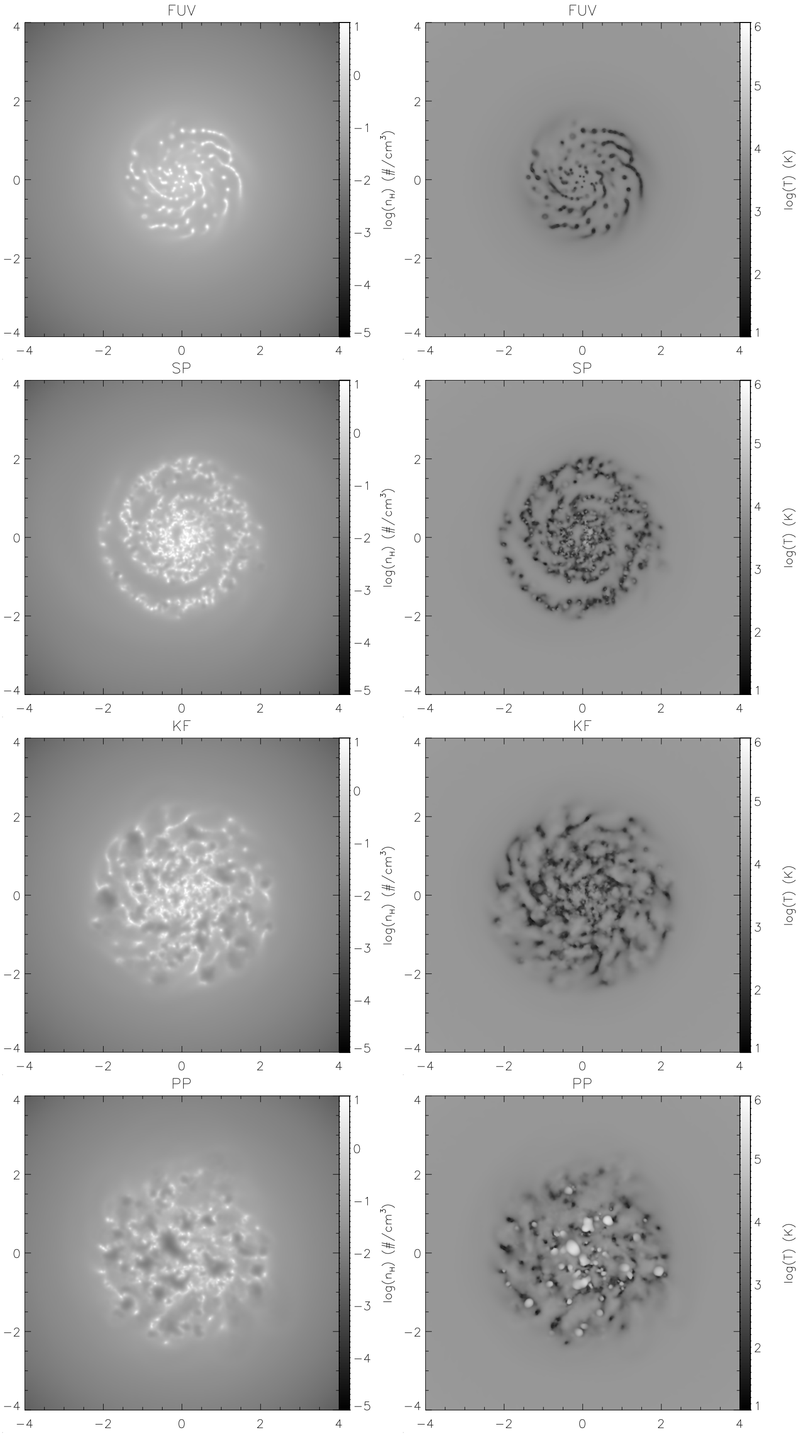

Figure 3.4: Density and temperature of the 200k runs. Shown are cuts through the midplane of H density (left panels) and temperature (right panels). Axes give image scale in kpc.

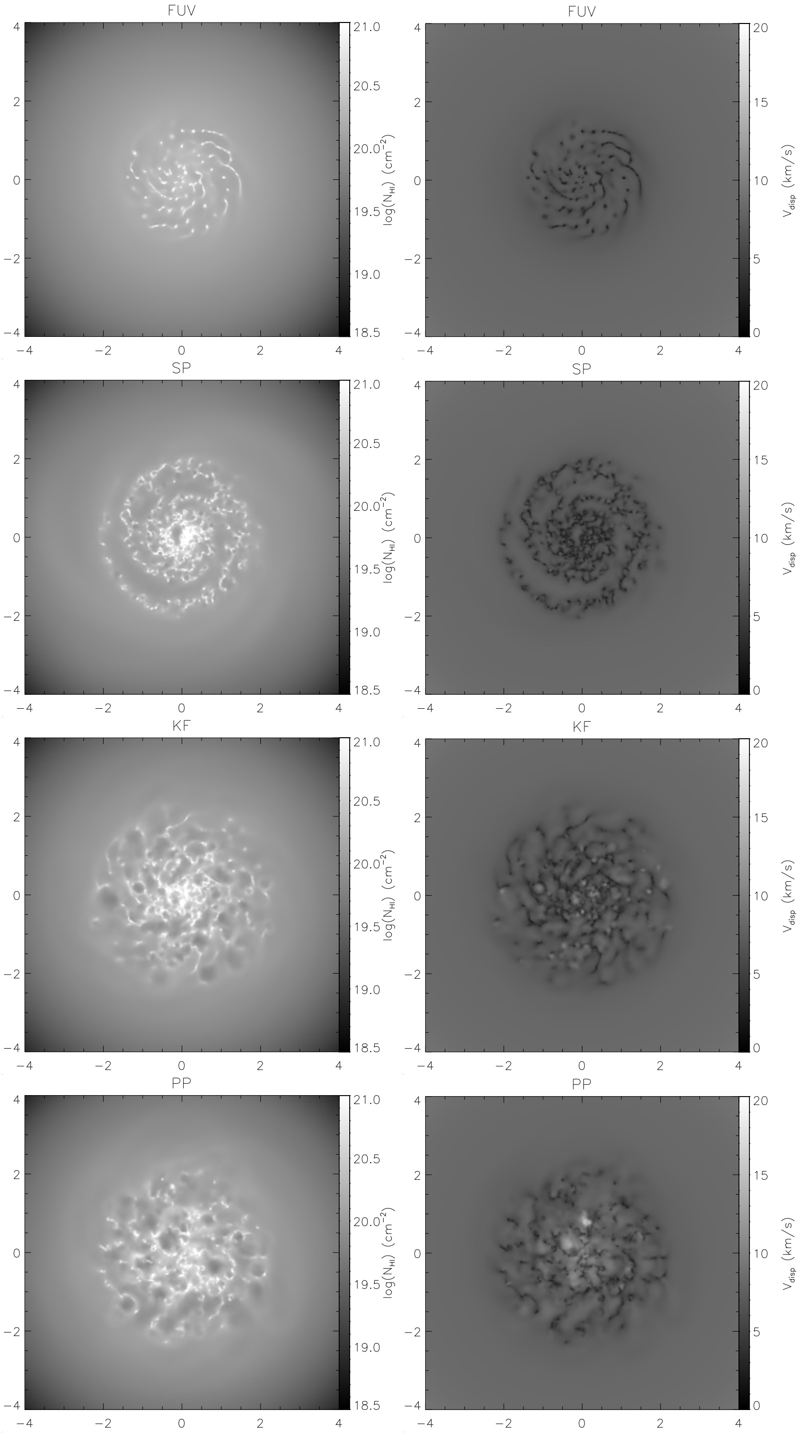

Figure 3.5: HI column density (left panels) and velocity dispersion (right panels) maps of the 200k runs. Axes give image scale in kpc.

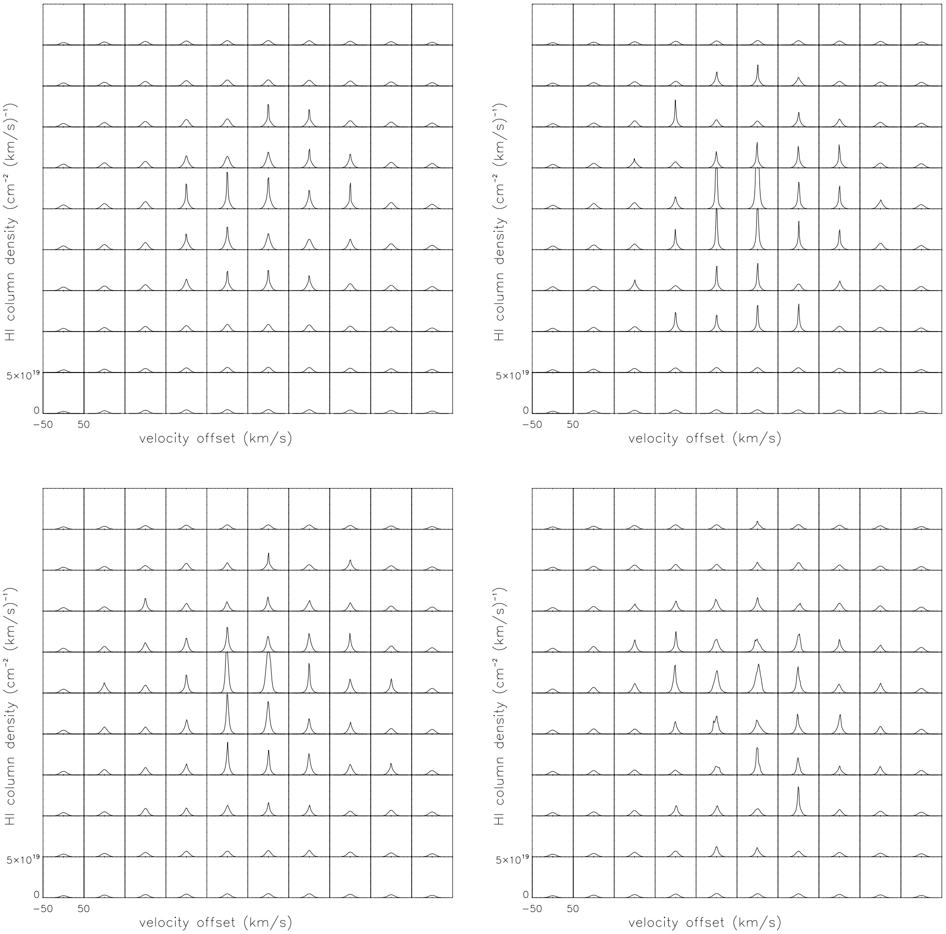

Figure 3.6: HI line profiles, averaged over 200 × 200 pc regions. **top left:** FUV, **top right:** SP, **bottom left:** KF, **bottom right:** PP.

to extract from face-on observation of the model galaxy (however, no noise or instrumental effects are added, so it is not a real synthetic observation). In Fig. 3.5 we map HI column density and velocity dispersion of our simulated data cubes, while in Fig. 3.6 we have plotted line profiles extracted from them. If we compare these HI maps to observations we see that the FUV feedback shows a regular spiral structure that is generally not observed in dIrr. SP feedback gives a more realistic HI map, but there is still large coherent spiral structure visible. KF and PP feedback give more chaotic and realistic appearance.

We can try to confirm this subjective impression by examining power spectra of the HI maps. Analysis of the power spectra was done recently for a high resolution map of the Large Magellanic Cloud (LMC) by Elmegreen et al. (2001). The LMC is an ideal system for this comparison, as it is the dIrr that can be studied in most

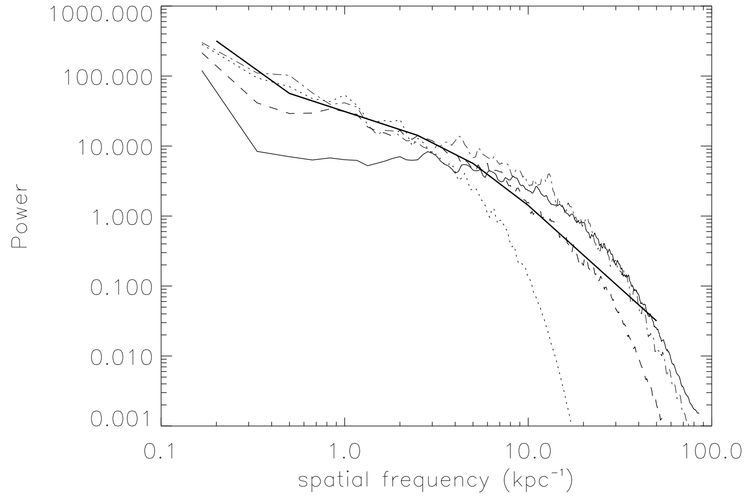

Figure 3.7: Power spectra of HI. Plotted are the power spectra obtained from averaging the 1-dimensional power spectra from the pixel lines of HI maps of simulated HI maps or an HI map of the LMC (Kim et al. 1998). *Thick drawn line:* power spectrum of the LMC (Elmegreen et al. 2001), the other spectra are from HI maps of the simulations (KF is omitted for clarity, it is very similar to PP): *thin drawn line:* FUV (200k), *dash-dotted:* SP (200k), *dotted:* PP (20k) and *dashed:* PP (200k). The scale of the power is arbitrary, but the same for all simulation spectra, for the LMC data it has been scaled to match the PP spectrum between 1 and 10 kpc^{-1}.

detail. For the central 6×6 kpc of our HI maps, we construct 1024×1024 maps (such that the sampling scale is clearly smaller than the smallest resolved structures of the simulation, which are about 20 pc in size). Subsequently we calculate power spectra by summing the 1-dimensional power spectra obtained from the HI map pixel rows. As has been discussed in Elmegreen (2001) this procedure yields information about the contribution of structures at different scales to the HI distribution: the scale-free power law spectra of the LMC (and similar analysis for the SMC and other galaxies) have been interpreted as evidence for a fractal gas distribution. Fig. 3.7 shows the spectra of the simulations together with the spectrum from the LMC (data of this plot is taken from figure 3 of Elmegreen et al. 2001). The spectrum of the PP (and also KF) simulation is remarkably similar to the LMC, and fits much better than either FUV or SP. The FUV simulation shows a lack of power at kpc scales compared to simulations with feedback and the LMC map. This suggests that *energy input from stars is important for structure at kpc scales,* and that gravity and the thermal instability act on smaller scales. Note that the PP spectrum deviates (as do the other feedback methods) at large frequencies because of a steep drop in power at small scales. This is due to the resolution limits of our simulation: the low resolution simulation correspondingly falls off sooner, while giving roughly the same spectrum at large scales.

In the dispersion maps (Fig. 3.5) we can see the presence of gas of low and high dispersion. The WNM has an thermal velocity dispersion of $8 - 10$ km/s, the CNM of 1 km/s. The minimum velocity dispersion of the cold gas is about 3 km/s and is the same for all simulations. Dispersion above 10 km/s are only present in the KF and PP simulations. Note that the correspondence of the dispersion of the cold component of the simulation ($3-5$ km/s) with observed HI velocity dispersions (also in this range) is somewhat fortuitous, because the velocity dispersion which is observed may originate from turbulence at sub cloud scales, that are not resolved in our simulation. Nevertheless the basic picture that comes out of our simulation is realistic: a two component ISM, where lines of sight dominated by the WNM have velocity dispersions in the order of 10 km/s while regions dominated by the CNM have lower velocity dispersions (but higher than the dispersion of 1 km/s corresponding to typical CNM temperatures of 100 K).

Young et al. (2003) studied line profiles of HI observations of a number of dIrrs and derived the presence of two components, one with a velocity dispersion of ≈ 10 km/s, which was present at all locations, and one with a lower dispersion of ≈ 5 km/s with a more patchy distribution. These can be interpreted as being the WNM and a cloud ensemble of CNM clouds. This interpretation is consistent with our simulation. If we look at the line profiles in Fig. 3.6 we see the presence of these two components in the peaked line profiles. Note also that, whereas the profiles of FUV, SP and KF are very regular, PP shows lopsided and irregular profiles, and also double peaks indicative of expanding shells.

HI: relation with star formation

In the literature a number of relations between the properties of the HI distribution and star formation (as traced by Hα) are reported.

Comparing HI surface density and Hα, there seems to be a minimum HI column density below which star formation cannot take place: a threshold column of about $N_{HI} \approx 3-10 \times 10^{20}$ cm^{-2} is found if the azimuthally averaged HI and Hα emission are examined as a function of radius (Kennicutt 1989, Hunter et al. 1998), while the threshold also seems to hold locally (Stil 1999). It is not completely clear what the nature of this threshold is, for normal Sc spiral galaxies Kennicutt (1989) showed that it could be understood in terms of critical surface density Σ_c for disk instabilities, $\Sigma_c = \alpha\kappa\sigma/\pi G$, with epicyclic frequency κ and dispersion velocity σ. However this criterion seems to fail for dIrr galaxies, even when the value of the constant α is allowed to vary from its value of $\alpha = 0.7$, empirically derived for spiral galaxies (Hunter et al. 1998).

Examining the relation of star formation with HI kinematics a number of authors (Dickey 1990, Young & Lo 1997,1996,Stil 1999, a.o.) found, perhaps somewhat surprisingly, that a positive correlation between local Hα intensity and HI velocity dispersion is *not* observed. As has been extensively discussed by Stil (1999) this is contrary to expectation if supernovae explosions and winds from young stars are the source of mechanical energy in the ISM, thus casting some doubt on young stars as the main stirring agent of the ISM.

We check these findings for the corresponding relations of our models using KF and PP feedback by making projections of the luminosity of stellar particles in ionizing photons (in lieu of Hα) and compare these maps with the HI maps. In Fig. 3.8 we have plotted a scatter diagram of pixel values of the HI maps and "Hα" maps, in Fig. 3.9 the pixel values of the dispersion map and the Hα maps are plotted. We can clearly see that our simulation reproduces the threshold density (Fig. 3.8), albeit at

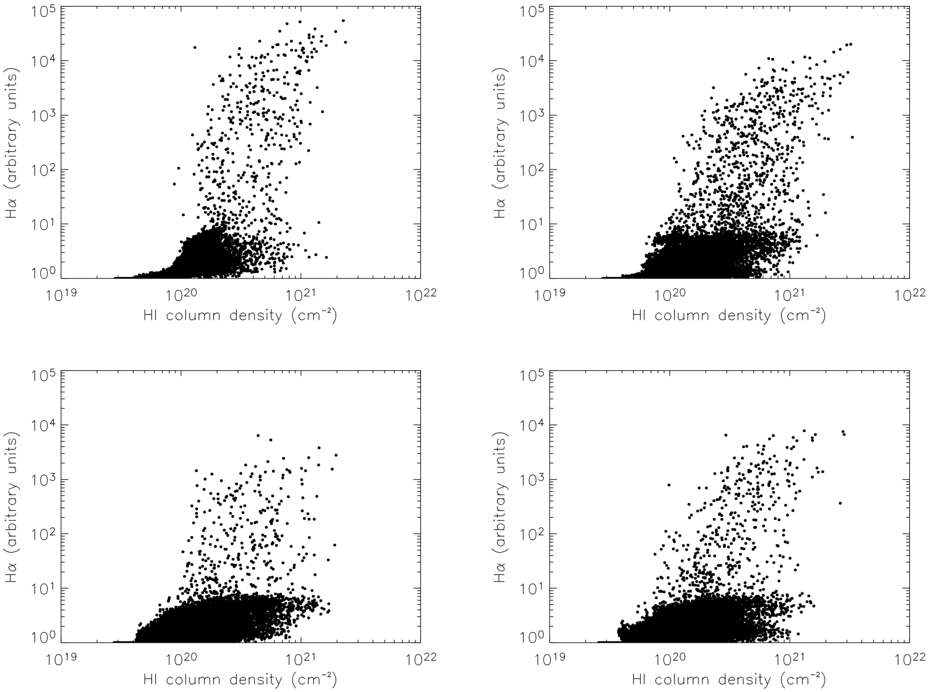

Figure 3.8: HI Column density vs Hα. **top left:** FUV, **top right:** SP, **bottom left:** KF, **bottom right:** PP.

$\mathrm{N} = 1-2\times10^{20}$ cm^{-2}, which is at the low end of the threshold densities reported (e.g. Kennicutt 1989). This shows that in addition to the radial cutoff of star formation, which Gerritsen & Icke showed is natural result of the requirement for cold gas to form in our model, we also reproduce the local threshold. It is purely a result of the ISM model and star formation recipe, as all feedback methods show a similar threshold.

If we look at relation between velocity dispersion and Hα, we see that for the case of FUV and SP feedback Hα emission is seen preferentially at lower dispersion, and only below 7 km/s. Higher dispersions for these feedback methods indicate WNM dominated regions, where star formation cannot take place. For KF and PP feedback high Hα occurs at the whole range of dispersion values, but there is no positive correlation between Hα and velocity dispersion. The reason for this is twofold: 1) Star formation will preferentially occur in quiet regions, where low dispersions allow for large regions of the ISM to collapse (this occurs also in the simulations with inefficient feedback) and 2) the production of ionizing photons by a young stellar cluster occurs mainly in the very beginning of the lifetime of a cluster, and the maximum effect of feedback is delayed with respect to the peak in ionizing luminosity. This is visible in the KF and PP plot as a tendency for Hα values to be higher in low dispersion regions, then as the cluster gets older and less luminous, the HI velocity dispersion increases.

It is remarkable that our simulation reproduces the absence of a strong positive

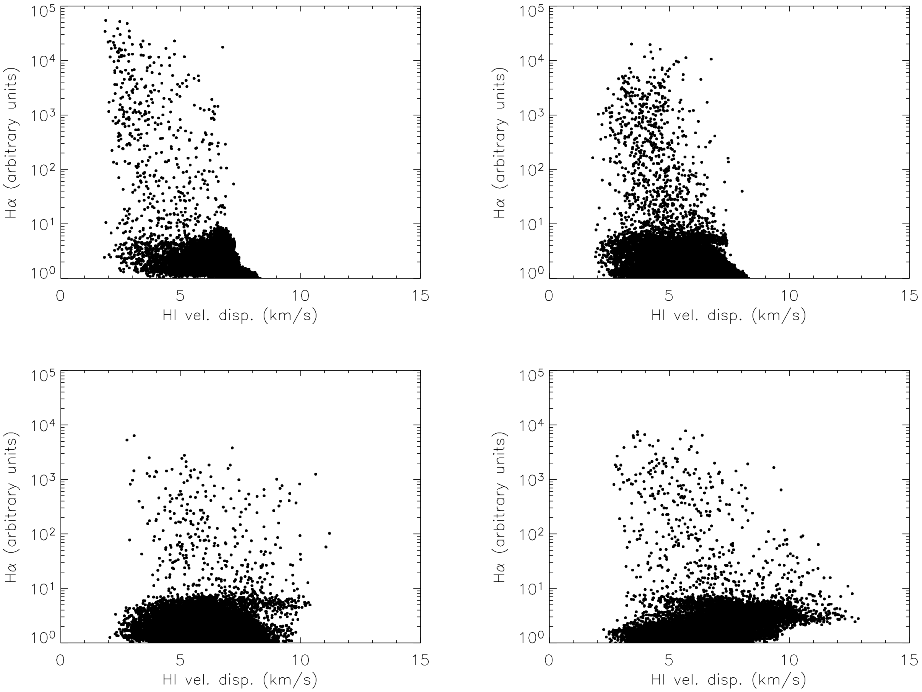

Figure 3.9: HI velocity dispersion vs Hα. **top left:** FUV, **top right:** SP, **bottom left:** KF, **bottom right:** PP.

correlation of velocity dispersion and Hα: we know for sure that the high dispersions in the simulation are caused by feedback. This means that the naive reasoning behind the expectation of a positive correlation is false, and shows the necessity of exploring star formation and feedback in fully dynamic models.

3.6 Conclusions

In this work we have examined two new methods (which we designated the KF and PP method respectively) for implementing feedback in galaxy simulations using SPH. The KF method returns the mechanical energy of young star clusters as a random velocity perturbation. The PP method constructs a *pressure particle*, which is the zero mass limit of an ordinary SPH particle, at the site of new stellar associations. They have been designed specifically to circumvent the loss of feedback energy occurring in normal particle heating. We have checked the results of the new methods against normal energy injection for the Sedov blast wave test. Next we have examined their behaviour in detailed simulations of star formation in dwarf galaxies. Our findings are the following:

- Both the KF and PP feedback method are equivalent to normal particle heating in simple Sedov blast wave tests.

- The morphology and kinematics of simulated dIrr galaxies for the new methods shows holes and shells similar to those observed in dIrr galaxies, while applying no feedback or returning SN energy as thermal energy allows for a sharply defined spiral structure to form.

- Comparison of the power spectra of HI maps of the simulations with LMC observations shows that the KF and PP feedback methods reproduce the spectra obtained from observations, down to the resolution limit of the simulation. Furthermore, comparison of the spectra shows that stellar energy input determines the ISM structure at kiloparsec scales, while structures at smaller scales are determined by gravitational collapse and/ or thermal instability.

- The resulting model galaxies reproduce the observed relations of HI and Hα. An HI threshold for star formation is found, which is the result of the star formation recipe. The new feedback methods are necessary to reproduce the absence of correlation between Hα emission and HI velocity dispersion over the full range of observed velocity dispersions. The surprising fact that the Hα emission and HI velocity dispersion are not correlated is due differences in timing between local stirring of the gas by feedback and the maximum Hα luminosity of young stellar clusters and as a result of the preference of star formation for low dispersion regions.

The fact that the new methods reproduce observed dwarf galaxies in detail, including the general morphology, kinematics, the power law behaviour of the spectra of HI maps and the relations between star formation and velocity dispersion show that feedback is a necessary ingredient, and that the KF and PP methods represent the effects of feedback significantly better than previous methods. Of the two methods we have presented we have a slight preference for the PP method, as this method gives sharper defined structure and higher velocity dispersions. Furthermore it has a well defined input model. An advantage of the KF method is that it is more efficient, allowing for larger time steps (the extra computational costs incurred by the additional work load of feedback routines themselves is in both cases negligible).

References

Buonomo, F., Carraro, G., Chiosi, C., & Lia, C., 2000, *MNRAS* **312**, 371

Burkert, A., 1995, *ApJ* **447**, L25+

Elmegreen, B. G., Kim, S., & Staveley-Smith, L., 2001, *ApJ* **548**, 749

Fragile, P. C., Murray, S. D., Anninos, P., & Lin, D. N. C., 2003, *ApJ* **590**, 778

Gerritsen, J. P. E., 1997, *Ph.D. thesis*, Groningen University

Gerritsen, J. P. E. & Icke, V., 1997, *A&A* **325**, 972

Gingold, R. A. & Monaghan, J. J., 1977, *MNRAS* **181**, 375

Hernquist, L. & Katz, N., 1989, *ApJS* **70**, 419

Hunter, D., 1997, *PASP* **109**, 937

Hunter, D. A., Elmegreen, B. G., & Baker, A. L., 1998, *ApJ* **493**, 595

Katz, N., 1992, *ApJ* **391**, 502

Kay, S. T., Pearce, F. R., Frenk, C. S., & Jenkins, A., 2002, *MNRAS* **330**, 113

Kennicutt, R. C., 1989, *ApJ* **344**, 685

Kennicutt, R. C., 1998, *ApJ* **498**, 541

Kuijken, K. & Dubinski, J., 1995, *MNRAS* **277**, 1341

Landau, L., 1987, *Fluid Mechanics (Course of Theoretical Physics)*, Vol. 6, Butterworth-Heinemann, second edition

Leitherer, C., Schaerer, D., Goldader, J. D., Delgado, R. M. G., Robert, C., Kune, D. F., de Mello, D. F., Devost, D., & Heckman, T. M., 1999, *ApJS* **123**, 3

Lucy, L. B., 1977, *AJ* **82**, 1013

Mac Low, M. & Ferrara, A., 1999, *ApJ* **513**, 142

Mac Low, M. & Klessen, R. S., 2004, *Rev. of Mod. Phys.* **76**, 125

Mihos, J. C. & Hernquist, L., 1994, *ApJ* **437**, 611

Monaghan, J. J., 1992, *ARA&A* **30**, 543

Monaghan, J. J. & Lattanzio, J. C., 1985, *A&A* **149**, 135

Mori, M., Yoshii, Y., Tsujimoto, T., & Nomoto, K., 1997, *ApJ* **478**, L21+

Navarro, J. F. & White, S. D. M., 1993, *MNRAS* **265**, 271

Oey, M. S. & Clarke, C. J., 1997, *MNRAS* **289**, 570

Semelin, B. & Combes, F., 2002, *A&A* **388**, 826

Shu, F. H., Adams, F. C., & Lizano, S., 1987, *ARA&A* **25**, 23

Silich, S. A., Franco, J., Palous, J., & Tenorio-Tagle, G., 1996, *ApJ* **468**, 722

Springel, V., 2000, *MNRAS* **312**, 859

Springel, V. & Hernquist, L., 2002, *MNRAS* **333**, 649

Springel, V. & Hernquist, L., 2003, *MNRAS* **339**, 289

Stil, J. M., 1999, *Ph.D. thesis*, Leiden University

Stil, J. M. & Israel, F. P., 2002a, *A&A* **389**, 29

Stil, J. M. & Israel, F. P., 2002b, *A&A* **389**, 42

Thacker, R. J. & Couchman, H. M. P., 2000, *ApJ* **545**, 728

Walter, F., 1999, *Publications of the Astronomical Society of Australia* **16**, 106

Young, L. M., van Zee, L., Lo, K. Y., Dohm-Palmer, R. C., & Beierle, M. E., 2003, *ApJ* **592**, 111

Chapter 4

Periodic bursts of star formation in irregular galaxies

Abstract

We present N-body/SPH simulations of the evolution of an isolated dwarf galaxy including a detailed model for the interstellar medium (ISM), star formation and stellar feedback. Depending on the strength of the feedback, the modelled dwarf galaxy shows periodic or quasi-periodic bursts of star formation of moderate strength. The period of the variation is related to the dynamical timescale, of the order of $1.5\ 10^8$ yr. We show that the results of these simulations are in good agreement with recent detailed observations of dwarf irregulars (dIrr) and that the peculiar kinematic and morphological properties of these objects, as revealed by high resolution HI studies, are fully reproduced. We discuss these results in the context of recent surveys of dwarf galaxies and point out that if the star formation pattern of our model galaxy is typical of dwarf irregulars this could explain the scatter of observed properties of dwarf galaxies. Specifically, we show that the time-sampled distribution of the ratio between the instantaneous star formation rate (SFR) and the mean SFR is similar to the distribution in observed samples of dwarf galaxies.

Pelupessy F. I., van der Werf P. P., Icke V., 2004, A&A 422, p.55-64

4.1 Introduction

The nature of the processes regulating star formation in irregular galaxies is poorly understood. While there is at least some understanding of star formation in regular spiral galaxies, this is less so for irregulars. For spiral galaxies the guiding observation that the star formation rate (SFR) is related to the gas surface density by the Schmidt law has given rise to a number of competing theories that reproduce the general features of star formation in large spiral galaxies (Elmegreen 2002, Dopita

& Ryder 1994). These systems seem to be regulated by large-scale gravitational instabilities. Star formation in irregular galaxies has proven to be more difficult to understand. Irregulars have a widely varying SFR, spanning 4 orders of magnitude for the normalised SFR/area (Hunter 1997), possibly due to the fact that gas thermodynamics, governed by varying heating and cooling processes, plays the decisive role (Elmegreen 2002). But why do some irregulars have very high SFRs relative to their mass, while others hardly show any activity? Are there any intrinsic properties of the galaxies that can explain this disparity between SFRs or do all dwarf galaxies exhibit episodes of high star formation?

In recent years a number of studies have highlighted these questions by investigating samples of dwarf galaxies and comparing their properties as derived from photometry, HI and Hα observations. van Zee (2000, 2001) investigated a sample of isolated dwarf galaxies and found no strong correlation between star formation and independent physical parameters. Hunter et al. (1998) tested different regulating processes, amongst which disk instabilities, thermal and shear regulated star formation, but found that none could explain patterns of star formation. Stil (1999) investigated the relation between star formation and HI gas kinematics.

On the other hand, detailed studies of a number of nearby dwarf galaxies have fully revealed the complex structure of the ISM in these systems. High resolution aperture synthesis mapping (e.g. Kim et al. 1998, Wilcots & Miller 1998, Puche et al. 1992, Walter & Brinks 2001) of their HI has shown the ISM of these dwarfs to have a frothy structure, with holes of varying sizes, shells and filaments, even extending far beyond the optical radius. From velocity dispersion studies (Young & Lo 1997) the presence of cold and warm neutral components predicted by the two phase model for the ISM (Field 1965) has been deduced. Comparison with Hα and UV observations shows that the dense walls of these holes are the sites of star formation (Walter et al. 2001), and suggest 'chains' of successive star forming sites (Stewart et al. 2000). The cause of the holes in the HI distribution seems to be the energy input from ionizing radiation, stellar winds and supernovae, although Rhode et al. (1999) and Efremov et al. (1998) discuss other possible scenarios.

Together these two types of observations have painted a picture of the complex interaction between star formation and the ISM of these systems that is challenging to capture theoretically. Some early attempts have been made to understand star formation qualitatively by the application of stochastic self-propagating star formation (SSPSF) models to dwarf galaxies (Gerola & Seiden 1980, Comins 1983). While they probably capture some general characteristics of star formation, they are phenomenological and do not include the underlying physics of the ISM.

Efforts to investigate the influence of star formation on the ISM of dwarf galaxies have mainly concentrated on the effects of large (central) bursts and on questions concerning the ejection of gas and the distribution of metals (e.g. Mac-Low & Ferrara 1999, Mori et al. 1997). Recently there also have been some simulations addressing the question of survival of small galaxies (Mori et al. 2002). Generally these simulations have not tried to set up a self consistent model for the ISM and star formation, but prescribed a certain SFR.

The importance of a good model for the ISM and feedback has been recognized by a number of authors. Andersen & Burkert (2000) formulated an extensive model for the ISM in terms of a phenomenological model for the interstellar clouds. Their model showed self regulating star formation and they found moderate fluctuations in SFR. Berczik & Hensler (2003) incorporated such a cloud model into a chemo-dynamical galaxy evolution code. Semelin and Combes (2002) formulated a model with similar characteristics, representing clouds by sticky particles, but did not apply these to dwarf galaxies. Springel & Hernquist (2003) formulated a sub-grid model for the multiphase interstellar medium, producing a quiescent self-regulating ISM. However, relatively little effort has been directed towards resolving the normal evolution of irregular dwarfs and providing the connection with detailed studies of single systems and extensive unbiased samples. Nevertheless dwarf galaxies are good test systems for exploring star formation in galaxies: they are dynamically simple systems in the sense that they do not exhibit spiral density waves or shear. Furthermore their small size means that simulations can follow the various physical processes at finer linear and density scales. *As the small scale physics of star formation and feedback presumably do not differ between normal and dwarf galaxies, we can use results obtained from these simulations and apply the same methods to larger systems*. Here we present results of a simulation of the evolution of a normal dwarf irregular galaxy including a detailed model for the ISM, star formation and feedback. The distinguishing characteristics of this work are that the model for the ISM we employ does not explicitly postulate the presence of a two phase medium, rather it forms it as a result of the physics of the model. Furthermore we take special care in formulating a star formation model that is solely based on the Jeans instability, and we formulate a feedback scheme that gives us unambiguous control over the strength of the feedback. We will discuss the results of the simulation both in relation to detailed observations of comparable single systems, as well as in the context of recent surveys of dwarf galaxies.

4.2 Method

We employ an N-body/SPH code for the evolution of a general astrophysical fluid on galactic scales, extended from TreeSPH (Hernquist & Katz 1989), to simulate the evolution of an isolated dwarf galaxy. We use the conservative SPH formulation of Springel & Hernquist (2002). Main features of our code are: a realistic model for the ISM solving for the ionization and thermal balance for the neutral and ionized components of the ISM, star formation based on a gravitational instability model for clouds, and a new method of including feedback for SPH. We will summarise the features of the code with an emphasis on the aspects most relevant for the present work.

4.2.1 Model for the ISM

Our model for the ISM is, although simplified, qualitatively similar to the model for the Cold Neutral Medium (CNM) and Warm Neutral medium (WNM) of Wolfire et al. (1995, 2003). We consider a gas with arbitrary but fixed chemical abundances X_i, scaled to the target metallicity from the solar abundances of Grevesse & Sauval (1998). We solve for the ionization and thermal evolution of the gas. The various processes included are given in Table 4.1. A similar model to that employed here was used by Gerritsen & Icke (1997) and Bottema (2003) for galaxy simulations.

process	comment	ref.
heating		
Cosmic Ray	ionization rate $\zeta_{\mathrm{CR}} = 1.8\ 10^{-17}\ \mathrm{s}^{-1}$	1
Photo Electric	FUV field from stars	1
cooling		
e,H_0 impact	H,He,C,N,O,Si,Ne,Fe	2,4
ionization & recombination		
UV	ionization assumed for species with $\mathrm{E_i} < 13.6$ eV	
Cosmic Ray	H, He only; primary & secondary ionizations	1
Collisional	H, He only	3
Radiative recombination	H, He only	3
CIE	assumed for metals	

Table 4.1: Overview of the processes included in the ISM model used. For H and He ionization equilibrium is explicitly calculated, for other elements collisional ionization equilibrium (CIE) is assumed. Both the heating and cooling strongly depend on the ionization fraction $\mathrm{x_e}$. Exact expressions adopted for the various processes can be found in: 1) Wolfire et al. 1995, 2) Raga et al. 1997 , 3) Verner & Ferland 1996, 4) Silva & Viegas 2001

The main differences are the following: we use more accurate cooling, that is calculated in accordance with the chemical composition, we have included a solver for the ionization balance, and we use the full photoelectric heating efficiency as given in Wolfire et al. (1995). Gerritsen & Icke (1997) found that the structure of the resulting ISM depended strongly on the ionization fraction they assumed, as this strongly influences the cooling. We do not have to assume an ionization fraction, as we calculate it (on the other hand, we do assume a cosmic ray ionization rate that is poorly constrained). Our use of the full heating efficiency means that FUV heating will become less efficient for high radiation fields, due to grain charging. In our model supernova (SN) heating is more important in regulating star formation than it was for Gerritsen & Icke (1997).

A concise overview of the ISM model is given in Fig. 4.1. The plots in this figure show that as density varies, the equilibrium state of the gas changes from a high temperature/high ionization state ($\mathrm{T} = 10000$ K, $\mathrm{x_e} \approx 0.1$) at low densities, to a low temperature/low ionization state ($\mathrm{T} < 100$ K, $\mathrm{x_e} < 10^{-3}$) at high densities. In between is a density domain where the negative slope of the P-n relation indicates that the gas is unstable to isobaric pressure variations, the classic thermal instability (Field 1965). The shape of these curves and hence the exact densities of the thermal instability vary locally throughout the simulation according to the conditions of UV and supernova heating. The gas in the simulation may be out of equilibrium, although the timescales for reaching equilibrium are generally short, $< 10^6$ yr. In principle the cooling properties of the gas depend on the local chemical composition. In practice, only small metallicity gradients are observed in dwarfs (Pagel & Edmunds 1981), so we take constant metallicity ($\mathrm{Z} = 0.2 \times \mathrm{Z}_{\odot}$). Potentially more serious is the fact that we assume a constant cosmic ray ionization rate ζ throughout the galaxy. The

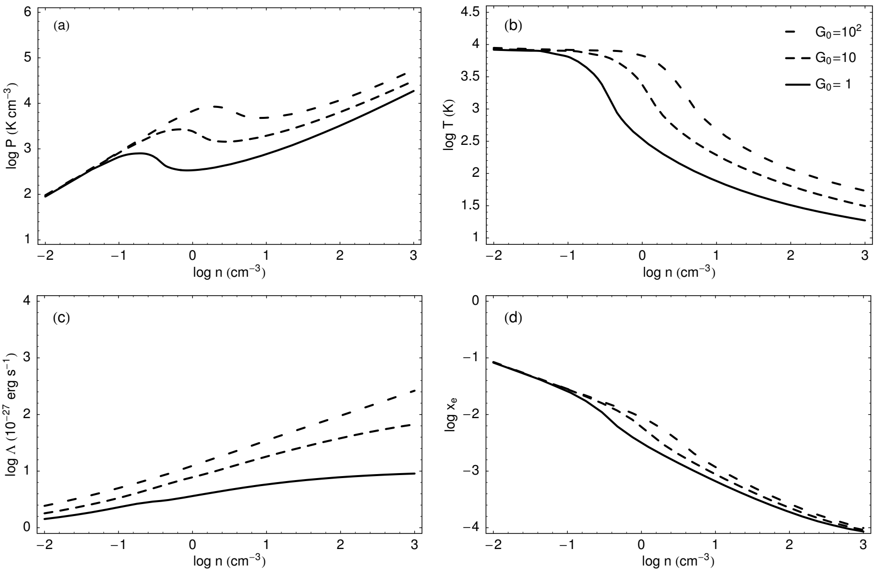

Figure 4.1: Overview of the ISM model: Equilibrium plots of (a) pressure P, (b) temperature T, (c) cooling rate Λ and (d) electron fraction $\mathrm{x_e}$ as a function of density n for three different values of the UV field $\mathrm{G_0}$ (given in units of 1.6×10^{-3} erg cm^{-2} s^{-1})

low energy ($\approx$ 100 MeV) cosmic rays that are important for heating and ionization of the ISM, have relatively short mean free paths ($<$ 10 pc) so probably ζ will vary substantially across a galaxy. However, the exact sources, let alone production rates, of these low energy cosmic rays are not well known. Hence a satisfying model for the distribution of cosmic rays is difficult to formulate. We take a 'standard' value of $\zeta = 1.8\ 10^{-17}\ \mathrm{s}^{-1}$. For this value cosmic ray heating only becomes important in the outer parts of the galaxy (it may be substantially too low, see McCall et al. 2003).

The FUV luminosities of the stellar particles, which are needed to calculate the local FUV field used in the photoelectric heating, are derived from Bruzual & Charlot (1993, and updated) population synthesis models for a Salpeter initial mass function (IMF) with cutoffs at $0.1\ \mathrm{M_\odot}$ and $100\ \mathrm{M_\odot}$. In the present work we do not account for dust extinction of UV light.

4.2.2 Star formation and Feedback

We use the star formation recipe of Gerritsen & Icke (1997). A region is considered unstable to star formation if the local Jeans mass $\mathrm{M_J}$ is smaller than the mass of a typical molecular cloud $\mathrm{M_{ref}} \approx 10^5 \mathrm{M_\odot}$. The rate of star formation is set to scale with the local free fall time: $\tau_{\mathrm{sf}} = \mathrm{f_{sf} t_{ff}} = \frac{\mathrm{f_{sf}}}{\sqrt{4\pi \mathrm{G}\rho}}$. The delay factor $\mathrm{f_{sf}}$ is uncertain, but from observations a value $\mathrm{f_{sf}} \approx 10$ seems reasonable (Zuckerman & Palmer 1974). Once a gas particle is determined to be forming stars, a fraction $\epsilon_{\mathrm{sf}} = 0.25$ of the mass is converted to stars. This sets a minimum to the star formation efficiency (a neighbourhood of gas particles of about 64 particles that has become capable of star formation will thus form at least a fraction $.25/64 = .004$ of stars). The actual efficiency of star formation is determined by the number of stars needed to quench star formation locally by the UV and SN heating and is determined by the cooling properties of the gas and the energy input from the stars.

The recipe is certainly not unique, we have based our choice on the following considerations: it is simple and based on presence of substructure and the driving role of gas self gravity, and it reproduces the Schmidt law without actually imposing it (Gerritsen & Icke1997). An additional advantage is the fact that the Jeans mass criterion for star formation also prevents the simulation from violating the resolution requirements for self gravitating SPH (Bate & Burkert 1997, Whitworth 1998). It does assume substructure to be present (actually its assumption is more restrictive still, namely that substructure is mainly at $\mathrm{M}_{\mathrm{ref}}$ sized clouds, but this is not overly important). For this type of simulation one is always restricted by the limited ability to follow the star-formation process, so we are forced to adopt a phenomenological description at some level. Another concern that could be addressed is that the SF according to this recipe is independent of metallicity, other than that induced by the metallicity dependence of the cooling. Furthermore, we assume the stellar IMF to be universal.

The inclusion of feedback in SPH simulations is complicated by the fact that the most straightforward implementation of the return of mechanical energy to the ISM, namely as thermal energy, is not effective. This is due to to fact that the estimated ISM densities are much higher than those of the hot gas in superbubbles, hence the energy is radiated away quickly (Katz 1992). A number of methods have been devised to overcome this, based on the return of energy as either thermal (Thacker & Couchman 2000, Gerritsen 1997) or kinetic energy (Navarro & White 1993, Springel & Hernquist 2003). None has been entirely satisfactory as the former requires the artificial suppression of cooling, while the latter suffers from too strong effects for feedback, unless an unrealistically low SN efficiency is adopted or the affected particles are decoupled from the gas dynamics. Here, we employ a new method. It is based on the creation at the location of young stellar clusters of a zero mass SPH particle. Its contribution to gas forces on neighbouring gas particles is determined by taking the formal zero mass limit with constant particle energy E_{SN} of the usual SPH equations of motion (see Chapter 3 for more details). The amount of feedback (the energy E_{SN} given to the zero mass SPH particle) is an important and uncertain parameter; we estimate it by multiplying the number of type II supernovae per mass of stars formed, $0.009 {\mathrm{M}_\odot}^{-1}$, with the effective energy per supernova, $\approx 10^{50}$ erg, thus assuming that 90% of the energy is radiated away, a value which comes from more detailed simulations of the effect of supernova and stellar winds on the ISM (Silich et al. 1996), and is also used in other simulations of galaxy evolution (e.g. Semelin & Combes 2002, Springel & Hernquist 2002, Buonomo et al. 2000). This energy is then gradually added to the supernova particle over a period of 30 Myr, the lifetime of SN progenitors, after which it is ceases to exist. This model for the mechanical energy input from stellar clusters resembles the one adopted by Oey & Clarke (1997), who have shown that it is fully consistent with the differential size distribution of superbubbles in a.o. the SMC and Holmberg II. We do not include the effect of SN Ia, which are mainly important for the chemical enrichment.

4.2.3 Initial conditions

Here we will restrict ourselves to following the evolution of an isolated dwarf galaxy in an attempt to understand the interplay between star formation and the ISM. These processes play a role for dwarf galaxies in general, and indeed in all places were star formation is happening. It is important to keep in mind, however, that dwarf galaxy evolution is easily influenced by external factors such as infall of gas, collisions, and recently receiving much attention, ram pressure stripping by the inter galactic medium and tidal stripping by galactic potentials (see e.g. Marcolini et al. 2003, Mori & Burkert 2000 and Mayer et al. 2001, Pasetto et al. 2003 for recent work on these). Nevertheless the isolated case remains very relevant as it allows a straightforward comparison with suitably selected samples of observed galaxies which exist in the literature (e.g. van Zee 2001), unaffected by the uncertainties of additional external influences. The understanding of the complex processes of star formation and feedback gained from the isolated case can then be applied to more general evolution scenarios.

We thus set up a model dwarf galaxy resembling current dIrrs. Although these exhibit a wide range of morphologies, they are very similar in their averaged radial profiles to scaled down versions of ordinary disk galaxies. Hence we take for the initial condition a three component model for a small disc galaxy, consisting of a gas disk, a stellar disk and a dark halo, modelled loosely on the properties of DDO 47 and similar dIrrs. The gas disk we construct with a radial surface density profile,

$$\Sigma = \Sigma_{\rm g}/(1 + {\rm R}/{\rm R}_{\rm g}), \tag{1}$$

with central density $\Sigma_{\rm g} = 0.01 \times 10^9 {\rm M}_\odot/{\rm kpc}^2$ and radial scale ${\rm R}_{\rm g} = .75$ kpc, truncated at 6 kpc. It is somewhat involved, due to the thickness of the gas disk, to solve its vertical structure exactly. Hence, before we start the simulation proper, we set up the galaxy with an quadratically rising gas scale height and we it run isothermally(${\rm T} = 10^4$ K) and without star formation and feedback for some time until it settles in equilibrium. This results in a scale height set by hydrostatic equilibrium of ${\rm h}_{\rm g} = 100$ pc at the centre to ${\rm h}_{\rm g} = 1$ kpc at ${\rm R} = 6$ kpc.An exponential stellar disk,

$$\rho_{\rm disk}({\rm R}, {\rm z}) = \frac{\Sigma_0}{2{\rm h}_{\rm z}} \exp(-{\rm R}/{\rm R}_{\rm d}) {\rm sech}^2({\rm z}/{\rm h}_{\rm z}) \tag{2}$$

with central surface density $\sigma_0 = 0.3 \times 10^9 {\rm M}_\odot/{\rm kpc}^2$, ${\rm R}_{\rm d} = 0.5$ kpc and vertical scale height ${\rm h}_{\rm z} = 0.2$ kpc, is constructed as in Kuijken & Dubinski (1995). The total mass of the gas is ${\rm M}_{\rm g} = 2 \times 10^8\ {\rm M}_\odot$ and the total mass of the stellar disk is ${\rm M}_{\rm d} = 1.5 \times 10^8\ {\rm M}_\odot$. Both the gas disk and stellar disk are represented by ${\rm N} = 10^5$ particles. The ages of the initial population of stars are distributed according to a constant SFR of 0.007 ${\rm M}_\odot$/yr.

Dwarf galaxies are amongst the most dark matter dominated objects, exhibiting dark to luminous matter ratios of 10-100. Their rotation curves are best fit by flat central density cores (Flores & Primack 1994, Burkert 1995). Therefore we take a halo profile

$$\rho_{\rm halo}({\rm r}) = \rho_0 \frac{\exp(-{\rm r}^2/{\rm r}_{\rm c}^2)}{1 + {\rm r}^2/\gamma^2} \tag{3}$$

with core radius $\gamma = 2$ kpc, cutoff radius $\mathrm{r_c} = 20$ kpc and central density $\rho_0 = 2 \times 10^7\ \mathrm{M_\odot}$/kpc^3, for a total mass of $\mathrm{M_{halo}} = 15 \times 10^9\ \mathrm{M_\odot}$ and a peak rotation velocity of about 50 km/s. The profile (3) is very similar to the Burkert (1995) profile for dwarf galaxies, differing in its asymptotic behaviour for $\mathrm{r} \to \infty$. This will only give significant deviations well outside the region of interest for our simulations. We represent the dark halo by a static potential. This is deemed sufficient for the dynamical modelling presented here, as we evolve the galaxy in isolation and the perturbations in the gaseous and stellar disk are expected to have only minor impact on the halo structure. Furthermore, discreteness noise of a particle halo can induce bars to form, and excite spiral structure or bending modes in the stellar and gaseous disk (Kuijken & Dubinski 1995, Hernquist 1993).

4.3 Simulation results

In Fig. 4.2 a range of snapshots of the simulated dwarf galaxy is shown, taken after about 1 Gyr of evolution and spaced about 50 million years apart. Shown are UBV composite maps, the upper panels of Fig. 4.3 show the distribution of HI. If we look at these we see that the HI distribution of the galaxy is dominated by holes of varying sizes. Dense shells of HI combine to form big HI clouds, which correspond to the sites of intense star formation. Sometimes structures resembling spiral arms form, but generally there are no spiral density waves in gas or stars, and, due to the low shear, a flocculent spiral structure also does not develop. As the cold clouds move about in the galaxy they are in turn destroyed by mechanical feedback from the stars to perpetuate the cycle of star formation, cloud destruction and formation. Clearly the ISM of the galaxy is in a very dynamical state. This can only be fully appreciated while looking at the time sequence of the complete simulation. *The ISM of dwarf irregulars is continously stirred and material from different radii is mixed through the action of supernovae and stellar winds*. While this may have been expected beforehand from energy considerations, it is nonetheless an important and often overlooked fact. As such it should not be surprising that irregulars often show very little radial metallicity gradients (apart from the fact that metals may be lost from hot outflows). Note that the presence of the hydrodynamics of the ISM is a fundamental difference between classical SSPSF and phenomological models and our full dynamical simulations.

If we look at the UBV images we see that the appearance of the galaxy varies with time. Episodes of strong star formation (e.g. at 1024 Myr) are followed by quiescent phases (1071 and 1118 Myr). During star formation bursts the galaxy is dominated by a few very active star formation sites, during quiet times the galaxy fades and seems relatively featureless. If we compare the stellar and HI distribution of Fig. 4.2 and 4.3 to observed systems, it is striking how similar these are. For example Holmberg II and NGC 4214, which have been studied in great detail (Puche et al. 1992, Walter & Brinks 2001), show an HI distribution with a similar number of holes of similar sizes. Also the extent of structure in the gas outside the optical disk is reproduced in the simulations. Large regions of star formation are associated with the highest contours of HI (corresponding to a column density of about $\mathrm{N} = 2 \times 10^{21}\ \mathrm{cm^{-2}}$), which is also found in comparisons of optical and HI morphology for observed systems.

As we have a complete representation of the neutral phases of the ISM we can also

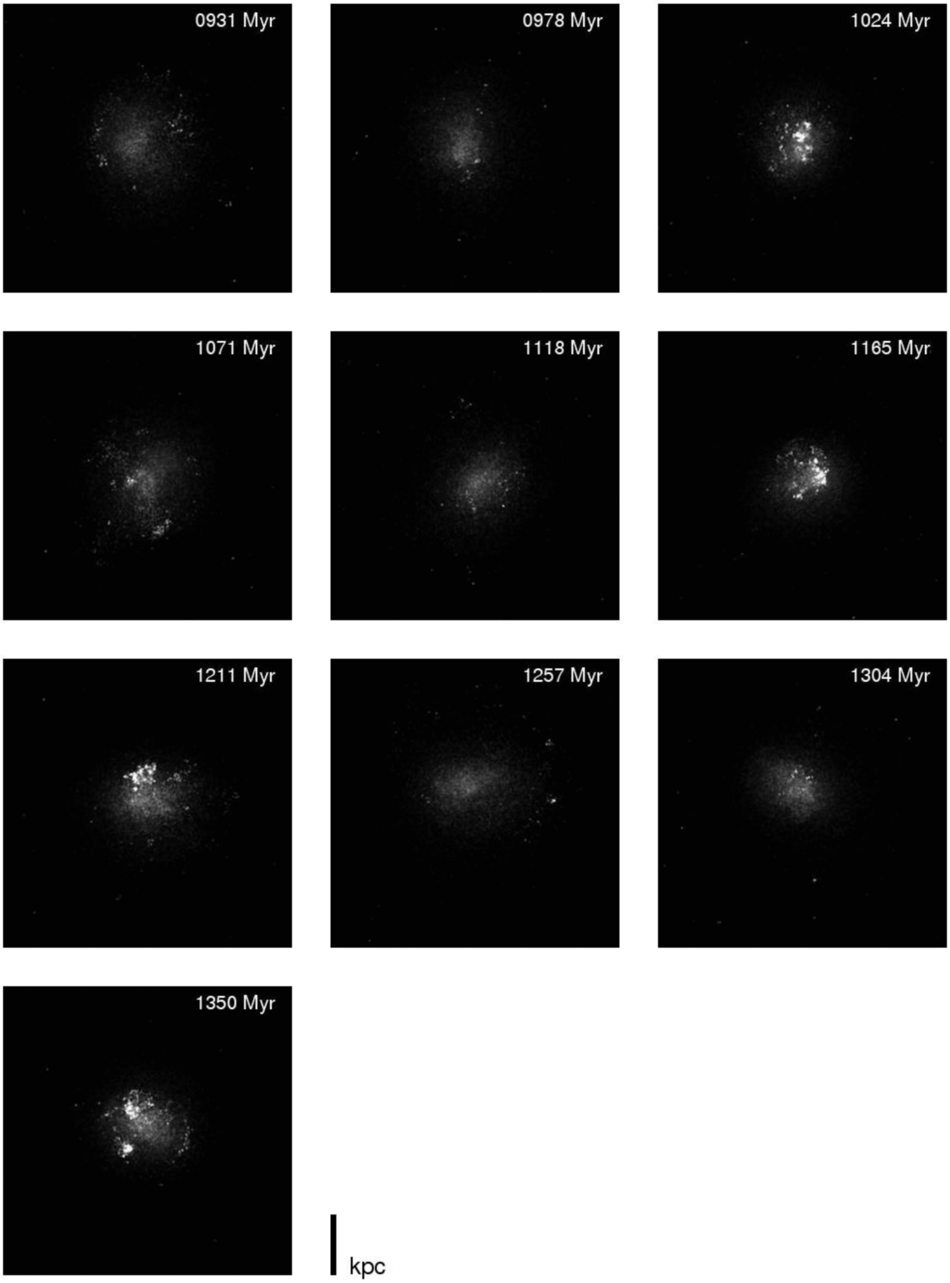

Figure 4.2: Simulated dwarf galaxy after $\approx$ 1 Gyr. Shown are UBV composite pictures at different times (see appendix for colour).

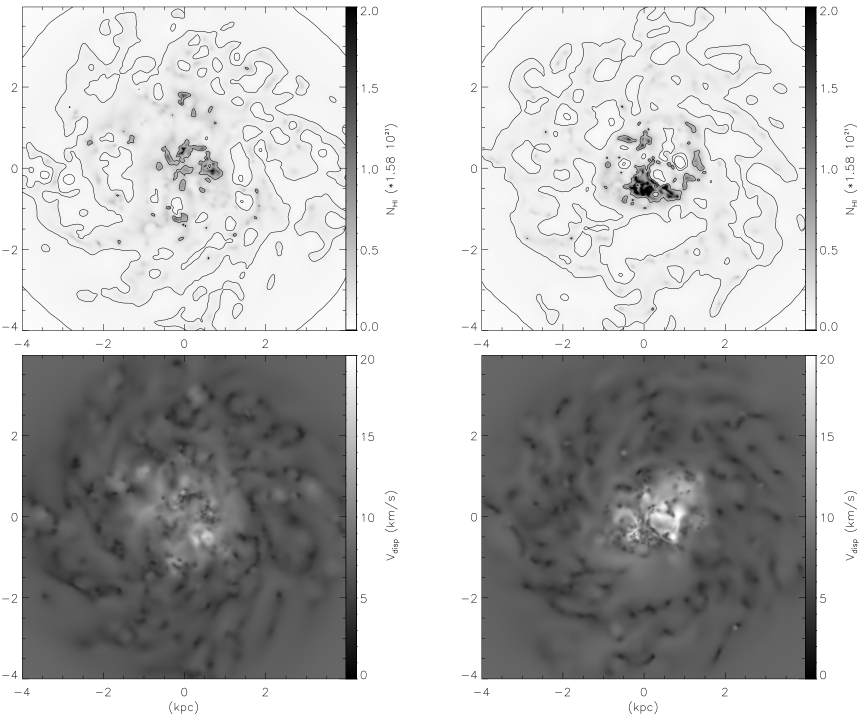

Figure 4.3: HI surface density & velocity dispersion map in quiescent phase (left, taken at 1118 Myr) and in burst phase (right, at 1211 Myr).

compare our simulation with the HI kinematics of observed systems. In Fig. 4.3 we have plotted maps of the HI density and the (line of sight) velocity dispersion of the gas. The gas typically has random velocities of the order of $3 - 10$ km/s, with regions of higher (up to 20 km/s) velocity dispersion associated with expanding bubbles, in good agreement with observations (Stil 1999, Young & Lo 1997).

The evolution of the SFR is shown in Fig. 4.4. It shows a gray scale plot of the temporal evolution of the (azimuthally averaged) star formation density and below it the resulting total SFR. We see that after an initial transient period the galaxy settles in a mode of periodically varying star formation, with a minimum SFR of about $0.003 \mathrm{M}_{\odot}$/yr while the peak SFR is about a factor of 10 higher. Also plotted are the results for a run with reduced feedback strength. In this case variations are smaller in amplitude, and quasi-periodic. Even lower feedback strengths would probably quench the variations completely, but in that case morphology and kinematics of the gas would no longer match observed systems. In the upper panel of Fig. 4.4 we see the pattern of propagating star formation. The azimuthally averaged density plot may give the false impression that star formation is happening in inward and outward moving rings; however visual inspection shows that it moves around in patches and partial rings: if some region starts to form stars, nearby dense regions will be triggered

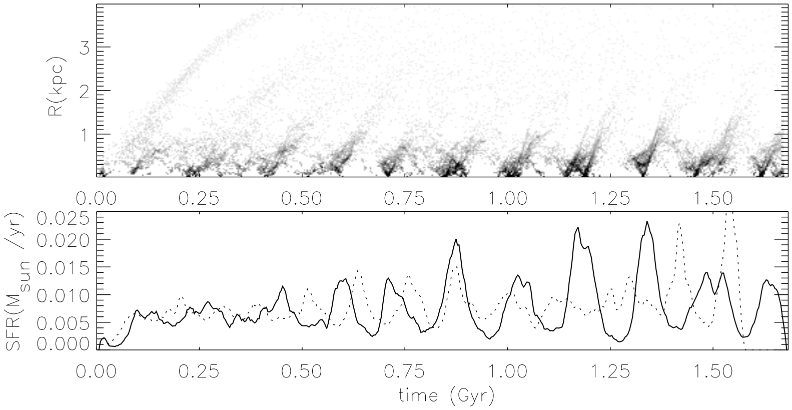

Figure 4.4: Star Formation History of a simulated dwarf galaxy. Upper panel: density plot of the azimutally averaged star formation rate. Lower Panel: total star formation rate. The dotted line indicates the SFR for a run with 50% reduced feedback strength.

to form stars, often moving the star formation in a particular direction along a dense filament or bridge. Furthermore we see that periodic bursts happen only relatively close to the centre of the galaxy, whereas in the outer parts stars form at a more or less constant low rate. This behaviour is expected (see Ehlerová & Palouš 2002) because star formation can only be triggered in the expanding shells around the holes induced by feedback if the column density is high enough, $\mathrm{N} \approx 10^{20-21}$ cm^{-2}. So we see that the galaxy has three different SF regimes: an outer region where the gas density is generally not high enough for the CNM to form (beyond the so called thermal cut off, see Elmegreen & Parravano 1994 and Gerritsen & Icke 1997) so SF will be strongly supressed there; a region at intermediate radii where the gas density is high enough to be thermally unstable, and where star formation proceeds at a steady pace; and a central region that is both thermally unstable and unstable to shell instabilities, where the dominant mode of SF is triggered star formation. Fig. 4.5 shows a plot of the resulting radial dependence of the star forming density, clearly visible are the three different regions with different star forming behaviour. The bursting region is confined within 1.5 kpc, while star formation extends further out, stopping abruptly at ≈ 4 kpc, well short of the edge of the gasdisk. Interestingly, De Blok & Walter (2003) found evidence for similar low level star formation outside the optical disk of NGC 6822.

The cyclical pattern of star formation raises a number of further questions: What is the driver of these variations? What determines the period and amplitude of the oscillation? Why is star formation apparently synchronized over the whole galaxy? While some previous models of galaxies have shown variations of the star formation rate, these were either connected to an imposed time scale (the duration of supernova feedback, Wada & Norman 2001) or due to random scatter of a probabilistic model (Gerola et al. 1980). Significant quasi random variations in SF rate were found by Carraro et al. (2001) to happen during formation of dwarf ellipticals (dEs), in their case caused by local depletion of the starforming gas reservoir, happening on timescales of $\approx 10^{8-9}$ yr. Similar variations driven mainly by internal proccesses were

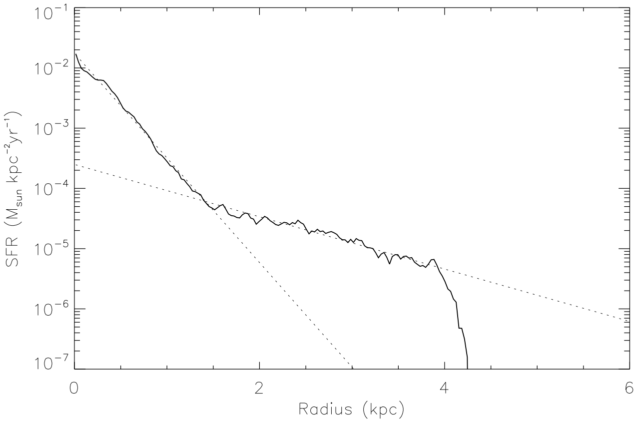

Figure 4.5: Radial profile of the mean star formation density (drawn line, dotted lines are exponentials with scalelengths of 0.25 and 1 kpc).

found by Pasetto et al. (2003) even for dIrrs subjected to tidal stirring. In our case the timescale of the variations is related to a physical time scale: the period of the oscillation is about 165 Myr, which is slightly larger than double the dynamical time scale of the dark halo, ($t_{\rm dyn} = \sqrt{\frac{3\pi}{16G\rho}} = 80$ Myr). This suggests that supernova feedback provides the kick for the oscillation, expelling gas and increasing the velocity dispersion and thus inflating the gas disk, after which the gas falls back for the next cycle on a dynamical time scale. The period is thus determined by the density of the halo (the main mass component of dwarf galaxies), while the amplitude is related to the strength of the supernova feedback. Note that this would not be sufficient to account for the regularity of the variations: in general one would expect that gas from different parts of the gas disk would experience kicks of different strength, and would fall back on different time scales, giving rise to a more chaotic pattern of star formation. However dwarf galaxies are in solid body rotation and thus their potential corresponds to a harmonic oscillator, which means that material flung out of the disc falls back in the same time, irrespective of location and speed, synchronizing the SFR over the whole galaxy. This effect certainly adds to the phenomenon shown in Fig. 4.4, namely that the overall star formation cycle looks remarkably regular.

4.4 Star formation: comparison with observations

When we compare the star formation in our model and observed SFR (for example in van Zee 2001) we see that the agreement is quite good: our values fall well within the range of observed rates of $0.001M_\odot$/yr to $0.1M_\odot$/yr, although admittedly the star formation rate in our model does depend fairly strongly on poorly constrained quantities such as the shape of the IMF, the amount of energy released in SN and stellar winds, and the various parameters regulating star formation. It is however encouraging that we can use reasonable values for the parameters and get SFR that are close to observed rates.

In our model the star formation rate is seen to vary over time. This is difficult to verify in real dwarf galaxies. One would have to derive accurate SFH over hundreds of Myr for galaxies, and variations of within a factor ≈ 3 of the mean as observed in our model would not be too conspicous in the data. For most dwarf galaxies the long term star formation histories determined from global colours indicate an approximately constant SFR. Detailed examinations of nearby resolved dwarfs do show evidence of variations in the SFR (Dohm-Palmer et al. 1998, 2002) of the correct order of magnitude. Strong additional evidence for variations in the SFR is the observed scatter in the ratio of current star formation to past star formation: the Scalo b parameter. If the variations in our model were generic for isolated dwarf galaxies, this would explain the observed distribution of b. To see this we have plotted in Fig. 4.6 the histograms of $\mathrm{SFR}/\langle\mathrm{SFR}\rangle_\mathrm{t}$ for our simulation together with the distribution of b for a sample of isolated dwarf galaxies as derived by van Zee (2001). Clearly these two are qualitatively the same. There are two main differences: (1) the distribution of our model extends to higher and lower ratios and (2) the galaxy sample contains galaxies with $\mathrm{b} > 4$, which are extreme bursting systems. The first difference would be remedied by decreasing the strength of feedback. We also have plotted the results for a run with 50% less feedback. In this case the amplitude of variations is somewhat too small (although both are in good agreement with the observed distribution given the uncertainties inherent in deriving it, see discussion in van Zee 2001). For the second point we should mention that our simulation really only samples a limited number of cycles; the bursts may be rarer events that have not (yet) happened in the simulation. Ofcourse it also possible that high powered bursts are due to outside influences, such as interactions or infalling gas clouds, ingredients of galaxy evolution not present in our model.

The distribution of b is a highly degenerate indicator of the SF history, and we are aware that the above comparison presupposes a number of properties for the population of dwarf galaxies: the assumption that the dwarf galaxies form a homogeneous population; variations in SFR are assumed to be of similar strength and shape, independent of galaxy properties (although the b distribution is independent of the period); and that the variations in SFR are periodic. Nevertheless we think that this is the simplest explanation for the observed scatter and that our model captures a number of essential features of the variations in star formation given the characteristic shape of the observed b distribution, namely: moderate bursting, long periods of low SF, and the 'peakiness' of the SF enhancements. It is also difficult to see what would induce non-periodic variations in isolated galaxies, especially since no properties independent of the SFR that correlate with the SFR (van Zee 2001) have been found.

4.5 Discussion & conclusions

The model we employed to calculate the evolution of a single dwarf galaxy is quite extensive and complicated and necessarily contains a number of free parameters, some of which we tried to constrain using observational data or theory (as in the case of the supernova energy), yet some remain only constrained by physical intuition.

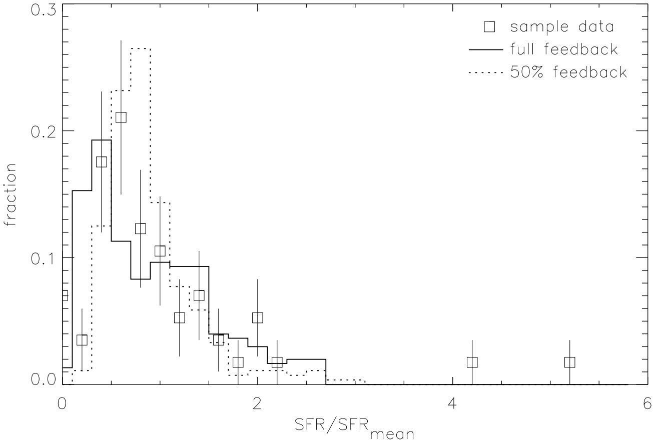

Figure 4.6: distribution of $\mathrm{SFR}/\langle\mathrm{SFR}\rangle_\mathrm{t}$ for a sample of isolated dwarfs (squares with error bars), a simulation with full feedback(drawn line) and a simulation with 50% feedback (dotted line). Data is taken from van Zee 2001.

Therefore, it is worthwhile to summarize the features of observed dwarf systems successfully reproduced by the model: 1) the morphology and kinematics of the HI distribution, 2) the two phase structure of the ISM, 2) the spatial pattern of star formation, 3) the star formation rate, 4) consistency with the observed distribution of Scalo b parameter. These provide strong and independent checks of our modelling approach as they result from the intricate interplay of the model for the ISM we employed, the scheme for star formation and the method of returning mechanical energy to the ISM. These successes give some confidence that the model captures the essentials of dwarf galaxy evolution and to its predictive power.

Comparing our model with recent simulations of dwarf galaxy evolution (e.g. Berzcik et al. 2003, Mayer et al. 2001, Andersen & Burkert 2000, Pasetto et al. 2003, Mori et al. 1997, 1999, Carraro et al. 2001) we see that our work differs from previous work in two crucial aspects: 1) the modelling of the physics of the neutral ISM, 2) the treatment of supernova feedback. We follow the evolution of the WNM and CNM of the ISM explicitly, this process being the upper part of a cascade leading down to star formation. Star formation in our model happens in cold ($\mathrm{T} \leq 200$ K) and dense ($\mathrm{n} = 1 - 10$ cm^{-3}) gas. These are realistic sites for star formation as we know that molecular clouds are embedded in neutral envelopes. The further stages of star formation, molecular cloud formation and collapse, are not included as they require prohibitive resolution and the inclusion of additional physics. These processes are only implicit in our star formation recipe, but at least our methods follows collapsing gas to the point that it has experienced a transition to a cold, dense state from which it may be trusted to form stars with rates and efficiencies that are constrained by observations. Some authors have tried to bypass this problem by formulating a phenomenological ISM model in terms of 'sticky' particles representing molecular clouds (Andersen & Burkert 2000), sometimes in addition to a smooth SPH component representing the WNM (Semelin & Combes 2002, Berczik et al. 2003). They also succesfully reproduce a selfregulated ISM, including some effects, like evaporation of molecular clouds that are probably not well represented in our model. In these models stars form from the cloud particles, imposing a Schmidt law, not, as in our model, from the consideration of the the instabilities in the ISM. Furthermore, our model has a consistent representation of the ISM linking phases by physical processes, rather than prescriptions.

Simulations of dwarf galaxy evolution that include supernova feedback have typically included this as a local heating term. This method for implementing supernova feedback is not effective in forming the structures associated with stellar feedback and simulations using it do not show any effect of SN feedback. This is a well understood numerical artefact and some authors have devised methods to prevent the radiative loss of mechanical energy that is the root of the problem (Springel & Hernquist 2003, Thacker & Couchman 2000, Gerritsen & Icke 1997, the problem is also not exclusive to SPH type codes see e.g. Fragile et al. 2003). They have not applied their methods to the evolution of dIrrs so a direct comparison is not yet possible. However, the notion that *the energy input from stellar winds and SN of young stellar clusters is crucial for the understanding the structure and kinematics of the ISM of dIrrs* is borne out by our simulations: if feedback is not included, the ISM stays in a smooth disk with very low random motions ($2-3$ km/s). The self propagating mode of star formation is absent in that case. The dwarf galaxy will only poorly resemble a real dIrr.

Chemical enrichment is not yet included in our code. We can estimate the importance of a changing chemical composition for our simulation. The total amount of metals $\mathrm{M_Z}$ produced during the simulation is $\mathrm{M_Z} \approx 0.015\Delta\mathrm{M}_\star = 1.6\times10^5\mathrm{M}_\odot$. This will raise the metallicity of the galaxy, under the assumption that the metals will be well mixed, with at most 25%, which is not entirely insignificant, although to first approximation the thermal evolution is independent of metallicity as both the cooling and UV heating scale with Z. Note also that metals may be lost from the galaxy in galactic winds. It does mean that we should include chemical enrichment to follow the evolution for longer timescales and especially if we want to investigate extremely metal-poor galaxies. In principle the inclusion of chemical enrichment will also add further constrains when comparing with observations, very important to asses the long term evolution of the model. Both these points, however, do not alter the conclusion for the simulations presented here.

The methods we use can be applied more generally. Questions that we plan to address are for example the following:

- In view of the recent realization that there is a deficit of observed small galaxies as compared to predictions of cold dark matter models of galaxy formation (Klypin et al. 1999) it is interesting to consider what happens for galaxies of progressively smaller mass. We are in the process of running a grid of models exploring this question, but some effects may be clear from the preceding: for smaller galaxies, variations will be on longer time scales (scaling as $\rho_{\mathrm{halo}}^{-0.5}$) and greater in amplitude (because the feedback becomes relatively stronger as the escape velocity decreases). Ultimately halos will be too small to retain their ISM, leaving them bare. The mass ranges for which this happens, the influence of other galactic parameters and the timescales on which these processes take place will be of interest to validate cosmological and galaxy formation models.

- We also plan to investigate a possible relation between dwarf irregulars and dwarf ellipticals. Although recent simulations (Mayer et al. 2001, Pasetto et al. 2003) have shown for satellite galaxies that a transition from dIrr to dE or dwarf Spheroidal (dSph) is plausible as a result of the action of tidal fields, it has not been conclusively determined whether a transition from dIrr to dE is to be expected in general. Various groups have put forward arguments in favour (Davies & Phillipps 1988) and against (Bothun et al. 1986, Marlowe et al. 1999) such a descendancy for the dE. Although the results presented here do not immediately illuminate this question, we think that additional simulations of the sort presented here, testing a wider range of galactic properties and following the evolution for longer time scales may answer whether this is a viable scenario and whether we can put the various classes of small galaxies into an unified evolutionary framework.

In summary, our model suggests that it is possible that a large part of the current dIrr population is in a quasi-periodic burst mode of star formation. The scatter in observed properties in this picture is mainly due to the fact that galaxies are observed at different phases of their evolution. The main difference between our model and classical SSPSF models is that in our models variations are due to the interplay of stellar feedback and gas dynamics, the galaxy being periodically stirred by bursts of star formation after which a quiescent period occurs during which gas falls back to the disk. In classical SSPSF models the variations are due to the fact that star formation is described by a correlated stochastic process and the small size of the galaxies, which induces large statistical variations. Our model predicts that the amplitude of the variations depends on the strength of the feedback and that the period depends on the dynamical time scale.

References

Andersen, R.-P. & Burkert, A., 2000, *ApJ* **531**, 296

Bate, M. R. & Burkert, A., 1997, *MNRAS* **288**, 1060

Berczik, P., Hensler, G., Theis, C., & Spurzem, R., 2003, *Ap&SS* **284**, 865

Bothun, G. D., Mould, J. R., Caldwell, N., & MacGillivray, H. T., 1986, *AJ* **92**, 1007

Bottema, R., 2003, *MNRAS* **344**, 358

Bruzual A., G. & Charlot, S., 1993, *ApJ* **405**, 538

Buonomo, F., Carraro, G., Chiosi, C., & Lia, C., 2000, *MNRAS* **312**, 371

Burkert, A., 1995, *ApJ* **447**, L25+

Carraro, G., Chiosi, C., Girardi, L., & Lia, C., 2001, *MNRAS* **327**, 69

Comins, N. F., 1983, *ApJ* **266**, 543

Davies, J. I. & Phillipps, S., 1988, *MNRAS* **233**, 553

de Blok, W. J. G. & Walter, F., 2003, *MNRAS* **341**, L39

Dohm-Palmer, R. C., Skillman, E. D., Gallagher, J., Tolstoy, E., Mateo, M., Dufour, R. J., Saha, A., Hoessel, J., & Chiosi, C., 1998, *AJ* **116**, 1227

Dohm-Palmer, R. C., Skillman, E. D., Mateo, M., Saha, A., Dolphin, A., Tolstoy, E., Gallagher, J. S., & Cole, A. A., 2002, *AJ* **123**, 813

Dopita, M. A. & Ryder, S. D., 1994, *ApJ* **430**, 163

Efremov, Y. N., Elmegreen, B. G., & Hodge, P. W., 1998, *ApJ* **501**, L163+

Ehlerová, S. & Palouš, J., 2002, *MNRAS* **330**, 1022

Elmegreen, B. G., 2002, *ApJ* **577**, 206

Elmegreen, B. G. & Parravano, A., 1994, *ApJ* **435**, L121+

Field, G. B., 1965, *ApJ* **142**, 531

Flores, R. A. & Primack, J. R., 1994, *ApJ* **427**, L1

Fragile, P. C., Murray, S. D., Anninos, P., & Lin, D. N. C., 2003, *ApJ* **590**, 778

Gerola, H., Seiden, P. E., & Schulman, L. S., 1980, *ApJ* **242**, 517

Gerritsen, J. P. E., 1997, *Ph.D. thesis,* Groningen University

Gerritsen, J. P. E. & Icke, V., 1997, *A&A* **325**, 972

Grevesse, N. & Sauval, A. J., 1998, *Space Science Reviews* **85**, 161

Hernquist, L., 1993, *ApJS* **86**, 389

Hernquist, L. & Katz, N., 1989, *ApJS* **70**, 419

Hunter, D., 1997, *PASP* **109**, 937

Hunter, D. A., Elmegreen, B. G., & Baker, A. L., 1998, *ApJ* **493**, 595

Katz, N., 1992, *ApJ* **391**, 502

Kim, S., Staveley-Smith, L., Dopita, M. A., Freeman, K. C., Sault, R. J., Kesteven, M. J., & McConnell, D., 1998, *ApJ* **503**, 674

Klypin, A., Kravtsov, A. V., Valenzuela, O., & Prada, F., 1999, *ApJ* **522**, 82

Kuijken, K. & Dubinski, J., 1995, *MNRAS* **277**, 1341

Mac Low, M. & Ferrara, A., 1999, *ApJ* **513**, 142

Marcolini, A., Brighenti, F., & D'Ercole, A., 2003, *MNRAS* **345**, 1329

Marlowe, A. T., Meurer, G. R., & Heckman, T. M., 1999, *ApJ* **522**, 183

Mayer, L., Governato, F., Colpi, M., Moore, B., Quinn, T., Wadsley, J., Stadel, J., & Lake, G., 2001, *ApJ* **559**, 754

McCall, B. J. et al., 2003, *Nature* **422**, 500

Mori, M. & Burkert, A., 2000, *ApJ* **538**, 559

Mori, M., Ferrara, A., & Madau, P., 2002, *ApJ* **571**, 40

Mori, M., Yoshii, Y., & Nomoto, K., 1999, *ApJ* **511**, 585

Mori, M., Yoshii, Y., Tsujimoto, T., & Nomoto, K., 1997, *ApJ* **478**, L21+

Navarro, J. F. & White, S. D. M., 1993, *MNRAS* **265**, 271

Oey, M. S. & Clarke, C. J., 1997, *MNRAS* **289**, 570

Pagel, B. E. J. & Edmunds, M. G., 1981, *ARA&A* **19**, 77

Pasetto, S., Chiosi, C., & Carraro, G., 2003, *A&A* **405**, 931

Puche, D., Westpfahl, D., Brinks, E., & Roy, J., 1992, *AJ* **103**, 1841

Raga, A. C., Mellema, G., & Lundqvist, P., 1997, *ApJS* **109**, 517

Rhode, K. L., Salzer, J. J., Westpfahl, D. J., & Radice, L. A., 1999, *AJ* **118**, 323

Semelin, B. & Combes, F., 2002, *A&A* **388**, 826

Silich, S. A., Franco, J., Palous, J., & Tenorio-Tagle, G., 1996, *ApJ* **468**, 722

Silva, A. I. & Viegas, S. M., 2001, *Computer Physics Communications* **136**, 319

Springel, V. & Hernquist, L., 2002, *MNRAS* **333**, 649

Springel, V. & Hernquist, L., 2003, *MNRAS* **339**, 289

Stewart, S. G., Fanelli, M. N., Byrd, G. G., Hill, J. K., Westpfahl, D. J., Cheng, K., O'Connell, R. W., Roberts, M. S., Neff, S. G., Smith, A. M., & Stecher, T. P., 2000, *ApJ* **529**, 201

Stil, J. M., 1999, *Ph.D. thesis*, Leiden University

Thacker, R. J. & Couchman, H. M. P., 2000, *ApJ* **545**, 728

van Zee, L., 2000, *AJ* **119**, 2757

van Zee, L., 2001, *AJ* **121**, 2003

Verner, D. A. & Ferland, G. J., 1996, *ApJS* **103**, 467

Wada, K. & Norman, C. A., 2001, *ApJ* **547**, 172

Walter, F. & Brinks, E., 2001, *AJ* **121**, 3026

Walter, F., Taylor, C. L., Hüttemeister, S., Scoville, N., & McIntyre, V., 2001, *AJ* **121**, 727

Webber, W. R., 1998, *ApJ* **506**, 329

Wilcots, E. M. & Miller, B. W., 1998, *AJ* **116**, 2363

Wolfire, M. G., Hollenbach, D., McKee, C. F., Tielens, A. G. G. M., & Bakes, E. L. O., 1995, *ApJ* **443**, 152

Wolfire, M. G., McKee, C. F., Hollenbach, D., & Tielens, A. G. G. M., 2003, *ApJ* **587**, 278

Young, L. M. & Lo, K. Y., 1997, *ApJ* **490**, 710

Zuckerman, B. & Evans, N. J., 1974, *ApJ* **192**, L149

Chapter 5

Small star forming galaxies: the role of gas and halo parameters

Abstract

In this chapter we examine whether the observed structural differences between blue compact dwarfs (BCDs) and dwarf Irregular (dIrr) galaxies can explain the differences in star formation patterns for the two classes of dwarf galaxies. We concentrate on the role of the gas distribution and the central density of the dark halo, running N-body/smoothed particle hydrodynamics (SPH) simulations for galaxy models with different parameters. The simulations include a full model for the interstellar medium (ISM), star formation and feedback, and thus our simulations test for the first time the relation between BCD and dIrr galaxies in the context of a self-consistent model of a star forming galaxy. We find that our models show a variety of star formation patterns. High central gas surface densities show high star formation rates, while the presence of a high central halo density will produce a central starburst. Comparing our simulations with observations we conclude that both high central gas surface and a high central halo density are necessary for a system to exhibit BCD features.

5.1 Introduction

Compared with normal dwarf irregular (dIrr) galaxies, blue compact dwarfs (BCDs) have more centrally concentrated HI distributions and higher central halo densities, resulting in more steeply rising rotation curves (Meurer et al. 1998, van Zee et al. 2001). The classification of a galaxy as a BCD, which is made on the basis of the scale length of the light distribution, UBV colours and the presence of emission lines (Thuan & Martin 1981), implies that it undergoes an intense central burst of star formation, not sustainable over cosmological timescales. The gas consumption times of BCDs are in the order of about a Gyr (Thuan & Martin 1981, van Zee et al. 1998, Hunter & Elmegreen 2004). This, coupled to their low metallicity has been put forward as an argument for BCDs to be young systems experiencing their first starbursts. This notion has been discredited by the detection of aged stellar populations in BCDs (Papaderos et al. 1996, and references therein). Some systems may be truly young systems (e.g. Izotov & Thuan 2004), but these do not seem to be typical. While dIrr have widely varying properties, star formation in these systems is generally more spread throughout the disk and the rates of star formation are lower than for BCDs, with gas consumption timescales in the order of tens of Gyr (van Zee 2001). The ages of stars, as indicated by their colours are consistent with a more or less constant star formation history (SFH) on timescales of the order of 10 Gyr.

The differences in star formation properties between BCDs and dIrrs can be understood in general terms as resulting from the observed differences in halo and gas structure (see also the discussion in van Zee et al. 2001). The dependence of the star formation rate (SFR) on the gas surface density ($\Sigma_{\rm g}$) can be fitted for a wide range of environments by the *Schmidt Law:* $\mathrm{SFR} \propto \Sigma_{\rm g}^{1.5}$ (Schmidt 1959, Kennicutt 1989), and thus more intense star formation is expected for systems with a higher central gas surface density. The steeply rising rotation curve, on the other hand, will stabilise BCDs against star formation, perhaps allowing for a larger supply of fuel to accrete, which enables a more intense starburst when star formation does start (van Zee et al. 1998).

However, these qualitative explanations should be tested in the context of a self consistent description of the star forming ISM. Clearly the complexities of the processes of star formation and feedback from young stars mean that the resulting system properties may not follow straightforwardly from empirical relations or plausibility arguments. For example, the instability criteria such as those based on the Toomre Q have been shown to be of limited value in predicting the amount and location of star formation in dwarf galaxies (Hunter et al. 1998). Also, the above argument does not answer the question what BCDs will look like after the current starburst, and which systems are candidates to be classified as quiescent BCDs, nor does it say anything about the extent to which ordinary dIrr can experience BCD phases.

Thus, numerical simulation of these systems with a code that includes the relevant physics of star formation and feedback, such as the code we have employed in Chapter 4, may be a useful tool to investigate star formation in these systems. Furthermore, a good “laboratory” model for star forming dwarf galaxies could be used for more detailed examinations of the evolutionary links between dIrr, BCD and dwarf Ellipticals (dE). Ultimately, one may be able to predict (or derive) from numerical simulations the star formation properties of a galaxy from the mass and angular momentum distribution and determine whether the mode of star formation could change over time, and thus obtain a theoretical framework linking the different species of dwarf galaxies.

For numerical modelling of galaxies one always encounters poorly constrained free parameters that arise because of the fact that processes, such as star formation and feedback are not fully represented. Matching between large surveys of dwarf galaxies and theoretical models would help to constrain these free parameters. This would also give information about the underlying distribution of cosmological initial conditions from which the current population of dwarf galaxies is formed. This is difficult to obtain because information about the primordial density spectrum on these scales is heavily convoluted with the effects of star formation and gas physics.

In this study we will examine dwarf galaxy evolution using N-body/SPH simulations. We will limit ourselves to a simple numerical experiment: what happens if we confront the observed gas and dark matter distributions with a numerical code that includes a realistic description of the ISM, star formation and feedback? The goal of this study is to examine whether the differences between the distribution of dark matter and gas found for dIrr and BCD are enough to explain the differences in star formation properties. Our numerical approach complements the large body of literature devoted to observational studies on this subject. Amongst the questions that we will try to answer are: do the simulated systems look similar to observed dwarf systems? How do the simulated systems evolve in time? Can BCD types and dIrr types morph into another? In Section 5.2 will first give a short description of the simulation method. We will discuss the range of our parameter study in Section 5.3, where we will also describe the initial conditions. In Sections 5.4 and 5.5 we present the results of our simulations and the observational characteristics that the simulated systems would present. Section 5.6 concludes with a discussion of the implications of our models for the classification of small star forming galaxies.

5.2 Method

We will run models for BCD and dIrr galaxies consisting of gas, stars and dark matter using an N-body/SPH code for the evolution of astrophysical fluids. The model we use was extensively described in previous chapters. Here we summarise the most important features and indicate the parameter choices made. Stars and gas are represented by particles. The stars only experience gravitational forces, calculated using the Barnes-Hut algorithm (Barnes & Hut 1986), whereas the gas particles also experience forces representing gas dynamical forces by use of the smoothed particle hydrodynamics (SPH). To model the interstellar medium we add a model for the neutral gas physics, star formation and for feedback from young stellar clusters.

Model for the interstellar medium

We will use the full model as described in Chapter 2 (“model D”), which is a representation of the neutral phases of the ISM that solves for the thermal and ionization evolution, including cosmic ray ionization and UV heating, including the effects of grain charging. We will run models with a metallicity of $\mathrm{Z} = \mathrm{Z}_{\odot}/5$, scaled from solar. For the primary ionization rate ζ_{CR} we take $\zeta_{\mathrm{CR}} = 3.6 \times 10^{-17}\ \mathrm{s}^{-1}$.

Star formation recipe

We use the star formation recipe of Gerritsen & Icke (1997). A region is considered unstable to star formation if the local Jeans mass, which for density ρ and sound speed c is given by

$$\mathrm{M_J} = \frac{\pi\rho}{6}\left(\frac{\pi \mathrm{c}^2}{\mathrm{G}\rho}\right)^{3/2}, \tag{1}$$

is smaller than a reference mass $\mathrm{M_{ref}}$,

$$\mathrm{M_J < M_{ref}}. \tag{2}$$

The rate of star formation is set to scale with the local free fall time,

$$\tau_{\mathrm{sf}} = \mathrm{f_{sf} t_{ff}} = \frac{\mathrm{f_{sf}}}{\sqrt{4\pi \mathrm{G}\rho}} \tag{3}$$

The reasoning behind the choice of $\mathrm{M_{ref}}$ and $\mathrm{f_{sf}}$ was described in the discussion of the star formation recipe in Chapter 2. For the models presented here $\mathrm{M_{ref}} = 2 \times 10^5\ \mathrm{M_\odot}$. The delay factor $\mathrm{f_{sf}}$ was chosen to be 2.5. This delay accounts for the fact that the collapse of molecular clouds is inhibited by either turbulence or magnetic fields. Its value is uncertain, and while the dependence of star formation on this parameter was discussed in Gerritsen & Icke (1997), for the models we will present here a subtle issue related to variations in the star formation rate may be raised. Namely, for densities in the order of $\mathrm{n} = 10 - 100\ \mathrm{cm}^-3$, which are the typical densities of star forming particles in our simulation, the free-fall times are in the order of $\tau_{\mathrm{ff}} \approx 5$ Myr. A delay factor $\mathrm{f_{sf}}$ may then suppress variations of the star formation rate on timescales shorter than $\mathrm{f_{sf}}\tau_{\mathrm{ff}}$ Myr. For the simulations presented here we have checked that the results do not differ qualitatively in the range $\mathrm{f_{sf}} = 2.5 - 20$.

The star particles that are formed are assumed to represent stellar associations with a mass distribution formed according to a Salpeter initial mass function (IMF) with a lower mass limit of $0.1\ \mathrm{M_\odot}$ and an upper mass limit of $100\ \mathrm{M_\odot}$.

Feedback from supernova and stellar winds

The feedback method we use is the *pressure particle* feedback method described in chapter 3. This method consists of the creation at the site of a newly formed star particle of a gas-like particle that acts on the surrounding gas as an ordinary SPH particle in the limit of zero mass at constant internal energy. The evolution of the energy of this particle is a model input. We take the following prescription: After an initial time lag $\mathrm{t_l}$ yr, which accounts for the time needed for the heaviest stars of the star cluster to evolve into their terminal phases (thus $\mathrm{t_l} \approx 3 \times 10^6$ yr for an IMF with a $100\ \mathrm{M_\odot}$ upper limit), a constant energy injection rate $\dot{\mathrm{E}}$ is assumed up to the time $\mathrm{t_{sn}}$ at which the last stars of the cluster explode as SN II, hence $\dot{\mathrm{E}} = \epsilon_{\mathrm{sn}} \mathrm{n_{sn} E_{sn}} / (\mathrm{t_{sn}} - \mathrm{t_l})$, with $\mathrm{E_{sn}} = 10^{51}$ erg the supernova energy, $\epsilon_{\mathrm{sn}} = 0.05 - 0.1$ the efficiency of feedback, $\mathrm{n_{sn}} = 0.009\ \mathrm{M_\odot}^{-1}$ the number of supernovae per solar mass of stars formed and $\mathrm{t_{sn}} = 3 \times 10^7$, the lifetime of an $8\ \mathrm{M_\odot}$ star. The efficiency ϵ_{sn} thus assumes that $90\% - 95\%$ of the original supernova energy is radiated away, a value derived from more detailed simulations of the effect of supernova and stellar winds on the ISM (Silich et al. 1996).

Compared with the simulations presented in Chapter 4 we have added a correction for momentum losses. These losses stem from the fact that we fix the pressure particles to the stellar particle to which it is associated (this is necessary because, carrying no mass, they cannot be assigned an acceleration, see Chapter 3). The effect of this is that the models presented here show somewhat less evolution. Note, however, that hot gas that escapes from the galaxy may in fact carry away angular momentum, and thus the simulations with momentum losses may in fact not be completely unrealistic.

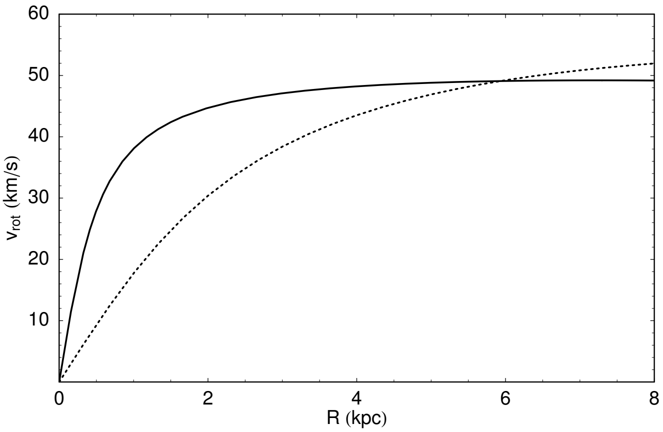

Figure 5.1: Dark halo rotation curves. **Drawn line:** model A, **dotted line:** model B.

5.3 Initial conditions

As we have discussed in the introduction, the central halo density and the angular momentum of the gas disk seem to be the parameters that determine whether a given dIrr galaxy will exhibit BCD features. We will examine the role of these parameters by running models with different halo and gas distributions, chosen to be representative of either BCD or dIrr. Other parameters like the masses of the gaseous, stellar and dark components, will be kept the same.

We will run simulations for dwarf galaxies in isolation. Note that the environment of dwarf galaxies may have a strong effect on their evolution, and indeed environment has been shown to correlate with galaxy type, with early type dwarfs showing a preference for dense cluster environments (Binggeli et al. 1990). Ram pressure stripping, tidal interactions and collisions with HI clouds all may act to perturb the ISM of dwarf galaxies and lead to enhancements of the SFR, or, in drastic cases, total removal of the ISM. Also note that interactions may very well change the distribution of angular momentum and thus affect the gas distribution or dark matter distribution; these are separate sources of evolution we will not consider (see e.g. Marcolini et al. 2003, Mori & Burkert 2000 and Mayer et al. 2001, Pasetto et al. 2003 for recent work on these).

Meurer et al. (1998) noted that the halo densities for the BCD NGC 1705 and 2915 are in the range $0.1 - 0.3$, a factor 10 higher than for normal dIrr. This is also consistent with the steeply rising rotation curves of BCDs found by other people (e.g. van Zee et al. 2001), as these imply high halo densities if these BCDs are dominated at all radii by the dark halo (as is probably the case). Thus we will consider two different halo models: one sharply peaked BCD-like, designated with A, and one with a large constant density core typical for dIrr, designated B. Both models will be chosen such that the rotation velocity of the halo is about the same at a radius of 6 kpc. To be specific, we take a density profile

$$\rho_{\rm h}({\rm r}) = \rho_0 \frac{\exp(-{\rm r}^2/{\rm r}_{\rm c}^2)}{1+{\rm r}^2/\gamma^2}. \tag{4}$$

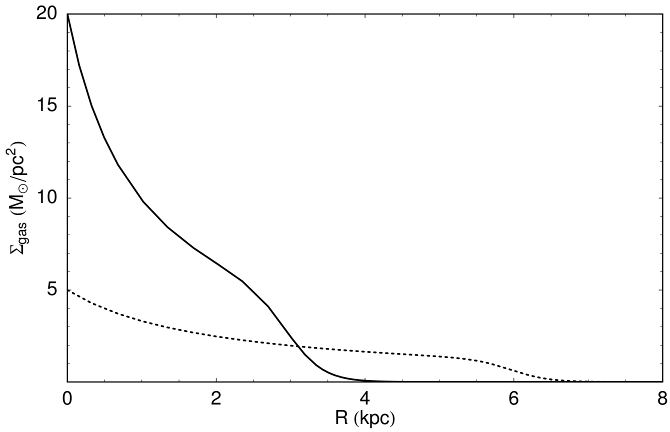

Figure 5.2: Gas surface density of the galaxy models. **drawn line:** model 1, **dotted line:** model 2. Both models have the same total mass.

For the model A we take a central halo density $\rho_0 = 0.32\ \mathrm{M_\odot/pc^3}$ and a core radius $\gamma = 0.4$ kpc, while for model B we take $\rho_0 = 0.02\ \mathrm{M_\odot/pc^3}$ and $\gamma = 2$ kpc. In both cases the cutoff radius $\mathrm{r_c}$ is taken to be $\mathrm{r_c} = 20$ kpc. The halos are represented by static potentials. A plot of the resulting halo rotation curves is given in Fig. 5.1.

An indication of the typical range of central gas surface densities for BCDs and dIrr can be found in van Zee et al. (2001). In their Figure 10 a sample of BCDs has its gas density profile compared to a dIrr sample. BCDs shown there have central densities in the order of $20\ \mathrm{M_\odot/pc^2}$, where dIrr show lower surface densities, in the range $3 - 10\mathrm{M_\odot/pc^2}$. For the gas disk we take then the following parametrization of the surface density,

$$\Sigma = \frac{\Sigma_\mathrm{g}}{1 + \mathrm{R/R_g}} \frac{1}{1 + \mathrm{e}^{(\mathrm{r-R_t})/\Delta \mathrm{R_t}}}, \tag{5}$$

where we will examine two different models, both with a mass of about $\mathrm{M_{gas}} = 2 \times 10^8\ \mathrm{M_\odot}$, with gas disk 1 having radial scale $\mathrm{R_g} = 0.98$ kpc, central surface density $\Sigma_\mathrm{g} = 20\ \mathrm{M_\odot/pc^2}$ and a truncation radius at $\mathrm{R_t} = 3$ kpc, while disk 2 has $\mathrm{R_g} = 1.96$ kpc, $\Sigma_\mathrm{g} = 5\ \mathrm{M_\odot/pc^2}$ and $\mathrm{R_t} = 6$ kpc. In both cases $\Delta\mathrm{R_t} = 0.25$ kpc. The two gas distributions are plotted in Fig. 5.2.

Combining halo and gas disk we get a 2×2 grid of models A1, A2, B1 and B2. the A1 model resembles an archetypical BCD, while “normal” dIrrs are more like model B2. The two other models A2 and B1 are of mixed type and serve to disentangle the effect of the halo parameters from that of the gas distribution (but note that these models are not less realistic, because in principle the gaseous and dark components can undergo wholly different evolution).

The initial stellar distribution is taken the same for all models, namely an exponential disk with a sech-squared z distribution,

$$\rho_\mathrm{disk}(\mathrm{R,z}) = \frac{\Sigma_0}{2\mathrm{h_z}} \exp(-\mathrm{R/R_d}) \mathrm{sech}^2(\mathrm{z/h_z}) \tag{6}$$

with central surface density $\Sigma_0 = 200\ \mathrm{M_\odot/pc^2}$, a radial scale length $\mathrm{R_d} = 0.6$ kpc and a vertical scale height $\mathrm{h_z} = 250$ pc. It is constructed using the method described in

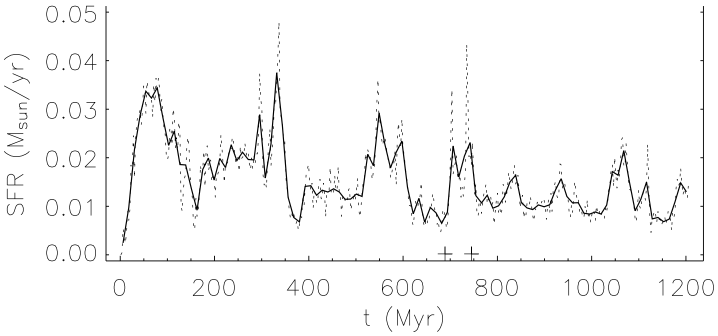

Figure 5.3: Total star formation rate of model A1. Drawn line indicates the SFR determined by binning star formation events in 10 Myr intervals, dotted line is the same for 2 Myr bins. Crosses indicate the times for which the snapshots shown in Fig. 5.8 are taken.

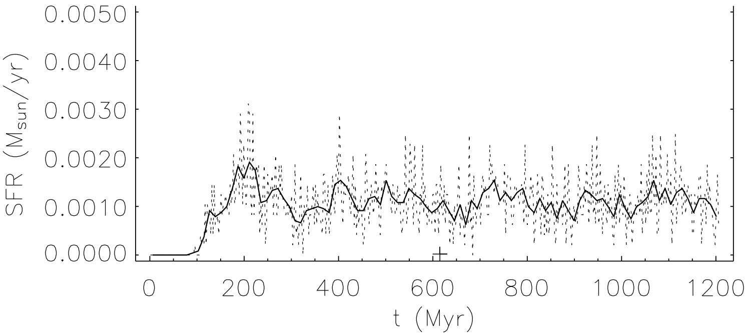

Figure 5.4: Total star formation rate of model B2. Drawn line indicates the SFR determined by binning star formation events in 10 Myr intervals, dotted line is the same for 2 Myr bins. The cross is the time of the snapshot shown in Fig.5.10.

Kuijken & Dubinski (1995), calculating an approximate 3 integral distribution function accounting for the halo and gas potentials. The total mass of the stellar disk is $\mathrm{M_d} = 10^8\ \mathrm{M}_\odot$. The initial ages of the stars are distributed according a star formation rate of $0.008\ \mathrm{M}_\odot/\mathrm{yr}$

The simulations shown here are run with 50k gas particles and 50k star particles. We take some care in preparing the gas disks, especially for the A1 and B1 model. As these models can show disruptive bursts of star formation (up to $0.1 - 0.2\ \mathrm{M}_\odot/\mathrm{yr}$) if the initial particle dispersion is chosen too low (lower than about 10 km/s).

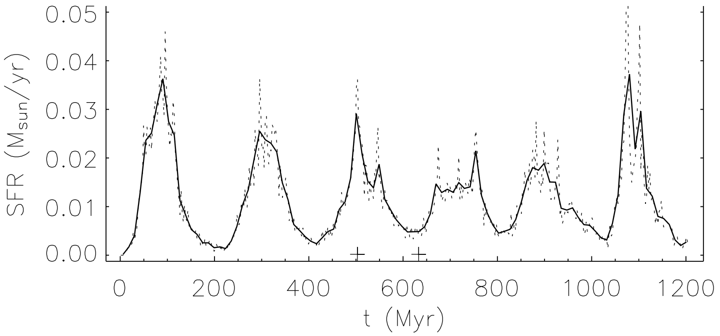

Figure 5.5: Star formation rate of model B1. Drawn line indicates the SFR determined by binning star formation events in 10 Myr intervals, dotted line is the same for 2 Myr bins. Crosses indicate the times for which the snapshots shown in Fig. 5.9 are taken.

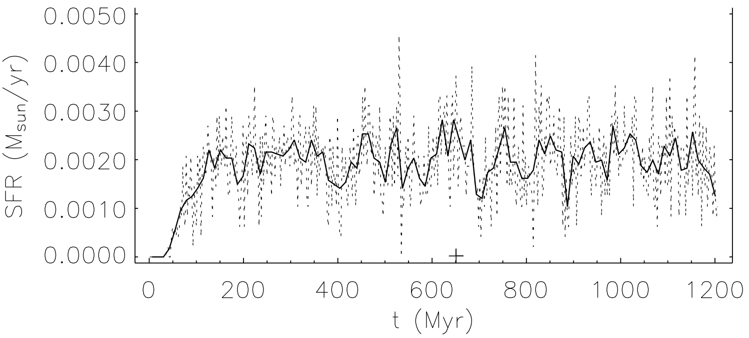

Figure 5.6: Total star formation rate of model B2. Drawn line indicates the SFR determined by binning star formation events in 10 Myr intervals, dotted line is the same for 2 Myr bins. The cross is the time of the snapshot shown in Fig.5.10.

5.4 Results

We run the simulations for about 1500 Myr, which is long enough for a quasi steady state to develop, but short enough so that the effects of sources of evolution not included in the model (e.g. enrichment, gas infall or interaction) can be ignored.

In Fig. 5.3 and 5.4 we have plotted the resulting star formation rate of the “pure” BCD model A1 and the dIrr model B2. We see that, while the total gas content is equal, the two models show drastically different star formation properties. The A1 model has a typical star formation rate of about $0.015\ \mathrm{M}_\odot$/yr, with sizable excursions up to $0.05\ \mathrm{M}_\odot$/yr, while the B2 model has a much lower star formation rate, $\approx 0.001\ \mathrm{M}_\odot$/yr, with also much smaller variations. The variations that are visible are for a large part statistical variations due to the finite size of the star particles that are formed.

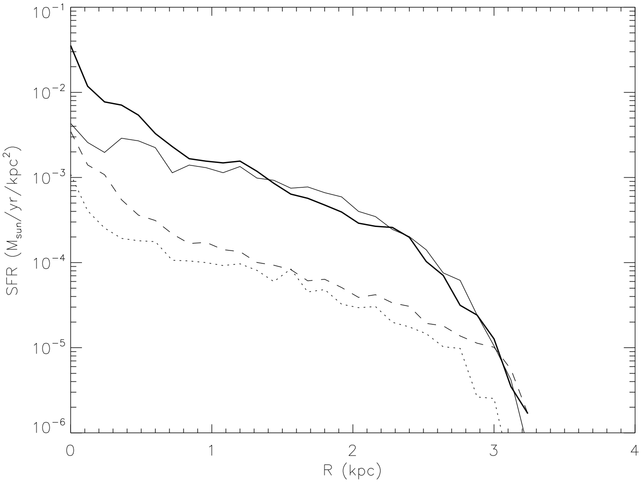

Figure 5.7: Mean star formation density as a function of radius. **Thick line:** A1 model, **thin line:** B1 model, **dashed:** A2 model and **dotted:** B2 model.

If we look at the star formation rate of the B1 and A2 models (Fig. 5.5 and 5.6), we again see the same big difference in star formation rate for the high surface density and low surface density models. The star formation rate of the low surface density model (A2) shows little variations, being very similar to the B2 model, although slightly higher with a $\mathrm{SFR} \approx 0.002$. On the other hand, while for the A1 and B1 model the SFR are about the same, we see that the variations in star formation rate follow a much more regular pattern in the case of B1 model. This is due to the large constant density core of this model (see also the discussion in chapter 4).

More information about the spatial distribution of star formation is given by Fig. 5.7, where the time averaged star formation density is plotted as a function of radius. A number of observations can be made on the basis of this picture. First, if we look at the differences between the A1 model and B1 model we see that, while the star formation rate per unit area is about the same at the outskirts, in the center it is about a factor of 10 higher for the A1 model. This difference does not translate into a big difference in the overall (mean) star formation rate. The A2 and B2 models have lower star formation densities than the models with a concentrated gas distribution, but otherwise a very similar dependence on radius. The star formation of the model run with halo A again peaks higher than the B halo. We see that the star formation rate is mainly set by the gas (surface) density (as expected). A denser halo will enhance the star formation in the central region.

Note that for all models the star formation drops at a radius of about 3 kpc. To some extent this is a coincidence because the threshold radius can be shifted by changing the cosmic ray heating (see Chapter 2). For higher cosmic ray fluxes star formation will be confined to a smaller region. However, 3 kpc is also close to the radius at which the stellar disk is terminated. This may point to a connection of star formation with previous existing stellar populations. This is supported by the fact that the

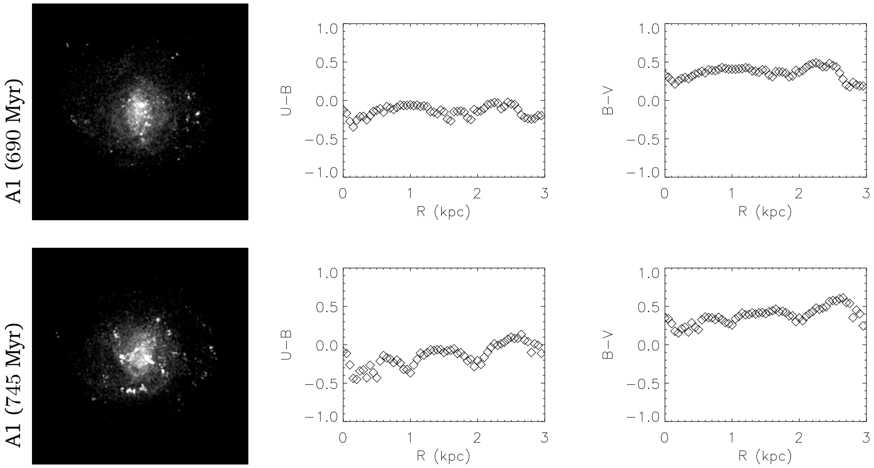

Figure 5.8: Optical properties of model A1. UBV composites (see appendix for colour) and plots of U − B and B − V colours at simulation times of 690 Myr (upper panels) and 745 Myr (lower panels).

scale height of the gas disk as function of radius shows a kink where the stellar disks terminates.

5.5 Observational properties of simulated galaxies

From the stellar distributions, the ages of the stellar particles and the Bruzual & Charlot (1993) population synthesis tables we construct U, B and V maps. In Fig. 5.8 we have plotted for the A1 simulation UBV composites as well as the radial dependence of the U − B and B − V colours. These are shown for two representative frames, chosen to be at a time of relatively low star formation (at a simulation time of 690 Myr) and the other at a time of increased star formation (745 Myr). If we compare the UBV composites with analogous maps for the B1 simulation (Fig. 5.9) and the A2 and B2 models (Fig. 5.10) we see that the A1 snapshots show a strong centrally concentrated light distribution, whereas the B1 model shows more widely distributed patches of star formation. The A2 and B2 composites show little features.

The colours of dIrr and BCD galaxies are generally quite blue (with $U - B \lesssim -0.1$ and $B - V \lesssim 0.5$). Comparing BCD with dIrr, the former have less colour gradients than the latter, with BCDs having positive radial U − B and B − V gradients, and thus reddening on the outside. The azimuthally averaged colour plots from the simulated U, B and V maps shown in Figures 5.8, 5.9 and 5.10 should be seen as rough approximations only. We do not take into account extinction. Furthermore, the initial stellar population is taken to be the same for all simulations. This means the colours are not realistic, because the colours depend on the total star formation history. Nevertheless we can look at general trend and compare the different models. We see that the A1 and B1 models are much bluer than the A2 and B2 model, this is due to the initial stellar population (too much old stars are present for the A2 and

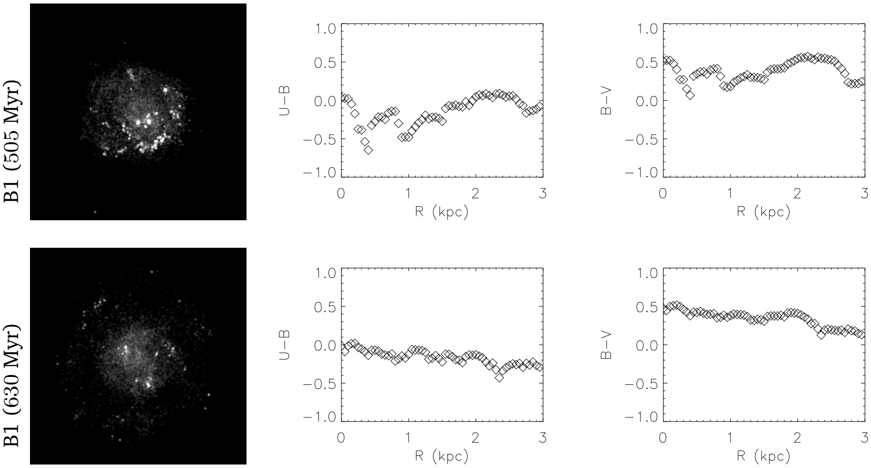

Figure 5.9: Optical properties of model B1. UBV composites and plots of U − B and B − V colours at simulation times of 690 Myr (upper panels) and 745 Myr (lower panels).

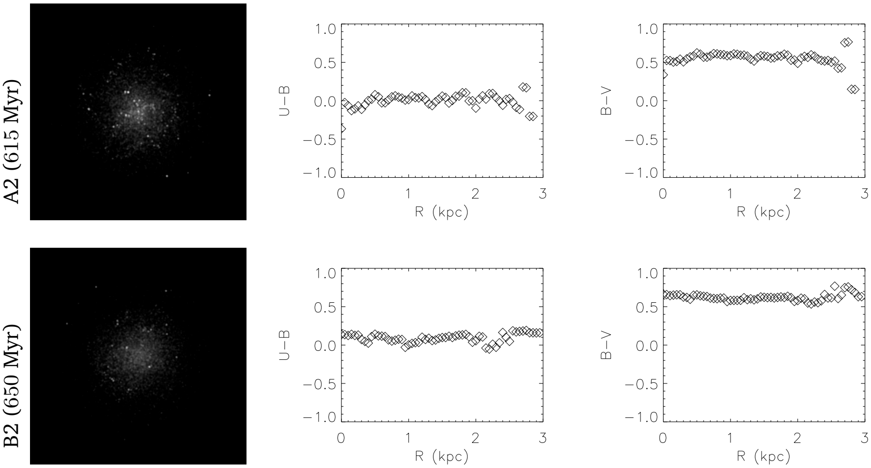

Figure 5.10: Optical properties of models A2 (upper panels) and B2 (lower panels). UBV composites and plots of U − B and B − V colours.

B2 models in relation to their current star formation). If we look at the radial colour distribution we see that the A1 models show either no colour gradient or reddening from the inside to the outside, whereas the B1 model shows little trend or a negative colour gradient. The A2 and B2 show no colour gradients.

5.6 Discussion and conclusions

If we would classify our galaxies on the basis of the optical characteristics given in Figures 5.8, 5.9 and 5.10, the A1 model would be a good BCD candidate, the B2 model a vigorously star forming dIrr and B2 and A2 model would represent low surface brightness dwarfs. The A1 model has many of the the characteristics associated with the BCD phenomenon: central star formation, compact optical scale lengths, reddening with increasing radius. That such a system is the outcome of a model galaxy made according to the characteristic halo and gas distribution of observed BCDs is confirmation that these properties are indeed the determining factors for the BCD mode of star formation. Note that we have shown that both a compact gas distribution *and* a centrally concentrated halo are necessary. A high gas surface density will imply a high star formation rate, but the central concentration is a result of the high halo density. This does not mean that dIrr with a low central halo density could not experience a central bursts of star formation (and thus maybe classified as BCDs), but only that on the basis of our simulations we expect such a burst to be a transient 'false' BCD phase. On the other hand, we have not found that the A1 model undergoes phases of low star formation: it seems to stay in a BCD mode, essentially until the gas reservoir is (locally) depleted.

Our low surface density simulations (A2 and B2) show low star formation, regardless of halo density. We do not expect dIrrs with low gas densities to undergo large star formation bursts, unless perturbed by some external effect.

There are some areas that still need to be explored. One is the effect of a halo built from particles as opposed to a halo consisting of a static potential. Such a halo can react dynamically on perturbations. The other is role the metallicity. We chose a metallicity of $Z = Z_{\odot}/5$, which is realistic for both normal dIrr and BCDs, although a bit on the high side for BCDs. A lower metallicity may have an effect on star formation. Also, our simulation does not answer the question why the BCDs should have lower metallicity. It could be that BCDs have had too little time for enrichment. The fact that our simulations imply that the BCD phase persists until gas depletion automatically implies that current BCDs can only be a few Gyr old, younger than dIrr. This would be consistent with the presence of BCD systems that are proven to be very young (less than 1 Gyr, Izotov & Thuan 2004). "Old" BCDs, meaning systems that have "turned" on more than a few Gyrs ago, would then have evolved, due to gas depletion into the general dIrr population, changing into a more leisurely mode of star formation or they may have turned into dEs. In the process they could lose their centrally condensed halo due to mass loss effects (Navarro & White 1993). It is interesting to note that BCD-like systems are thought to constitute the building blocks of galaxies at high redshifts. It may that the current population of BCDs are just a trickle of late galaxy formation, and that they are relics of a bygone era.

References

Barnes, J. & Hut, P., 1986, *Nature* **324**, 446

Binggeli, B., Tarenghi, M., & Sandage, A., 1990, *A&A* **228**, 42

Bruzual A., G. & Charlot, S., 1993, *ApJ* **405**, 538

Gerritsen, J. P. E. & Icke, V., 1997, *A&A* **325**, 972

Hunter, D. A. & Elmegreen, B. G., 2004, *AJ* **128**, 2170

Hunter, D. A., Elmegreen, B. G., & Baker, A. L., 1998, *ApJ* **493**, 595

Izotov, Y. I. & Thuan, T. X., 2004, *ApJ* **616**, 768

Kennicutt, R. C., 1989, *ApJ* **344**, 685

Kuijken, K. & Dubinski, J., 1995, *MNRAS* **277**, 1341

Marcolini, A., Brighenti, F., & D'Ercole, A., 2003, *MNRAS* **345**, 1329

Mayer, L., Governato, F., Colpi, M., Moore, B., Quinn, T., Wadsley, J., Stadel, J., & Lake, G., 2001, *ApJ* **559**, 754

Meurer, G. R., Staveley-Smith, L., & Killeen, N. E. B., 1998, *MNRAS* **300**, 705

Mori, M. & Burkert, A., 2000, *ApJ* **538**, 559

Navarro, J. F. & White, S. D. M., 1993, *MNRAS* **265**, 271

Papaderos, P., Loose, H.-H., Thuan, T. X., & Fricke, K. J., 1996, *A&AS* **120**, 207

Pasetto, S., Chiosi, C., & Carraro, G., 2003, *A&A* **405**, 931

Schmidt, M., 1959, *ApJ* **129**, 243

Silich, S. A., Franco, J., Palous, J., & Tenorio-Tagle, G., 1996, *ApJ* **468**, 722

Thuan, T. X. & Martin, G. E., 1981, *ApJ* **247**, 823

van Zee, L., 2001, *AJ* **121**, 2003

van Zee, L., Salzer, J. J., & Skillman, E. D., 2001, *AJ* **122**, 121

van Zee, L., Skillman, E. D., & Salzer, J. J., 1998, *AJ* **116**, 1186

Chapter 6

Molecular gas and star formation

Abstract

We present models of the coupled evolution of the gaseous and stellar content of dwarf galaxies using a hybrid N-body/hydrodynamics code and a Jeans mass criterion to describe the onset of star formation from gas. We now incorporate for the first time the formation of H_2 gas as part of the model. We do so by formulating a sub-grid model for molecular clouds, assumed to obey well-known scaling relations, and solving for the HI$\leftrightarrow$$H_2$ balance set by the H_2 formation on dust grains and its FUV-induced photodissociation. This then allows the tracking of the evolution of the molecular gas of galaxies seamlessly along with that of its precursor cold neutral medium HI gas. The thermal and dynamic evolution of gas as dense as $\sim 2 \times 10^2$ cm^{-3} and as cold as $\mathrm{T_k} \sim 40$ K (where most of the HI$\rightarrow$$H_2$ transition is expected) is probed in our simulations. We are thus able to identify the molecular regions of the interstellar medium during the evolution of a typical dwarf galaxy. We find a significant dependence of the HI$\rightarrow$$H_2$ transition and the resultant H_2 gas mass on the ambient metallicity and the H_2 formation rate, results we expect to be valid in all other types of galaxies for which the dense and cool HI precursor and the resulting H_2 gas phases are currently inaccessible by high resolution numerical studies (e.g. large spirals).

6.1 Introduction

Stars form in molecular clouds, and most stars form in the large complexes of giant molecular clouds (GMCs). A general theory to predict the location and amount of star formation in galaxies does not exist yet. The global drivers of star formation are generally sought in large scale processes that can form concentrations of HI gas (Elmegreen 2002), for example gravitational instabilities in disk galaxies, or compression by galaxy interactions or mergers. These concentrations of neutral gas are then assumed to be the sites of molecular cloud and ultimately star formation. Computer simulations of galaxies have followed this lead and base their star formation model usually on the local density directly using a Schmidt law (Mihos & Hernquist 1994, Springel 2000, Semelin & Combes 2002), or on the consideration of gravitational instability using a Jeans mass criterion (Katz 1992, Gerritsen & Icke 1997), and none explicitly consider molecular gas.

The interstellar medium (ISM) consists of gas with a wide ranging properties, from cold, dense molecular clouds to the cold and warm neutral medium (CNM, WNM) and the hot ionized medium intermixed in fractal-like structures. The physical processes governing the state of the ISM have been progressively identified in the last few decades, but the precise working of these, amongst which various heating, cooling and ionization processes, is still an area of active research (Vázquez-Semadeni 2002). Most galactic scale simulations include only one phase, best thought of as the warm neutral medium (Katz 1992, Navarro & White 1993, Springel 2000). Some authors have tried to include more physics to model a two phase medium (Gerritsen & Icke 1997, Gerritsen & de Blok 1999), or incorporated an empirical model for a multiphase ISM (Springel & Hernquist 2002, Semelin & Combes 2002, Andersen & Burkert 2000). The inclusion of the molecular component into simulations of the ISM of galaxies on galactic scale is generally not attempted, and so such simulations cannot be compared directly to the numerous observations of H_2 gas distribution in galaxies (as revealed by its tracer molecule CO).

Thus, apart from the obvious fallacy of forming stars out of atomic gas, the absence of molecular gas deprives the simulation of a valuable diagnostic tool that one could use to constrain the many free parameters that are part of this type of modelling: molecular gas in galaxies is observationally well studied and a host of empirical relations have been established between molecular gas and star formation. For example the Schmidt law has been demonstrated to be a much tighter relation for molecular, rather than HI gas (Wong & Blitz 2002). Recently, CO observations are beginning to yield complete surveys of metal-rich molecular gas of nearby galaxies (Engargiola et al. 2003, Mizuno et al. 2001, Helfer et al. 2001, Regan et al. 2001). The catalogues of molecular clouds from these works can be matched against Hα observations, which yields information regarding lifetimes of giant molecular clouds. On a more detailed level, studies of molecular gas in the dense shells around superbubbles in for example the Large Magellanic Cloud (LMC) are used to unravel the star formation sequence (Yamaguchi et al. 2001). Thus, while the study of the relation between molecular gas and star formation is part and parcel of observational studies of galaxies, the theoretical approach of study of these complex systems by numerical simulation lacks such a possibility, simply because of the computational demands of following the formation of molecules from first principles.

For primordial gas, where H_2 forms in the gas phase and no radiation sources are present, simulations have followed the H_2 chemistry (Abel 1997), but these are not applicable to current star forming galaxies. Some pioneering work to include H_2 into simulations of star forming spiral galaxies has been done by Hidaka & Sofue (2002) but they did not consider a time dependent HI→H_2 transition, which as we will argue below, is essential. In this chapter, we will describe a method to incorporate a realistic H_2 formation criterion into simulations of galaxies. It is based on the application of a time-dependent HI→H_2 transition to a sub-grid model for interstellar clouds. This method allows us to simulate galaxies without omitting an important ISM component which constitutes the “fuel” of all star formation activity in galaxies. We implement our method in an N-body/SPH code - although we want to emphasize that it can be implemented in more general types of code for the simulation of the ISM. First results for dwarf irregulars indicate the critical role of metallicity and the H_2 formation rate on the distribution and total amount of H_2 present. Thus, this work contributes to filling two gaps in the literature. First, the H_2 formation criterion makes a connection between galaxy-sized simulations and molecular cloud theory, making the results of numerous theoretical studies of cloud formation accessible and applicable to such simulations. Secondly, our method can be used to explore the connection between large scale instabilities and the formation of molecular gas complexes. Star formation and molecular gas can then be studied in the dynamic setting of realistic galaxy models that include effects of e.g. spiral density waves, self propagating star formation, galaxy interactions and mergers.

In Section 6.2 we will first give an overview of a simplified version of the theory of H_2 formation and destruction, in sections 6.3 and 6.4 we will discuss the N-body/SPH code we use and the actual implementation of our H_2 criterion, whereafter we present the first results of our modelling in section 6.5.

6.2 H_2 formation and destruction

The formation of H_2 in galaxies has already been studied by Elmegreen (1989, 1993), where the important role of ambient metallicity and pressure has been described. Subsequent efforts to incorporate his approach into analytical models of galactic disks (Honma et al. 1995) or numerical simulations (Hidaka & Sofue 2002) have adopted stationary models, namely once an H_2 formation criterion is satisfied the $HI\rightarrow H_2$ transition is set to be instantaneous. The time-dependence of several factors affecting this transition (e.g. the ambient H_2-dissociating radiation field) and the various gas heating and cooling processes were not considered. This seriously restricts the ability of such models to track the evolution of the ISM and particularly its H_2 gas phase. This is because the conditions affecting the $HI\leftrightarrow H_2$ equilibrium can vary over timescales comparable to or shorter than that needed for equilibrium to be reached.

Dust grains, when present, are the sites where H_2 mostly forms. The H_2 formation rate $\mathrm{R_f}$ for gas with temperature $\mathrm{T_k}$ and metallicity Z can then be expressed as

$$\mathrm{R_f} = \frac{1}{2}\sigma_\mathrm{d}\langle \mathrm{v_H}\rangle \mathrm{S_H}\gamma_{\mathrm{H_2}} = 3.5\times 10^{-18}\mu \mathrm{Z}\mathrm{T_k^{1/2}}\mathrm{S_H}\gamma_{\mathrm{H_2}}\ \mathrm{cm^3\ s^{-1}}, \qquad (1)$$

(e.g. Hollenbach, Werner, & Salpeter 1971; Cazaux & Tielens 2002, 2004). This equation expresses the rate of collisions resulting in H_2 formation of H atoms, having mean velocities $\langle \mathrm{v_H}\rangle$, with interstellar dust particles with effective surface σ_d. The grain surface (and thus the formation rate) is assumed to scale linearly with metallicity Z, $\sigma_\mathrm{d} = \sigma_\mathrm{g}\mathrm{n_g}/\mathrm{n} = 4.9\times 10^{-22}\mathrm{Z\ cm^2}$, for grain surface σ_g and ratio of grain density to hydrogen density $\mathrm{n_g}/\mathrm{n}$. The functions $\mathrm{S_H} = \mathrm{S_H}(\mathrm{T_k})$ and $\gamma_{\mathrm{H_2}} = \gamma_{\mathrm{H_2}}(\mathrm{T_{dust}})$ express the HI grain-sticking , and H_2 formation probability (once HI is on the grain surface) respectively. Laboratory experiments usually constrain only the product $\mathrm{S_H}\gamma_{\mathrm{H_2}}$ for various temperature domains rather than provide any analytical fits for each function separately (e.g. Pirronello et al. 1997; Katz et al. 1999). The theoretical study of Buch & Zhang (1991) yields a function $\mathrm{S_H} = [1 + (\mathrm{k_B T_k/E_\circ})]^{-2}$ ($\mathrm{E_\circ/k_B} = 102$ K) valid for $\mathrm{T_k} \lesssim 300$ K, which we adopt in the present work. We incorporate the uncertainties of the H_2 formation rate into a constant parameter μ. These uncertainties reside mainly in the formation probability, but also in the effective surface for H_2 formation. This surface may be bigger than the value σ_d, which is actually the value for the effective visual extinction cross-section. A value of $\mu = 3.5$ corresponds to the canonical formation rate $\mathrm{R_f} = 3 \times 10^{-17}$ cm^3 s^{-1} (e.g. Jura 1974, 1975), for typical CNM HI gas conditions ($\mathrm{T_k} \sim 100$ K), but values up to $\mu \sim 18$ are not excluded. Early suggestions for a high value of μ emerged from the study of rovibrational infrared lines of H_2 in reflection nebulae (Sternberg 1988), and more recently from the detections of particularly intense H_2 rotational lines with the Infrared Space Observatory (ISO) in photodissociation regions (Habart et al. 2000; Li et al. 2002).

The timescale associated with H_2 formation is (e.g. Goldshmidt & Sternberg 1995)

$$\tau_\mathrm{f} = (2\mathrm{nR_f})^{-1} = 5 \times 10^7 \left(\frac{\mathrm{T_k}}{100\ \mathrm{K}}\right)^{-1/2} \left(\frac{\mathrm{n}}{10\ \mathrm{cm^{-3}}}\right)^{-1} [\mu \mathrm{Z S_H(T_k)}]^{-1}\ \text{yrs}, \quad (2)$$

where n and $\mathrm{T_k}$ are the density and temperature of HI. For $\mathrm{n} \sim 50$ cm^{-3} and $\mathrm{T_k} \sim 100$ K, typical of the Cold Neutral Medium HI gas out of which H_2 clouds form, $\tau_\mathrm{f} \sim 10^7$ yrs. This is comparable to the timescales of a wide variety of processes expected to fully disrupt or otherwise drastically alter typical molecular clouds and their ambient environments. Some of the most important ones are star formation, with the disruptive effects of OB associations (e.g. Bash et al. 1977), turbulent dissipation (Stone et al. 1998; MacLow et al. 1998), and inter-cloud clump-clump collisions (Blitz & Shu 1980). The *mean* FUV field driven by the evolution of continously forming stellar populations throughout a galaxy evolves over similar timescales (e.g. Parravano, Hollenbach & McKee 2003), and the same is the case for the ambient pressure environment and its perturbations by passing supernova (SN) induced shocks (e.g. Wolfire et al. 2003). *Hence a realistic model of the HI→H_2 transition in galaxies must be time-dependent.*

6.2.1 Equilibrium molecular fraction

The equilibrium molecular gas fraction per cloud, under a given ambient FUV field, can be estimated by considering the formation/destruction equilibrium for a plane parallel cloud illuminated by a radiation field $\mathrm{G_\circ}$. In equilibrium formation balances destruction, hence

$$\mathrm{R_f n n_1} = \mathrm{G_\circ k_\circ f(N_2) e^{-\tau} n_2} \quad (3)$$

which must hold at any depth. The densities $\mathrm{n_1}$ and $\mathrm{n_2}$ denote the HI and H_2 densities, while the total hydrogen density is $\mathrm{n} = \mathrm{n_1} + 2\mathrm{n_2}$. The H_2 dissociation rate $\mathrm{k_\circ} = 4 \times 10^{-11}\ \mathrm{s^{-1}}$ is normalised for an ambient FUV field in units of the Habing (1968) field value ($\mathrm{G_\circ} = 1$). The factor $\mathrm{f(N_2)}$ is the normalised H_2 self-shielding function which describes the decrease in dissociation rate due to absorption by the molecular column, $\mathrm{N_2}$. Furthermore, $\tau = \sigma(\mathrm{N_1} + 2\mathrm{N_2})$ is the FUV continuum optical depth due to grain extinction, with a dust FUV absorption cross-section $\sigma = \xi_\mathrm{FUV}\sigma_\mathrm{d}$ for $\xi_\mathrm{FUV} = 2 - 4$. Eq. (3) can be converted to a separable differential equation for the columns $\mathrm{N_1}$ and $\mathrm{N_2}$ (e.g. Goldshmidt & Sternberg 1995) which, when integrated by parts for a uniform cloud, yields an HI transition column density

$$\mathrm{N_{tr}(HI)} = \frac{1}{\sigma}\ln\left(1 + \frac{\mathrm{G_\circ k_\circ}}{\mathrm{nR_f}}\Phi\right). \tag{4}$$

This is the total HI column density marking the HI/$\mathrm{H_2}$ transition zone from the surface of the cloud for a uniform one-side illuminated cloud. The factor Φ is an integral of the self-shielding function over the $\mathrm{H_2}$ column (Goldshmidt & Sternberg 1995), which for $\mathrm{f(N_2)} \sim \mathrm{N_2^{-k}}$,

$$\Phi = 2^{\mathrm{k}-1}\left(\mathrm{N_{ch}}\sigma\right)^{\mathrm{k}} \int_0^\infty \mathrm{x^{-k}e^{-x}dx} = 6.6 \times 10^{-6}\sqrt{\pi}\,\mathrm{Z}^{1/2}\xi_{\mathrm{FUV}}^{1/2}, \tag{5}$$

and encompasses the details of the $\mathrm{H_2}$ self-shielding. Its numerical value was obtained for $\mathrm{k} = 1/2$ and a characteristic column density of $\mathrm{N_{ch}} = 1.75 \times 10^{11}\ \mathrm{cm^{-2}}$ (Jura 1974).

The equation of the HI$\leftrightarrow$$\mathrm{H_2}$ balance still yields an analytical expression for $\mathrm{N_{tr}(HI)}$ for clouds with density profile: $\mathrm{n(r) = n_{ex}(r/R)^{-1}}$, with R the cloud radius. Such a profile results from cloud models using a logotropic equation of state (Mclauglin & Pudritz 1996) hence we will refer to them as ”logotropic clouds,” but the reason we will consider such profiles here is that this is a rough representation of sub-resolution, non-uniform, GMC density structure. For a radial incident interstellar radiation field, such a density profile yields

$$\mathrm{N_{tr}(HI)} = \frac{\nu_\circ}{\sigma}\ln\left(1 + \nu_\circ^{-1}\frac{\mathrm{G_\circ k_\circ}}{\mathrm{n_{ex}R_f}}\Phi\right), \tag{6}$$

where $\nu_\circ = \mathrm{n_{ex}R}\sigma\left(1 + \mathrm{n_{ex}R}\sigma\right)^{-1}$. For $\mathrm{R} \to \infty$ we obtain $\nu_\circ \to 1$ and Eq. (6) reduces to Eq. (4) as expected for uniform density clouds ($\mathrm{n(r) \to n_{ex}}$). The visual extinction corresponding to (6) is given by (using the expressions for $\mathrm{R_f}$ and ϕ, (1) and (5))

$$\mathrm{A_v^{(tr)}} = 1.086\nu_\circ\xi_{\mathrm{FUV}}^{-1}\ln\left[1 + \frac{\nu_\circ^{-1}\mathrm{G_\circ}}{\mu\mathrm{S_H(T_k)}}\left(\frac{\xi_{\mathrm{FUV}}}{\mathrm{ZT_k}}\right)^{1/2}\left(\frac{\mathrm{n_{ex}}}{135\ \mathrm{cm^{-3}}}\right)^{-1}\right]. \tag{7}$$

It is then easy to show that the $\mathrm{H_2}$ gas mass fraction contained inside the HI transition zone marked by $\mathrm{A_v^{(tr)}}$ is given by

$$\mathrm{f_m} = \frac{\mathrm{M(H_2)}}{\mathrm{M_c}} = \left(1 - \frac{4\mathrm{A_v^{(tr)}}}{3\langle \mathrm{A_v}\rangle}\right)^3, \tag{8}$$

for constant density clouds, and

$$\mathrm{f_m} = \frac{\mathrm{M(H_2)}}{\mathrm{M_c}} = \exp\left[-4\frac{\mathrm{A_v^{(tr)}}}{\langle \mathrm{A_v}\rangle}\right] \tag{9}$$

for logotropic clouds. Here, $\langle \mathrm{A_v}\rangle$ is the average extinction for a spherical cloud measured by an outside observer.

We consider the cloud fraction f_m to be a measure of the local molecular gas content of the ISM. Here, the implicit assumption is that most of the HI/H_2 gas mass ultimately can be traced in such cloud structures. For CNM HI and the resulting H_2 clouds this is a reasonable assumption. In certain models this is predicted to be the final configuration of any initial gas mass which quickly cools and fragments in an environment of constant “background” pressure (Chièze 1987; Chièze & Pineau des Forêts 1987).

To derive f_m we need some measure of the average cloud extinction $\langle A_v \rangle$. The crucial assumption we make in order to derive this is that all unresolved cloud structures in the ISM where the HI/H_2 transition takes place obey the widely observed density-size power law (e.g. Larson 1981). The bulk of the H_2 gas is assembled in Giant Molecular Clouds, the sites of most star formation activity in galaxies, and which are observed to be virialised entities (e.g. Larson 1981, Elmegreen 1989 and references therein). Indeed their well known density/size scaling relation can be readily reproduced from the virial theorem applied for clouds under a given boundary pressure P_e (Elmegreen 1989). In this case it can be shown that the average H density is given by

$$\langle n \rangle = n_\circ \left(\frac{P_e/k_B}{10^4\ \mathrm{K\ cm^{-3}}} \right)^{1/2} R_{pc}^{-1}, \tag{10}$$

where R_{pc} is the cloud radius in parsecs. The range of the normalising constant $n_\circ$ ($\mathrm{cm^{-3}}$) can be determined theoretically by choosing a range of plausible polytropic solutions to the cloud density profiles (e.g. Elmegreen 1989), or from the *observed* n-R relations for galactic molecular clouds. The latter approach, after using the scaling relation $n(H_2) = 1700 R_{pc}^{-\alpha}\ \mathrm{cm^{-3}}$ reported by Larson (1981) ($\alpha \sim 1$), yields $n_\circ \sim 1520\ \mathrm{cm^{-3}}$. In estimating $n_\circ$ from the observed n-R scaling relation we took into account that for the galactic midplane molecular clouds the outer pressure $P_\circ/k_B \sim 10^4\ \mathrm{K\ cm^{-3}}$, but the boundary pressure on the molecular part of the cloud $P_e = P_{e,m} \sim 5P_\circ$ (Elmegreen 1989). Using (10) we estimate the average extinction of a cloud with radius R as measured from the outside as

$$\langle A_v \rangle = 2 k_g \langle n \rangle R \sigma_d, \tag{11}$$

with a geometric factor $k_g = 2/3$ (for a spherical cloud). After substituting $\langle n \rangle$ from Eq. (10) we get,

$$\langle A_v \rangle = 0.22 Z \left(\frac{n_\circ}{100\ \mathrm{cm^{-3}}} \right) \left(\frac{P_e/k_B}{10^4\ \mathrm{K\ cm^{-3}}} \right)^{1/2}. \tag{12}$$

The cloud boundary pressure is due to thermal and macroscopic motions (Elmegreen 1989), assuming the latter to be isotropic, P_e can be expressed as

$$P_e = n_{ex} k_B T_k + \frac{1}{3} \rho_e \sigma_{vel}^2 = \left[1.085 T_k + 54 \left(\frac{\sigma_{vel}}{\mathrm{km\ s^{-1}}} \right)^2 \mathrm{K} \right] n_{ex} k_B, \tag{13}$$

where σ_{vel} is the 3-dimensional velocity dispersion of the gas due solely to macroscopic motions. From (8), (9), and (12) it is obvious that high pressure gas will tend to be molecular, a result already known from the analytical/steady-state models of the HI→H_2 transition in galactic disks (Elmegreen 1993; Honma et al. 1995).

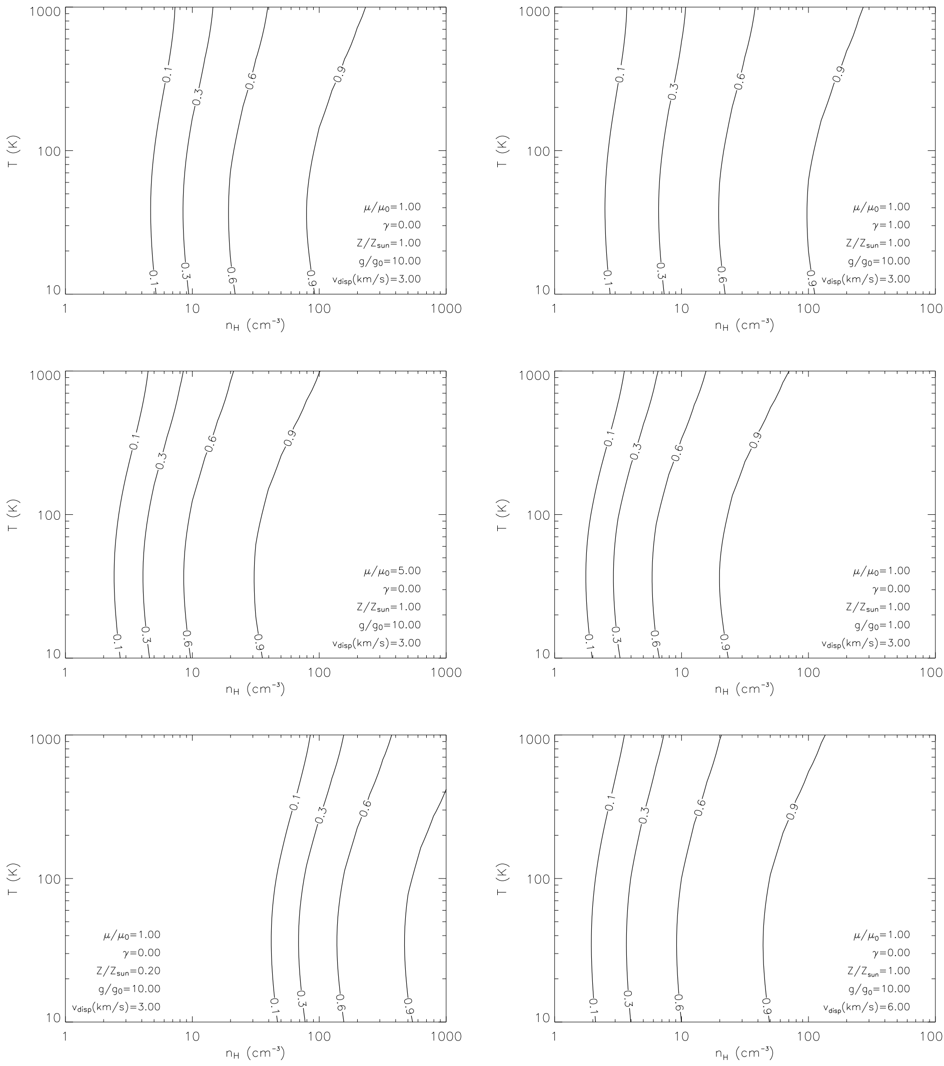

Figure 6.1: The Equilibrium molecular fraction f_m. Plotted are contours of f_m labelled with the contour value. Above 1000 K the formation rate is taken to be zero. γ indicates the power law index of the cloud density profile ($n \propto r^{-\gamma}$), thus $\gamma = 0$ means constant density clouds, $\gamma = 1$ logotropic clouds.

We can now calculate the equilibrium $\mathrm{f_m}$ for a given parcel of interstellar gas of temperature T and density n using Eqs. (8) or (9). Input parameters are the radiation field $\mathrm{G_0}$, metallicity Z, velocity dispersion σ_{vel} and our $\mathrm{H_2}$ formation rate parameter μ. In Fig. 6.1 we have plotted the resulting equilibrium fraction $\mathrm{f_m}$ for a number of typical values of these parameters.

The true equilibrium molecular gas content will most likely be higher than $\mathrm{f_m}$ since the real ISRF incident on GMCs is not radial and thus falls off more rapidly inside the absorbing cloud layers. Higher gas densities that exist deeper in the clouds as part of the considerable spatial and density substructure/clumping observed in the ISM will act to raise the true $\mathrm{f_m}$. In that respect logotropic clouds are more realistic than those with uniform density.

6.2.2 Time-dependence of the HI/H_2 equilibrium

The time dependent HI/$\mathrm{H_2}$ transition can be approximated from the solution of Equation (22) of Goldshmidt & Sternberg (1995), which describes the evolution of the total HI column $\mathrm{N_t r(HI)}$ in the HI→$\mathrm{H_2}$ transition layer of a plane parallel slab of $\mathrm{H_2}$ gas with an impinging dissociating radiation field:

$$\tau_{\mathrm{f}} \frac{\mathrm{d}\sigma \mathrm{N_{tr}(HI,t)}}{\mathrm{dt}} = \mathrm{r_{dis}} \mathrm{e}^{-\sigma \mathrm{N_{tr}(HI,t)}} - \sigma \mathrm{N_{tr}(HI,t)}, \tag{14}$$

where $\tau_{\mathrm{f}} = 1/(2\mathrm{nR_f})$ is the $\mathrm{H_2}$ formation time and the quantity $\mathrm{r_{dis}}$ quantifies the local balance between $\mathrm{H_2}$ dissociation and formation and is given by

$$\mathrm{r_{dis}} = \frac{\mathrm{G_o k_o}}{\mathrm{nR_f}} \Phi = 2.67 \frac{\mathrm{G_o}}{\mu \mathrm{S_H(T_k)}} \left(\frac{\xi_{\mathrm{FUV}}}{\mathrm{ZT_k}} \right)^{1/2} \left(\frac{\mathrm{n}}{50\ \mathrm{cm}^{-3}} \right)^{-1}. \tag{15}$$

The assumption underlying the validity of Eq. (14) is that of an extremely narrow HI/$\mathrm{H_2}$ transition layer, which thus separates the slab into a fully atomic and a fully molecular section. In the case of steady state Eq. (14) reduces to

$$\mathrm{r_{dis}} \mathrm{e}^{-\sigma \mathrm{N_{tr}(HI)}} = \sigma \mathrm{N_{tr}(HI)}, \tag{16}$$

which does not yield $\mathrm{N_{tr}(HI)}$ as expressed in Eq. (4), though solutions of Eq. (16) for $\mathrm{N_{tr}(HI)}$ differ $\lesssim 30\%$. This is not surprising given that Eq. (4) does not involve the approximation of a sharp HI/$\mathrm{H_2}$ transition. It is easy to see at what step of deducing Eq. (4) the assumption of a sharp HI/$\mathrm{H_2}$ transition layer yield the result expressed in Eq. (16). From Goldshmidt and Sternberg (their Equation 2)

$$\mathrm{R_f n dN(HI)} = \mathrm{G_o k_o f[N(H_2)]} \mathrm{e}^{-2\sigma \mathrm{N(H_2)}} \mathrm{e}^{-\sigma \mathrm{N(HI)}} \mathrm{dN(H_2)}. \tag{17}$$

If not much HI exists within the sharp HI/$\mathrm{H_2}$ transition zone to significantly add up to the total HI transition column density we can replace $\mathrm{e}^{-\sigma \mathrm{N(HI)}}$ by $\mathrm{e}^{-\sigma \mathrm{N_{tr}(HI)}}$ The latter is then treated as a constant of integration over the $\mathrm{H_2}$ column density and kept in the right part of the latter equation yielding Eq. (16).

A fully time-dependent treatment of the HI/$\mathrm{H_2}$ transition is conveniently provided by solving Eq. (14) for $\mathrm{A_{FUV}^{(tr)}} = \sigma \mathrm{N_{tr}(HI,t)}$ and finding the corresponding $\mathrm{f_m(t)}$ from Eq. (8). Although the approximation of a narrow transition layer is not strictly valid, the time dependent solution of the full integro-differential equation would be too costly for use in numerical simulations, and also the uncertainties inherent in our model would not justify the additional expense for the more exact solution.

Analytical approximations of time varying H_2 transition

It is interesting to examine approximate analytical solutions, if only for the reason of checking the more general solution of Eq. (14) in limiting cases. This can be done for two particular domains, namely that of rapidly increasing and rapidly decreasing $A_{FUV}^{(tr)}(t)$. For $\tau_f dA_{FUV}^{(tr)}/dt \ll 0$ we can approximate Eq. (14) as

$$\frac{dA_{FUV}^{(tr)}}{dt} = -\frac{1}{\tau_f} A_{FUV}^{(tr)} \Rightarrow A_{FUV}^{(tr)} = A_{FUV}^{(tr)}(0) e^{-t/\tau_f}. \tag{18}$$

In the case of $\tau_f dA_{FUV}^{(tr)}/dt \gg 1$, and thus a decreasing molecular mass fraction, we approximate Eq. (14) as

$$\frac{dA_{FUV}^{(tr)}}{dt} = \frac{r_{dis}}{\tau_f} e^{-A_{FUV}^{(tr)}} = 2G_\circ k_\circ \Phi e^{-A_{FUV}^{(tr)}}, \tag{19}$$

hence

$$A_{FUV}^{(tr)}(t) = \ln\left(e^{A_{FUV}^{(tr)}(0)} + 2G_\circ k_\circ \Phi t\right), \tag{20}$$

which in the case of $R_f = 0$, provides a convenient solution describing the photodestruction of molecular clouds.

The case of logotropic clouds

Eq. (14) is derived under the assumption of the HI/H_2 transition being sharp and under the assumption of a uniform density. In the case of a radial density profile the latter is no longer the case, but the approximation of a sharp HI/H_2 transition can be maintained. In the case of a logotropic density profile the modification of Eq. (14) (or Eq. (22) of Goldshmidt and Sternberg (1995)) turns out to be particularly simple,

$$\frac{1}{2}\frac{dN(HI,t)}{dt} = \frac{G_\circ k_\circ \Phi}{\sigma} e^{-\sigma N(HI,t)} - R_f \int_0^{r_{HI}} n(r) n(HI) dr, \tag{21}$$

where r_{HI} marks the depth of the pure HI layer. Using the relation $n(r) = n_{ex} e^{N(r)/N_\circ}$ ($N_\circ = n_{ex} R$) valid for a logotropic density profile, Eq. 21 eventually yields

$$\tau_f \frac{d\sigma N_{tr}(HI,t)}{dt} = r_{dis} e^{-\sigma N_{tr}(HI,t)} - \sigma N_\circ \left(e^{\sigma N_{tr}(HI,t)/\sigma N_\circ} - 1\right). \tag{22}$$

where τ_f and r_{dis} are calculated with n_{ex}. It can be easily seen that for $N_\circ = n_{ex} R \to \infty$ ($e^{N(HI,t)/N_\circ} \to 1 + N(HI,t)/N_\circ$), signifying a uniform density cloud $n = n_{ex}$ (or one with so large of a radius where the density of outer layers hardly changes), the latter reverts back to Eq. (14). Again we solve for $A_{FUV}^{(tr)} = \sigma N_{tr}(HI,t)$.

For $dA_{FUV}^{(tr)}(t)/dt \gg 0$ the solution of Eq. (22) remains the same as that of Eq. (14) with only $n_{ex} = 2/3\langle n \rangle$ replacing n. So in case of cloud destruction when $R_f = 0$ Eq. (20) again gives the time dependence of the transition layer. In the case of $dA_{FUV}^{(tr)}(t)/dt \ll 0$, Eq. (22) is now approximated by ($A_\circ = \sigma N_\circ$)

$$\tau_f \frac{dA_{FUV}^{(tr)}(t)}{dt} = -A_\circ \left[e^{A_{FUV}^{(tr)}(t)/A_\circ} - 1\right], \tag{23}$$

The solution of this being

$$A_{\rm FUV}^{\rm (tr)}(t) = A_\circ \ln\left[1 + (e^{A_{\rm FUV}^{\rm (tr)}(0)/A_\circ} - 1)e^{-t/\tau_f}\right] \tag{24}$$

The latter equation reduces to Eq. (18) when $N_\circ \to \infty$ ($A_\circ \to \infty$), as expected.

6.2.3 Collisional destruction of H_2 at high temperatures

At high temperatures the above is not a good description to follow the H_2 content. Once the temperature of the gas reaches $T_k \gtrsim 1000$ K, H_2 formation effectively becomes zero (Cazaux & Tielens 2004). Moreover, at high temperatures the cloud scaling laws (and hence the expressions used to estimate f_m) no longer hold since the observed "cloud" line widths would now be mostly thermal and thus no longer scale with size.

For temperatures above $T_k \gtrsim 3 \times 10^3$ K the H_2 fraction will be controlled by collisional destruction processes according to

$$\frac{dn(H_2)}{dt} = -\gamma_1(T_k)n(H_2)n(HI) - \gamma_2[n(H_2)]^2, \tag{25}$$

where $\gamma_1(T_k)$ and $\gamma_2(T_k)$ are the H_2-HI and H_2-H_2 collisional destruction coefficients. Their values can be found in Martin, Keogh, & Mandy (1998) where it can be seen that they are strongly temperature dependent($\propto T^{12}$). Also it turns out that the HI collisions are much more efficient in destroying H_2 than those with H_2 itself.

Indeed $[\gamma_1(T_k)/\gamma_2(T_k)]_{\rm min} = 10$ at $T_k \sim 3 \times 10^4$ K and it is much bigger for lower gas temperatures. Thus for the H_2 collisions to be more important the condition

$$\frac{\gamma_2(T_k)[n(H_2)]^2}{\gamma_1(T_k)n(H_2)n(HI)} > 1 \Rightarrow \frac{n(H_2)}{n(HI)} > \frac{\gamma_1(T_k)}{\gamma_2(T_k)} \gtrsim 10. \tag{26}$$

must be satisfied. In the WNM gas phase such a high percentage of remaining H_2 (remaining from the dominant FUV destruction mechanisms operating in the CNM, CNM-to-WNM phases) is unlikely. We thus consider only the HI collisional destruction term as important and then Eq. (25) becomes

$$\frac{dn(H_2)}{dt} = -\gamma_1(T_k)\left[n - 2n(H_2)\right]n(H_2), \tag{27}$$

where $n = n(HI) + 2n(H_2)$ is the total density. Solving the latter eventually yields

$$f_m(t) = \frac{2n(H_2)}{n} = \frac{m_\circ e^{-n\gamma_1(T_k)t}}{1 - m_\circ e^{-n\gamma_1(T_k)t}}, \ \text{where} \ m_\circ = \frac{f_\circ}{1 - f_\circ}. \tag{28}$$

The value $f_\circ$ is the last value that f_m has before conditions change so that we switch to Eq. (28) to describe the evolving HI/H_2 equilibrium. Here we must mention that we assumed that in the WNM phase there is no FUV-induced HI/H_2 spatial segregation. If there is some remnant spatial segregation H_2 would be destroyed by the much less effective H_2 collisions, thus our assumption may somewhat overestimate the level of collisional H_2 destruction.

We now have all ingredients to build a H_2 formation module into numerical code for the simulation of the ISM of galaxies. Given the local conditions in the ISM we can follow the HI/H_2 transition using Eqs (14) or (22) for gas with $T < 1000$ K. Above 1000 K, it is $\mathrm{R_f} = 0$ and in this case these equations describe the photo-destruction of clouds. For $\mathrm{T} > 3000$ K, Eq. (28) is used as a rough approximation of the collisional destruction process. We have implemented a module using the above prescription in an N-body/SPH code that includes a detailed model for the neutral phases. We will estimate the local H_2 content using a sub-grid model calculating the solution to the time dependent Eq. (14) at every particle position in our simulation. Before we detail the precise algorithm we will first give some background of the code.

6.3 Implementation

The code we use is an N-body/SPH code for the simulation of galaxy sized objects. Details of the code are explained in previous chapters. Here we will use the complete model for the ISM described in Chapter 2 ("model D"). The main features of the code that make it especially attractive to follow the formation and destruction of molecular gas is the fact that our code includes an extensive ISM model as well as star formation and feedback. The ISM model lets the gas cool down to temperatures of $\mathrm{T} \leq 100$ K and the densities that are reached are of order $\mathrm{n} \approx 100$ cm^{-3}. As we will discuss below this is just the ISM phase we expect the transition to molecular gas to occur.

N-body/SPH codes are in routine use within the astrophysical community as tools to explore problems of galaxy evolution and formation and a description of this method can be found elsewhere (Hernquist & Katz 1989, Monaghan 1992). We use the conservative SPH formulation of Springel & Hernquist (2002). We employ a model for the WNM and CNM that was extended from Gerritsen & Icke (1997) and Bottema (2003). We will summarise the most important features here.

6.3.1 Neutral ISM model

Our model for the ISM is similar to the equilibrium model for the CNM and WNM of Wolfire et al. (1995, 2003). We solve for the ionization and thermal evolution of the gas including the various processes given in Table 6.1. An overview of the ISM model is given in Fig. 6.2, where we have plotted the equilibrium temperature, ionization fraction and pressure as a function of density. The plots in this figure show that as density varies, the equilibrium state of the gas changes from a high temperature/high ionization state ($\mathrm{T} = 10^4$ K, $\mathrm{x_e} \approx 0.1$) at low densities, to a low temperature/low ionization state ($\mathrm{T} < 100$ K, $\mathrm{x_e} < 10^{-3}$) at high densities. In between there is a density domain where the negative slope of the P-n relation indicates that the gas is unstable to isobaric pressure variations, the classic thermal instability (Field 1965). The shape of these curves and hence the exact densities of the thermal instability vary locally throughout the simulation under the influence of the local time-varying UV radiation field and supernova heating. We assume a constant cosmic ray ionization rate ζ_{CR} throughout the galaxy. We take a value of $\zeta_{\mathrm{CR}} = 3.6 \times 10^{-17}$ s^{-1}.

The FUV luminosities of the stellar particles, which are needed to calculate the local FUV field used in the photoelectric heating and that also will be used to calculate

Table 6.1: Overview of the processes included in the ISM model used. For H and He ionization equilibrium is explicitly calculated, for other elements collisional ionization equilibrium (CIE) is assumed. references: 1) Wolfire et al. 1995, 2) Raga et al. 1997 , 3) Verner & Ferland 1996, 4) Silva & Viegas 2001

process	comment	ref.
heating		
Cosmic Ray	ionization rate $\zeta_{\rm CR} = 3.6\ 10^{-17}\ {\rm s}^{-1}$	1
Photo Electric	FUV field from stars	1
cooling		
e, $\rm H_0$ impact	H,He,C,N,O,Si,Ne,Fe	2,4
ionization		
& recombination		
UV	ionization assumed for species with $E_i < 13.6$ eV	
Cosmic Ray	H, He only; primary & secondary ionizations	1
Collisional	H, He only	3
Radiative recombination	H, He only	3
CIE	assumed for metals	

$\rm H_2$ destruction, are derived from Bruzual & Charlot (1993, and updated) population synthesis models for a Salpeter initial mass function (IMF) with cutoffs at $0.1\ \rm M_\odot$ and $100\ \rm M_\odot$. In the present work we do not account for dust extinction of UV light, except for the fact that young stars are shrouded in their natal cloud: for young stellar clusters we decrease the amount of UV extinction from 75% to 0% in 4 Myr (Parravano et al. 2003).

6.3.2 Star formation and feedback

The coldest and densest phase in our model is best identified with the CNM, where giant molecular clouds are embedded and form. We use a simple prescription for star formation, based on the assumption that star formation is governed by the gravitational stability in the GMCs. A region is considered unstable to star formation if the local Jeans mass $\rm M_J$ is smaller than a reference mass $\rm M_c$. The rate of star formation is set to scale with the local free fall time:

$$\tau_{\rm sf} = {\rm f_{sf}} {\rm t_{ff}} = \frac{\rm f_{sf}}{\sqrt{4\pi {\rm G}\rho}} \tag{29}$$

The delay factor $\rm f_{sf}$ is uncertain, as we will discuss below this factor may influence the amount of $\rm H_2$ formed. We will take values ranging from $\rm f_{sf} = 2.5 - 20$. The actual efficiency of star formation is then determined by the balance between the cooling of the gas and the UV and SN heating. Note that our star formation does not depend on the formation of molecular gas. This is reasonable as in this picture star formation is a process associated with collapse through self-gravity and, though in practice always

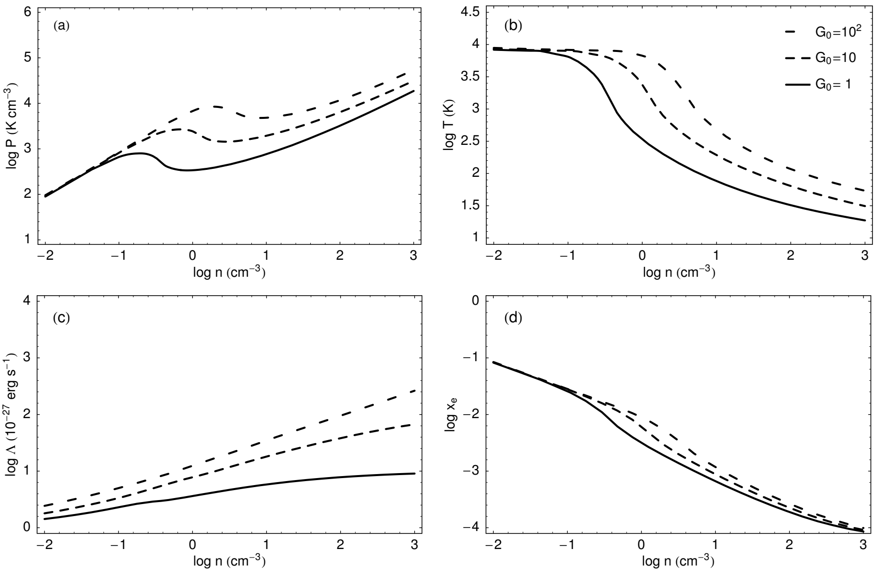

Figure 6.2: Overview of the ISM model: Equilibrium plots of (a) pressure P, (b) temperature T, (c) cooling rate Λ and (d) electron fraction $\mathrm{x_e}$ as a function of density n for three different values of the UV field $\mathrm{G_0}$ (given in units of 1.6×10^{-3} erg cm^{-2} s^{-1})

related to H_2 formation, it is independent of the gas phase. A "sanity" check on our model is thus simply to see if substantial star formation happens in regions with low H_2 content.

Feedback from stellar winds and supernovae is essential for regulating the ISM. While the mechanical energy output of stars is reasonably well known, it has proven to be difficult to include it completely self-consistently in galaxy sized simulations of the ISM. The reason for this is that the effective energy of feedback depends sensitively on the energy radiated away in thin shells around the bubbles created. This will mean that the effect of feedback is not reliable unless prohibitively high resolution is used. In SPH codes there have been conventionally two ways to account for feedback: by changing the thermal energy input and by acting on particle velocities. Both are unsatisfactory, as the thermal method suffers from over cooling (Katz 1992) and the kinetic method seems to be too efficient in disturbing the ISM (Navarro & White 1993). Here we use a new method based on the creation at the site of young stellar clusters of a *pressure particle* that acts as a normal SPH particle in the limit of the mass of the particle $\mathrm{m} \rightarrow 0$, for constant energy. For the energy injection rate we take $\dot{\mathrm{E}} = \epsilon_{\mathrm{sn}} \mathrm{n_{sn}} \mathrm{E_{sn}}/\Delta \mathrm{t}$, with $\mathrm{E_{sn}} = 10^{51}$ erg, $\epsilon_{\mathrm{sn}} = 0.1$, $\mathrm{n_{sn}} = 0.009$ per $\mathrm{M}_\odot$ and $\Delta \mathrm{t} = 3 \times 10^7$ yr. The efficiency ϵ_{sn} thus assumes that 90% of the energy is radiated away, a value which comes from more detailed simulations of the effect of supernova and stellar winds on the ISM (Silich et al. 1996), and is also used in other simulations of galaxy evolution (e.g. Semelin & Combes 2002, Springel & Hernquist 2002, Buonomo et al. 2000). The feedback model is explained in more detail in chapter 3.

6.3.3 H_2 formation

For our H_2 formation model we follow the same philosophy as for the star formation model: unresolved structure is assumed to be present at the SPH particle positions. In this case the underlying cloud structures are assumed to conform to the relation (12) for the mean cloud extinction, derived from the observed density/size scaling relation (10). However, this equation is not expected to be valid everywhere in our simulation domain. Regions where Eq. (10) will fail are those with low density and pressure. In those regions our algorithm as detailed in section 6.2 will not give sensible outcomes. To be specific, if pressure is low, Eq. (10) predicts very large cloud sizes, such that the resulting photo-destruction of H_2 proceeds very slowly. To circumvent this problem we modify Eq. (10) for pressures below $\mathrm{P_{trans}}$:

$$\langle \mathrm{n} \rangle = \mathrm{n_\circ} \left(\frac{\mathrm{P_{trans}/k_B}}{10^4 \ \mathrm{K\ cm^{-3}}} \right)^{-1/2} \left(\frac{\mathrm{P_e/k_B}}{10^4 \ \mathrm{K\ cm^{-3}}} \right) \mathrm{R_{pc}^{-1}}, \tag{30}$$

where we take $\mathrm{P_{trans}} \approx 1000\ \mathrm{K\ cm^{-3}}$. This is just a convenient patch, which however in low pressure environments does scale the "clouds" according to the $\mathrm{n_{ex}} \propto \mathrm{P_e}$ scaling appropriate for diffuse clouds (Elmegreen 1993), and with this minor modification we can apply the sub-grid model to all ISM conditions.

For the macroscopic pressure $\mathrm{P_e}$ that enters in Eq. (12) we need the local velocity dispersion σ_{vel}. For this velocity dispersion we take the formal SPH estimate

$$\sigma_{\mathrm{j}}^2 = \sum_{\mathrm{i}} \frac{\mathrm{m_i}}{\rho_{\mathrm{j}}} (\mathrm{v_i} - \langle \mathrm{v} \rangle_{\mathrm{j}})^2 \mathrm{W}(|\mathrm{r_{ij}}|, \mathrm{h_j}) \tag{31}$$

with $\mathrm{v_i}$ and $\mathrm{m_i}$ the particle velocities and masses, $\langle \mathrm{v} \rangle_{\mathrm{j}}$ the local bulk velocity. A number of subtle issues are connected with the choice of the dispersion. Eq. (31) describes the interparticle velocity dispersion, while the dispersion that enters in the pressure (13) is really an inter-cloud velocity dispersion. Even if we assume these to be equivalent, the problem remains that Eq. (31) samples a velocity dispersion on scales of the smoothing lengths $\mathrm{h_i}$. We can try to account for this by scaling σ_{j}, using for example the relation for Kolmogorov turbulence,

$$\sigma'_{\mathrm{j}} = \sigma_{\mathrm{j}} \left(\frac{\mathrm{h_j}}{\mathrm{R_{cloud}}} \right)^{-1/3}, \tag{32}$$

but in practice this has very little influence on H_2 formation.

Depending on the cloud model assumed, Eq. (14) or (22) then describes the evolution of the HI layer during a simulation time step dt, given an initial $\mathrm{A_{FUV}^{(tr)}}$. The density that enters is assumed to be the mean density $\langle \mathrm{n} \rangle$ given by the SPH density at the particle position, and the temperature the particle temperature (both taken constant for the time step). The radiation field is calculated from the distribution of stars, where the assumption is that extinction from dust, or from molecular clouds is not important (apart from extinction from the natal cloud). After we have evolved the transition $\mathrm{A_{FUV}^{(tr)}}$ for the time step dt the resulting $\mathrm{f_m}$ (Eqs (8) and (9)) is calculated and assigned to the SPH particle for the duration of the next time step (where it can be used to calculate for example cooling). At the next time step this value is retained and used to calculate the initial $A^{(tr)}_{FUV}$, given the new average cloud extinction $\langle A_v \rangle$. The $\langle A_v \rangle$ may have changed from the previous time step, if for example the pressure P_e has changed. The choice to keep f_m constant rather than $A^{(tr)}_{FUV}$ is dictated by H_2 mass conservation, and the decision to assign all variations of f_m to the time varying UV field.

6.4 Application to a dwarf galaxy model

Our first application and test of the H_2 formation model will be a model for a dwarf irregular galaxy. There are a number of practical reasons to choose this type of system as a test model, as well as some interesting questions particular to the H_2 gas presence in dwarf galaxies that can be explored using our model.

Firstly, the small sizes of these systems allow relatively high resolution with modest computational effort. In our present work the choice of dwarf galaxies as modelling templates allows a given numerical simulation to probe small physical scales and high gas densities, the latter being of crucial importance if the HI→H_2 phase transition is to be incorporated successfully. Insight gained from simulating these systems, whose properties are constrained by a wealth of observational data (e.g. van Zee 2001; Barone et al. 2000; de Paz et al. 2003), furthermore it holds the promise of yielding good constraints about physical processes that are expected to be universal in galaxies (as we have done for SN feedback strength; see Pelupessy et al. 2004).

Aside from being excellent testbeds for quantifying phenomena expected to be common across the Hubble sequence, dwarf galaxies are important systems on their own right because of their crucial role in current galaxy formation theories as the building “blocks” of larger systems (Kauffmann, White, & Guiderdoni 1993), and as major “polluters” of the intergalactic medium with metals (Ferrara & Tolstoy 2000).

6.4.1 Simulation setup

We construct a simple model of a dwarf irregular with gas mass of $M_{gas} = 10^8\ M_\odot$ and a stellar mass of $M_{star} = 10^8\ M_\odot$. The dark halo is constructed with a flat core, in agreement with Burkert (1995).

Specifically, the gas disk has radial surface density profile

$$\Sigma = \Sigma_g/(1 + R/R_g), \tag{33}$$

with central density $\Sigma_g = 10\ M_\odot/pc^2$ and radial scale $R_g = 0.33$ kpc, truncated at 4 kpc. An exponential stellar disk,

$$\rho_{disk}(R, z) = \frac{\Sigma_0}{2h_z} \exp(-R/R_d) \mathrm{sech}^2(z/h_z) \tag{34}$$

with central surface density $\Sigma_0 = 300\ M_\odot/pc^2$, $R_d = 0.5$ kpc and vertical scale height $h_z = 0.2$ kpc, is constructed as in Kuijken & Dubinski (1995). The ages of the initial population of stars are distributed according to a constant SFR and an age of 13 Myr.

We take a halo profile

$$\rho_{\mathrm{halo}}(\mathrm{r}) = \rho_0 \frac{\exp(-\mathrm{r}^2/\mathrm{r}_\mathrm{c}^2)}{1+\mathrm{r}^2/\gamma^2} \tag{35}$$

with core radius $\gamma = 2$ kpc, cutoff radius $\mathrm{r_c} = 20$ kpc and central density $\rho_0 = 2 \times 10^7\ \mathrm{M}_\odot/\mathrm{kpc}^3$, for a total mass of $\mathrm{M_{halo}} = 15 \times 10^9 \mathrm{M}_\odot$ and a peak rotation velocity of about 50 km/s. We represent the dark halo by a static potential.

6.4.2 Practical considerations

For H_2 to be able to form in the simulation two requirements must be met: we must probe in our simulation the gas densities where H_2 is expected to form, and at these densities stars must not form before H_2 has had a chance to form, as star formation will inhibit H_2 formation by irradiating and heating the gas. We can derive some minimum requirements in order for our model to be able to follow the HI→H_2 transition as well as some constraints on the $\mathrm{f_{sf}}$ star formation parameter. In addition, it may be necessary to consider the effect of H_2 cooling.

The necessary resolution, the choice of $\mathrm{M_{ref}}$

Simulations of self-gravitating fluids done with insufficient numerical resolution can suffer from artifacts: artificial clumping or inhibition of gravitational collapse may occur. For SPH simulations including self-gravity these effects can arise if the local Jeans mass is not resolved (Bate & Burkert 1997, Whitworth 1998). Hence, this requires for our simulation that

$$\mathrm{M_J} \equiv \frac{\pi\rho}{6}\left(\frac{\pi \mathrm{s}^2}{\mathrm{G}\rho}\right)^{3/2} > \mathrm{N m_{SPH}}, \tag{36}$$

with s the sound speed, N the number of SPH neighbours and $\mathrm{m_{SPH}}$ is the particle mass. For our simulation, this requirement is met by a choosing the parameters of our star formation recipe such that violation of (36) is precluded by star formation. A gas particle will spawn star particles, and thus be subjected to heating that raises its Jeans mass, if $\mathrm{M_J} < \mathrm{M_{ref}}$. Taking $\mathrm{M_{ref}} \approx \mathrm{N m_{SPH}}$ the particle mass $\mathrm{m_{SPH}}$ will then determine the densities probed by the simulation. In figure 6.1 we can see that densities in the order of $50 - 100\ \mathrm{cm}^{-3}$ are sufficient to follow the HI→H_2 transition, while somewhat higher densities may be necessary for low metallicity gas. For such densities and typical CNM temperatures of 100 K Eq (36) corresponds to a Jeans mass of $\approx 10^4 \mathrm{M}_\odot$, well below the typical GMC mass scales. Hence, running the simulation with particle masses of $\mathrm{m_{SPH}} \approx 500 \mathrm{M}_\odot$ allows a good resolution of the aforementioned mass scale.

The choice of $\mathrm{f_{sf}}$: the role of H_2 and star formation

In our star formation recipe the delay for star formation to occur is set by the free parameter $\mathrm{f_{sf}}$. We will examine various values for this parameter and its effect on H_2 formation. It may seem somewhat odd that this parameter could determine whether

H_2 formation can happen, normally one views H_2 formation as a prerequisite for star formation, but remember that in our simulation these two are not causally linked.

We can use the timescale for the formation of H_2 along with the well-established empirical fact that everywhere in the local Universe stars seem to form out of molecular clouds rather than atomic gas to deduce a lower limit on the value of $\mathrm{f_{sf}}$. For H_2 formation to remain always ahead of star formation it must be $\tau_{\mathrm{f}}(\mathrm{H_2}) \leq \tau_{\mathrm{sf}}$, which from Eqs 2 and 29 becomes,

$$\mathrm{f_{sf}} \gtrsim 5.33 \left(\frac{\langle \mathrm{n} \rangle}{\mathrm{cm^{-3}}}\right)^{-1/2} \left(\frac{\mu \mathrm{Z}}{3.5}\right)^{-1} \left[\frac{(1+\mathrm{T}/100\ \mathrm{K})^2}{(\mathrm{T}/100\ \mathrm{K})^{1/2}}\right]. \tag{37}$$

Since CNM HI gas is the most likely precursor phase of the H_2 gas, for typical CNM conditions of $\mathrm{T_k} \sim (100-200)$ K and $\langle \mathrm{n} \rangle \sim (10-50)\ \mathrm{cm^{-3}}$, the latter equation yields $\mathrm{f_{sf}} \gtrsim 3-10$. These values are roughly similar to those deduced using the constraints on the observed star formation rate in the Galaxy. Given the uncertainties inherent in e.g. the $\mathrm{S_H}(\mathrm{T_k})$ function, such a rough agreement is noteworthy and here it is worth mentioning that $\tau_{\mathrm{f}}(\mathrm{H_2})$ is also a good approximation of chemical equilibrium timescales in FUV-illuminated clouds (e.g. Hollenbach & Tielens 1999). Thus the rough agreement of the constraint set by Eq. 37 with what are considered reasonable $\mathrm{f_{sf}}$ values may signify an important role for cloud chemistry in setting the average star formation rate. This is not far-fetched since molecule formation enables totally different cooling functions for the gas and thus drastically alters its thermodynamic state allowing to eventually cool and fragment further (e.g. Chièze & Pineau des Forêts 1987).

Cooling by H_2

A recent calculation of the cooling by H_2 was done by Le Bourlot et al. (1999). At high and intermediate temperatures ($1000-8000$ K) H_2 is a more efficient coolant than the major coolants of atomic gas (C and Fe). Hence even a low (10^{-4}) remnant abundance of molecular gas in the diffuse WNM can have an impact on the cooling at high temperatures. Indeed some people have included H_2 cooling in their cooling curves, but without calculating the abundance of molecules (Carraro et al. 1998). Admittedly our accuracy in following the amount of warm molecular gas is limited, but to get some idea of the possible effect of this warm molecular gas it is nevertheless interesting to do some calculations including H_2 cooling. For this we use the Le Bourlot cooling curve, where we use a limited set of data (low density limit, constant ortho to para ratio, only H_2-H collision excitation), appropriate for our purposes. Note that some observations find abundances of H_2 gas the order of $10^{-4}-10^{-3}$ in diffuse HI gas, even in regions of the ISM hostile to H_2 formation, like galactic high velocity clouds (Richter et al. 2001).

6.5 Results for the dwarf galaxy model

In a model that incorporates H_2 formation the two most important parameters that should be explored are the formation rate μ and the metallicity Z. The formation rate is uncertain by a factor of 5-10, and this obviously introduces some uncertainty in the

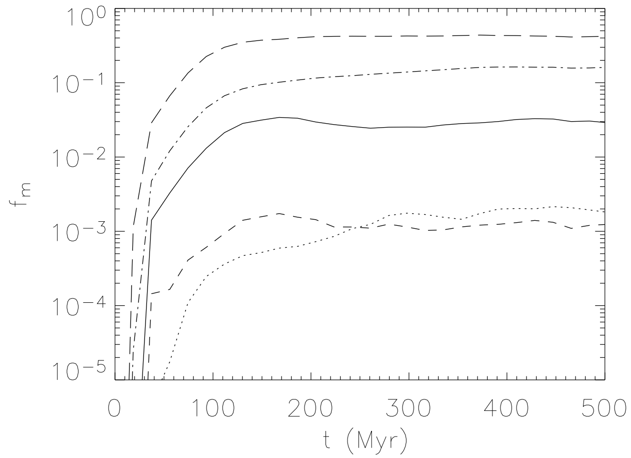

Figure 6.3: H_2 fraction. The lines indicate the time dependence of the molecular fraction f_m for different values of Z and μ. With, from top to bottom, **long-dashed line:** $\mu = 17.5, Z = Z_\odot$, **dash-dotted line:** $\mu = 17.5, Z = Z_\odot/5$, **drawn line:** $\mu = 3.5, Z = Z_\odot$, **Dashed line:** molecular fraction f_m for $\mu = 3.5, Z = Z_\odot/5$, and **Dotted line:** $\mu = 3.5, Z = Z_\odot/5$ with logotropic clouds. Simulations are started with $f_m = 0$.

theoretically calculated H_2 content. For high formation rates large amounts of warm and diffuse H_2 may be present in the outer parts of spiral galaxies (Papadopoulos et al. 2002). Metals play an important role: the H_2 formation rate is directly proportional to the dust surface available, and we take this surface to be proportional to Z. Dust also plays an important role shielding molecules from UV radiation. Observations of low metallicity systems, like dwarf irregulars, using CO as a tracer give low molecular gas contents (e.g. Barone et al. 2000). However, the interpretation of these observations are complicated by the fact that the conversion factor from CO flux to H_2 mass under these conditions may not be reliably known: for low metallicity environments not enough C may be present to build self-shielding CO cores (Israel 1997).

Hence, we explore a small 2x2 grid of models using a formation rate of $\mu = 3.5$ and $\mu = 17.5$, and metallicities of either $Z = Z_\odot/5$ or $Z = Z_\odot$. Note that for our model dwarf galaxy the high metallicity is somewhat unrealistic, because normally dwarf galaxies have lower metal content. We included this to explore H_2 formation under conditions more pertinent to other systems. Note also that for simulations without H_2 cooling our sub-grid model only follows the H_2 content as a passive tracer of the history of the local conditions, thus the simulations for high and low formation rate will be identical except for the amount of H_2.

6.5.1 Spatial and temporal distribution of H_2 gas

We start the simulation with a gas disk that has a temperature of $T \approx 8000$ K, and with a molecular fraction $f_m = 0$. After the start of the simulation the gas cools and collapses on itself in the z-direction, forming regions of cold and dense gas in the

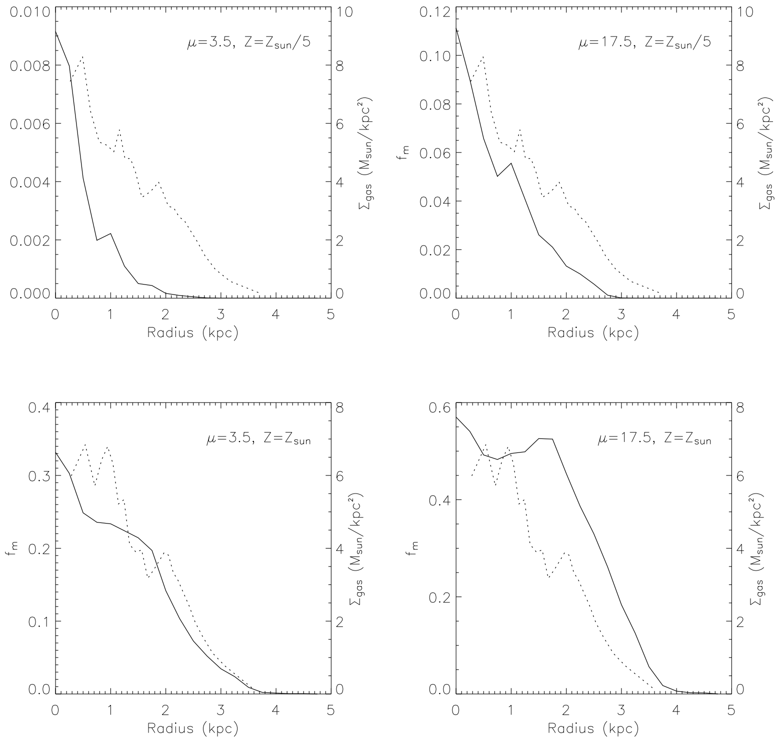

Figure 6.4: Radial dependence of the molecular fraction. **Drawn line:** mean molecular fraction as a function of radius (scale on left y-axes), and **dotted line:** total gas surface density (scale on right y-axes). Note that the y-axis scales are not the same for the different panels.

midplane. There, H_2 starts to form and after some time star formation starts taking place as well. An equilibrium fraction of H_2 is reached (Fig. 6.3) on a timescale of $\approx 50 - 100$ Myr. This agrees with our earlier estimate of Eq. (2). For this model galaxy, the mean star formation rate (SFR) is about $\mathrm{SFR} = 0.002\ \mathrm{M_\odot/yr}$ for low Z and $\mathrm{SFR} = 0.003\ \mathrm{M_\odot/yr}$ for high Z, with modest variations that cause some variations in f_m, visible also in Fig. 6.3.

Furthermore we see that, as expected, the low μ/ low Z simulation has the lowest equilibrium molecular fraction of about $f_m = 0.001$. A higher formation rate μ will boost that to $f_m = 0.03$ for $\mu = 17.5$. For high metallicities, molecular fractions of $f_m = 0.17$ ($\mu = 3.5$) and $f_m = 0.4$ ($\mu = 17.5$) form. Also drawn in Fig. 6.3 is time dependence of the molecular fraction for a low μ/low Z simulation with logotropic clouds. As can be seen the difference between constant density and logotropic clouds is not very large, certainly smaller than the differences due to the formation rate parameter (this is also evident in the equilibrium f_m shown in the panels in Fig.6.1, where the main difference between constant density and logotropic clouds was that for logotropic clouds small fractions f_m remain at low densities).

In Figs. 6.4 and 6.5 we have plotted the (mean) molecular fraction as a function

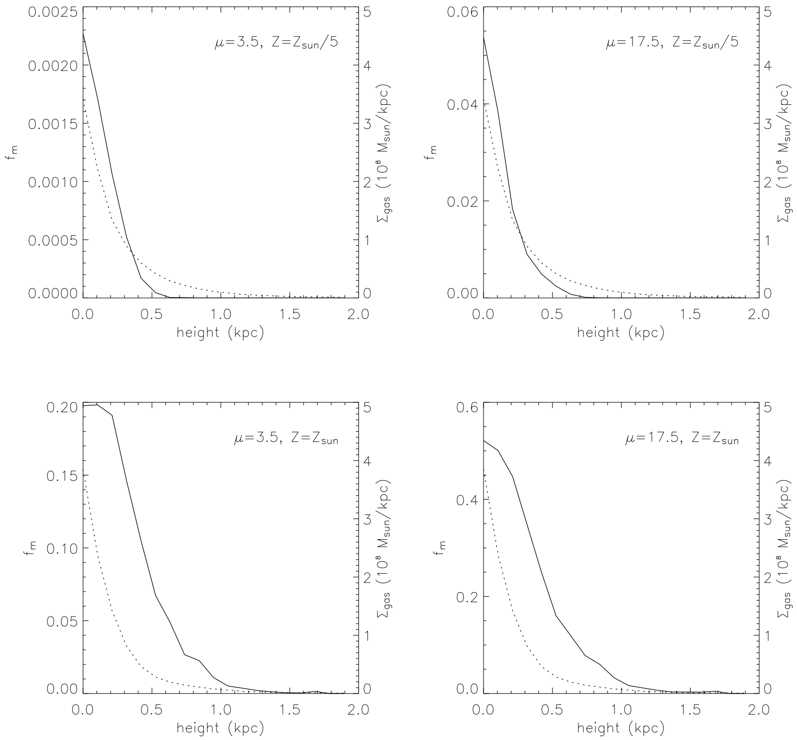

Figure 6.5: z-Height dependence of the molecular fraction. **Drawn line:** mean molecular fraction as a function of height above the disk plane (scale on left y-axes), and **dotted line:** total gas mass distribution (scale on right y-axes). Note that the y-axis scales are not the same for the different panels.

of radius and height above the disk-plane for the four simulations. We see that, as expected, molecules form mostly in the central regions and in the midplane. Note also that for high metallicity and high formation rate the molecular fraction seems to have a tendency to "saturate" in the central regions at a fixed value, in this case $f_m = 0.6$.

Looking in more detail at the spatial distribution of H_2, Fig. 6.6, we see that H_2 is concentrated in the dense clumps and filaments of the HI distribution. Note also that if we compare the low and high μ simulations, we see that the distribution is similar: *the uncertainty in the formation parameter is mainly an uncertainty in the amount of H_2 formed, not in the locations of H_2 formation*. The relative distribution of H_2 is represented by our simulation, but the exact amount of H_2 is more difficult to determine exactly, as this depends on the formation rate parameter (as we will discuss further on, comparison with observations to constrain μ is not straightforward). If we look at the high metallicity simulations, we can see that, apart from the clumpy distribution there is also a sizable mass of "diffuse" H_2, where H_2 is more widespread, but still mainly confined to gas filaments.

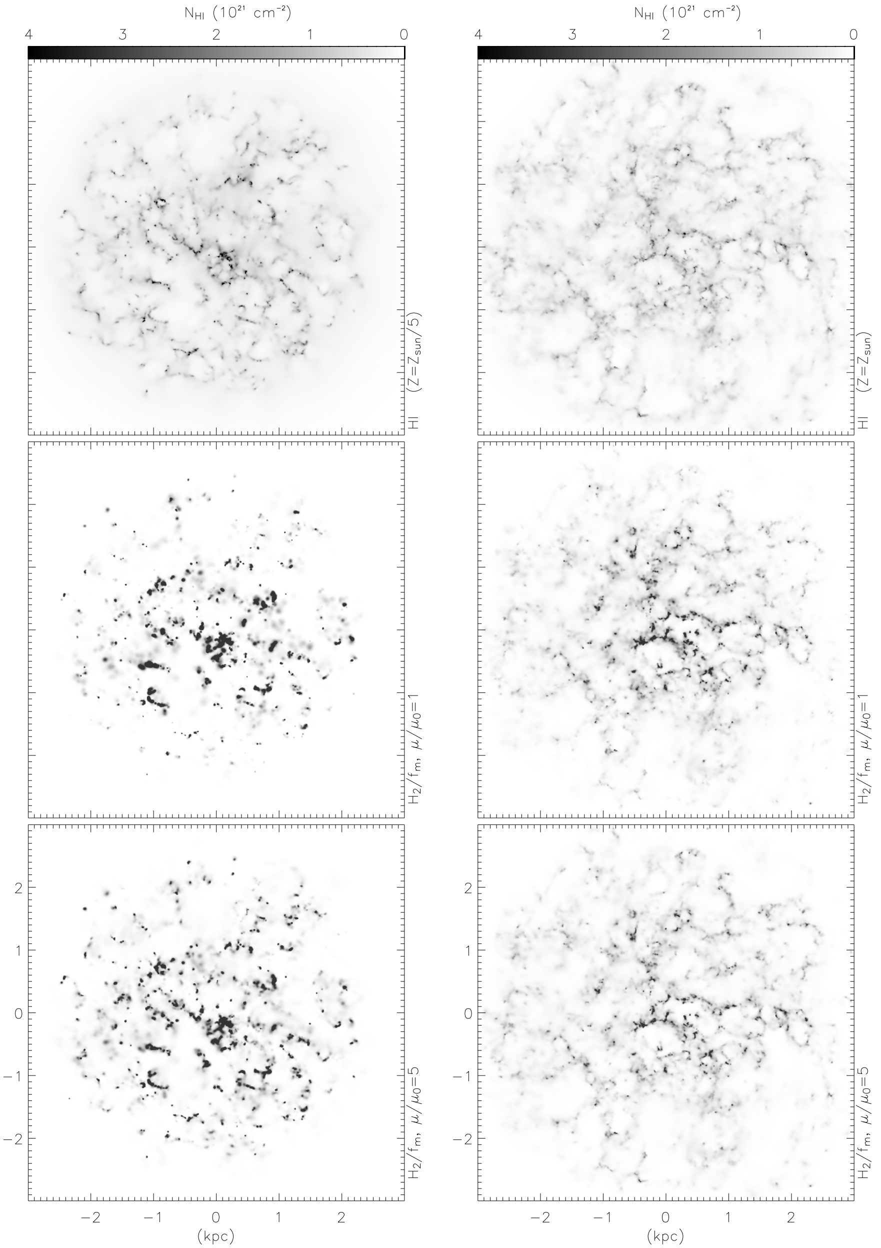

Figure 6.6: HI and H_2 maps. **Left panels:** results for $Z = Z_\odot/5$, **right panels:** $Z = Z_\odot$. Shown are, from top to bottom, the HI distribution, the H_2 distribution for $\mu = 3.5$ and for $\mu = 17.5$. The HI maps of low and high μ simulations are very similar, shown are only the maps for $\mu = 3.5$. The H_2 maps have been divided by the global molecular fraction such that the differences with the HI distribution can be seen more clearly.

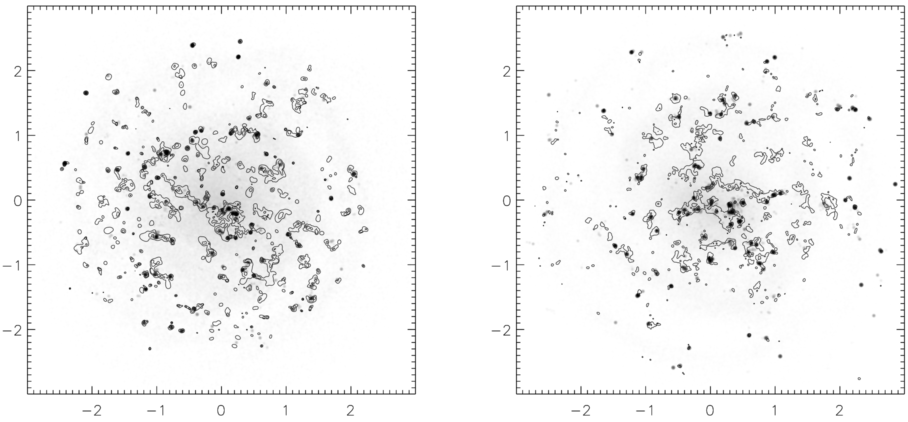

Figure 6.7: Hα and H$_2$: simulated Hα maps (greyscales) with H$_2$ contours. Left panel shows the maps for the $Z = Z_\odot/5$, $\mu = 3.5$ simulation (contours at column densities of $N_{HI} = 2\times10^{19}$ and 10^{20} cm^{-2}) while the right panel shows the $Z = Z_\odot$, $\mu = 17.5$ run (contours at column densities of $N_{HI} = 2 \times 10^{20}$ and 10^{21} cm^{-2}).

Finally we look at the relation between star formation and H$_2$. In Fig. 6.7 we have plotted a simulated map of "Hα" (actually a map of the luminosity of the stars in ionizing photons), overplotted with contours of H$_2$ gas. The contours are chosen such that the plots show the relation of star formation with the densest parts of the H$_2$ distribution. As can be seen star formation is almost always associated with some nearby complex of H$_2$ gas, while some H$_2$ clumps do not show Hα emission, these have not yet formed stars.

6.5.2 The influence of the collapse time

Apart from the parameters directly related to H$_2$ formation, f_m will also depend on the delay factor f_{sf}. As discussed in section 6.3.2, this parameter accounts for the fact that a region unstable to star formation does not collapse in the free-fall time τ_{ff}. The fact that we have time-dependent H$_2$ formation means that the total amount of H$_2$ is sensitive to the time regions stay in a cold and dense phase conducive to molecule formation. Indeed, comparing models run with different values for f_{sf}, we see that the total amount of molecular gas is strongly dependent on this parameter (Fig. 6.8). In our model the formation of stars and the formation of molecules are in competition. Thus we cannot make the delay factor too small as this would completely quench molecule formation. As we discussed in section 6.4.2, the chosen typical values of f_{sf}, as constrained by the observed H$_2$ mass in GMCs and the star formation rate in e.g. the Galaxy, satisfy Eq. 37 and thus H$_2$ formation always precedes star formation.

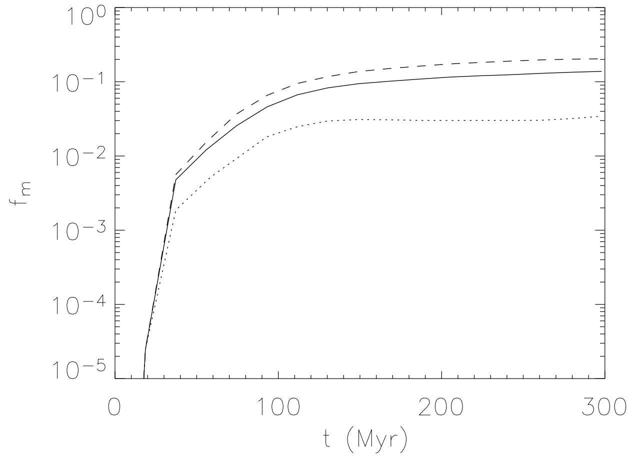

Figure 6.8: H_2 fraction vs time for simulations with different f_{sf}. **Dotted line:** $f_{sf} = 2.5$, **drawn line:** $f_{sf} = 10$, **dashed line:** $f_{sf} = 20$ (for all three: $\mu = 3.5$ and $Z = Z_{\odot}$).

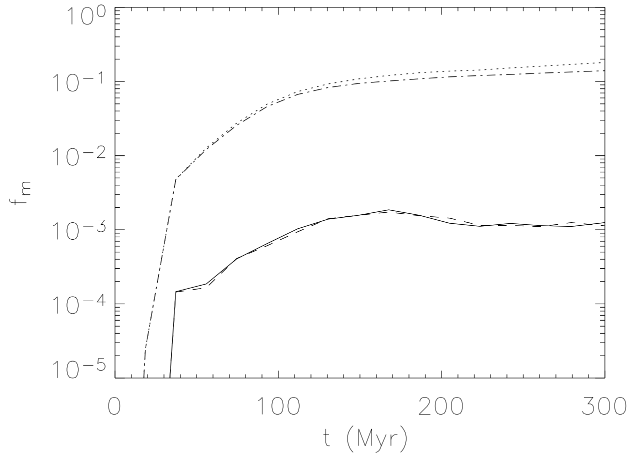

Figure 6.9: H_2 fraction vs time for simulations with cooling. **Drawn line:** $Z = Z_{\odot}/5$, **dashed line:**$Z = Z_{\odot}/5$ with H_2 cooling, **dash-dotted line:** $Z = Z_{\odot}$ and **dotted:** $Z = Z_{\odot}$ with H_2 cooling. For all: $\mu = 3.5$.

6.5.3 Simulations with H_2 cooling

The inclusion of the cooling by H_2 affects the simulation in a number of ways. As an extra coolant it will increase the amount of gas in a cold state. This in turn will increase the formation of H_2. However, star formation may also increase, and thus also the UV field. In Fig. 6.9 the effect of cooling on f_m is illustrated for the $\mu = 3.5$ simulations . As can be seen, cooling has only some influence for the high Z simulation. For the low Z simulation the molecular fractions are too low to substantially alter the results. Note that while H_2 is a strong coolant at high temperatures (of a few thousand K), where it will dominate the cooling for $f_m > 0.001$, the effect of the extra cooling is limited because of the small amount of gas at these temperatures.

6.5.4 Discussion

Detection and mapping of the molecular component of dwarf galaxies is usually done by mapping of the $^{12}CO(J = 1 \rightarrow 0)$ line (e.g. Barone et al. 2000, Mizuno et al. 2001) or by UV absorption studies (Tumlinson et al. 2002). The derived H_2 fractions are in the order of 1-10 percent, but for low metallicity systems CO is often not detected giving only upper limits for the molecular fraction in the order of a percent. A direct comparison with our simulations must be made cautiously because our simulations do not follow the formation of CO, in fact we cannot probe the state of gas where the formation of CO will take place, because of the high densities and low temperatures needed. Hence we cannot determine CO luminosity directly, although in principle empirical relations for the ratio M_{H_2}/L_{CO}, the so-called X_{CO} factor, as a function of G_0 and Z could be used to derive expected CO brightness distributions (Israel 1997). Nonetheless, the molecular fractions we derive seem to be reasonable, although for low μ/ low Z the derived fraction of f_m is rather low. This could indicate that a higher formation rate is likely. The molecular fraction may increase somewhat for a simulation run at higher resolution, because in metal poor environments the HI→H_2 transition is taking place above $n = 100$ cm^{-3}, this can increase f_m by a factor 2-5.

For the galaxy models run with high metallicity and/or formation rate we find quite substantial fractions of H_2, of $f_m = 0.17 - 0.4$. However we also find suprisingly high values, $f_{H_2} \approx 0.001 - 0.01$, of the diffuse warm neutral medium to be molecular. To illustrate this we have plotted in Fig.6.10 the molecular fraction as a function of total column density for a face-on projection. There is a clear column density threshold for the presence of H_2 for the low metallicity simulation. For high metallicity even low column density regions (which are also of low density and high temperature) show fractions of $f_{H_2} \approx 0.001 - 0.01$. We can compare this to studies done with the Far Ultraviolet Spectroscopic Explorer (Tumlinson et al. 2002), where typical upper limits of $f_m \leq 10^{-6}$ are found for such low column density regions. Furthermore the state of the gas (low density, high temperature) is also not typically associated with the presence of such quantities of molecular gas. There is no - or very little - formation of molecular gas going on in this gas phase and any H_2 present should dissociate. In fact, destruction is taking place in the simulation, but the timescales of destruction are quite long. For the thermal dissociation this is due to the low density of the gas: for temperatures of $T = 5000$ K and density of $n_H = 0.3$ cm^{-3} the collisional destruction timescale (for neutral gas) is still $\tau_{col} \approx 10^8$ yr. Furthermore, for

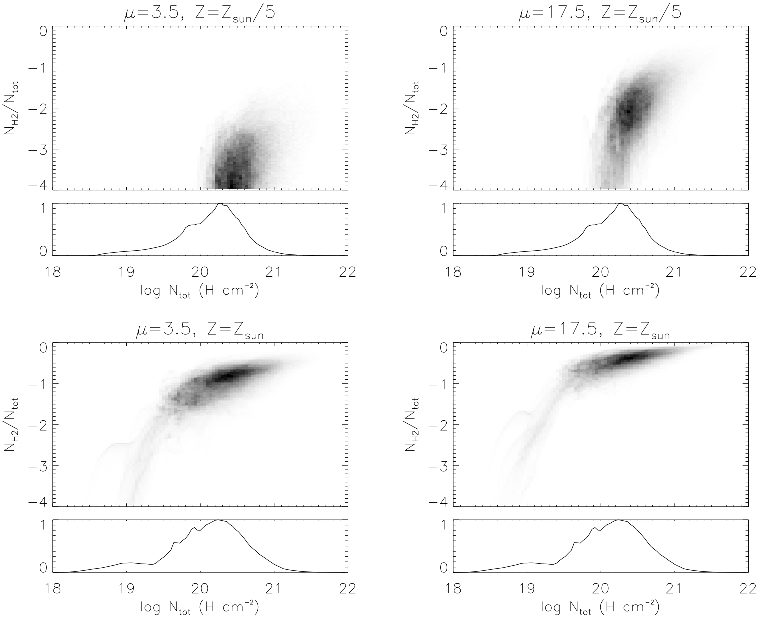

Figure 6.10: Fraction of H_2 vs total column densities.

our model galaxy the radiation fields in quiescent regions are quite low, $G_0 \lesssim 0.1$, due to the low star formation, so the radiative dissociation timescales are also in the order $\tau_{\rm rad} = 1.3/G_0 \times 10^7$ yr$\approx 10^8$ yr. So we see that the fact that H_2 can survive some time in lukewarm gas is not unrealistic. Note however that the simulation may not represent the dispersion of H_2 from dense regions realistically: molecular gas is formed in star forming regions, where radiation fields are higher (for our model up to $G_0 = 100$). As the star formation heats the surrounding gas it will destroy H_2, the amount of molecular gas that ”escapes” destruction is then sensitive to for example the time it is exposed to the high radiation field or the combination of high density/ high temperature. Also, destruction by supernova shocks is not represented very well, because the interaction of the supernova shocks with the (sub resolution) molecular clouds is absent. Nevertheless, our simulations indicate that in so far as the molecular gas is not destroyed, it will survive and so the warm medium of quiescent dwarf galaxies may still contain significant amounts of H_2. More active galaxies will destroy H_2 effectively by UV irradiation. Note that for similar reasons H_2 in the outer regions of spiral galaxies may survive for long times. This result may indicate the origin of the H_2 rotational emission from the disk of NGC891, where an extended and pervasive component of warm H2 with a scale length larger than that of the cooler molecular gas traced by CO was found (Valentijn & Van der Werf 1999). This warm H_2 can then by identified with the warm, extended, moderate density transition zones between GMCs and the WNM, and trace amounts of H_2 in the WNM that has espaced destruction in relatively quiescent regions.

6.6 Conclusions

We have presented a method to calculate the local H_2 content in simulations of the ISM based on a subgrid model for the formation and destruction of molecular clouds. The model includes the formation of H_2 on dust grains and destruction of molecules by UV irradiation, including the effects of shielding by dust and self-shielding. Its main assumption is that the formation of H_2 takes place in structures that conform to observed density/size scaling relations, and that are present on scales not directly probed by the hydrodynamic code of the simulation. We presented steady state solutions of the model for the molecular fraction $\mathrm{f_m}$ as a function of the macroscopic density, temperature, velocity dispersion, radiation field, and metallicity. The effect of cloud substructure is roughly accounted for by taking $1/\mathrm{r}$ density profiles for the model clouds, but this has only modest effect on the derived H_2 fractions.

A simple time-dependent formulation of the same model can be coupled to hydrodynamic simulations, and thus calculate the local evolution of $\mathrm{f_m}$ according to the local macroscopic quantities. We have implemented the model in an N-body/SPH code for the simulation of galaxy sized objects. We applied this model to a model low surface brightness dwarf, and found the following:

- We found that our model reproduces reasonable molecular fractions ranging from $\mathrm{f_m} = 0.001 - 0.03$ for low metallicity systems to $\mathrm{f_m} = 0.17 - 0.4$ for solar metallicity.
- The biggest uncertainty is the exact value of the formation rate parameter μ adopted, however the general features of the H_2 spatial distribution do not depend on μ.
- The molecular fraction also shows a strong dependence on the metallicity Z. This is physically reasonable. However our model run for high metallicity shows surpising amounts of “diffuse” H_2, possibly due to the low radiation fields outside star forming regions. This may be analogous to what happens in the outer regions of spiral galaxies where the radiation field drops, and a diffuse H_2 gas phase may be present.
- Our model for molecular hydrogen is sensitive to details of our star formation recipe, as star formation controls the destruction of H_2.
- H_2 cooling has only a minor impact for our model.

Summarizing, we have developed an algorithm to calculate the evolution of the molecular phase of galaxies, coupled to the evolution of their gaseous and stellar components. Strong points are that it is simple, physically motivated and not computationally expensive. It is well suited to galaxy-sized simulations where a complete treatment of the physics involved in the formation of the H_2 clouds is not yet attainable, and in our case it complements our ISM description of the neutral phases. The astrophysical questions that it may be applied to include the question of the distribution and role of H_2 in irregular dwarf galaxies such as the LMC, where complete cloud surveys have recently become available. Also interesting would be application of the model to mergers of spiral galaxies, as observations show that large concentrations of molecular gas are present in between the cores of the merging galaxies (e.g. Stanford et al. 1990), preceding or concurrent with the starbursts associated with these events. The concentrations of molecular gas are possibly forming out of the disrupted HI that "rushes" towards such regions. A direct example is furnished by the advanced merger NGC6240 (Van der Werf et al 1993), where the molecular gas is located between the remnant stellar nuclei. Here the strong emission from H2 in rotational and vibrational lines provides a direct measurement of the cooling radiation, showing that in extreme cases the additional cooling by molecular gas does play an important role. This effect is further enhanced by the suppression of [CII] $158\,\mu$m emission in these objects (e.g., Malhotra et al 1997), which is one of the principal coolers in more diffuse gas. Our model can be used to investigate the emergence of such a merger-induced molecular gas phase along with the evolving morphology and star formation rate. The fact that our prescripition takes account of the role of the macroscopic pressure for the formation of H_2 may be important for a complete understanding of this class of objects since the ISM pressure environment is expected to be rapidly evolving.

References

Abel, T., Anninos, P., Zhang, Y., & Norman, M. L., 1997, *New Astronomy* **2**, 181

Andersen, R.-P. & Burkert, A., 2000, *ApJ* **531**, 296

Barone, L. T., Heithausen, A., Hüttemeister, S., Fritz, T., & Klein, U., 2000, *MNRAS* **317**, 649

Bash, F. N., Green, E., & Peters, W. L., 1977, *ApJ* **217**, 464

Bate, M. R. & Burkert, A., 1997, *MNRAS* **288**, 1060

Blitz, L. & Shu, F. H., 1980, *ApJ* **238**, 148

Bottema, R., 2003, *MNRAS* **344**, 358

Bruzual A., G. & Charlot, S., 1993, *ApJ* **405**, 538

Buch, V. & Zhang, Q., 1991, *ApJ* **379**, 647

Buonomo, F., Carraro, G., Chiosi, C., & Lia, C., 2000, *MNRAS* **312**, 371

Burkert, A., 1995, *ApJ* **447**, L25+

Carraro, G., Lia, C., & Chiosi, C., 1998, *MNRAS* **297**, 1021

Cazaux, S. & Tielens, A. G. G. M., 2002, *ApJ* **575**, L29

Cazaux, S. & Tielens, A. G. G. M., 2004, *ApJ* **604**, 222

Chièze, J. P., 1987, *A&A* **171**, 225

Chièze, J.-P. & Pineau Des Forêts, G., 1987, *A&A* **183**, 98

Elmegreen, B. G., 1989, *ApJ* **338**, 178

Elmegreen, B. G., 1993, *ApJ* **411**, 170

Elmegreen, B. G., 2002, *ApJ* **577**, 206

Engargiola, G., Plambeck, R. L., Rosolowsky, E., & Blitz, L., 2003, *ApJS* **149**, 343

Ferrara, A. & Tolstoy, E., 2000, *MNRAS* **313**, 291

Field, G. B., 1965, *ApJ* **142**, 531

Gerritsen, J. P. E. & de Blok, W. J. G., 1999, *A&A* **342**, 655

Gerritsen, J. P. E. & Icke, V., 1997, *A&A* **325**, 972

Gil de Paz, A., Madore, B. F., & Pevunova, O., 2003, *ApJS* **147**, 29

Goldshmidt, O. & Sternberg, A., 1995, *ApJ* **439**, 256

Habart, H., Boulanger, F., Verstraete, L., Pineau des Forêts, G., Falgarone, E., & Abergel, A., 2000, in *ESA SP-456: ISO Beyond the Peaks*, pp 103–+

Habing, H. J., 1968, *Bull. Astron. Inst. Netherlands* **19**, 421

Helfer, T. T., Regan, M. W., Thornley, M. D., Wong, T., Sheth, K., Vogel, S. N., Bock, D. C.-J., Blitz, L., & Harris, A., 2001, *Ap&SS* **276**, 1131

Hernquist, L. & Katz, N., 1989, *ApJS* **70**, 419

Hidaka, M. & Sofue, Y., 2002, *PASJ* **54**, 223

Hollenbach, D. J. & Tielens, A. G. G. M., 1999, *Rev. of Mod. Phys.* **71**, 173

Hollenbach, D. J., Werner, M. W., & Salpeter, E. E., 1971, *ApJ* **163**, 165

Honma, M., Sofue, Y., & Arimoto, N., 1995, *A&A* **304**, 1

Israel, F. P., 1997, *A&A* **328**, 471

Jura, M., 1974, *ApJ* **191**, 375

Jura, M., 1975, *ApJ* **197**, 575

Katz, N., 1992, *ApJ* **391**, 502

Katz, N., Furman, I., Biham, O., Pirronello, V., & Vidali, G., 1999, *ApJ* **522**, 305

Kauffmann, G., White, S. D. M., & Guiderdoni, B., 1993, *MNRAS* **264**, 201

Kuijken, K. & Dubinski, J., 1995, *MNRAS* **277**, 1341

Larson, R. B., 1981, *MNRAS* **194**, 809

Le Bourlot, J., Pineau des Forêts, G., & Flower, D. R., 1999, *MNRAS* **305**, 802

Li, W., Evans, N. J., Jaffe, D. T., van Dishoeck, E. F., & Thi, W., 2002, *ApJ* **568**, 242

Malhotra, S. et al., 1997, *ApJ* **491**, L27+

Martin, P. G., Keogh, W. J., & Mandy, M. E., 1998, *ApJ* **499**, 793

McLaughlin, D. E. & Pudritz, R. E., 1996, *ApJ* **469**, 194

Mihos, J. C. & Hernquist, L., 1994, *ApJ* **437**, 611

Mizuno, N., Yamaguchi, R., Mizuno, A., Rubio, M., Abe, R., Saito, H., Onishi, T., Yonekura, Y., Yamaguchi, N., Ogawa, H., & Fukui, Y., 2001, *PASJ* **53**, 971

Monaghan, J. J., 1992, *ARA&A* **30**, 543

Navarro, J. F. & White, S. D. M., 1993, *MNRAS* **265**, 271

Papadopoulos, P. P., Thi, W.-F., & Viti, S., 2002, *ApJ* **579**, 270

Parravano, A., Hollenbach, D. J., & McKee, C. F., 2003, *ApJ* **584**, 797

Pelupessy, F. I., van der Werf, P. P., & Icke, V., 2004, *A&A* **422**, 55

Pirronello, V., Liu, C., Shen, L., & Vidali, G., 1997, *ApJ* **475**, L69+

Raga, A. C., Mellema, G., & Lundqvist, P., 1997, *ApJS* **109**, 517

Regan, M. W., Thornley, M. D., Helfer, T. T., Sheth, K., Wong, T., Vogel, S. N., Blitz, L., & Bock, D. C.-J., 2001, *ApJ* **561**, 218

Richter, P., Sembach, K. R., Wakker, B. P., & Savage, B. D., 2001, *ApJ* **562**, L181

Semelin, B. & Combes, F., 2002, *A&A* **388**, 826

Silich, S. A., Franco, J., Palous, J., & Tenorio-Tagle, G., 1996, *ApJ* **468**, 722

Silva, A. I. & Viegas, S. M., 2001, *Computer Physics Communications* **136**, 319

Springel, V., 2000, *MNRAS* **312**, 859

Springel, V. & Hernquist, L., 2002, *MNRAS* **333**, 649

Stanford, S. A., Sargent, A. I., Sanders, D. B., & Scoville, N. Z., 1990, *ApJ* **349**, 492

Sternberg, A., 1988, *ApJ* **332**, 400

Stone, J. M., Ostriker, E. C., & Gammie, C. F., 1998, *ApJ* **508**, L99

Tumlinson, J. et al., 2002, *ApJ* **566**, 857

Vázquez-Semadeni, E., 2002, in *ASP Conf. Ser. 276: Seeing Through the Dust: The Detection of HI and the Exploration of the ISM in Galaxies*, pp 155–+

Valentijn, E. A. & van der Werf, P. P., 1999, *ApJ* **522**, L29

van der Werf, P. P., Genzel, R., Krabbe, A., Blietz, M., Lutz, D., Drapatz, S., Ward, M. J., & Forbes, D. A., 1993, *ApJ* **405**, 522

van Zee, L., 2001, *AJ* **121**, 2003

Verner, D. A. & Ferland, G. J., 1996, *ApJS* **103**, 467

Webber, W. R., 1998, *ApJ* **506**, 329

Wolfire, M. G., Hollenbach, D., McKee, C. F., Tielens, A. G. G. M., & Bakes, E. L. O., 1995, *ApJ* **443**, 152

Wolfire, M. G., McKee, C. F., Hollenbach, D., & Tielens, A. G. G. M., 2003, *ApJ* **587**, 278

Wong, T. & Blitz, L., 2002, *ApJ* **569**, 157

Yamaguchi, R., Mizuno, N., Onishi, T., Mizuno, A., & Fukui, Y., 2001, *PASJ* **53**, 959

Chapter 7

Density Estimators in Particle Hydrodynamics

Abstract

We present a study comparing density maps reconstructed by the Delaunay Tessellation Field Estimator (DTFE) and by regular smoothed particle hydrodynamics (SPH) kernel-based techniques. The density maps are constructed from the outcome of an SPH simulation of a multiphase interstellar medium. The comparison between the two methods clearly demonstrates the superior performance of the DTFE with respect to conventional SPH methods, in particular at locations where SPH appears to fail. Filamentary and sheetlike structures form telling examples. The DTFE is a fully self-adaptive technique for reconstructing continuous density fields from discrete particle distributions, and is based upon the corresponding Delaunay tessellation. Its principal asset is its complete independence of arbitrary smoothing functions and parameters specifying the properties of these. As a result it manages to reproduce the anisotropies of the local particle distribution and through its adaptive and local nature proves to be optimally suited for uncovering the full hierarchical structures in the density distribution. Through the improvement in local density estimates, calculations invoking the DTFE will yield a much better representation of physical processes which depend on density. This will be crucial in the case of feedback processes, which play a major role in galaxy and star formation issues. The presented results form an encouraging step towards the application and insertion of the DTFE in astrophysical hydrocodes. We describe an outline for the construction of a particle hydrodynamics code in which the DTFE replaces kernel-based methods. Further discussion addresses the issue and possibilities for a moving grid based hydrocode invoking the DTFE, and Delaunay tessellations, in an attempt to combine the virtues of the Eulerian and Lagrangian approaches.

Pelupessy F. I., Schaap W. E., van de Weygaert R., 2003, A&A 403, p.389-398

7.1 Introduction

Smoothed Particle Hydrodynamics (SPH) has established itself as the workhorse for a range of astrophysical fluid dynamical computations (Lucy 1977, Ginghold & Monaghan 1977). In a wide variety of astrophysical environments this Lagrangian scheme offers substantial and often crucial advantages over Eulerian, usually grid-based, schemes. Astrophysical applications such as cosmic structure formation and galaxy formation, the dynamics of accretion disks and the formation of stars and planetary systems have testified of its versatility and successful performance (for an enumeration of applications, and corresponding references, see e.g. the reviews by Monaghan 1992 and Bertschinger 1998).

A crucial aspect of the SPH procedure concerns the proper estimation of the local density, i.e. the density at the location of the particles which are supposed to represent a fair – discrete – sampling of the underlying continuous density field. The basic feature of the SPH procedure for density estimation is based upon a convolution of the discrete particle distribution with a particular user-specified kernel function W. For a sample of N particles, with masses $\mathrm{m_j}$ and locations $\mathbf{r}_\mathrm{j}$, the density ρ at the location $\mathbf{r}_\mathrm{i}$ of particle i is given by

$$\rho(\mathbf{r}_\mathrm{i}) \,=\, \sum_{\mathrm{j}=1}^{\mathrm{N}} \mathrm{m_j}\, \mathrm{W}(\mathbf{r}_\mathrm{i}-\mathbf{r}_\mathrm{j},\mathrm{h_i})\,, \tag{1}$$

in which the kernel resolution is determined through the smoothing scale $\mathrm{h_i}$. Notice that generically the scale $\mathrm{h_i}$ may be different for each individual particle, and thus may be set to adapt to the local particle density. Usually the functional dependence of the kernel W is chosen to be spherically symmetric, so that it is a function of $|\mathbf{r}_\mathrm{i}-\mathbf{r}_\mathrm{j}|$ only.

The evolution of the physical system under consideration is fully determined by the movement of the discrete particles. Given a properly defined density estimation procedure, the equations of motion for the set of particles are specified through a suitable Lagrangian, if necessary including additional viscous forces (see e.g. Rasio 1999).

In practical implementations, however, the SPH procedure involves a considerable number of artefacts. These stem from the fact that SPH particles represent functional averages over a certain Lagrangian volume. This averaging procedure is further aggravated by the fact that it is based upon a rather arbitrary user-specified choice of both the adopted resolution scale(s) $\mathrm{h_i}$ and the functional form of the kernel W. Such a description of a physical system in terms of user-defined fuzzy clouds of matter is known to lead to considerable complications in realistic astrophysical circumstances. Often, these environments involve fluid flows exhibiting complex spatial patterns and geometries. In particular in configurations characterised by strong gradients in physical characteristics – of which the density, pressure and temperature discontinuities in and around shock waves represent the most frequently encountered example – SPH has been hindered by its relative inefficiency in resolving these gradients.

Given the necessity for the user to specify the characteristics and parameter values of the density estimation procedure, the accuracy and adaptability of the resulting SPH implementation hinges on the ability to resolve steep density contrasts and the capacity to adapt itself to the geometry and morphology of the local matter distribution. A considerable improvement with respect to the early SPH implementations, which were based on a uniform smoothing length h, involves the use of adaptive smoothing lengths h_i (Hernquist & Katz 1989), which provides the SPH calculations with a larger dynamic range and higher spatial resolution. The mass distribution in many (astro)physical systems and circumstances is often characterised by the presence of salient anisotropic patterns, usually identified as filamentary or planar features. To deal with such configurations, additional modifications in a few sophisticated implementations attempted to replace the conventional – and often unrealistic and restrictive – spherically symmetric kernels by ones whose configuration is more akin to the shape of the local mass distribution. The corresponding results do indeed represent a strong argument for the importance of using geometrically adaptive density estimates. A noteworthy example is the introduction of ellipsoidal kernels by Shapiro et al. (1996). Their shapes are stretched in accordance with the local flow. Yet, while evidently being conceptually superior, their practical implementation does constitute a major obstacle and has prevented wide scale use. This may be ascribed largely to the rapidly increasing number of degrees of freedom needed to specify and maintain the kernel properties during a simulation.

Even despite their obvious benefits and improvements, these methods are all dependent upon the artificial parametrization of the local spatial density distribution in terms of the smoothing kernels. Moreover, the specification of the information on the density distribution in terms of extra non physical variables, necessary for the definition and evolution of the properties of the smoothing kernels, is often cumbersome to implement and may introduce subtle errors (Hernquist 1993, see however Nelson & Papaloizou 1994 and Springel & Hernquist 2002). In many astrophysical applications this may lead to systematic artefacts in the outcome for the related physical phenomena. Within a cosmological context, for example, the X-ray visibility of clusters of galaxies is sensitively dependent upon the value of the local density, setting the intensity of the emitted X-ray emission by the hot intergalactic gas. This will be even more critical in the presence of feedback processes, which for sure will be playing a role when addressing the amount of predicted star formation in simulation studies of galaxy formation.

Here, we seek to circumvent the complications of the kernel parametrization and propose an alternative to the use of kernels for the quantification of the density within the SPH formalism. This new method, based upon the Delaunay Tessellation Field Estimator (DTFE, Schaap & van de Weygaert 2000), has been devised to mould and fully adapt *itself* to the configuration of the particle distribution. Unlike conventional SPH methods, it is able to deal self-consistently and naturally with anisotropies in the matter distribution, even when it concerns caustic-like transitions. In addition, it manages to successfully treat density fields marked by structural features over a vast (dynamic) range of scales.

The DTFE produces density estimates on the basis of the particle distribution, which is supposed to form a discrete spatial sampling of the underlying continuous density field. As a linear multidimensional field interpolation algorithm it may be regarded as a first-order version of the natural neighbour algorithm for spatial interpolation (Sibson 1981, also see e.g. Okabe et al. 2000). In general, applications of the DTFE to spatial point distributions have demonstrated its success in dealing with the complications of anisotropic geometry and dynamic range (Schaap & van de Weygaert 2000). The key ingredient of the DTFE procedure is that of the Delaunay triangulation, serving as the complete covering of a sample volume by mutually exclusive multidimensional linear interpolation intervals.

Delaunay tessellations (Delaunay 1934; see e.g. Okabe et al. 2000 for extensive review) form the natural framework in which to discuss the properties of discrete point sets, and thus also of discrete samplings of continuous fields. Their versatility and significance have been underlined by their widespread applications in such areas as computer graphics, geographical mapping and medical imaging. Also, they have already found widespread application in a variety of 'conventional'grid-based fluid dynamical computation schemes. This may concern their use as a non-regular application-oriented grid covering of physicalsystems, which represents a prominent procedure in technological applications. More innovating has been their use in Lagrangian 'moving-grid' implementations (see Mavriplis 1997 for a review, and Whitehurst 1995 for a promising astrophysical application).

It seems therefore a good idea to explore the possibilities of applying the DTFE in the context of a numerical hydrodynamics code. Here, as a first step, we wish to obtain an idea of the performance of a hydro code involving the use of DTFE estimates with respect to an equivalent code involving regular SPH density estimates. The quality of the new DTFE method with respect to the conventional SPH estimates, and their advantages and disadvantages under various circumstances, are evaluated by a comparison between the density field which would be yielded by a DTFE processing of the resulting SPH particle distribution and that of the regular SPH procedure itself. In this study, we operate along these lines by a comparison of the resulting matter distributions in the situation of a representative stochastic multiphase density field. This allows us to make a comparison between both density estimates in a regime for which an improved method for density estimates would be of great value. We should point out a major drawback of our approach, in that we do not really treat the DTFE density estimate in a self-consistent fashion. Instead of being part of the dynamical equations themselves we only use it as an analysis tool of the produced particle distribution. Nevertheless, it will still show the value of the DTFE in particle gas dynamics and give an indication of what kind of differences may be expected when incorporating in a fully self-consistent manner the DTFE estimate in an hydrocode.

On the basis of our study, we will elaborate on the potential benefits of a hydrodynamics scheme based on the DTFE. Specifically, we outline how we would set out to develop a complete particle hydrodynamics code whose artificial kernel based nature is replaced by the more natural and self-adaptive approach of the DTFE. Such a DTFE based particle hydrodynamics code would form a promising step towards the development of a fully tessellation based quasi-Eulerian moving-grid hydrodynamical code. Such would yield a major and significant step towards defining a much needed alternative and complement to currently available simulation tools.

7.2 DTFE and SPH density estimates

The methods we use for SPH and DTFE density estimates have been extensively described elsewhere (Hernquist & Katz 1989, Schaap & van de Weygaert 2000). Here, we will only summarise their main, and relevant, aspects.

7.2.1 SPH density estimate

Amongst the various density recipes employed within available SPH codes, we use the Hernquist & Katz (1989) symmetrized form of Eq. 1, using adaptive smoothing lengths:

$$\hat{\rho}_\mathrm{i} = \frac{1}{2} \sum_\mathrm{j} \mathrm{m_j} \, \{ \mathrm{W}(|\mathrm{r_i} - \mathrm{r_j}|, \mathrm{h_i}) + \mathrm{W}(|\mathrm{r_i} - \mathrm{r_j}|, \mathrm{h_j}) \} \, , \tag{2}$$

The smoothing lengths $\mathrm{h_i}$ are chosen such that the sum involves around 40 nearest neighbours. For the kernel W we take the conventional spline kernel described by Monaghan (1992). Other variants of the SPH estimate produce comparable results.

7.2.2 DTFE density estimate

The DTFE density estimating procedure consists of three basic steps.

Starting from the sample of particle locations, the first step involves the computation of the corresponding Delaunay tessellation. Each Delaunay cell $\mathrm{T_m}$ is the uniquely defined tetrahedron whose four vertices (in 3-D) are the set of 4 sample particles whose circumscribing sphere does not contain any of the other particles in the set. The Delaunay tessellation is the full covering of space by the complete set of these mutually disjunct tetrahedra. Delaunay tessellations are well known concepts in stochastic and computational geometry (Delaunay 1934, for further references see e.g. Okabe et al. 2000, Møller 1994 and van de Weygaert 1991).

The second step involves estimating the density at the location of each of the particles in the sample. From the definition of the Delaunay tessellation, it may be evident that there is a close relationship between the volume of a Delaunay tetrahedron and the local density of the generating point process (telling examples of this may be seen in e.g. Schaap & van de Weygaert 2003). Evidently, the "empty" circumscribing spheres corresponding to the Delaunay tetrahedra, and the volumes of the resulting Delaunay tetrahedra, will be smaller as the number density of sample points increases, and vice versa. Following this observation, a proper density estimate $\hat{\rho}$ at the location $\mathbf{x}_\mathrm{i}$ of a sampling point i is obtained by determining the properly calibrated inverse of the volume $\mathcal{W}_\mathrm{Vor,i}$ of the corresponding *contiguous Voronoi cell*. The contiguous Voronoi cell $\mathcal{W}_\mathrm{Vor,i}$ is the union of all Delaunay tetrahedra $\mathrm{T_{m,i}}$ of which the particle i forms one of the four vertices, i.e. $\mathcal{W}_\mathrm{Vor,i} = \bigcup_\mathrm{m} \mathrm{T_{m,i}}$. In general, when a particle i is surrounded by $\mathrm{N_T}$ Delaunay tetrahedra, each with a volume $\mathcal{V}(\mathrm{T_{m,i}})$, the volume of the resulting contiguous Voronoi cell is

$$\mathcal{W}_\mathrm{Vor,i} = \sum_\mathrm{m=1}^\mathrm{N_T} \mathcal{V}(\mathrm{T_{m,i}}) \, . \tag{3}$$

Note that $\mathrm{N_T}$ is not a constant, but in general may acquire a different value for each point in the sample. For a Poisson distribution of particles this is a non-integer number in the order of $\langle \mathrm{N_T} \rangle \approx 27$ (van de Weygaert 1994). Generalising to an arbitrary D-dimensional space, and assuming that each particle i has been assigned a mass $\mathrm{m_i}$, the estimated density $\hat{\rho}_{\rm i}$ at the location of particle i is given by (see Schaap & van de Weygaert 2000)

$$\hat{\rho}(\mathbf{r}_{\rm i}) \,=\, ({\rm D}+1)\,\frac{\rm m_i}{\mathcal{W}_{\rm Vor,i}}\,, \tag{4}$$

In this, we explicitly express $\mathcal{W}_{\rm Vor,i}$ for the general D-dimensional case. The factor $({\rm D}+1)$ is a normalisation factor, accounting for the $({\rm D}+1)$ different contiguous Voronoi hypercells to which each Delaunay hyper"tetrahedron" is assigned, one for each vertex of a Delaunay hyper"tetrahedron".

The third step is the interpolation of the estimated densities $\hat{\rho}_{\rm i}$ over the full sample volume. In this, the DTFE bases itself upon the fact that each Delaunay tetrahedron may be considered the natural multidimensional equivalent of a linear interpolation interval (see e.g Bernardeau & van de Weygaert 1996). Given the $({\rm D}+1)$ vertices of a Delaunay tetrahedron with corresponding density estimates $\hat{\rho}_{\rm j}$, the value $\hat{\rho}(\mathbf{r})$ at any location $\mathbf{r}$ within the tetrahedron can be straightforwardly determined by simple linear interpolation,

$$\hat{\rho}(\mathbf{r}) \,=\, \hat{\rho}(\mathbf{r}_{\rm i0}) \,+\, (\hat{\nabla}\rho)_{\rm Del,m}\,\cdot\,(\mathbf{r}-\mathbf{r}_{\rm i0})\,, \tag{5}$$

in which $\mathbf{r}_{\rm i0}$ is the location of one of the Delaunay vertices i. This is a trivial evaluation once the value of the (linear) density gradient $(\hat{\nabla}\rho)_{\rm Del,m}$ has been estimated. For each Delaunay tetrahedron $\rm T_m$ this is accomplished by solving the the system of D linear equations corresponding to each of the remaining D Delaunay vertices constituting the Delaunay tetrahedron $\rm T_m$. The "minimum triangulation" property of Delaunay tessellations underlying this linear interpolation, minimum in the sense of representing a volume-covering network of optimally compact multidimensional "triangles", has been a well-known property utilised in a variety of imaging and surface rendering applications such as geographical mapping and various computer imaging algorithms.

7.2.3 Comparison

Comparing the two methods, we see that in the case of SPH the particle 'size' and 'shape' (i.e. its domain of influence) is determined by some arbitrary kernel $\rm W(r,h_i)$ and a fortuitous choice of smoothing length $\rm h_i$ (assuming, along with the major share of SPH procedures, a radially symmetric kernel). In the case of the DTFE method the particles' influence region is fully determined by the sizes and shapes of the Delaunay cells $\rm T_{m,i}$, themselves solely dependent on the particle distribution. In other words, in regular SPH the density is determined through the kernel function $\rm W(\mathbf{x})$, while in DTFE it is solely the particle distribution itself setting the estimated values of the density. Contrary to the generic situation for the kernel dependent methods, there are no extra variables left to be determined. One major additional advantage is that it is therefore not necessary to worry about the evolution of the kernel parameters.

Both methods do display some characteristic artefacts in their density reconstructions (see Fig.7.1). To a large extent these may be traced back to the implicit assumptions involved in the interpolation procedures, a necessary consequence of the finite amount of information contained in a discrete representation of a continuous field. SPH density fields implicitly contain the imprint of the specified and applied kernel which, as has been discussed before, may seriously impart its resolving power and capacity to trace the true geometry of structures. The DTFE technique, on the other hand, does produce triangular artefacts. At instances conspicuously visible in the DTFE reconstructed density fields, they are the result of the linear interpolation scheme employed for the density estimation at the locations not coinciding with the particle positions. In principle, this may be substantially improved by the use of higher order interpolation schemes. Such higher-order schemes have indeed been developed, and the ones based upon the natural neighbour interpolation prescription of Sibson (1981) have already been successfully applied to two-dimensional problems in the field of geophysics (Braun & Sambridge 1995) and solid state physics (Sukumar 1998).

7.3 Case study: two-phase interstellar medium

For the sake of testing and comparing the SPH and DTFE methods, we assess a snapshot from a simulation of the neutral ISM. The model of the ISM is chosen as an illustration rather than as a realistic model.

The "simulation" sample of the ISM consists of HI gas confined in a periodic simulation box with a size $\mathrm{L} = 0.6$ kpc^3. The initially uniform density of the gas is $\mathrm{n_H} = 0.3$ cm^{-3}, while its temperature is taken to be $\mathrm{T} = 10000$ K. No fluctuation spectrum is imposed to set the initial featureless spatial gas distribution. To set the corresponding initial spatial distribution of the $\mathrm{N} = 64000$ simulation particles, we start from relaxed initial conditions according to a "glass" distribution (e.g. White 1996).

The evolution of the gas is solely a consequence of fluid dynamical and thermodynamical processes. No self gravity is included. As for the thermodynamical state of the gas, cooling is implemented using a fit to the Dalgarno-McCray (1972) cooling curve. The heating of the gas is accomplished through photo-electric grain heating, attributed to a constant FUV background ($1.7\ \mathrm{G_0}$, with $\mathrm{G_0}$ the Habing field) radiation field. The parameters are chosen such that after about 15 Myrs a two-phase medium forms which consists of warm (10000 K) and cold (> 100 K) HI gas.

The stage at which a two-phase medium emerges forms a suitable point to investigate the performance of the SPH and DTFE methods. At this stage we took a snapshot from the simulation, and subjected it to further analysis. For a variety of reasons, the spatial gas distribution of the snapshot is expected to represent a challenging configuration. The multiphase character of the resulting particle configuration is likely to present a problem for regular SPH. Density contrasts of about four orders of magnitude separate dense clumps from the surrounding diffuse medium through which they are dispersed. Note that a failure to recover the correct density may have serious repercussions for the computed effects of cooling. In addition, we notice the presence of physical structures with conspicuous, aspherical geometries (see Fig. 1 & 2), such as anisotropic sheets and filaments as well as dense and compact clumps, which certainly do form a challenging aspect for the different methods.

7.3.1 Results

Fig. 7.1 offers a visual impression of the differences in performance between the SPH and DTFE density reconstructions. The greyscale density maps in Fig. 7.1 (lower left:

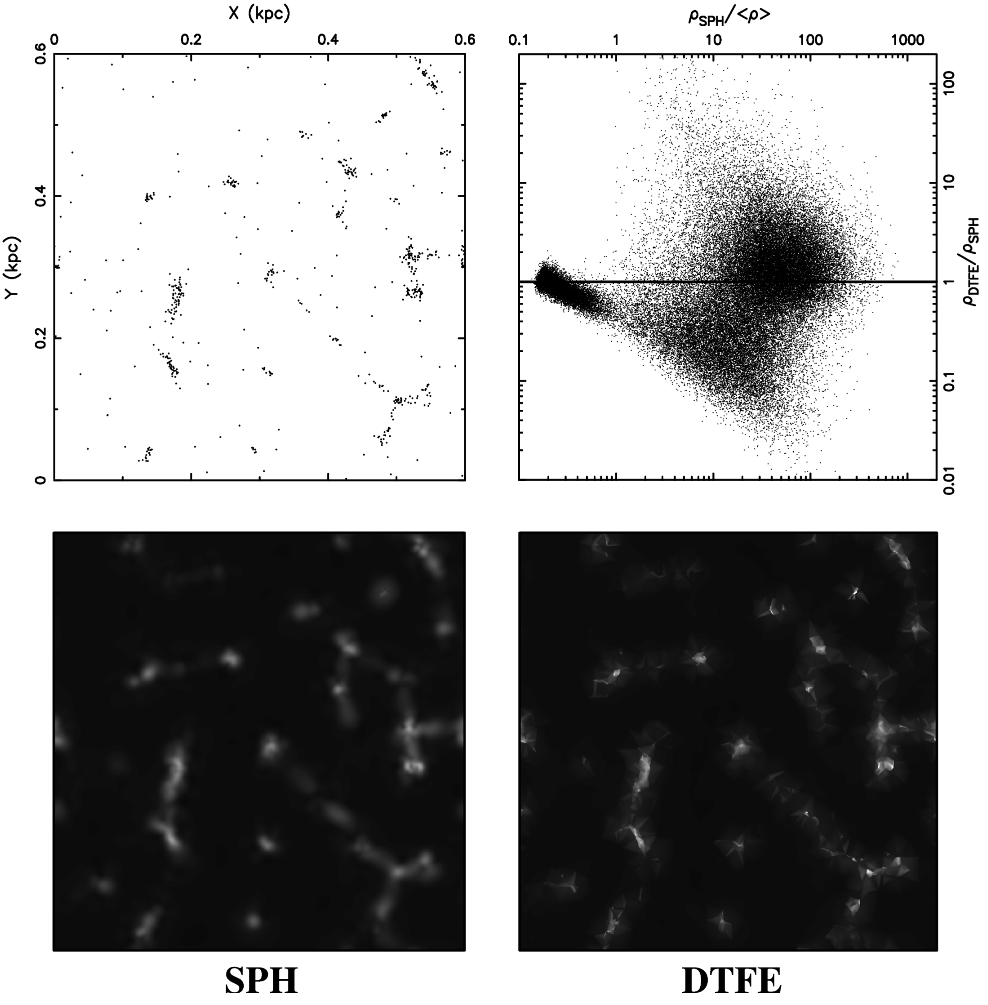

SPH **DTFE**

Figure 7.1: Comparison of the DTFE performance versus that of the regular SPH method in a characteristic configuration, that of a hydrodynamic simulation of the multiphase interstellar medium. Top left panel: the particle distribution in a 0.6×0.6 kpc simulation region, within a slice with a width of 0.005 kpc. Bottom left frame: 2-D slice through the resulting (3-D) SPH density field reconstruction. Bottom right frame: the corresponding (3-D) density field reconstruction produced by the DTFE procedure. Top righthand frame: summary, in terms of a quantitative point-by-point comparison between the DTFE and SPH density estimates, $\rho_{\rm DTFE}$ and $\rho_{\rm SPH}$. Abscissa: the value of the SPH density estimate (normalised by the average density $\langle\rho\rangle$). Ordinate: the ratio of DTFE estimate to the SPH density estimate, $\rho_{\rm DTFE}/\rho_{\rm SPH}$. These quantities are plotted for each particle location in the full simulation box.

SPH, lower right: DTFE) represent 2-D cuts through the corresponding 3-D density field reconstructions (note that contrary to the finite width of the corresponding particle slice, upper left frame, these constitute planes with zero thickness).

Immediately visible is the more crispy appearance of the DTFE density field, displaying substantially more contrast in conjunction with more pronounced structural features. Look e.g. at the compact clump in the lower righthand corner ($\mathrm{X} \approx 0.5, \mathrm{Y} \approx 0.12$), forming a prominent and tight spot in the DTFE density field. The clump at ($\mathrm{X} \approx 0.48, \mathrm{Y} \approx 0.52$) represents another telling example, visible as a striking peak in the DTFE rendering while hardly noticeable in the SPH reconstruction. Structures in the SPH field have a more extended appearance than their counterparts in the DTFE field, whose matter content has been smeared out more evenly, over a larger volume, yielding features with a significantly lower contrast. In this assessment it becomes clear that the DTFE reconstruction adheres considerably closer to the original particle distribution (top lefthand frame). Apparently the DTFE succeeds better in rendering the shapes, the coherence and the internal composition in the displayed particle distribution. At various locations, the DTFE even manages to capture structural details which seem to be absent in the SPH density field.

To quantify the visual impressions of Fig. 7.1, and to analyse the nature of the differences between the two methods, we plot the ratio $\rho_{\mathrm{DTFE}}/\rho_{\mathrm{SPH}}$ as a function of the SPH density estimate $\rho_{\mathrm{SPH}}/\langle\rho\rangle$ (in units of the average density $\langle\rho\rangle$). Doing so for all particles in the sample (Fig. 7.1, top righthand, Fig. 7.2, top lefthand) immediately reveals interesting behaviour. The scatter diagram does show that the discrepancies between the two methods may be substantial, with density estimates at various instances differing by a factor of 5 or more.

Most interesting is the finding that we may distinguish clearly identifiable and distinct regimes in the scatter diagram of $\rho_{\mathrm{DTFE}}/\rho_{\mathrm{SPH}}$ versus $\rho_{\mathrm{SPH}}/\langle\rho\rangle$. Four different sectors may be identified in the scatter diagram. Allowing for some arbitrariness in their definition, and indicating these regions by digits 1 to 4, we may organize the particles according to density-related criteria, roughly specified as (we refer to Fig. 7.2, top left frame, for the precise definitions of the domains):

1. low density regions:
   $\rho_{\mathrm{SPH}}/\langle\rho\rangle \;<\; 1$
2. medium density regions, DTFE smaller than SPH:
   $\rho_{\mathrm{DTFE}} \;<\; \rho_{\mathrm{SPH}}; \quad 1 < \rho_{\mathrm{SPH}}/\langle\rho\rangle < 10$
3. medium density regions, DTFE larger than SPH:
   $\rho_{\mathrm{DTFE}} \;>\; \rho_{\mathrm{SPH}}; \quad 1 < \rho_{\mathrm{SPH}}/\langle\rho\rangle < 10$
4. high density regions:
   $\rho_{\mathrm{DTFE}} \gtrsim \rho_{\mathrm{SPH}}; \quad \rho_{\mathrm{SPH}}/\langle\rho\rangle \;>\; 10$

The physical meaning of the distinct sectors in the scatter diagram becomes apparent when relating the various regimes with the spatial distribution of the corresponding particles. This may be appreciated from the five subsequent frames in Fig. 7.2, each depicting the related particle distribution in the same slice of width 0.04 kpc. The centre and bottom frames, numbered 1 to 4, show the spatial distribution of each group of particles, isolated from the complete distribution (top right frame, Fig. 2).

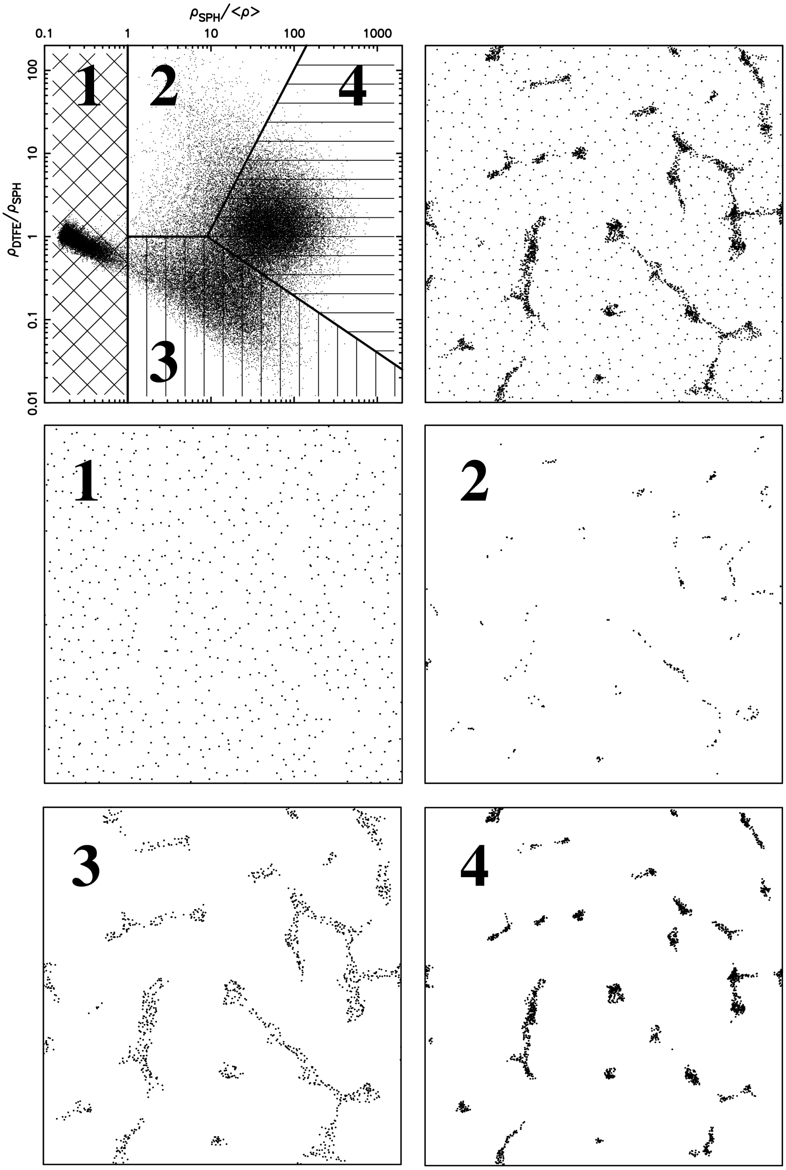

Figure 7.2: Systematic analysis of the differences between the DTFE and SPH density estimates, ρ_{DTFE} and ρ_{SPH}. Basis of the analysis is a point-by-point comparison of these two density estimates. Top lefthand frame: diagram of the value of the ratio $\rho_{\mathrm{DTFE}}/\rho_{\mathrm{SPH}}$ (ordinate) versus $\rho_{\mathrm{SPH}}/\langle\rho\rangle$ (abscissa) for each of the points in the simulation volume. Indicated in this scatter diagram are four sectors, each of which corresponds to particles residing in a physically different regime/phase. On the basis of this identification, the full set of particles is dissected into the corresponding four composing particle samples. Top righthand frame: the spatial distribution of the full set of particles in a 0.04 kpc wide slice. The subsequent 4 frames (from central left to bottom right) show, for each indicated sector in the scatter diagram, the spatial distribution of the corresponding particles (within the same 0.04 kpc slice).

These particle slices immediately reveal the close correspondence between any of the sectors in the scatter diagram and typical features in the spatial matter distribution of the two-phase interstellar medium. This systematic behaviour seems to point to truly fundamental differences in the workings of the SPH and DTFE methods, and would be hard to understand in terms of random errors. The separate spatial features in the gas distribution seem to react differently to the use of the DTFE method.

We argue that the major share of the disparity between the SPH and DTFE density estimates has to be attributed to SPH, mainly on the grounds of the known fact that SPH is poor in handling nontrivial configurations such as encountered in multiphase media. By separately assessing each regime, we may come to appreciate how these differences arise. In sector 1, involving the diffuse low density medium, the DTFE and SPH estimates are of comparable magnitude, be it that we do observe a systematic tendency. In the lowest density realms, whose relatively smooth density does not raise serious obstacles for either method, DTFE and SPH are indeed equal (with the exception of variations to be attributed to random noise). However, near the edges of the low density regions, SPH starts to overestimate the local density as the kernels do include particles within the surrounding high density structures. The geometric interpolation of the DTFE manages to avoid this systematic effect (see e.g. Schaap & van de Weygaert 2003), which explains the systematic linear decrease of the ratio $\rho_{\mathrm{DTFE}}/\rho_{\mathrm{SPH}}$ with increasing $\rho_{\mathrm{SPH}}/\langle\rho\rangle$. To the other extreme, the high density regions in sector 4 are identified with compact dense clumps as well as with their extensions into connecting filaments and walls. On average DTFE yields higher density estimates than SPH, frequently displaying superior spatial resolution (see also greyscale plot in Fig. 7.1). Note that the repercussions may be far-reaching in the context of a wide variety of astrophysical environments characterised by strongly density dependent physical phenomena and processes ! The intermediate regime of sectors 2 and 3 clearly connects to the filamentary structures in the gas distribution. Sector 2, in which the DTFE estimates are larger than those of SPH, appears to select out the inner parts of the filaments and walls. By contrast, the higher values for the SPH produced densities in sector 3 are related to the outer realms of these features. This characteristic distinction can be traced back to the failure of the SPH procedure to cope with highly anisotropic particle configurations. While it attempts to maintain a fixed number of neighbours within a spherical kernel, it smears out the density in a direction perpendicular to the filament. This produces lower estimates in the central parts, which are compensated for with higher estimates in the periphery. Evidently, the adaptive nature of DTFE does not appear to produce similar deficiencies.

7.4 The DTFE particle method

Having demonstrated the improvement in quality of the DTFE density estimates, this suggests a considerable potential for incorporating the DTFE in a self-consistent manner within a hydrodynamical code. Here, we first wish to indicate a possible route for accomplishing this in a particle hydrodynamics code through replacement of the kernel based density estimates (1) by the DTFE density estimates. We are currently in the process of implementing this. The formalism on which this implementation is based can be easily derived, involving nontrivial yet minor modifications. Essentially, it uses the same dynamic equations for gas particles as those in the regular SPH formalism, the fundamental adjustment being the insertion of the DTFE densities instead of the regular SPH ones. In addition, a further difference may be introduced through a change in treatment of viscous forces. Ultimately, this will work out into different equations of motion for the gas particles. A fundamental property of a DTFE based hydrocode, by construction, is that it conserves mass exactly and therefore obeys the continuity equation. This is not necessarily true for SPH implementations (Hernquist & Katz 1989).

The start of the suggested DTFE particle method is formed by the discretized expression for the Lagrangian L for a compressible, non-dissipative flow,

$$\mathrm{L} = \sum_{\mathrm{i}} \mathrm{m_i} \left(\frac{1}{2} \mathrm{v_i^2} + \mathrm{u_i}(\rho_{\mathrm{i}}, \mathrm{s_i}) \right) , \tag{6}$$

where $\mathrm{m_i}$ is the mass of particle i, $\mathrm{v_i}$ its velocity, $\mathrm{s_i}$ the corresponding entropy and $\mathrm{u_i}$ its specific internal energy. In this expression, ρ_{i} is the density at location i, as yet unspecified. The resulting Euler-Lagrange equations are

$$\frac{\mathrm{dv_i}}{\mathrm{dt}} = -\sum_{\mathrm{j}} \mathrm{m_j} \left(\frac{\partial \mathrm{u_j}}{\partial \rho_{\mathrm{j}}} \right)_{\mathrm{s}} \frac{\partial \rho_{\mathrm{j}}}{\partial \mathrm{x_i}} . \tag{7}$$

The standard SPH equations of motion then follow after inserting the SPH density estimate (Eq. 1). Instead, insertion of the DTFE density (Eq. 4) will lead to the corresponding equations of motion for the DTFE-based formalism. Note that the usual conservation properties related to Eq. 6 remain intact. After some algebraic manipulation, thereby using the basic thermodynamic relation for a gas with equation of state $\mathrm{P}(\rho)$,

$$\left(\frac{\partial \mathrm{u_i}}{\partial \rho_{\mathrm{i}}} \right)_{\mathrm{s}} = \frac{\mathrm{P_i}}{\rho_{\mathrm{i}}^2} , \tag{8}$$

we finally obtain for the gas particles moving in D-dimensional space,

$$\frac{\mathrm{dv_i}}{\mathrm{dt}} = \frac{1}{\mathrm{D}+1} \sum_{\mathrm{m}=1}^{\mathrm{N_T}} \mathrm{P}(\mathrm{T_{m,i}}) \frac{\partial \mathcal{V}(\mathrm{T_{m,i}})}{\partial \mathrm{x_i}} . \tag{9}$$

This expression involves a summation over all $\mathrm{N_T}$ Delaunay tetrahedra $\mathrm{T_{m,i}}$, with volumes $\mathcal{V}(\mathrm{T_{m,i}})$, which have the particle i as one of its four vertices. The pressure term $\mathrm{P}(\mathrm{T_{m,i}})$ is the sum over the pressures $\mathrm{P_j}$ at the four vertices j of tetrahedron $\mathrm{T_{m,i}}$, $\mathrm{P}(\mathrm{T_{m,i}}) = \sum \mathrm{P_j}$.

As an interesting aside, we point out that unlike in the conventional SPH formalism, this procedure implies an exactly vanishing acceleration $\mathrm{dv_i}/\mathrm{dt}$ in the case of a constant pressure P at each of the vertices of the Delaunay tetrahedra containing particle i as one of their vertices. The reason for this is that one can then invoke the definition of the volume of the contiguous Voronoi cell corresponding to point i (Eqn. 3), yielding

$$\frac{\mathrm{dv_i}}{\mathrm{dt}} = \frac{1}{\mathrm{D}+1} \mathrm{P} \frac{\partial \mathcal{W}_{\mathrm{Vor,i}}}{\partial \mathrm{x_i}} . \tag{10}$$

Since the volume of the contiguous Voronoi cell does not depend on the position of particle i itself (it lies in the interior of the contiguous Voronoi cell), the resulting acceleration vanishes. Another interesting notion, which was pointed out by Icke (2002), is that Delaunay tessellations also provide a unique opportunity to include a natural treatment of the viscous stresses in the physical system. We intend to elaborate on this possibility in subsequent work dealing with the practical implementation along the lines sketched above.

7.5 Delaunay tessellations and 'moving grid' hydrocodes

Ultimately, the ideal hydrodynamical code would combine the advantages of the Eulerian as well as of the Lagrangian approach. In their simplest formulation, Eulerian algorithms cover the volume of study with a fixed grid and compute the fluid transfer through the faces of the (fixed) grid cell volumes to follow the evolution of the system. Lagrangian formulations, on the other hand, compute the system by following the ever changing volume and shape of a particular individual element of gas

For a substantial part the success of the DTFE may be ascribed to the use of Delaunay tessellations as an optimally covering grid. This suggests that they may also be ideal for the use in moving grid implementations for hydrodynamical calculations. As in our SPH application, such hydrocodes with Delaunay tessellations at their core would warrant a close connection to the underlying matter distribution. Indeed, attempts towards such implementations have already been introduced in the context of a few specific, mainly two-dimensional, applications (Whitehurst 1995, Braun & Sambridge 1995, Sukumar 1998). Alternative attempts towards the development of moving grid codes, in an astrophysical context, have shown their potential (Gnedin 1995, Pen 1998).

For a variety of astrophysical problems it is indeed essential to have such advanced codes at one's disposal. An example of high current interest may offer a good illustration. Such an example is the reionization of the intergalactic medium by the ionizing radiation emitted by the first generation of stars, (proto)galaxies and/or active galactic nuclei. These radiation sources will form in the densest regions of the universe. To be able to resolve these in sufficient detail, it is crucial that the code is able to focus in onto these densest spots. Their emphasis on mass resolution makes Lagrangian codes – including SPH – usually better equipped to do so, be it not yet optimally. On the other hand, it is in the low density regions that most radiation is absorbed at first. In the early stages the reionization process is therefore restricted to the huge under-dense fraction of space. Simulation codes should therefore properly represent and resolve the gas density distribution within these void-like regions. The uniform spatial resolution of the Eulerian codes is better suited to accomplish this. Ideally, however, a simulation code should be able to combine the virtues of both approaches, yielding optimal mass resolution in the high density source regions and a proper coverage of the large under-dense regions. To achieve this there recently have been many efforts in the context of Eulerian codes towards the development of Adaptive Mesh Refinement (AMR) algorithms, which use multiple nested grids to achieve this. Moving grid methods, of which Delaunay tessellation based ones will be a natural example, may indeed be the best alternative, as the reionization simulations by Gnedin (1995) appear to indicate.

The advantages of a moving grid fluid dynamics code based on Delaunay tessellations have been most explicitly demonstrated by the implementation of a two-dimensional Lagrangian hydrocode (FLAME) by Whitehurst (1995). These advantages will in principle apply to any such algorithm, in particular also for 3 dimensional implementations (of which we are currently unaware). Whitehurst (1995) enumerated various potential benefits in comparison with conventional SPH codes, most importantly the following:

1. SPH needs a smoothing length h.
2. SPH needs an arbitrary kernel function W.
3. The moving grid method does not need an (unphysical) artificial viscosity to stabilise solutions.

The validity of the first two claims has of course also been demonstrated in this study for particle methods based on DTFE. Whitehurst showed additionally that there is an advantage of moving grid methods over Eulerian grid-based ones. The implementation of Whitehurst, which used a first-order solver, was far superior to all tested first-order Eulerian codes, and superior to many second-order ones as well. The adaptive nature of the Lagrangian method and the fact that the resulting grid has no preferred directions are key factors in determining the performance of moving grid methods such as FLAME. For additional convincing arguments, including the other claims, we may refer the reader to the truly impressive case studies presented by Whitehurst (1995).

7.6 Summary & discussion

Here we have introduced the DTFE as an alternative density estimator for particle fluid dynamics. Its principle asset is that it is fully self-adaptive, resulting in a density field reconstruction which closely reproduces, usually in meticulous detail, the characteristics of the spatial particle distribution. It may do so because of its complete independence of arbitrary user-specified smoothing functions and parameters. Unlike conventional methods, such as the kernel estimators used in SPH, it manages to faithfully reproduce the anisotropies in the local particle distribution. It therefore automatically reflects the genuine geometry and shape of the structures present in the underlying density field. This is in marked contrast with kernel based methods, which almost without exception produce distorted shapes of density features, the result of the convolution of the real structure with the intrinsic shape of the smoothing function. Its adaptive and local nature also makes it optimally suited for reconstructing the hierarchy of scales present in the density distribution. In kernel based methods the internal structural richness of density features is usually suppressed on scales below that of the characteristic (local) kernel scale. DTFE, however, is solely based upon the particle distribution itself and follows the density field wherever the discrete representation by the particle distribution allows it to do so. Its capacity to resolve structures over a large dynamic range may prove to be highly beneficial in many astrophysical circumstances, quite often involving environments in which we encounter a hierarchical embedding of small-scale structures within more extended ones.

In this study we have investigated the performance of the DTFE density estimator in the context of a Smooth Particle Hydrodynamics simulation of a multiphase interstellar medium of neutral gas. The limited spatial resolution of current particle hydrodynamics codes are known to implicate considerable problems near regions with e.g. steep density and temperature gradients. In particular their handling of shocks forms a source of considerable concern. SPH often fails in and around these regions, so often playing a critical and vital role in the evolution of a physical system. Our study consists of a comparison and confrontation of the conventional SPH kernel based density estimation procedure with the corresponding DTFE density field reconstruction method.

The comparison of the density field reconstructions demonstrated convincingly the considerable improvement embodied by the DTFE procedure. This is in particular true at locations and under conditions where SPH appears to fail. Filamentary and sheetlike structures provide telling examples of the superior DTFE handling with respect to the regular SPH method, with the most pronounced improvement occurring in the direction of the steepest density gradient.

Having shown the success of the DTFE, we are convinced that its application towards the analysis of the outcome of SPH simulations will prove to be highly beneficial. This may be underlined by considering a fitting illustration. Simulations of the settling and evolution of the X-ray emitting hot intra-cluster gas in forming clusters of galaxies do represent an important and cosmologically relevant example (see Borgani & Guzzo 2001 and Rosati et al. 2002 for recent reviews). The X-ray luminosity is strongly dependent upon the density of the gas. The poor accuracy of the density determination in regular SPH calculations therefore yields deficient X-ray luminosity estimates (see Bertschinger 1998 and Rosati et al. 2002 for relevant recent reviews). Despite a number of suggested remedies, such as separating particles according to their temperature, their ad-hoc nature does not evoke a strong sense of confidence in the results. Numerical limitations will of course always imply a degree of artificial smoothing, but by invoking tools based upon the DTFE technique there is at least a guarantee of an optimal retrieval of information contained in the data.

Despite its promise for the use in a variety of analysis tools for discrete data samples, such as particle distributions in computer simulations or galaxy catalogues in an observational context, its potential would be most optimally exploited by building it into genuine new fluid dynamics codes. Some specific (two-dimensional) examples of successful attempts in other scientific fields were mentioned, and we argue for a similar strategy in astrophysics. One path may be the upgrade of current particle hydrodynamics codes by inserting DTFE technology. In this study, we have outlined the development of such a SPH-like hydrodynamics scheme in which the regular kernel estimates are replaced by DTFE estimates. One could interpret this in terms of the replacement of the user-specified kernel by the self-adaptive contiguous Delaunay cell, solely and merely dependent on the local particle configuration. An additional benefit will be that on the basis of the localised connections in a Delaunay tessellations it will be possible to define and derive a more physically motivated artificial viscosity term.

The ultimate hydrodynamics algorithm would combine the virtues of Eulerian and Lagrangian techniques. Considering the positive experiences with DTFE, it appears to be worthwhile within the context of 'moving grid' or 'Lagrangian grid' methods to investigate the use of Delaunay tessellations for solving the Euler equations. With respect to a particle hydrodynamics code, the self-adaptive virtues of DTFE and its ability to handle arbitrary density jumps with only one intermediate point may lead to significant improvements in the resolution and shock handling properties. Yet, for grid based methods major complications may be expected in dealing with the non-regular nature of the corresponding cells, complicating the handling of flux transport along the boundaries of the Delaunay tetrahedra.

The computational cost of DTFE resembling techniques is not overriding. The CPU time necessary for generating the Delaunay tessellation corresponding to a point set of N particles is in the order of $O(N \log N)$, comparable to the cost of generating the neighbour list in SPH. Within an evolving point distribution these tessellation construction procedures may be made far more efficient, as small steps in the development in the system will induce a correspondingly small number of tetrahedron (identity) changes. Such dynamic upgrading routines are presently under development.

In summary, in this work we have argued for and demonstrated the potential and promise of a natural computational technique which is based upon one of the most fundamental and natural tilings of space, the Delaunay tessellation. Although the practical implementation will undoubtedly encounter a variety of complications, dependent upon the physical setting and scope of the code, the final benefit of a natural moving grid hydrodynamics code for a large number of astrophysical issues may not only represent a large progress in a computational sense. Its major significance may be found in its ability to address fundamental astrophysical problems in a new and truly natural way, leading to important new insights in the workings of the cosmos.

References

Bernardeau, F. & van de Weygaert, R., 1996, *MNRAS* **279**, 693

Bertschinger, E., 1998, *ARA&A* **36**, 599

Borgani, S. & Guzzo, L., 2001, *Nature* **409**, 39

Braun, J. & Sambridge, M., 1995, *Nature* **376**, 655

Dalgarno, A. & McCray, R. A., 1972, *ARA&A* **10**, 375

Delaunay, B., 1934, *Bull. Acad. Sci. USSR: Classe Sci. Mat.* **7**, 793

Gingold, R. A. & Monaghan, J. J., 1977, *MNRAS* **181**, 375

Gnedin, N. Y., 1995, *ApJS* **97**, 231

Hernquist, L., 1993, *ApJS* **86**, 389

Hernquist, L. & Katz, N., 1989, *ApJS* **70**, 419

Icke, V., 2002, *Priv. comm.*

Lucy, L. B., 1977, *AJ* **82**, 1013

Mavriplis, D. J., 1997, *Ann. Rev. Fluid Mech* **29**, 473

Møller, J., 1994, *Lectures on Random Voronoi Tessellations. Lecture notes in statistics*, Vol. 87, Springer-Verlag, Berlin

Monaghan, J. J., 1992, *ARA&A* **30**, 543

Nelson, R. P. & Papaloizou, J. C. B., 1994, *MNRAS* **270**, 1

Okabe, A., Boots, B., Sugihara, K., & Nok Chiu, S., 2000, *Spatial Tessellations, Concepts and Applications of Voronoi Diagrams*, John Wiley & Sons Ltd, Chichester, second edition

Pen, U., 1998, *ApJS* **115**, 19

Rasio, F. A., 1999, *arXiv:astro-ph/9911360* p. 13

Rosati, P., Borgani, S., & Norman, C., 2002, *ARA&A* **40**, 539

Schaap, W. E. & van de Weygaert, R., 2000, *A&A* **363**, L29

Schaap, W. E. & van de Weygaert, R., 2003, in E. Feigelson & G. Babu (eds.), *Statistical challenges in astronomy*, pp 483–484, Springer, New York

Shapiro, P. R., Martel, H., Villumsen, J. V., & Owen, J. M., 1996, *ApJS* **103**, 269

Sibson, R., 1981, in V. Barnet (ed.), *Interpreting Multivariate Data*, p. 21, Wiley, Chichester

Springel, V. & Hernquist, L., 2002, *MNRAS* **333**, 649

Sukumar, N., 1998, *Ph.D. thesis*, Northwestern University, Evanston, IL

van de Weygaert, R., 1991, *Ph.D. thesis*, Leiden University

van de Weygaert, R., 1994, *A&A* **283**, 361

White, S., 1996, in Schaeffer, R and Silk, J. and Spiro, M. and Zinn-Justin, J. (ed.), *Cosmology and Large Scale Structure*

Whitehurst, R., 1995, *MNRAS* **277**, 655

Appendix: colour plates

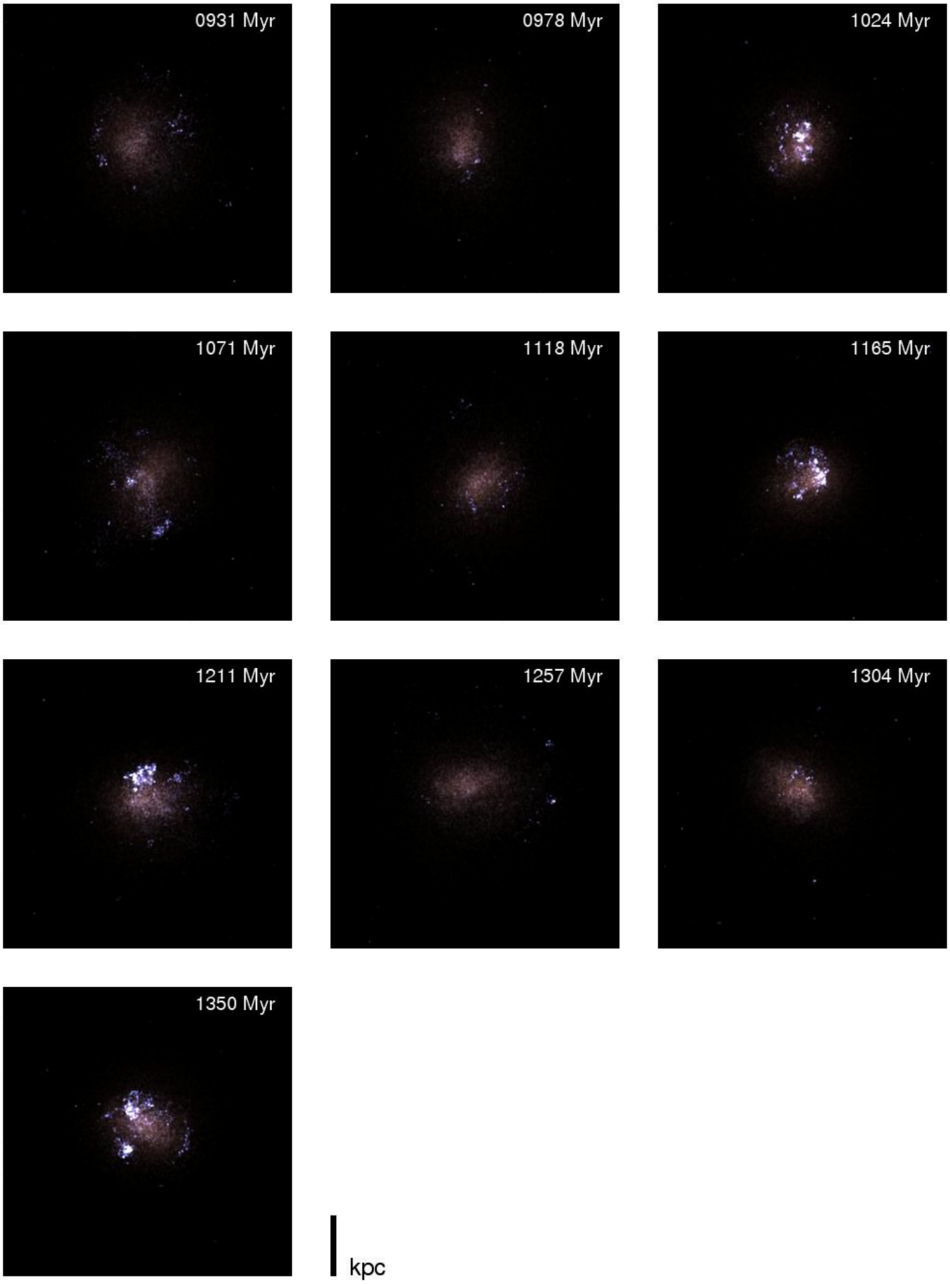

Fig. 4.2: UBV composites.

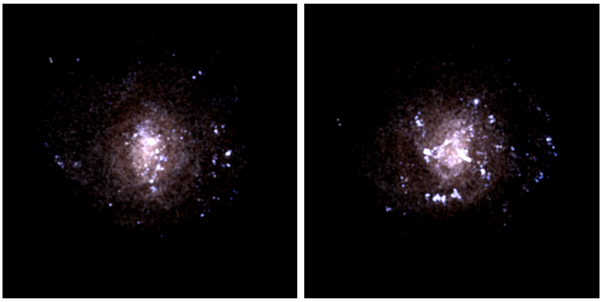

Fig. 5.8: Optical properties of model A1: UBV composites at 690 (left panel) and 745 (right panel) Myr.

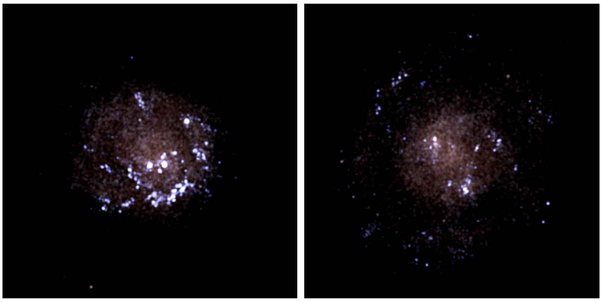

Fig. 5.9: Optical properties of model B1: UBV composites at (left panel) 505 and 630 (right panel) Myr.

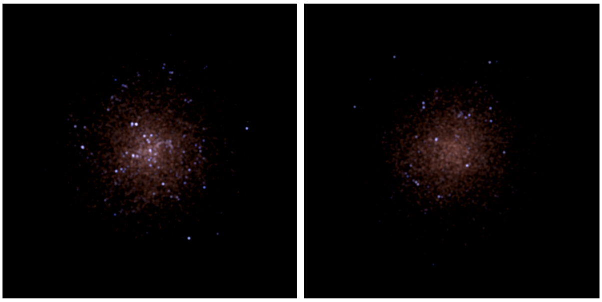

Fig. 5.10: Optical properties of model A2 (left panel) and B2 (right panel): UBV composites.

Numerieke Studies van het interstellair medium op galactische schaal

(Samenvatting)

Het bestaan van op koolwaterstoffen gebaseerde levensvormen als U en ik en van de aarde als geheel is mogelijk doordat sterren en het gas tussen de sterren deel uit maken van een complexe cyclus van geboorte, vernietiging en wedergeboorte.

Alle elementen zwaarder dan helium, “metalen” in sterrenkundig jargon, worden gevormd in de gigantische drukvaten die we sterren noemen. In het centrum van alle sterren vinden onder het gewicht van de bovenliggende gaslagen en de extreme temperaturen die er heersen (meer dan 10 miljoen graden Celsius) kernreacties plaats. Nadat een ster gevormd is uit een samentrekkende gaswolk, is deze het grootste deel van haar bestaan bezig met het omzetten van het eenvoudigste en meest veelvoorkomende element, waterstof, in het op-één-na eenvoudigste en op-één-na meest veelvoorkomende element, helium. Uit deze reactie putten sterren de energie die verdere ineenstorting tegenhoudt en zo kunnen zij miljoenen of zelfs miljarden jaren een precair evenwicht in stand houden.

Het opraken van het waterstof luidt het einde van de levensloop van de ster in. Wat er vervolgens gebeurt hangt af van de totale massa van de ster. Na 10 miljard jaar zal een middelgrote ster als onze zon, het onvermijdelijke einde enigszins rekkend door de fusie van helium tot koolstof, krimpen tot een gedegenereerde dwergster. Daarbij zwellen de buitenlagen van de ster op tot een rode reuzen ster. Uiteindelijk zullen deze ontsnappen en zich verspreiden door het omliggende gas. Voor zware sterren (zwaarder dan ongeveer 8× de massa van de zon) komt het einde sneller, na ongeveer 10 miljoen jaar, en verlopen de terminale fases complexer: doordat grotere verhitting en druk mogelijk zijn kunnen uiteindelijk alle elementen gevormd worden, tot aan ijzer toe. Hierna kan geen energie meer geproduceerd worden uit kernfusie en stort het centrum van de ster ineen tot een neutronenster of zwart gat. Als gevolg van de schokgolf die dit teweegbrengt ontploft de rest van de ster als supernova. Zo’n supernova explosie is enkele weken lang even helder als een heel melkwegstelsel en het omliggende gas wordt heftig verstoord. Echter, ook voordat dit gebeurt hebben zware sterren al een grote invloed op hun omgeving: ze vormen een krachtige bron van UV stralen welke de belangrijkste bron van verhitting is voor het gas tussen de sterren, en ze zijn tijdens hun levensloop al bezig het grootste deel van hun massa, inclusief een deel van de zware elementen die de ster gevormd heeft, weg te blazen met enorme snelheden, tot 2000 kilometer *per seconde*.

Groepjes van zulke zware sterren zijn het meest opvallende kenmerk van stervormende melkwegstelsels. Ze verhitten het omliggende gas door UV straling, en de gezamenlijke effecten van de gasstromen en supernova explosies, vaak aangeduid als de mechanische helderheid van de cluster, zorgen voor de vorming van een cocon van heet gas om de cluster. Deze bel heet gas expandeert en het omliggende gas wordt heftig verstoord. Zo heftig, in feite, dat de vorming van sterren door de afkoeling en samentrekking van gaswolken in de omgeving van een jonge cluster sterren onmogelijk wordt. Edoch, het kan zijn dat zich op de rand van deze groeiende bel zoveel gas ophoopt dat dit gas onstabiel wordt en dat er later in deze gaswolken nieuwe sterren worden gevormd, in gas dat verrijkt is met metalen uit de vorige generatie sterren.

De hoeveelheid en plaats van stervorming in een melkwegstelsel liggen dus niet van tevoren vast. Ze worden bepaald door het ingewikkelde samenspel van de koelingseigenschappen van het gas, de werking van de zwaartekracht, verhitting door jonge sterren en de dynamische reactie op krachtige gasstromen en explosies die het gevolg zijn van stervorming.

Welnu, dit proces van stervorming en terugkoppeling is het onderwerp van dit proefschrift! Het onderzoek dat hier gepresenteerd wordt is een poging de complexe processen die plaatsvinden in melkwegstelsels te volgen met behulp van computer modellen. Deze modellen moeten de evolutie beschrijven van de verdeling van gas en sterren in een melkwegstelsel, dat wil zeggen in gebieden van tienduizenden lichtjaren groot. Door dit te doen kunnen we onderzoeken wat in werkelijkheid honderden miljoenen jaren of zelfs miljarden jaren nodig heeft om te gebeuren.

Resultaten van dit proefschrift

In hoofdstuk 2 presenteren we een model voor het gas tussen de sterren, het interstellair medium. Dit model is realistischer dan voorgaande modellen doordat het, behalve de thermische evolutie, ook de ionisatie van het interstellair gas berekent en doordat het rekening houdt met de effecten van geladen stof op de UV verhitting en met kosmische straling. Dit model passen we toe in onze simulatie code, die, behalve deze aspecten van gasfysica en de bewegingen van gas en sterren onder invloed van de zwaartekracht ook berekent waar stervorming plaats zal vinden Zo verkrijgen we een programma dat zeer flexibel is en waarmee we het gedrag van uiteenlopende types melkwegstelsels kunnen onderzoeken en aldus inzicht kunnen krijgen in hun ontwikkeling.

Het is redelijk precies bekend hoeveel licht een gegeven cluster sterren produceert en wat de mechanische helderheid is. Deze mechanische helderheid kan in principe als een gewone verhittingsbron worden beschouwd bij het berekenen van de locale temperatuursveranderingen van het gas. Echter, hierbij doet zich een probleem voor: namelijk het feit dat de supernova ontploffingen zeer klein beginnen en zich dan snel ontwikkelen. Deze ontwikkeling is niet goed te volgen met een code die op grote schalen werkt. Als we de supernova energie gebruiken om het gas te verhitten, zal deze snel weer verloren gaan doordat het gas energie verliest door straling uit te zenden. In hoofdstuk 3 presenteren we twee nieuwe methoden om het effect van de mechanische verhitting op het interstellair medium in de berekening op te nemen, die dit probleem niet hebben.

Vervolgens passen we in Hoofdstuk 4 het model voor het interstellair medium en de supernovas toe in een model van een dwergstelsel. Zulke dwergstelsels zijn ongeveer 100 keer zo klein als ons eigen melkwegstelsel, en over het algemeen vertonen ze niet de spiraalstructuren die zo kenmerkend zijn voor stelsels als ons eigen melkwegstelsel. Dit maakt deze stelsels ideaal om stervorming te bestuderen. In normale spiraal stelsels wordt de stervorming namelijk voor een groot deel bepaald door deze spiraal structuur. In dwergstelsels is de stervorming in zijn meest eenvoudige vorm te bestuderen. Voor onze model dwerg vinden we een kenmerkend patroon van regelmatige variaties: de stervorming verloopt in uitbarstingen die zich elke 160 miljoen jaar herhalen. Het feit dat stelsels, die verder vrijwel identiek zijn, toch verschillend stervormingsgedrag kunnen vertonen zou dan verklaard kunnen worden door aan te nemen dat deze stelsels tijdens verschillende stadia in hun cyclus worden waargenomen.

In hoofdstuk 5 onderzoeken we wat de invloed is van de massa verdeling van een dwergstelsel op de stervorming. We laten zien dat de kenmerken van een speciaal type onregelmatige dwergstelsels, de zogenaamde blauwe compacte dwergstelsels (BCDs) het resultaat zijn van hun bijzondere bouw. De waarnemingen lijken namelijk uit te wijzen dat deze stelsels gemiddeld compacter gebouwd zijn en bijvoorbeeld hogere centrale gas (oppervlakte) dichtheden hebben. Voor het eerst laten we nu zien dat het karakteristieke stervormingspatroon van dit type stelsel, namelijk een heftige uitbarsting in het centrum, inderdaad volgt uit de waargenomen structurele kenmerken. Verder blijkt uit het tijdsverloop van de stervorming in deze stelsels dat de BCD geen duidelijke periodes van verminderde stervorming kennen. Hieruit volgt dat deze stelsels relatief jong zijn, omdat de waargenomen stervormingsintensiteit het reservoir aanwezige gas snel (dat wil zeggen in enkele miljarden jaren) uit zal putten.

We voegen in hoofdstuk 6 een belangrijke component toe aan ons computermodel, namelijk moleculair waterstof gas. Vorming van dit gas is de directe voorloper van stervorming en waarnemingen van moleculair gas vormen een zeer belangrijke onderdeel van observationele studies van eigenlijk alle soorten stervormende melkwegstelsels. Het is dan ook zeer wenselijk om de hoeveelheid moleculen H_2 theoretisch te kunnen bepalen, echter dit is zeer lastig om te doen, door de complexiteit van de natuurkundige processen die hierbij spelen. We hebben een methode bedacht om dit toch te doen door gebruik te maken van simpele oplossingen voor de balans tussen de vorming van waterstof moleculen op stofdeeltjes en de vernietiging van deze moleculen door UV fotonen voor eenvoudige structuren en deze te generaliseren door gebruik te maken van de waargenomen relatie tussen de grootte en gemiddelde dichtheid van wolken. We laten zien dat het model goede resultaten geeft bij toepassing op het probleem van de verdeling van moleculair gas in dwergstelsels.

Als laatste presenteren we in hoofdstuk 7 een alternatief voor de methode om gasdynamica uit te rekenen die we tot nu toe hebben gebruikt. De methode die we gebruiken rekent het gedrag van gassen uit door de beweging te volgen van een beperkte set deeltjes. Om dit te kunnen doen heb je een methode nodig om uit de eindige hoeveelheid deeltjes een schatting te maken voor de gas dichtheid die deze deeltjesverdeling representeert. Dit wordt normaal gesproken gedaan door de deeltjes te zien als een soort onscherp bolletje. De massa van de deeltjes wordt dan uitgesmeerd volgens wat in mathematische termen een drager functie heet. De losse deeltjes geven dan de indruk van een aaneengesloten geheel, ongeveer zoals een pointillistisch schilderij van een afstandje volledig beschilderd lijkt. De nieuwe methode maakt in plaats van een drager functie gebruik van de zogenaamde Delaunay triangulatie, hierbij wordt de dichtheid op deeltjes positie bepaald door de massa van het deeltje verdeeld te zien over het gebied afgebakend door de dichtstbijzijnde deeltjes. We laten zien dat een dergelijke dichtheidsschatting in potentie zeer grote voordelen biedt boven de normale schatting.

Curriculum vitae

In september 2000 ben ik onder begeleiding van Vincent Icke en Paul van der Werf het onderzoek naar de evolutie van melkwegstelsels begonnen waar dit proefschrift het resultaat van is. Verscheidene malen eerder heb ik mijn werk gepresenteerd, op conferenties en workshops, onder andere op Tenerife en in Durham, Tokio, Cambridge, La Thuile, op de Nederlandse Astronomen conferentie en tijdens de Dutch Astrophysics Days. Tevens heb ik de NOVA herfstschool en de XIV IAC winterschool gevolgd. Naast onderzoek, heb ik in deze tijd ook het werkcollege stralingsprocessen en het sterrenkundig practicum gegeven, alsmede de contacten van de Sterrewacht met het grote publiek onderhouden in de commissie publiekscontact.

In Juni 2000 voltooide ik met onderzoek naar de verspreiding van bacterieën op intensive care units in ziekenhuizen mijn doctoraal wiskunde aan de Universiteit Utrecht. Hierbij werd ik door Odo Diekmann begeleid. In September 1999 studeerde ik af op een onderzoek naar roterende B[e] sterren onder begeleiding van Henny Lamers, eveneens aan de Universiteit Utrecht.

In Tilburg heb ik op de Montessoribasisschool en het Sint Odulphus Lyceum de lagere respectievelijk middelbare school doorlopen.

Ik werd geboren te Callao, Peru, op 25 juni 1977, om 3 uur ’s morgens.

Nawoord

Deze laatste bladzijde is voor iedereen die er toe bij heeft gedragen dat dit proefschrift er gekomen is.

Allereerst natuurlijk een woord van waardering voor degene die de Sterrewacht draaiende houden, het secretariaat en de computergroep. Zij hebben klaar gestaan voor mij vanaf het moment dat ik op de Sterrewacht begon. Ik wil speciaal David bedanken voor de vele keren dat hij mij uit de brand heeft geholpen.

Een aantal mensen hebben mij de afgelopen maanden bijgestaan bij het afronden van dit proefschrift: Patrick, Lottie, Rowin, Jelle, Pedro, Kirsten, dank hiervoor! De theoriegroep, Garrelt, Erik-jan, Sijme-jan, Peter, Natan, en andere (oud) leden, wil ik bedanken voor de nuttige en plezierige 'interactie.'

I enjoyed playing for the Sterrewacht indoor soccer team *Forza* with Davor, Matt, Gijs, Tom and the others. Menig wetenschappelijk en niet zo wetenschappelijke discussie pleeg ik te voeren met de leden van het dispuut Christiaan Huygens. Petra, Otto, Ard, Jaron, Jan Bouwe, Johan, Glenn, Siebe en de andere leden en gasten, bedankt. Maarten, Inge, Yvette, Kirsten, Sanne, Erwin en de rest van LUSV, dank voor de plezierige tijd op het veld en erbuiten!

Degene die het dichtstbij het 'epicentrum' zaten "und" derhalve het meeste geleden hebben moeten mijn kamergenoten zijn: Arjen, Padelis, jullie waren de beste kamergenoten die ik mij kon wensen, geconcentreerd werkend en stil danwel ...ahem, niet stil. Thanks for being great examples of combining the good life and science!

Philippe en Teresa, dank dat ik af en toe de was bij jullie kon doen. Florian, ik heb je pizza de afgelopen weken node gemist;-) Michael en Ingeborg, dank dat ik bij jullie kon uitblazen. Gaëlle, Didier en Thierry, fijn dat jullie af en toe op mij gepast hebben! Mijn ouders, Elizabeth & Wim, wil ik bedanken voor wat ze me bijgebracht hebben.

Esther, je bent er, dat is genoeg.